The Hubble Space Telescope and the Evolving Night Sky: From the Diffuse Sky Surface Brightness to Transients and Variable Nuclei

by

Rosalia Denise O'Brien

A Dissertation Presented in Partial Fulfillment
of the Requirements for the Degree
Doctor of Philosophy

Approved June 2025 by the
Graduate Supervisory Committee:

Rogier Windhorst, Chair
Rolf Jansen
Alexander van Engelen
Allison Noble
Sanchayeeta Borthakur

ARIZONA STATE UNIVERSITY

August 2025

ABSTRACT

Over the last three decades, the Hubble Space Telescope (HST) has transformed astronomy with its exceptional imaging stability, precision, and resolution. From measuring how the brightness of interplanetary dust appears to change as Earth moves through the Solar System, to detecting variable supermassive black holes billions of light-years away, HST is a prime instrument for imaging the evolving night sky. This dissertation leverages HST's unique capabilities through two major programs: SKYSURF and TREASUREHUNT.

Firstly, I present new measurements of the absolute sky surface brightness across more than 150,000 HST images as part of SKYSURF (O'Brien et al. 2023). I describe a sky surface brightness measurement algorithm designed for SKYSURF that can recover the input sky surface brightness from simulated images to within 1% uncertainty. These measurements provide the most stringent all-sky diffuse brightness constraints to date in the ultraviolet to near-infrared, revealing a significant diffuse light component of unknown origin.

Next, I investigate the variability of the extragalactic sky using deep ($m_{AB} \sim 29.5$ mag), time-separated HST imaging in the JWST North Ecliptic Pole Time-Domain Field (the "TREASUREHUNT" program, see O'Brien et al. 2024). I identify a population of 12 transients (primarily supernovae) and ∼110 weakly variable active galactic nuclei. My results provide baseline variability rates for future surveys and demonstrate the power of HST in discovering faint, variable phenomena.

Finally, I develop a new zodiacal light model optimized for HST's optical wavelengths (O'Brien et al., in prep). By fitting the albedo and scattering phase function of interplanetary dust to the SKYSURF sky brightness measurements, I produce a model that outperforms previous models at UV–optical wavelengths. The final model

will be publicly released and will support background subtraction and diffuse light studies across multiple space missions.

Together, these efforts establish a comprehensive view of the changing night sky. These studies demonstrate the enduring scientific value of HST and set the stage for future discoveries with the James Webb Space Telescope, the Roman Space Telescope, the Euclid Space Telescope, the SPHEREx mission, and beyond.

DEDICATION

To my best friend, Matthew, whose encouragement underpinned every step of this degree, and to my parents, whose roles as my most valuable mentors made my scientific career possible.

ACKNOWLEDGMENTS

This work is only possible thanks to the incredible support from my research group. Thank you to my advisors: Rogier Windhorst, Rolf Jansen, Timothy Carleton, and Seth Cohen. Your trust in my work and support of my ideas are why I feel capable of continuing to pursue this career. Thank you to Tyler McCabe for being a helpful mentor as I navigated grad school. Thank you to Marisol Diaz for being the literal backbone of the group and a wonderful role model. To my wonderful students, thank you for giving me the chance to mentor you and learn from you: Brenden, Hal, M, Logan, and Tejovrash.

I also extend my greatest thanks to the entire Windhorst research group, and SKYSURF, PEARLS, TREASUREHUNT, and SKYSURF-IR collaborators, from which there are too many of you to name.

I would especially like to thank my dear grad school friends. To Darby, Peter, Alejandro, Jorge, Eb, and Haylee, thank you for helping me through everything.

To my committee, thank you for being so supportive: Alexander van Engelen, Allison Noble, and Sanchayeeta Borthakur.

To the entire SESE department for being so inclusive, thank you, especially to Kim Baptista and Meg Hufford, for championing outreach in the department. I feel so grateful to have been a part of such inspiring outreach events.

Chapter 4 of this dissertation would not have been possible without the crucial support of Rick Arendt.

Thank you to Brendan O'Connor for including me in your insightful research into undergraduate research.

A huge thank you to Vince Estrada-Carpenter and Casey Papovich for taking

me on as an undergraduate at Texas A&M. My success at ASU is purely due to the invaluable skills you taught me.

Lastly, I acknowledge the Indigenous peoples of Arizona, including the Akimel O'odham (Pima) and Pee Posh (Maricopa) Indian Communities, whose care and keeping of the land have enabled us to be at ASU's Tempe campus in the Salt River Valley, where this work was conducted.

TABLE OF CONTENTS

LIST OF TABLES

LIST OF FIGURES

Figure Page

Chapter 1

INTRODUCTION

In the early 20th century, astronomer Edwin Hubble transformed our understanding of the Universe with groundbreaking discoveries. Before his work, astronomers observed beautiful, colorful nebulae scattered across the night sky, believing these were simply clouds of gas and dust a few thousand light-years away.

However, Hubble revealed a stunning truth: these nebulae were actually distant galaxies—vast collections of billions of stars—located millions to billions of light-years away (Hubble, 1926). He recognized that galaxies come in a huge range of colors and shapes, which often correlates directly with their evolution. With this revelation, he demonstrated that the Milky Way was just one among billions of galaxies spread throughout a vast universe.

In 1929, Hubble contributed to yet another revolutionary discovery, observing that these distant galaxies were not only incredibly far away but also moving rapidly away from us (Slipher, 1917; Lemaître, 1927; Hubble, 1929). These observations provided evidence that the universe itself was expanding.

In honor of his monumental contributions, the groundbreaking Hubble Space Telescope, launched in 1990, was named after Edwin Hubble. Like its namesake, this remarkable telescope has profoundly reshaped astronomy, delivering stunning images and unprecedented discoveries over the past three decades. The Hubble Space Telescope is widely regarded as one of humanity's most successful and transformative scientific endeavors, continuing Hubble's legacy by unveiling new mysteries of the universe and inspiring generations to look up and explore beyond the stars.

1.0.1 Introduction to The Hubble Space Telescope

The Hubble Space Telescope (HST) is a space-based observatory that has served the astronomy community for over 30 years. During its life, it has watched massive comets barrel through our solar system (Bernardinelli et al., 2021), witnessed a comet crashing into Jupiter (Hammel et al., 1995), discovered moons around Pluto (Showalter et al., 2011, 2012), observed planets orbiting distant stars (e.g., Wiser et al., 2024), provided the first look at a supermassive black hole at the center of a galaxy (Harms et al., 1994), looked back over 13 billion years to image the furthest galaxy ever recorded at the time (Oesch et al., 2016), and given the first precise measurements of the expansion of the accelerated Universe (Riess et al., 1998). As described in Windhorst et al. (2024), HST has had a profound global impact on science and public engagement, producing over 500 refereed papers per year, nearly a million citations, and more than 1,100 press releases (each reaching over 400 million readers) making it NASA's most publicized space astrophysics mission.

HST currently orbits approximately 515 kilometers above the Earth's surface, far beyond Earth's turbulent and light-polluted atmosphere. This position grants the telescope extraordinary clarity, enabling astronomers to achieve unprecedented resolution and sensitivity in their observations. Figure 1 shows HST floating above Earth after a servicing mission in 1999.

From its high vantage point, HST excels at capturing images in visible, ultraviolet, and infrared wavelengths. Traditionally, astronomers relied on telescopes that observed only visible light, similar to what our eyes can see. Hubble continues this legacy, capturing breathtaking images of stars, planets, and galaxies in the familiar visible spectrum. The higher-energy ultraviolet radiation is emitted predominantly by massive,

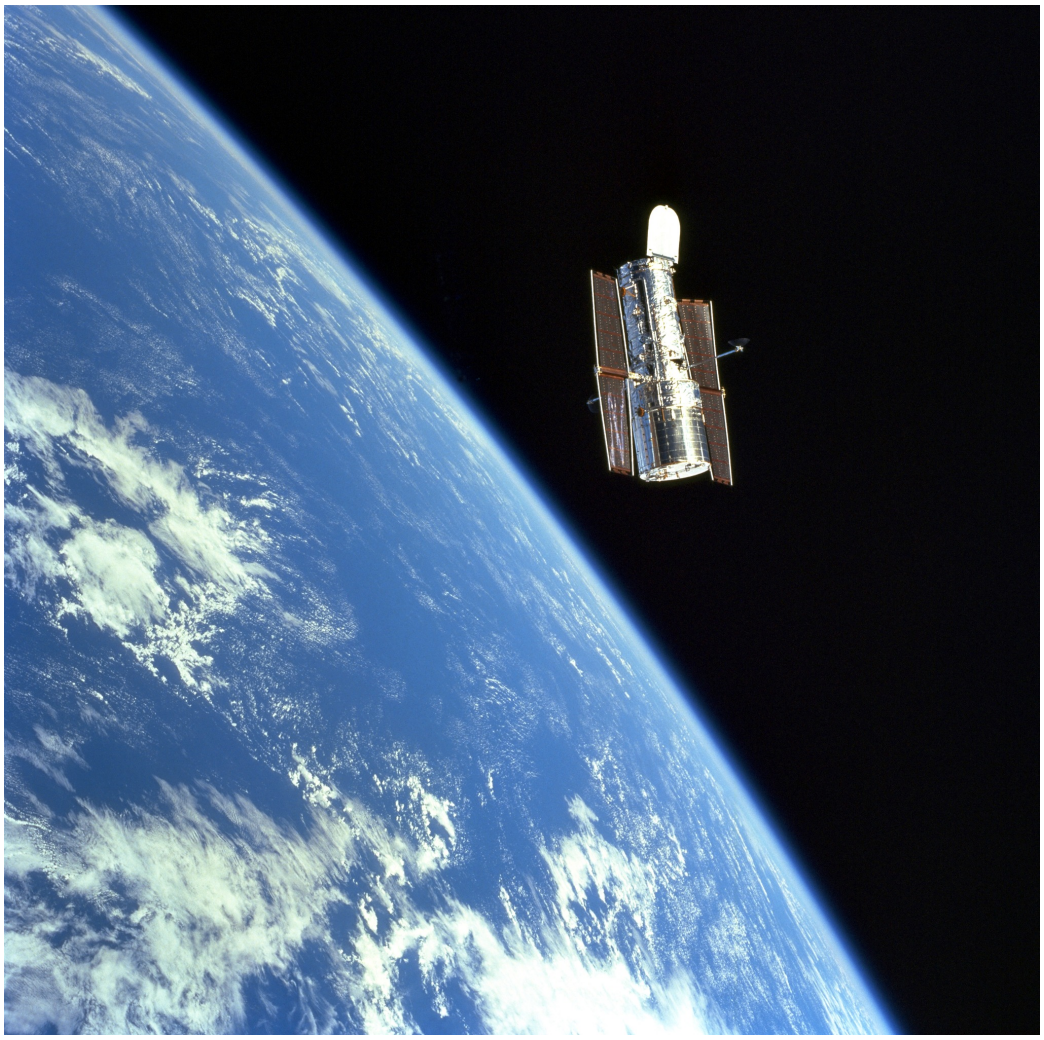

Figure 1. HST floats above Earth in December 1999, moments after being released by the Space Shuttle Discovery. This image can be found at science.nasa.gov.

short-lived stars, thereby tracing regions where stellar birth is happening. By capturing ultraviolet radiation, HST exposes energetic phenomena (such as newborn stars or the turbulent cores of young galaxies) that remain hidden in the visible spectrum. HST's infrared view (lower in energy than visible light) cuts through dusty veils that obscure much of the universe. This penetrating wavelength unveils distant galaxies and those shrouded in dust. By bridging these three wavelength regions of light, visible, ultraviolet, and infrared, HST enriches our understanding of the Universe.

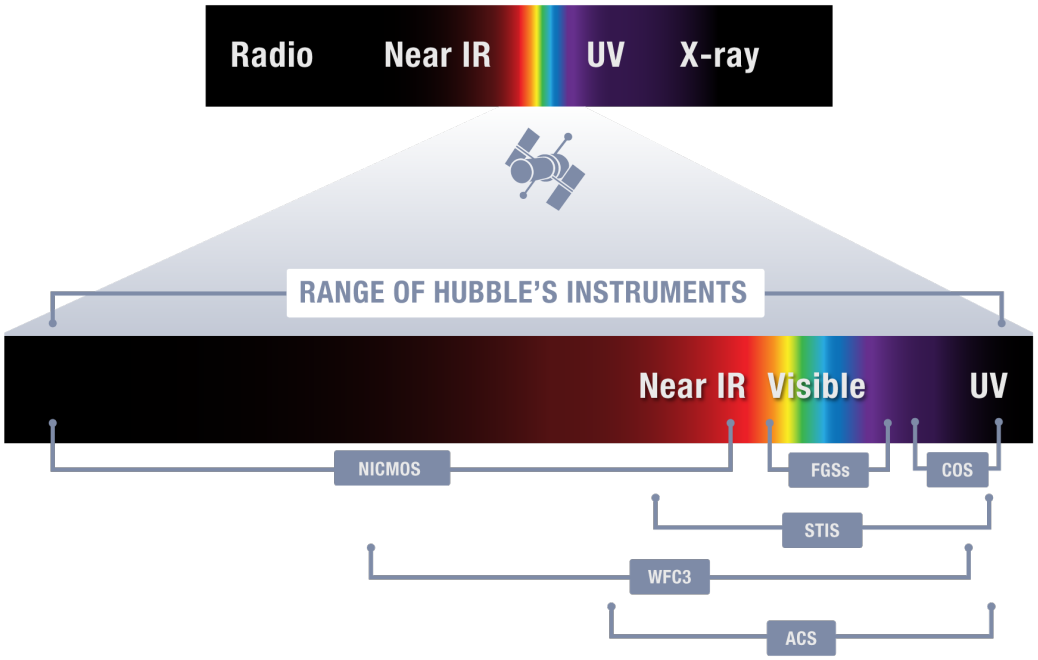

Figure 2. HST's instruments observe wavelengths from lower-energy infrared to higher-energy ultraviolet. The top of this figure showcases the electromagnetic spectrum from radio to X-ray, where HST only covers a small portion of it. The instruments on HST include the Near Infrared Camera and Multi-Object Spectrometer (NICMOS; decomissioned), Fine Guidance Sensors (FGSs), Cosmic Origins Spectrograph (COS), Space Telescope Imaging Spectrograph (STIS), Wide Field Camera 3 (WFC3), and the Advanced Camera for Surveys (ACS). Each instrument was designed to operate in a particular wavelength range. This image can be found on hubblesite.org.

To span this broad swath of wavelengths, HST carries five instruments, each with its own specialty. Figure 2 highlights the main instruments and the respective wavelength ranges they cover. This dissertation focuses on the two primary imagers: the Advanced Camera for Surveys (ACS) and Wide Field Camera 3 (WFC3). Both cameras isolate slices of the spectrum (i.e., short ranges in wavelength) with interchangeable filters (thin plates mounted on rotating wheels). A filter labeled "F606W", for instance, only allows light with a wavelength around 0.6 μm to pass through. This filter includes the hallmark wavelength of ionized hydrogen (Hα) that flags active star formation.

By selecting the appropriate filter, astronomers can target the precise colors of light needed to probe everything from newborn stars to distant galaxies.

HST is also an incredibly precise telescope, meaning it can stay very still when taking an image. This is very impressive, considering it is constantly orbiting Earth at 17,000 mph. HST's precision pointing system (enabled its Fine Guidance Sensors) keeps the telescope locked on a target with the steadiness of a laser, while its suite of instruments captures ultraviolet, visible, and near-infrared light in razor-sharp detail.

Thanks to this unique combination of stability, resolution, and broad wavelength coverage, HST has continuously produced amazing images. One of its most celebrated achievements is the Hubble Ultra Deep Field (HUDF), shown in Figure 3. To capture this image, Hubble patiently observed a single, tiny patch of sky (just 2.4 arcminutes across, roughly 1/10th the diameter of the Moon) for several days, collecting the faint photons from incredibly distant galaxies. This small region contains around 10,000 galaxies, some of which formed only a few hundred million years after the Big Bang. For a universe that is over 13 billion years old, these galaxies essentially exist when the Universe was still a baby.

The HUDF illustrates how HST's stable, high-resolution optics have expanded our view of the Universe. Observations like the HUDF are a testament to HST's extraordinary legacy as one of the most powerful and enduring observatories in history. Even today, its unmatched clarity at UV and optical wavelengths continues to unveil new wonders, serving as an inspiring reminder that space telescopes can forever change the way we see the Universe.

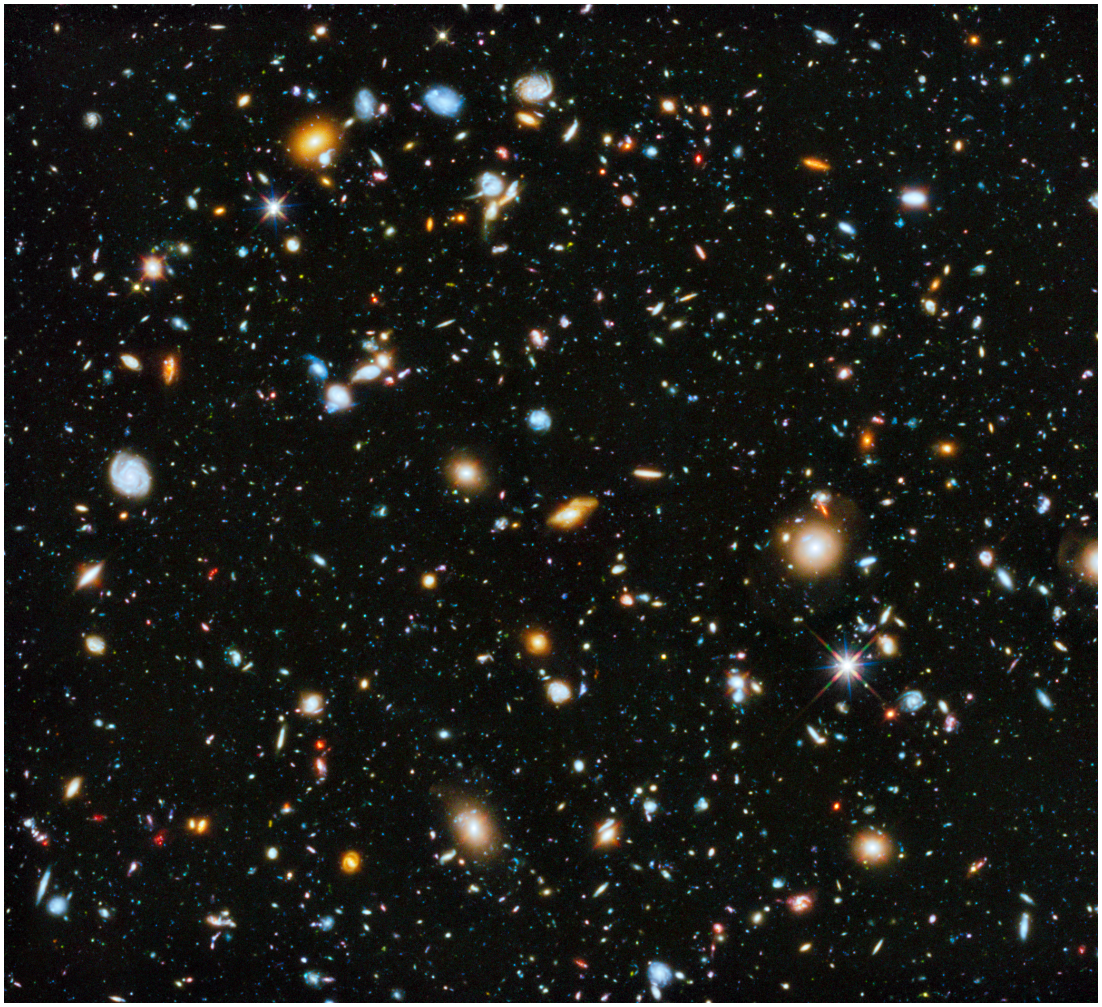

Figure 3. The Hubble Ultra Deep Field (2014) is one of HST's most famous images. It showcases the incredible variety of galaxy colors and shapes within a tiny region of the night sky. This image can be found on hubblesite.org.

1.0.2 Exploring the Time-Variable Universe with HST

HST has combined crisp, high-resolution images with a remarkably long operational life. Those two strengths, clarity and longevity, make HST much more than a camera for snapshots like the HUDF; they turn it into a time-lapse recorder for the Universe itself, able to capture how it changes with time.

Most cosmic processes unfold on timescales far longer than a human lifetime: the

Sun's eventual expansion into a red giant, or the Milky Way–Andromeda merger, lie millions to billions of years ahead. Yet many phenomena change quickly enough to watch in real time if we have the right instrument. For example, moving targets in our Solar System, like comets and asteroids, drift appreciably in just minutes to days. The brightness of pulsating variable stars (called RR Lyrae stars and Cepheids) rises and falls over days to weeks.

HST can even spot changes in galaxies millions to billions of light-years away. For example, when a massive star dies it detonates as a supernova, flaring to extreme brightness and then fading over just a few months, which HST can detect. In addition, HST can see the hot gas around supermassive black holes flicker. At the hearts of many galaxies, active galactic nuclei (AGN) are disks of super-hot gas spiraling into a supermassive black hole, which change in brightness as the black hole gobbles up new material. Because HST revisits thousands of sky fields, astronomers can line up earlier and later images to see these brief outbursts jump out against an otherwise steady background.

After three decades in orbit, HST has logged more than 1.5 million individual exposures, totaling 30 terabytes of science-grade data[1]. Figure 4 showcases how individual HST images are distributed over a large area of the night sky. Every calibrated image is publicly archived, giving astronomers baselines that now span a full generation. By aligning and subtracting these images we can trace light-sources that change with time.

Two HST programs exploit these strengths. They are the SKYSURF (Windhorst et al., 2022; Carleton et al., 2022) and TREASUREHUNT (O'Brien et al., 2024)

[1]NASA's Hubble Makes One Millionth Science Observation

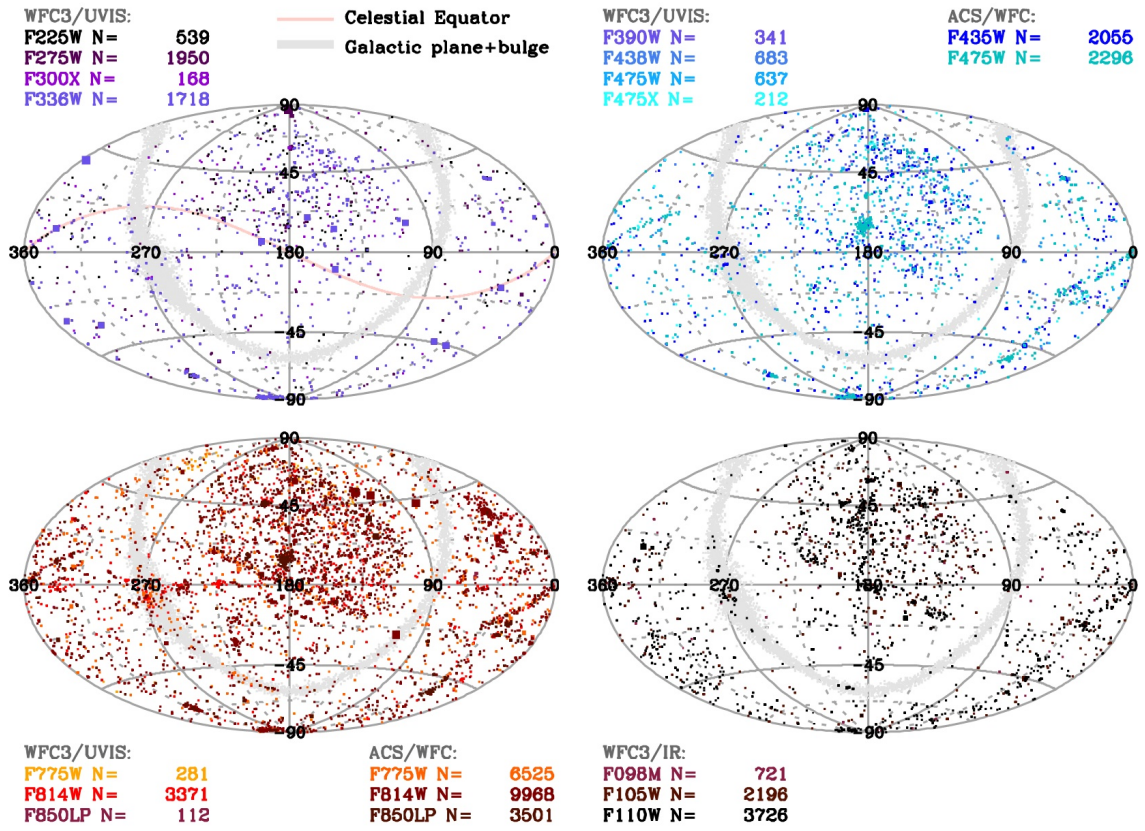

Figure 4. Representation of SKYSURF's full-sky coverage, where each point represents a single HST image, colored by wavelength. We show all ACS/WFC and WFC3/UVIS+IR images that are used in SKYSURF. The Milky Way plane is represented by the light gray band, and the Celestial Equator is indicated by the pink curve (upper left). The full version of this figure is presented in Windhorst et al. (2022).

programs. SKYSURF mines archival images to measure brightness fluctuations of the night sky, as observed by HST. TREASUREHUNT monitors a small portion of the night sky to discover supernovae, variable AGN, and other transients.

1.0.2.1 Project SKYSURF

The total sky brightness, as observed with HST in low-Earth orbit, is not constant with time. The dominant contributor to HST's night sky brightness is zodiacal light: sunlight scattered by microscopic dust that fills the space near the mid-plane of the Solar System. For context, zodiacal light supplies $> 90\%$ of the photons that HST has ever received (Windhorst et al., 2022). As Earth moves around the Sun, we look through slightly different parts of this dust cloud, so the sky can brighten or fade significantly.

Zodiacal light is considered a diffuse component of the night sky brightness, because it is not discrete like individual stars and galaxies. However, it is not the only diffuse component HST can see. Starlight from the Milky Way is reflected and re-emitted by interstellar dust, producing diffuse Galactic light. Diffuse Galactic light is strongest toward the Galactic center and can rival or exceed zodiacal light in those directions. Figure 5 shows both zodiacal light and diffuse Galactic light in a single wide-field photograph. Diffuse Galactic light does not change in brightness like zodiacal light does throughout the year, because the Milky Way is too large relative to our Solar System.

An even fainter component to the diffuse night sky brightness is the extragalactic background light (EBL), the sum of all photons being emitted by stars, dust, and growing black holes in galaxies outside of the Milky Way (e.g., McVittie & Wyatt, 1959; Partridge & Peebles, 1967a,b; Lagache et al., 2005; Kashlinsky, 2005; Finke et al., 2010; Domínguez et al., 2011; Dwek & Krennrich, 2013; Khaire & Srianand, 2015; Saldana-Lopez et al., 2021). At optical wavelengths, it consists mainly of light from stars within distant galaxies, with a smaller contribution from accretion onto

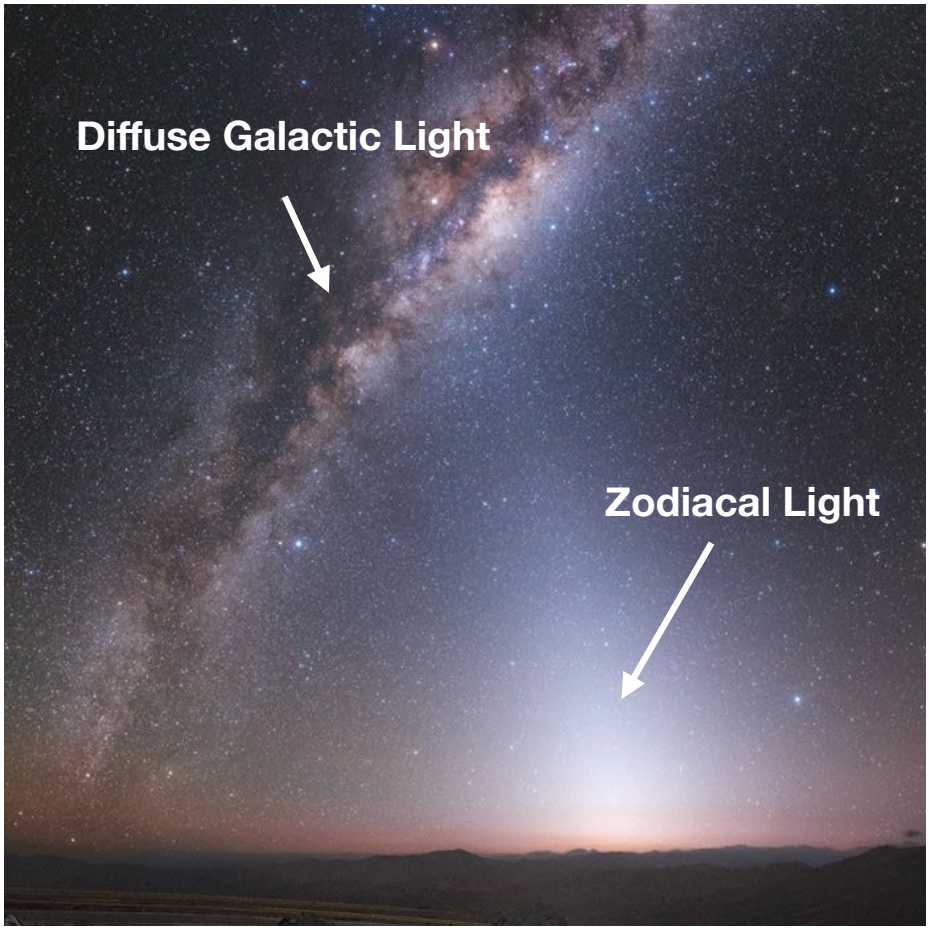

Figure 5. Image taken from Chile by Yuri Beletsky that showcases the Milky Way light (called diffuse Galactic light) and zodiacal light in a single image. Credit: Yuri Beletsky Nightscapes.

supermassive black holes (e.g., Alexander et al., 2005; Jauzac et al., 2011; Andrews et al., 2018).

From Earth, it is essentially impossible to see the EBL due to Earth's bright atmosphere, so it is not visible in Figure 5. However, Figure 3 encompasses what the EBL is very well: it is the total light seen from all galaxies in our universe. All the galaxies in Figure 3 contribute significantly to the EBL, where HST can resolve $> 97\%$ of it in this image (e.g., Windhorst et al., 2022). However, some of the EBL remains unresolved by HST. This diffuse portion is from galaxies that HST cannot

resolve because they are too faint or too distant. The diffuse component of the EBL can be measured by measuring the total light in between discrete stars and galaxies in Figure 3.

The EBL is a remarkable thing to study, because it encodes information about all stars and galaxies across cosmic time. As mentioned previously, we resolve a large portion of it with space telescopes like HST. However, the unresolved portion is just as interesting, because this is where we can study objects that may otherwise be impossible to detect. Hidden within measurements of the diffuse EBL is the light from the faintest galaxies in the universe, for which we do not yet have the technology to see. It may also carry the light from the very first stars and galaxies that are more than 13 billion light-years away and otherwise very difficult to detect (e.g., Salvaterra & Ferrara, 2003). Studying the EBL may even reveal contributions from never-before-seen exotic sources like dark matter powered stars (Maurer et al., 2012) or direct-collapse black holes (Yue et al., 2013).

Together, these sources make up the total night sky brightness, or the "sky surface-brightness", as seen by HST. It includes all the light in our Universe at these wavelengths, from the local interplanetary dust cloud that produces zodiacal light, to the most distant galaxies contributing to the EBL. The sky surface-brightness is an astrophysical source of light present in all astronomical images.

SKYSURF is the first HST program designed to measure these three components (zodiacal light, diffuse Galactic light, and the EBL) across the entire HST archive. By analyzing the sky brightness in more than 200,000 images (totaling $>$ 20 TB; Windhorst et al. 2022), SKYSURF aims to deliver the most accurate, wavelength-dependent measurements of each contributor. Ground telescopes cannot match this

because atmospheric airglow and light pollution mask much of the absolute sky surface-brightness.

1.0.2.2 Project TREASUREHUNT

There are always high energy processes happening throughout the universe. Supernovae are the explosions that happen at the end of the lives of short-lived massive stars, and can be seen from billions of light-years away. The supermassive black holes at the centers of galaxies can shine brighter than entire galaxies as they devour millions of stars in their wake. This emission is referred to as active galactic nuclei, or AGN, because these black holes are typically at the center (or nucleus) of their host galaxy.

HST is well equipped to study these objects due to its high resolution and sensitivity. It can see relatively fainter and more distant supernovae and AGN than most other telescopes since it avoids Earth's atmosphere. Due to its precision and stability, it can distinguish supernovae and AGN from their host galaxies, even for galaxies billions of light years away. In other words, you can see where a supernova or AGN is located within a galaxy. Figure 6 shows how these objects typically look with HST.

There is one area in the night sky that is particularly well suited for studying these time-variable objects. It is called the JWST North Ecliptic Pole Time Domain Field (see Figure 7), and TREASUREHUNT is an HST program to observe this field. It is a field optimized for the James Webb Space Telescope (JWST), a sister telescope to HST that observes at infrared wavelengths. HST and JWST cannot simply point anywhere at any time. For most parts of the sky, the Sun (and the Earth, for HST) restrict when they are observable. Only the Continuous Viewing Zones around the

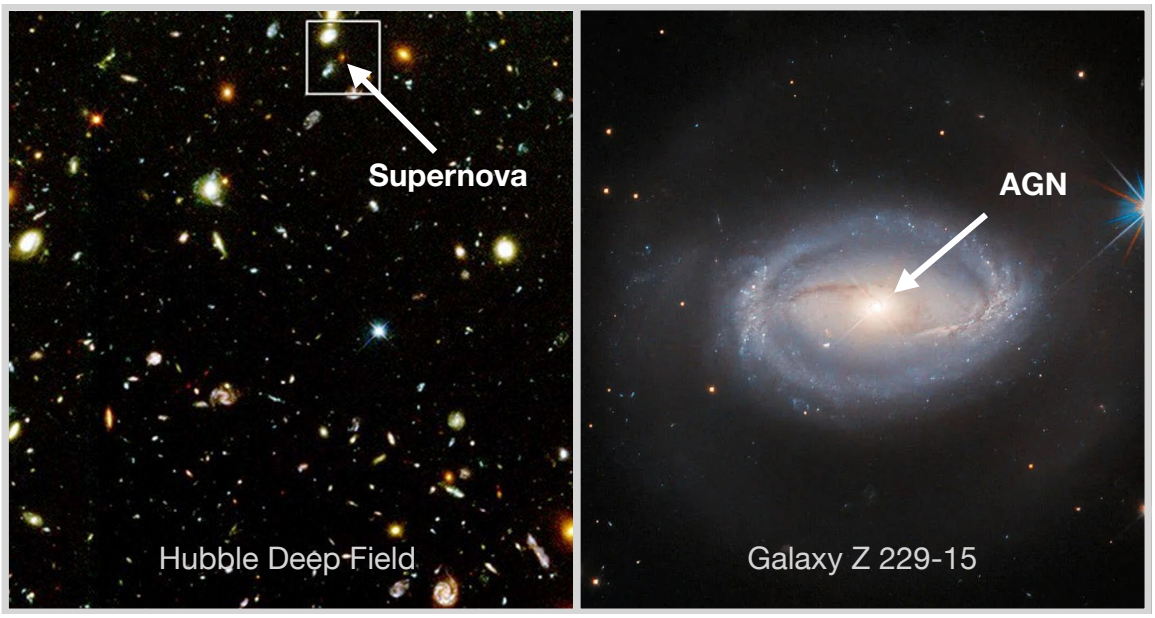

Figure 6. Supernovae and active galactic nuclei (AGN) often appear in HST images. **Left:** The tiny orange dot represents a supernova explosion from a star that died 10 billion light-years away. Discovered in the Hubble Deep Field in 1997, this was the furthest supernova ever seen at the time. Credit: NASA and A. Riess (STScI). **Right:** Galaxy Z 229-15 is a ring galaxy located 390 million light-years from Earth that likely hosts a supermassive blackhole, which creates the bright AGN visible at the center of the galaxy. Credit: ESA/Hubble & NASA, A. Barth, R. Mushotzky

ecliptic poles bypass these limits and offer uninterrupted year-round access. To exploit this advantage, Jansen & Windhorst (2018) defined the JWST North Ecliptic Pole Time-Domain Field. By being within JWST's Continuous Viewing Zone (and within HST's for a few times of the year), these telescopes can search for time-variable phenomena with significantly less restrictions. In addition, the region is free of bright stars (brighter than $m_K \approx 15.5$ mag), and bathed in exceptionally low and stable zodiacal light, which lets HST see very faint objects (as faint as $m_{AB} \sim 29$ mag).

The JWST North Ecliptic Pole Time Domain Field field has become a unique laboratory for studying objects that change in brightness or position. Thanks to its

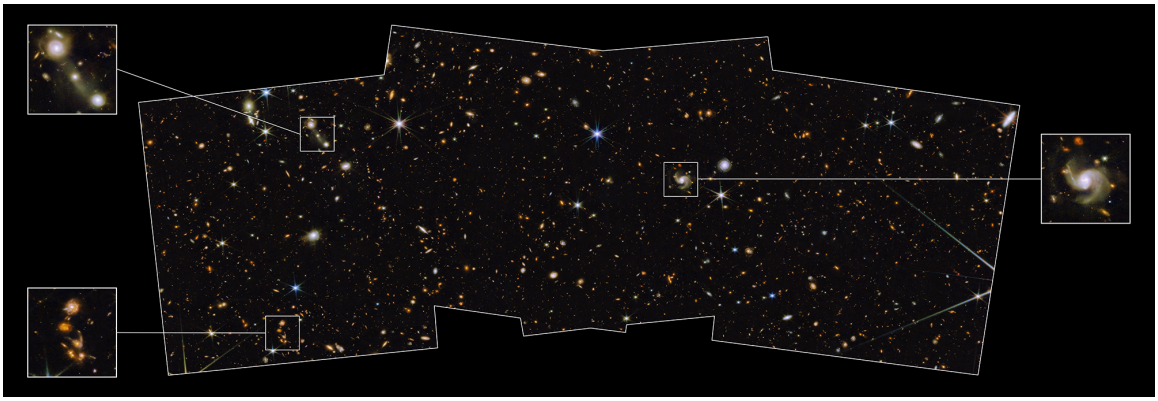

Figure 7. This portion of the JWST North Ecliptic Pole Time Domain Field covers just 2% of the full Moon's area and combines eight JWST images with three HST images, all at different wavelengths, capturing light from 0.25–5 μm. Credit: NASA, ESA, CSA, Rolf A. Jansen (ASU), Jake Summers (ASU), Rosalia O'Brien (ASU), Rogier Windhorst (ASU), Aaron Robotham (UWA), Anton M. Koekemoer (STScI), Christopher Willmer (University of Arizona), JWST PEARLS Team, with additional image processing by Alyssa Pagan (STScI).

sensitivity, HST can detect supernovae and AGN at depths unreachable from Earth's surface, unlocking key insights into dark energy, star formation, and black hole growth.

Different types of supernovae can teach us various things about the evolution of stars, star-formation within galaxies, and even the expansion of the Universe. Core-collapse supernovae are the typical type of stellar explosions that happen when a massive star runs out of fuel and collapses under its own gravity. Therefore, they trace the lives of massive stars, and enrich the cosmos with heavy elements (e.g., Matteucci & Greggio, 1986). Nonetheless their observed rates fall below expectations (e.g., Cappellaro, 2014), so identifying and studying them remains crucial. Type Ia supernovae are unique because they explode when a white dwarf star accretes too much mass and explodes due to runaway nuclear processes. Type Ia supernovae always explode with the exact same brightness, and therefore identifying them at a range of

distances makes them useful at attaining exact distances, and can be used to study the expansion rate and age of the Universe (e.g., Riess et al., 1998).

Finding and studying supernovae is a major focus for the astronomy community in the coming decades. Supernova surveys are a core part of future missions like the Roman Space Telescope and the Vera C. Rubin Observatory. They're also central to ongoing efforts like the Dark Energy Survey (DES), which aims to measure how the Universe is expanding by using Type Ia supernovae. For example, DES Collaboration et al. (2024) identified over 1,500 Type Ia supernova candidates in DES data (about 55 per square degree). While DES covers a wide area, it can't detect the faintest objects. This is where the HST has an advantage: it can detect supernovae that are too faint for ground-based telescopes, helping to complete the overall picture. O'Brien et al. (2024) found more than 200 supernova candidates per square degree using HST data. About half are likely to be Type Ia supernovae, although their selection criteria were less strict than those used by DES Collaboration et al. (2024).

Identifying and studying variable AGN are important to studying supermassive black holes and galaxy evolution. AGN variability correlates with changes in the structure of the gas disk surrounding the supermassive black hole, as well as the rate of matter accretion onto it (e.g., Shakura & Sunyaev, 1976; Ulrich et al., 1997; Kawaguchi & Mineshige, 1999). Therefore, the variability of AGN provides valuable insights into the structure and behavior of supermassive black holes, although we cannot see the black holes directly. In addition, these changes in brightness offer clues to how black holes co-evolve with their host galaxies (e.g., Gebhardt et al., 2000; Ferrarese & Merritt, 2000; Kormendy & Ho, 2013). In other words, as black holes grow and age, they can influence the structure and evolution of their galaxies, allowing us to better understand how galaxies like our own Milky Way came to be. Importantly,

identifying AGN via their variability has been proven to reveal faint or unusual AGN that are missed when using other methods (e.g., X-ray or infrared surveys, Boutsia et al., 2009; Pouliasis et al., 2019; Lyu et al., 2022). This approach helps build a more complete census of supermassive black holes in the Universe.

1.0.3 The Hubble Space Telescope and the Evolving Night Sky

In this dissertation, we explore how HST's unique abilities make it particularly suitable for studying the time-variable sky, as a part of the SKYSURF and TREASUREHUNT projects. Chapter 2 explores measurements of the sky surface brightness from HST, spanning over 150,000 images from the SKYSURF project, and was published as O'Brien et al. (2023). Chapter 3 explores the identification of supernovae and variable AGN as a part of the TREASUREHUNT program, and was published as O'Brien et al. (2024). Chapter 4 presents a new zodiacal light model, as a part of the SKYSURF project, and will be published as O'Brien et al. 2025. Finally, Chapter 5 provides a summary of this dissertation.

Chapter 2

SKYSURF: PANCHROMATIC HST ALL-SKY SURFACE-BRIGHTNESS MEASUREMENT METHODS AND RESULTS

2.1 Introduction

The diffuse sky is an extended source of light present in all astronomical images. It is responsible for the majority of all photons the Hubble Space Telescope (HST) receives (e.g., Windhorst et al., 2022), and yet remains one of the most challenging sources of light to study. The light from astrophysical sources that produce the diffuse sky are easily contaminated by several polluting sources of light. These components can be largely described by 1) light scattered and re-emitted from the Earth's surface (Earthshine), 2) the extended point spread function (PSF) of bright sources both in and out of the field of view and 3) instrumental effects (Borlaff et al., 2019). In this work, we present a novel method to isolate the diffuse sky surface brightness (sky-SB) from $0.2 - 1.6$ μm in over 140,000 HST images as part of the SKYSURF archival legacy program. Using this method, we present the first comprehensive study of the sky-SB as observed by HST using the entire Hubble Legacy Archive.

The measured sky-SB in HST images is a combination of both astrophysical sources and polluting stray light. Zodiacal Light (ZL) is the brightest of the astrophysical sources and is produced by the scattering and re-emitting of Sunlight from interplanetary dust particles concentrated in the inner Solar System (van de Hulst, 1947; Leinert et al., 1998; Kelsall et al., 1998; Sano et al., 2020; Korngut et al., 2022). ZL is so bright that it can account for more than 95% of the sky-SB at 1.25 μm. Another component

of the diffuse sky is the Diffuse Galactic Light (DGL), which is light scattered by dust and gas in the interstellar medium, as well as unresolved faint starlight. Finally, the faintest astrophysical contribution to the diffuse sky is the Extragalactic Background Light (EBL) consisting of *all* far-UV to far-IR extragalactic photons, including light from stars, AGN, and dust attenuation/ re-radiation (e.g., Andrews et al., 2017; Hill et al., 2018; Driver, 2021).

One key goal of SKYSURF is to provide a comprehensive archive of sky-SB measurements to improve existing ZL models. The ZL contains no resolvable structural component or strong spectral features from which to isolate it from other components of the sky-SB in HST images. In addition, the Earth orbits inside the Interplanetary Dust Cloud (IPD), making ZL especially difficult to constrain from Low Earth Orbit as there is no direction in which a space telescope can point to avoid it. Therefore, SKYSURF and many other programs rely on models of the IPD from historical observations of the sky-SB in order to isolate it from the DGL and EBL. However, ongoing discrepancies in ZL models make studies of the other components of the sky-SB difficult (e.g., Korngut et al., 2022).

The Kelsall et al. (1998) ZL model is widely used, as it was the first ZL model to utilize NASA's Cosmic Background Explorer (COBE) Diffuse Infrared Background Experiment (DIRBE). It characterizes the annual modulation of ZL emission to produce a three-dimensional model, covering a broad spectral range from 1.25 μm to 240 μm. COBE/DIRBE ZL emission maps have excellent relative accuracy of 1% to 2% (Leinert et al., 1998), but are limited to Sun angles of 94 deg $\pm$ 30 deg. In this work we define Sun angle to be the angle between the observation and the Sun, as shown in Figure 2 of Caddy et al. 2022. This range of Sun angles would allow the detection of any nearby spherically symmetric component of the IPD (Hauser

et al., 1998), where Sun angles furthest from 90° will show the greatest variation in brightness as a function of ecliptic latitude. This limited range of Sun angles would potentially miss a more distant spherical component (e.g., Sano et al., 2020), where the relative changes in brightness would be smaller. This more distant component would appear to be isotropic. In contrast, Wright (1998) used COBE/DIRBE data with the condition that the faintest 25 μm sky-SB at high ecliptic latitudes is only ZL. This condition means that the Wright (1998) model includes flux from any isotropic component that the Kelsall et al. (1998) model might not account for, but also runs the risk of attributing some EBL and DGL to ZL. In addition to these infrared ZL models, Leinert et al. (1998) introduced a parametric ZL model that incorporates optical wavelengths ($0.2 - 0.9$ μm) with limited data. This model assumes ZL to follow a reddened solar spectrum, which was later modified by Aldering (2001) based on observations at the North Ecliptic Pole.

In this work we present sky-SB measurements covering a more comprehensive range of Sun angles to build upon existing near infrared ZL models. We also present the first archive of sky-SB measurements with comprehensive optical sky coverage, which will help to better constrain ZL emission at these wavelengths. Quantifying the component of DGL in SKYSURF images is outside the scope of this work and will be addressed as part of future work.

Another key goal of SKYSURF is to derive robust upper limits on the EBL. A secure measurement of the EBL is vital to deriving constraints on galaxy formation and evolution (e.g., Domínguez et al., 2011; Somerville et al., 2012), as it as probes star formation, AGN activity, and dust properties over cosmic time (e.g., Andrews et al., 2017). However, due to the challenges involved in measuring the sky-SB that we have discussed, it remains the least understood component of the sky-SB (e.g., Hill

et al., 2018; Driver, 2021). Direct EBL measurements (e.g., Hauser et al., 1998; Dwek & Arendt, 1999; Cambresy et al., 2001; Matsumoto et al., 2005; Bernstein, 2007; Dole, H. et al., 2006; Matsuura et al., 2017; Lauer et al., 2021) require robust subtraction of foregrounds such as ZL and DGL, and absolute calibration of the instrument. Some experiments use unique methods to better account for ZL emission. The CIBER experiments (Matsuura et al., 2017; Korngut et al., 2022) use the calcium triplet absorption feature in the ZL spectrum to better estimate the intensity of the ZL. The Pioneer (Matsumoto et al., 2018) and New Horizons missions (Lauer et al., 2021; Lauer et al., 2022; Symons et al., 2023) leave the inner Solar System entirely to heliocentric distances where ZL emission is systematically reduced, providing improvements ($> 2\sigma$ significance) in direct measurements of EBL.

In contrast, an estimate of EBL can also be obtained by integrating the total flux from galaxy counts in deep surveys (e.g., Driver et al., 2016; Koushan et al., 2021; Windhorst et al., 2023). However, an interesting disparity is revealed when direct measurements of EBL are compared to these models derived from deep galaxy counts. This comparison yields 3–5$\times$ more EBL at optical wavelengths than we would expect based on galaxy counts alone (see Driver et al., 2016). We refer to this unaccounted-for signal as Diffuse Light (DL), as its origin is unknown.

There are many potential sources for DL, including missing galaxies (Conselice et al., 2016; Lauer et al., 2021), the extended outskirts of galaxies (e.g., Li et al., 2022; Gilhuly et al., 2022), intrahalo light (Bernstein et al., 1995; Rudick et al., 2011; Mihos, 2019), reionization (Santos et al., 2002; Cooray et al., 2004; Kashlinsky et al., 2004; Madau & Silk, 2005; Matsumoto et al., 2011), underestimated ZL or DGL models (Kawara et al., 2017; Korngut et al., 2021), telescope glow (Carleton et al., 2022), and Earthshine (Caddy et al., 2022), as well as more exotic sources such as dark matter

particles (Maurer et al., 2012; Gong et al., 2016) or black holes (Yue et al., 2013). See Windhorst et al. (2022) for a detailed summary.

The first step to better understanding the unaccounted for DL is reliable and robust sky-SB measurements. HST's capability as an ultra-sensitive, absolute photometer provides us with the necessary sensitivity to study the sky-SB. As a a result, our sky-SB measurements will enable the creation of improved, robust ZL models, and aid in constraining the amount of EBL and DL in the universe.

Windhorst et al. (2022, hereafter SKYSURF-1) summarizes Project SKYSURF, and Carleton et al. (2022, hereafter SKYSURF-2) provide in a pilot study upper limits to DL at three near-infrared wavelengths. This paper presents our methods and results for attaining robust panchromatic sky-SB measurements for all filters and all images in our SKYSURF database. In Section 2.2, we describe our SKYSURF database in detail. Section 2.3 then explains our methods for estimating the sky-SB from any HST image. In Section 2.4, we show our main sky-SB results across our entire database, including a SKYSURF spectral energy distribution (SED) of the sky-SB. We present updated SKYSURF DL limits in Section 2.5. Finally, Section 2.6 describes the SKYSURF data products that are released to the public.

2.2 SKYSURF Database

The SKYSURF database includes more than $140,000$ HST observations that are selected and summarized in Tables 1–3 of SKYSURF-1. In this paper, we focus on data taken with HST's newest cameras: the Wide Field Camera 3 (WFC3) and the Advanced Camera for Surveys (ACS). We utilize the UV-Optical (UVIS) and Infrared (IR) channels of WFC3, as well as the Wide Field Channel (WFC) of ACS.

By utilizing different cameras with similar bandpasses we are able to identify how different instrument calibration processes might affect the sky-SB.

With such a large database, we expect a varied range of target types (e.g., gas clouds, star clusters, sparse fields, resolved galaxies, etc) and exposure types (e.g., short and long imaging exposures, grism finder images or DASH observations). In the scope of the SKYSURF program, certain exposures are not useful for the purpose of probing the sky-SB SED or are likely to contain high systematic uncertainties. These include very short exposures, exposures taken through narrowband filters, quad filters, polarizers, and dispersive elements. Exposure times less than 200 seconds, where the read noise is relatively high, were not used. Experimentation with our sky measurement algorithms on simulated images showed that we were not able to get reliable sky measurements for these exposures. In addition, the sky-SB is so low in UV images with short exposure times that errors associated with post-flash (Biretta & Baggett, 2013) become a significant issue. The sky-SB measurement algorithms presented in Section 2.3 are optimized for intermediate to long exposures through HST's sensitive wider band filters. We also do not utilize images taken in a subarrayed mode, where only a specific portion of the detector is used. Finally, ACS includes linear ramp filters (full WFC coverage at continuously varying narrow bandwidth) which are not used for SKYSURF.

The standard WFC3 and ACS pipelines create two main types of bias-subtracted, dark-frame subtracted, flat-fielded images: `flt` and `flc` files, where the latter includes Charge Transfer Efficiency (CTE) corrections. Since CTE trails do not affect non-destructively read near-IR detectors, we use the `flt` files for WFC3/IR. We measure sky-SB levels on 143,231 WFC3 and ACS images. This includes 41,431 WFC3/IR `flt` images, 26,542 WFC3/UVIS `flc` images, and 75,258 ACS/WFC `flc` images. Within

this sample, there are 4,767 unique proposals and 22,883 unique target names. We report sky-SB measurements through 6 WFC3/IR, 14 WFC3/UVIS, and 8 ACS/WFC filters.

2.3 Sky-SB Measurement Methods

In order to produce robust sky-SB measurements with HST, we make use of sky-SB estimation algorithms designed for SKYSURF, careful consideration of uncertainties, and the removal of stray light dominated images from our sample.

2.3.1 Sky-SB Algorithms

As shown in SKYSURF-1 and Section 2.8.2, we tested various algorithms using simulated images. We simulate WFC3/IR F125W images with realistic galaxy and star counts. We explore a range of exposure times from 50 to 1302 seconds and sky-SB levels ranging from 0.22 to 3.14 electrons per second. In order to simulate the effects of out of field stray light and ZL gradients in our test images, we apply sky gradients to our simulated images ranging from 0% to 20% across the field of view. ZL gradients will be much smaller than 20% in a typical WFC3 or ACS field of view, but observations taken close to the Earth's limb may approach 20%. Testing images that contain these steep gradients allows us to ensure our algorithms can consistently isolate the true sky-SB even under the most challenging conditions. Section 2.8.1 describes the creation of these simulated images in detail.

We initially choose the two algorithms which are able to consistently retrieve the known input sky-SB from the simulated images: the ProFound Median (Pro-med)

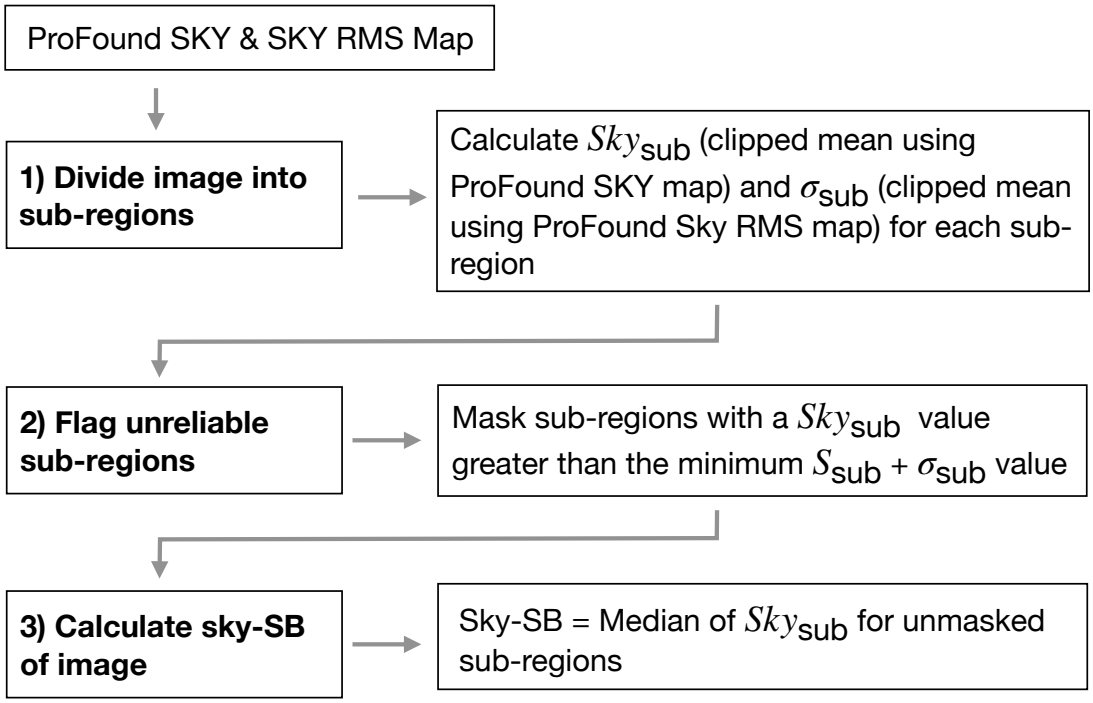

Figure 8. Flowchart of the ProFound Median (Pro-med) pipeline to estimate the sky-SB from an HST image.

method and the ProFound-5th (Pro-5th) method. Although these algorithms were developed independently, the Pro-med and Pro-5th algorithms are very similar, aside from the fact that the former uses a median and the latter uses a 5th-percentile. Nevertheless, both are found to be able to retrieve the input sky-SB to within 1% (see Figure 18). For this paper, we focus on the Pro-med algorithm, which is found to be most accurate in general. Nevertheless, Section 2.8.3 explains the Pro-5th method in detail, as well as details sky-SB measurements using this algorithm.

A flowchart showing our pipeline is given in Figure 8. We utilize sky-SB maps created with ProFound (Robotham et al., 2018), a source finding and image analysis package that is able to interpolate behind objects to create a map of the sky-SB. To

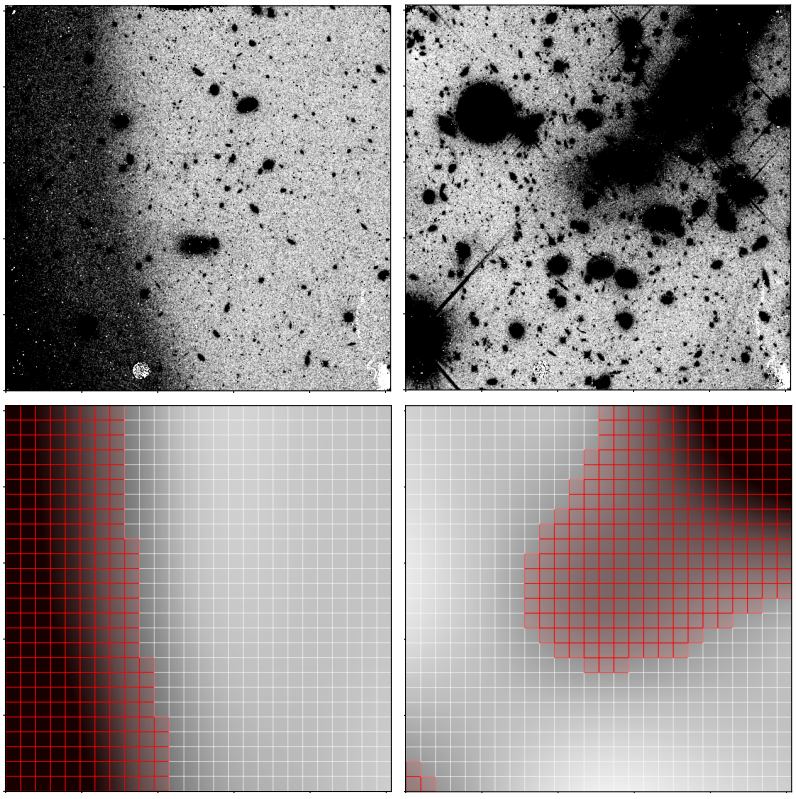

Figure 9. SKYSURF sky-SB estimation algorithms are able to mask areas of an image containing light from discrete objects or bright sky gradients. The top row shows two example images in our SKYSURF database. The bottom row shows corresponding ProFound SKY maps, with the borders of Pro-med sub-regions overlaid. The bottom left ProFound map corresponds to the top left image, and similarly for the right-most images. The sub-regions used for the Pro-med algorithm are overlaid with white or red borders. Red sub-regions are identified by our algorithms as likely containing light contamination, and are masked during sky-SB estimation. We show these images to demonstrate our ability to reject areas of an image, but emphasize that images like this are rejected for sky-SB analysis because they are too crowded, as identified by the amount of red sub-regions.

do this, ProFound utilizes a discrete boxcar filter on a grid. The resulting coarse grid is bicubic interpolated to construct the sky-SB map. Any objects detected in the image are masked. We refer to these ProFound sky-SB maps specifically as ProFound SKY maps herein. An example of ProFound SKY maps are shown in the bottom row of Figure 9.

We create ProFound SKY maps for all images in the SKYSURF database. We run

Uncertainty	WFC3/UVIS	WFC3/IR	ACS/WFC
Sky Algorithm	0.4%	0.4%	0.4%
Flat-field	1%	2%	2.2%
Zeropoint	0.2%	1.5%	1%
Non-linearity	N/A	0.5%	N/A
Bias	0.2 e^- (1.4%)	0.005 e^-/s (0.7%)	0.6 e^- (1.5%)
Dark	0.3 e^- (2.1%)	0.005 e^-/s (0.7%)	0.5 e^- (1.2%)
Thermal Dark	N/A	0.01 e^-/s (1.3%)	N/A
Post-flash	0.16 e^- (1.1%)	N/A	0.37 e^- (0.9%)
Total	3.0%	3.1%	3.2%

Table 1. Multiplicative uncertainties (top rows) are listed as a percent of the sky-SB for WFC3/UVIS, WFC3/IR, and ACS/WFC. Additive uncertainties (bottom rows) list the error in units of electrons (e^-) or electrons per second (e^-/s), with the average percent of the sky-SB shown in parenthesis. Sky Algorithm refers to the ability of our algorithm to retrieve the true input sky from simulated images, and follows from SKYSURF-1. Flat-field refers to uncertainties in flat-field correction. Zeropoint refers to uncertainties in detector zeropoints. Non-linearity refers to the non-linearity of WFC3/IR. Bias and Dark refer to subtraction uncertainties in bias and dark frames. Thermal Dark refers to uncertainties in the Thermal Dark signal (thermal noise from the telescope assembly and instruments) described in Carleton et al. (2022). Post-flash refers to uncertainties is post-flash subtraction. The last row shows the total error as a percent of the sky-SB, which is a median uncertainty of all images in the corresponding camera.
WFC3/UVIS: Flat-field (Mack et al., 2016), Zeropoint (Calamida et al., 2022), Bias (McKay & Baggett, 2017), Dark (Bourque & Baggett, 2016), Post-flash (SKYSURF-1)
WFC3/IR: Flat-field (Mack et al., 2021), Zeropoint (SKYSURF-1), Non-linearity (The WFC3 Instrument Handbook), Bias (SKYSURF-1), Dark (SKYSURF-1), Thermal Dark SKYSURF-2
ACS/WFC: Flat-field (Cohen et al., 2020), Zeropoint (Bohlin et al., 2020), Bias (Lucas & Rose, 2021), Dark (Anand et al., 2022), Post-flash (SKYSURF-1)

ProFound with a large `box` size of 1/3 of the image dimensions, which decreases the resolution of the SKY maps and helps smooth over any local effects from bright objects that can leave behind features. To best remove light from the outskirts of objects, we enlarge the object masks such that the sky-SB around the enlarged aperture is correct. In addition, we mask every pixel flagged in the image data quality extension, as well as its immediate neighboring pixels. ProFound was run using default parameters otherwise.

The Pro-med method follows three steps: 1) divide each ProFound SKY map into sub-regions and calculate sky-SB levels for each sub-region, 2) flag sub-regions with unreliable sky measurements, and 3) take the median of unflagged sub-regions to determine the sky-SB of the image. All WFC3/IR images in our sample are 1014×1014 pixels, and we create 39×39 pixel sub-regions, for a total of $26 \times 26 = 676$ sub-regions per SKY map. For WFC3/UVIS, a full-frame detector image has dimensions of 2051×4096 pixels. For this case, we make each sub-region 64×64 pixels, where the few remaining pixels will be added to the sub-regions on the top-most row and right-most columns. For ACS/WFC, the detector has dimensions 2048×4096, and we follow the same binning technique as for WFC3/UVIS. Both WFC3/UVIS and ACS/WFC images include two CCD detectors (stored as separate science extensions), and we perform sky-SB measurements on each detector independently.

Next, we calculate the sky level ($S_{\rm sub}$) for each sub-region in native pixel units: electrons per second for WFC3/IR and electrons for WFC3/UVIS and ACS/WFC. We first mask all outlier pixels within a single sub-region that are not part of the background using boundary values of -126.5 and 895.5, which were motivated by extremes in noisy WFPC2 data and are designed to eliminate the most obvious outliers. The mean ($S^{'}_{\rm sub}$) and standard deviation ($\sigma^{'}_{\rm sub}$) of the remaining pixels are then recorded. We then mask pixels which have a value less than $S^{'}_{\rm sub} - 5\times(\sigma^{'}_{\rm sub})$ or more than $S^{'}_{\rm sub} + 3\times(\sigma^{'}_{\rm sub})$. We are more stringent with the upper cutoff since, for normal images, the distribution of pixels leans towards the positive side. New values of $S^{'}_{\rm sub}$ and $\sigma^{'}_{\rm sub}$ are calculated for the remaining pixels. This process is repeated until there are no outlier pixels remaining. The median value of the last iteration is saved as the $S_{\rm sub}$ ($\sigma_{\rm sub}$) for that sub-region.

In order to mask sub-regions, we compare each $S_{\rm sub}$ in a single sub-region to all

the other $S_{\rm sub}$ values in a single image. If a $S_{\rm sub}$ value for a sub-region is greater than the minimum $S_{\rm sub}+\sigma_{\rm sub}$ of all the sub-regions, then we conclude that the sub-region likely contains light contamination from an object and this sub-region is masked. This step is critical to ensuring we are only utilizing sub-regions with the highest probability of being stray light free. Figure 9 shows examples of how this algorithm masks sub-regions on `flt`/`flc` files.

The final sky-SB level of a chip, $S_{\rm chip}$, is the median of the remaining $S_{\rm sub}$ values. To calculate $\sigma_{\rm sub}$, we use the same method used to calculate $S_{\rm sub}$ but instead perform it using the ProFound SKY RMS map. As shown in SKYSURF-1 and Section 2.8.2 here, this algorithm is demonstrated to recover the simulated sky-SB with an error of $< 0.4\%$ for expected sky gradients of $< 10\%$ on simulated F125W images.

As shown in Section 2.8.2, the Pro-med method is demonstrated to be the best estimator of the sky-SB. Therefore, the Pro-med method is chosen to derive robust sky-SB measurements in this paper, and thus produce the SKYSURF SED of the sky-SB presented in Section 2.4.

To further confirm that our sky-SB measurements are not contaminated by the light from discrete objects, we check whether our sky-SB measurements increase with the number of stars and galaxies in an image. If the sky-SB increased with the amount of light from discrete objects, it could indicate that our sky-SB measurements are accidentally picking up the faint outskirts of galaxies or the extended PSFs from stars. SKYSURF-1 performs this test for the F125W filter only and finds no increase in the sky-SB as a function of the amount of object light. We tested this also for F140W and F160W, and find the same results. Therefore, a Diffuse Light limit estimated using the sky-SB algorithms in this work is unlikely to come from the faint outskirts of galaxies.

We subtract from WFC3/IR estimates the thermal dark signal as described in SKYSURF-2. These values are listed in Table 2.

	Thermal Dark	
Filter	[e s^{-1}]	[MJy sr^{-1}]
F098M	0.0044	0.0023
F105W	0.0044	0.0013
F125W	0.0040	0.0012
F140W	0.0201	0.0050
F160W	0.0772	0.0308

Table 2. Thermal Dark values (Carleton et al., in prep) that are subtracted from sky-SB measurements in this work.

2.3.2 Flagging Unreliable Images

In addition to the broad filtering of images described in Section 2.2, after performing sky-SB measurements we filter out images where the sky-SB level is deemed unreliable. This includes measurements where the image is dominated by bright objects, images with very high sky-SB rms levels, or images where a guide star was lost. These measurements are still available for public use, but are not used in SKYSURF analysis.

Within the scope of this work, the sky-SB cannot be measured from images that are saturated with bright sources. These include exposures that contain star clusters, galaxies that take up a large portion of the field-of-view, or steep sky gradients. Since our algorithms record the number of sub-regions that are flagged as unreliable, a high number of unreliable sub-regions indicates that the sky-SB must also be unreliable. We reject sky-SB measurements where more than 30% of sub-regions are flagged as unreliable. These regions are shown as red in Figure 9.

A high sky-SB rms ($\sigma_{\rm chip}$) can also indicate an unreliable measurement. We predict

the sky-SB rms of an image to be a combination of expected Gaussian and Poisson noise (shot noise):

$$\sigma_{\text{predicted}} = \frac{\sqrt{R^2 + S_{\text{chip}} \times t}}{t}, \tag{2.1}$$

where $\sigma_{\text{predicted}}$ is the predicted sky-SB rms in electrons per second, R is the detector readnoise in electrons, S_{chip} is the sky-SB in electrons per second, and t is the exposure time in seconds. We reject images where $\sigma_{\text{chip}} > 2\sigma_{\text{predicted}}$.

In IR detectors an afterglow remains in pixels that were saturated in previous exposures. This phenomenon is called persistence and is known to affect WFC3/IR images. Therefore, we need to ensure it does not influence our sky-SB measurements. The standard pipeline for IR images does not eliminate flux from persistence. However, the WFC3 team has developed a software that estimates the amount of persistence per `flt` file. This produces pixel maps (labeled as `_persist.fits`) that estimate the amount of internal and external persistence for a given image (see Gennaro, 2018). We masked pixels in 30 random F160W images with values greater than 0.005 electrons per second in the `_persist.fits` file and reran our sky-SB algorithm. For most images, we did not find significant differences in the sky-SB level when masking pixels that are affected by persistence. We found $\sim$0.25% differences in sky-SB for images where more than 1% of the pixels are affected by persistence, where an affected pixel is defined to be one with $\text{Flux}_{\text{persistence}} > 0.01$ electrons per second. We therefore reject images where more than 1% of the pixels are affected by persistence.

To reduce the probability that images may be contaminated by sources like Earth's limb or the Milky Way, we follow the methods described in SKYSURF-1. We reject images within 20°of the galactic plane to reduce contamination due to Galactic cirrus, and densely populated star fields. To reduce the impact of Earthshine, images with

Sun altitudes greater than zero are also removed. Here we define Sun altitude as the mean angle of the Sun above the Earth's horizon over the duration of an observation. Finally, we reject images with Sun angles less than 80°and with Moon angles less than 50°. Section 4.3 and Appendix A.2.2 of SKYSURF-1 show that Sun angles less than 80° can be problematic. The minimum sky-SB for Sun angles $\lesssim$80° is greater than for Sun angles $\gtrsim$80°, in part due to increasing ZL intensity closer to the Sun, although the main cause is not known. For example, it is possible that Sun angles $\lesssim$80° are affected by scattered sunlight.

We carefully reject images taken too close to nearby galaxies and globular clusters that might take up HST's entire field of view. We utilize galaxies selected as listed in the Third Reference Catalog of Bright Galaxies (RC3, de Vaucouleurs et al., 1991). We locate the positions of all galaxies larger than 2 arcmin in diameter, and reject images that are within $1R_{\rm galaxy}$ to the center of the object. $R_{\rm galaxy}$ is adopted directly from the RC3, and is half the apparent major axis isophotal diameter of a galaxy measured at a surface brightness level of 25.0 B-mag per square arcsecond[2].

Critically, we opted to manually inspect our SKYSURF images to understand how well our algorithm performs and try and identify images that are not automatically flagged using the process described above. We flag images that are smeared (due to loss of a guide star), or are clearly saturated with objects. For our filter with the largest number of images, ACS/WFC F814W, $< 0.2\%$ of the images were flagged, confirming the above methods to reject unreliable images. We reject remaining images flagged during the manual inspection.

In addition, during the manual inspection, we flag images with visible satellite trails and artifacts like optical ghosts. These images are not rejected. However, to

[2]https://heasarc.gsfc.nasa.gov/W3Browse/all/rc3.html

ensure image artifacts are not accidentally recorded as objects, the list of satellite trails and optical artifacts are recorded for consideration for star and galaxy counts.

Table 3 shows the percent of images in each SKYSURF filter that are not flagged by the methods described here and are thus deemed reliable. The number of reliable images per filter is typically between 5–20%, however some filters exhibit lower reliability due to being used frequently in problematic observations (e.g., F555W is often used for stellar populations studies, and thus includes many observations of star clusters). We emphasize that many of the images rejected here are still beneficial for galaxy and star counts and reducing cosmic variance. As a result, while they are not used to derive sky-SB limits in this work they are not excluded from the SKYSURF database.

2.3.3 Sources of Uncertainty

There are many sources of uncertainty during data reduction and calibration that are inconsequential for studies of discrete objects, but remain important when measuring the sky-SB. SKYSURF-1 summarizes the main SKYSURF sources of error in detail. We summarize updated sources of uncertainty in Table 1.

We follow the methods of SKYSURF-1 to add our uncertainties in quadrature. We present our results assuming all systematics have been accounted for through various WFC3 and ACS Instrument Science Reports (e.g., Gennaro, 2018; Lucas & Rose, 2021). Therefore, SKYSURF sky-SB uncertainties represent *random* uncertainties in the ability to determine a bias frame, dark frame, flat-field, etc. In addition, SKYSURF-1 explains that the two dominant sources of error, which are zeropoint and flat-field uncertainties, are independent, and thus can be added in quadrature.

Camera	Filter	Reliable Images [#]	Reliable Images [%]
ACS/WFC	F435W	1664	15
ACS/WFC	F475W	915	8
ACS/WFC	F555W	196	4
ACS/WFC	F606W	4817	15
ACS/WFC	F625W	373	12
ACS/WFC	F775W	1888	10
ACS/WFC	F814W	8918	16
ACS/WFC	F850LP	5013	29
WFC3/UVIS	F225W	346	15
WFC3/UVIS	F275W	684	8
WFC3/UVIS	F300X	52	18
WFC3/UVIS	F336W	568	7
WFC3/UVIS	F390W	347	19
WFC3/UVIS	F438W	118	5
WFC3/UVIS	F475X	42	6
WFC3/UVIS	F475W	289	15
WFC3/UVIS	F555W	62	2
WFC3/UVIS	F606W	1138	10
WFC3/UVIS	F625W	61	7
WFC3/UVIS	F775W	43	7
WFC3/UVIS	F850LP	68	17
WFC3/UVIS	F814W	1241	9
WFC3/IR	F098M	205	18
WFC3/IR	F105W	1102	23
WFC3/IR	F110W	497	7
WFC3/IR	F125W	1109	20
WFC3/IR	F140W	768	16
WFC3/IR	F160W	2460	12

Table 3. Fraction of images with reliable sky-SB measurements for every SKYSURF filter. These images are chosen using the methods of Section 2.3.2. Reliable images have no more than 30% of sub-regions flagged, contain expected noise levels based on Gaussian and Poisson noise, are not manually flagged, and are not significantly affected by persistence. In addition, we remove images that are within 20° of the galactic plane, have sun altitudes greater than 0°, are too close to a large nearby galaxy, have Sun angles less than 80°, or have moon angles less than 50°. We list the number of reliable sky-SB measurements and the percent of total images in the SKYSURF database that are reliable.

Uncertainties for each camera are presented separately. We are careful to distinguish between multiplicative errors, which depend on the level of the sky-SB, and additive errors, which are the same regardless of image brightness. Further explanation of these uncertainties, as well as an exploration of the effect of crosstalk, amplifier differences, and flat-field residuals on sky-SB measurements, are presented in Section 2.8.4.

2.4 Sky-SB Measurement Results

We perform sky-SB measurements using the Pro-med algorithm and show our results here. The process for converting our images to units of flux density is described in Section 2.8.5.

2.4.1 Sky-SB versus Ecliptic Latitude

Figures 10-13 show our results as a function of Ecliptic Latitude. Results for some duplicated filters are presented independently for each camera, as the filters will have a different bandpass when paired with each camera. In addition, given their subtle zeropoint differences, this provides an independent check on the sky-SB values with different instruments.

The bottom row of Figure 13 includes the hyperbolic secant curves derived in SKYSURF-2 using the Kelsall et al. (1998) Zodiacal model. They represent the range in sky-SB values expected as a function of ecliptic latitude. SKYSURF-2 did not apply the same aggressive filtering of images described in this work. Therefore, our measurements don't span as large of a range as the grey curves might suggest. Overall, these limits are largely driven by Sun angle, where lower Sun angles result in brighter

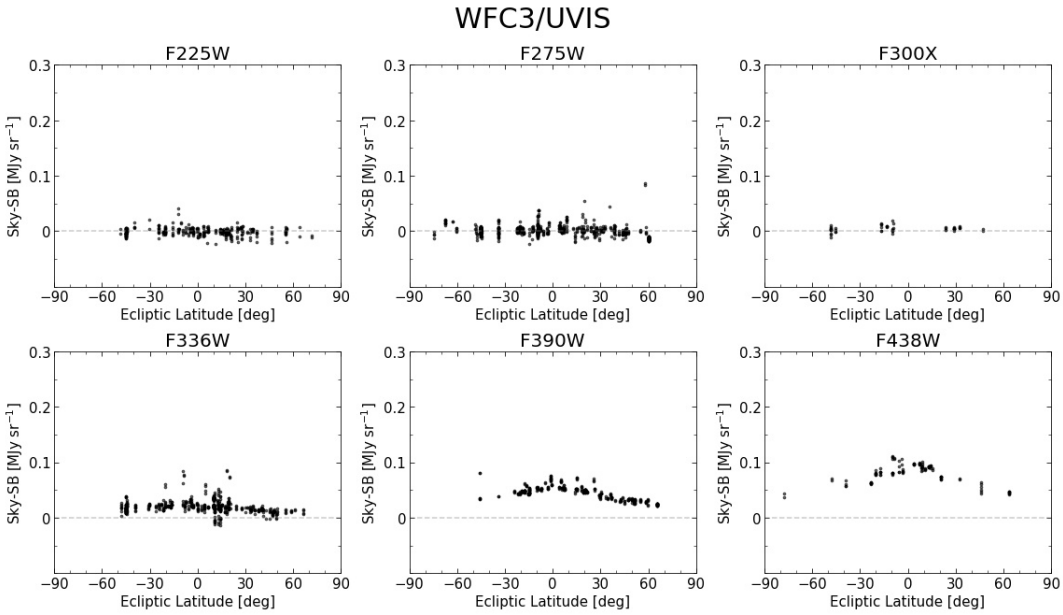

Figure 10. SKYSURF sky-SB measurements versus Ecliptic Latitude for WFC3/UVIS (UV filters), zoomed in to show the range between -0.1 to 0.3 MJy sr^{-1}.

sky-SB levels at the same ecliptic latitude. Therefore, the range in expected sky-SB levels is broader closer to the ecliptic plane due to the broader range of Sun angle's available here. Our measurements fall conservatively within these limits, showcasing our ability to successfully reject images from our database.

Some notable deviations from the expected sky-SB are the spike in sky-SB values at an ecliptic latitude of $-45°$ in F105W due to Hubble Ultra Deep Field observations. This is likely due to the 1.083 μm emission line present in this filter (Brammer et al., 2014). In addition, Earthshine can still affect images even after removing images with low Earth limb angles because the Earth limb angle is estimated for each image as an average over the entire exposure. Remaining outliers will be carefully considered and manually removed before performing Diffuse Light analysis in a future work.

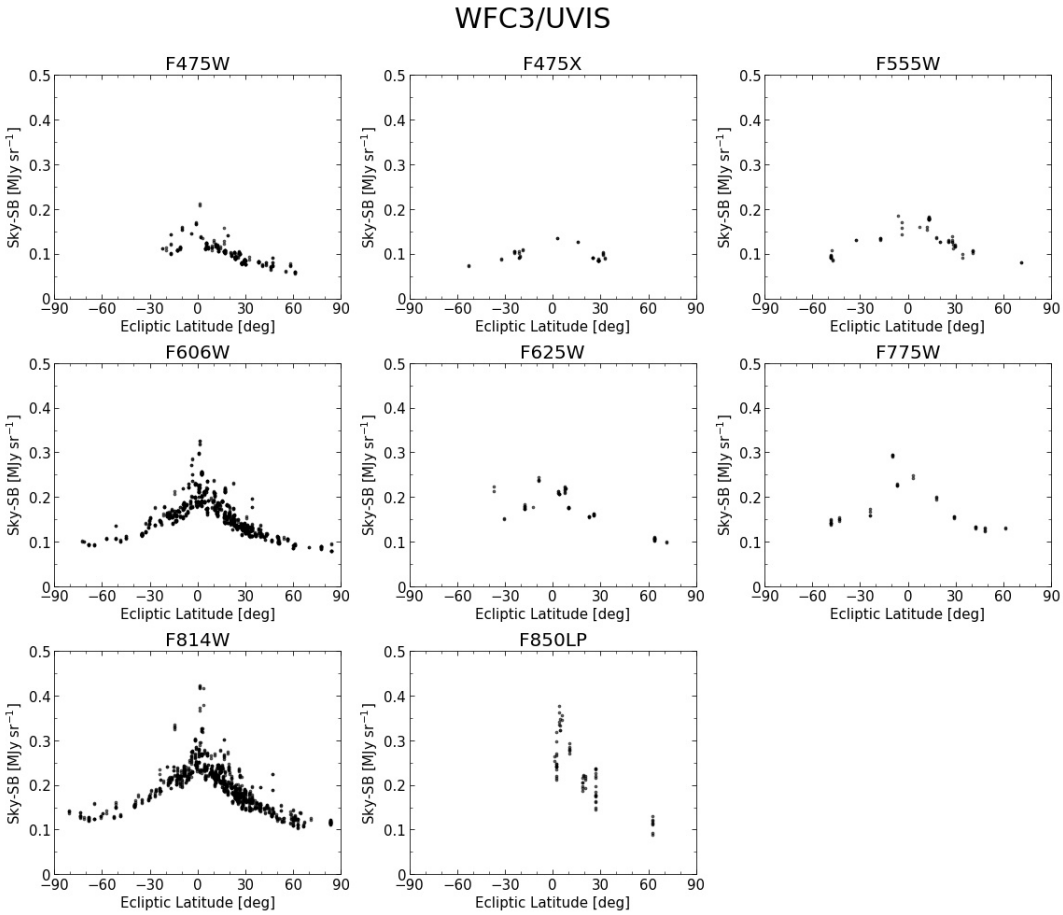

Figure 11. SKYSURF sky-SB measurements versus Ecliptic Latitude for WFC3/UVIS (Optical filters), zoomed in to show the range between 0 to 0.5 MJy sr^{-1}. There is a larger scatter in the F850LP filter due to the high sky-SB rms of this filter.

2.4.2 Sky-SB SED

In order to demonstrate how our generated sky-SB measurements can recover the ZL surface brightness and compare our results to the literature, we create a SED of the observed sky-SB at HST wavelengths. Figure 14 shows our sky-SB SED at high ecliptic latitude (within 40° of either ecliptic pole) where the sky-SB is darkest.

Systematic errors in estimating the sky-SB at a given position (e.g., fluctuations in DGL, faint stars, etc) are much bigger than the sub-percent statistical errors in sky-SB

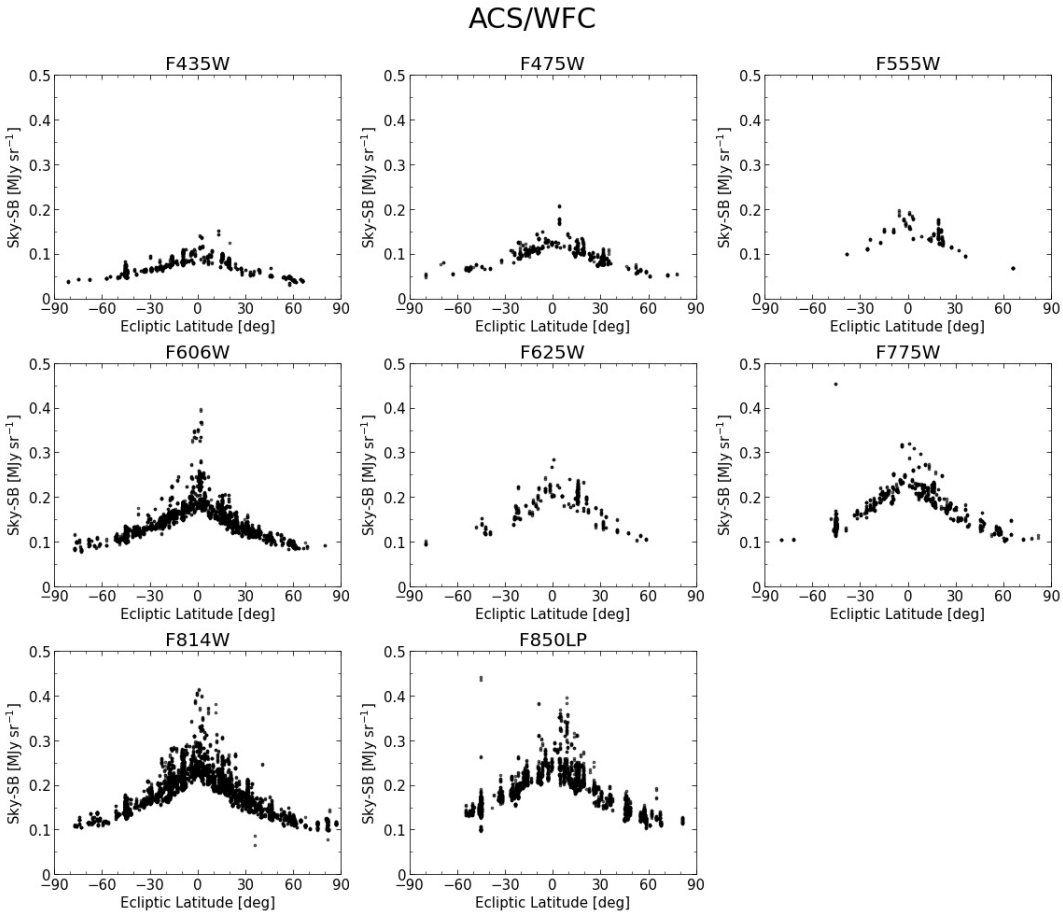

Figure 12. SKYSURF sky-SB measurements versus Ecliptic Latitude for ACS/WFC, zoomed in to show the range between 0 to 0.5 MJy sr^{-1}.

measurement. For the sake of creating a sky-SB SED, these systematic variations in the sky-SB can be resolved if we only keep one sky-SB measurement per position. We take the median sky-SB of all observations taken within 10 arcmin of each other, and define each of these 10 arcmin groups as a unique position. Each SKYSURF point in Figure 15 represents the median of all unique positions for every HST filter. The error bars are a combination of the standard error in sky-SB values along different unique positions ($\sigma_{\rm spread}$), and the sky-SB error ($\sigma_{\rm sky}$):

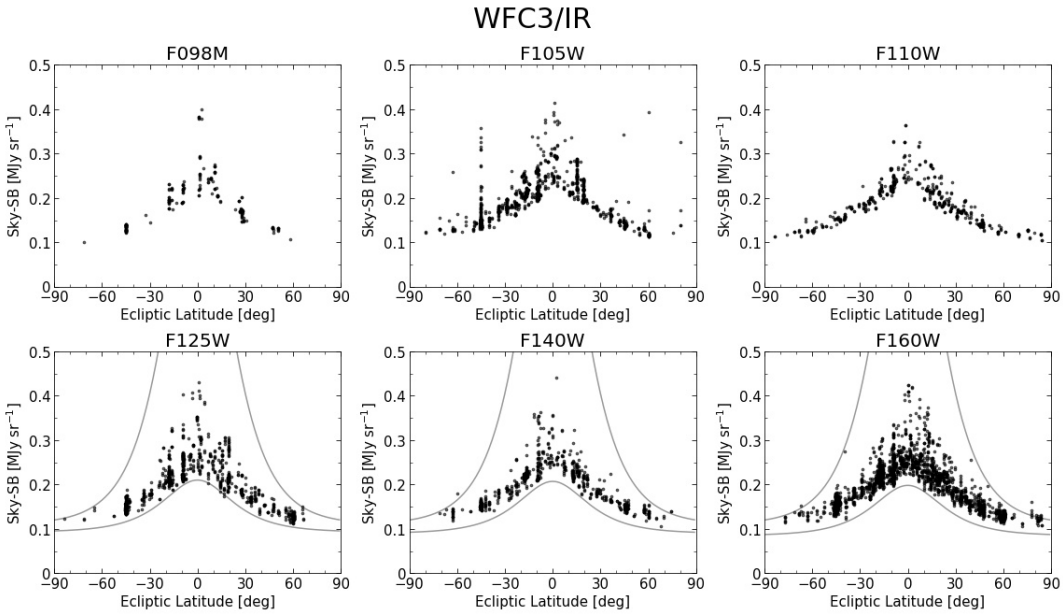

Figure 13. SKYSURF sky-SB measurements versus Ecliptic Latitude for WFC3/IR, zoomed in to show the range between 0 to 0.5 MJy sr^{-1}. The large scatter in points in the F105W filter at $-45°$ is due to observations of the Hubble Ultra Deep Field, where the 1.083 μm emission line (Brammer et al., 2014) present in this filter likely contaminated some of these measurements. As an example of the sky-SB measurements we expect, we include the F125W, F140W, and F160W *sech* curves from Figure 2 of SKYSURF-2, which are derived to match Kelsall et al. (1998) Zodiacal model predictions. Our measurements fall conservatively within these limits.

$$\sigma_{\rm spread} = \frac{\sigma_{\rm std}}{\sqrt{\#\text{ of Unique Positions}}}, \tag{2.2}$$

$$\text{Error Bar} = \sqrt{\sigma^2_{\rm spread} + \sigma^2_{\rm sky,\ med}}, \tag{2.3}$$

where $\sigma_{\rm std}$ is the standard deviation in sky-SB values, and $\sigma_{\rm sky,\ med}$ is a median of all sky-SB measurement errors (Table 1). Only filters with at least two unique positions are plotted.

We compare our sky-SB SED in Figure 14 to several different measurements of the dark sky-SB and estimates of ZL emission. SKYSURF measurements are shown as filled black squares (ACS/WFC), circles (WFC3/UVIS) and triangles (WFC3/IR).

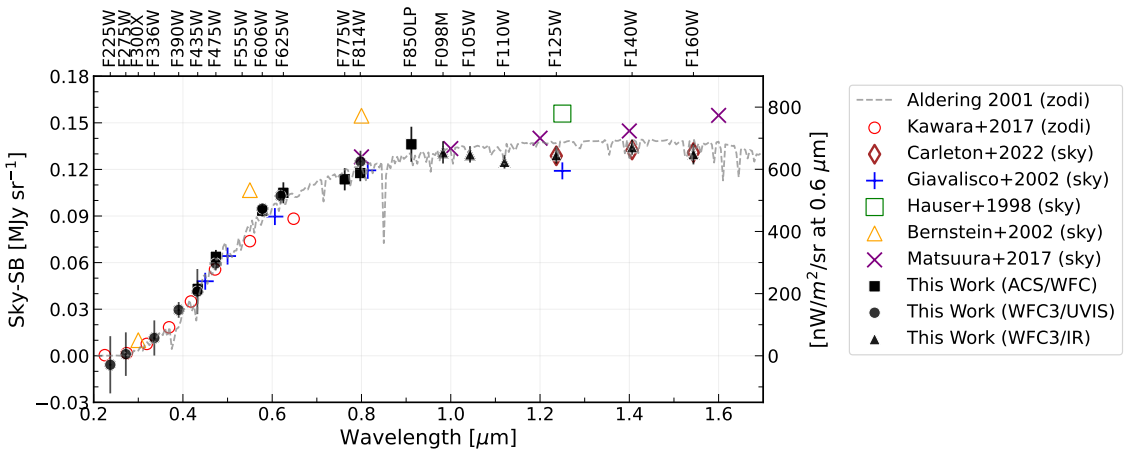

Figure 14. SKYSURF sky-SB SED for Ecliptic latitudes within 40° of the poles. Each black point is a ACS/WFC (square), WFC3/UVIS (circle) or WFC3/IR (triangle) median sky-SB measurement. The error bar is the standard error in unique positions in the sky and the sky-SB measurement error, added in quadrature (see Equation 2.3). Only filters with at least two unique positions are plotted. We compare our measurements to comparable measurements of the sky-SB taken near the ecliptic poles with space telescopes or sounding rockets (Giavalisco et al., 2002; Hauser et al., 1998; Bernstein et al., 2002; Matsuura et al., 2017; Carleton et al., 2022), a model of ZL emission (Aldering, 2001), and measurements of ZL emission (Kawara et al., 2017). Overall, SKYSURF sky-SB measurements agree well with other models and predictions, although some offsets remain present in studies where the light from discrete objects is not removed (Hauser et al., 1998; Bernstein et al., 2002; Matsuura et al., 2017).

The grey dashed line represents the parametric ZL emission model from Aldering (2001) (which is a modification of the Leinert et al. (1998) model). This is produced using the `gunagala sky` module (Robitaille et al., 2022), which calculates a ZL model at the ecliptic pole, from which a relative scaling to the appropriate ecliptic latitude is applied. Kawara et al. (2017) measurements of ZL emission taken with the HST's Faint Object Spectrograph are shown as open red circles, and are estimated for an ecliptic latitude of 85° using Table 2 and Equation 8 from Kawara et al. (2017). The open brown diamonds represent the sky-SB measurements used in SKYSURF-2, which were estimated using a preliminary sky estimation algorithm. Giavalisco et al. (2002) present sky-SB measurements scaled to the North Ecliptic Pole, shown as blue plus

signs, which include measurements from Leinert et al. (1998), the HDF Team, Wright (2001), and Aldering (2001).

As described in SKYSURF-1, we ignore all resolved galaxies in HST images, while other studies tend to include it during EBL analysis. Therefore, some sky-SB measurements are not comparable to ours because they include some or all of the flux from resolved galaxies and stars, and thus are higher in value. However, we show them to highlight general consistencies. The Hauser et al. (1998) sky-SB measurement, shown as an open green square, represents the COBE/ DIRBE sky-SB measurement that includes *all* EBL (discrete+diffuse). The open orange triangles show dark sky HST WFPC2 measurements from Bernstein et al. (2002), which excludes EBL coming from stars and galaxies with total magnitudes brighter than AB $\simeq$ 23 mag (in WFPC2 F555W filter). For comparison, the median SKYSURF exposure is complete to AB $\simeq$ 26 mag (SKYSURF-2). Finally, the purple X's represent sky spectra approximated from Figure 2 of Matsuura et al. (2017) for the North Ecliptic Pole, which were measured using the Low-resolution Spectrometer on the Cosmic Infrared Background Experiment (CIBER), and also include all EBL.

In summary the shape of our sky-SB measurements agree well with other models and predictions, although some differences are still present as discussed above. At wavelengths shortward of 0.5 μm, our sky-SB measurements in general agree with Kawara et al. (2017), Bernstein et al. (2002), and Giavalisco et al. (2002), which may suggest that the amount of EBL present at UV wavelengths is small.

Between 0.5 μm and 0.8 μm, some SKYSURF measurements do not seem to agree with other measurements. The Bernstein et al. (2002) points are expected to be higher since their measurements include the flux from objects fainter than AB $\simeq$ 23 mag, where SKYSURF excludes the flux from all resolved objects. The offset between

SKYSURF measurements and Kawara et al. (2017) indicates a potential for some Diffuse Light signal between 0.5 μm and 0.8 μm.

SKYSURF points greater than 0.8 μm agree with other measurements, although the Aldering (2001) ZL model appears to overestimate sky-SB levels in the near-IR. This model is a solar spectrum that has been reddened and scaled, and thus includes many free parameters that could cause the offset seen here (namely the reddening factor). The COBE/ DIRBE sky-SB measurement (Hauser et al., 1998) is brighter because it includes all EBL, while our sky-SB measurements ignores discrete objects. The CIBER (Matsuura et al., 2017) measurements also include all EBL flux. The offset in sky-SB measurements between this work and SKYSURF-2, most notably in F125W and F160W, imply that Diffuse Light limits will be lower than in SKYSURF-2. We describe this in detail in Section 2.5.

The top panel of Figure 15 displays our sky-SB SED for different ecliptic latitude (b) bins. We find the shape of the sky-SB SED to be largely similar, following a ZL SED at all ecliptic latitudes. Specifically, using a simple linear least-squares regression (Virtanen et al., 2020), the slope of log(sky-SB) versus log(λ) is consistently $\sim$2.2 across all ecliptic latitude bins. The $60^\circ < b < 80^\circ$ bin is an outlier, with a slope of $\sim$2.6. This implies that the sky-SB is dominated by ZL at all ecliptic latitudes. Following the trends seen in Figures 10–13, the darkest sky-SB levels correspond to the highest ecliptic latitudes.

The bottom panel of Figure 15 displays the sky-SB SED for different Sun angle bins. Caddy et al. (2022) and Leinert et al. (1998) show that Sun angle can influence the brightness of ZL emission, and thus the observed sky-SB. Sun angle can correlate with ecliptic latitude, where high ecliptic latitudes will always have Sun angles $\sim$90°. Therefore, we limit our Sun angle bins to have ecliptic latitudes $-30^\circ < b < 30^\circ$. We

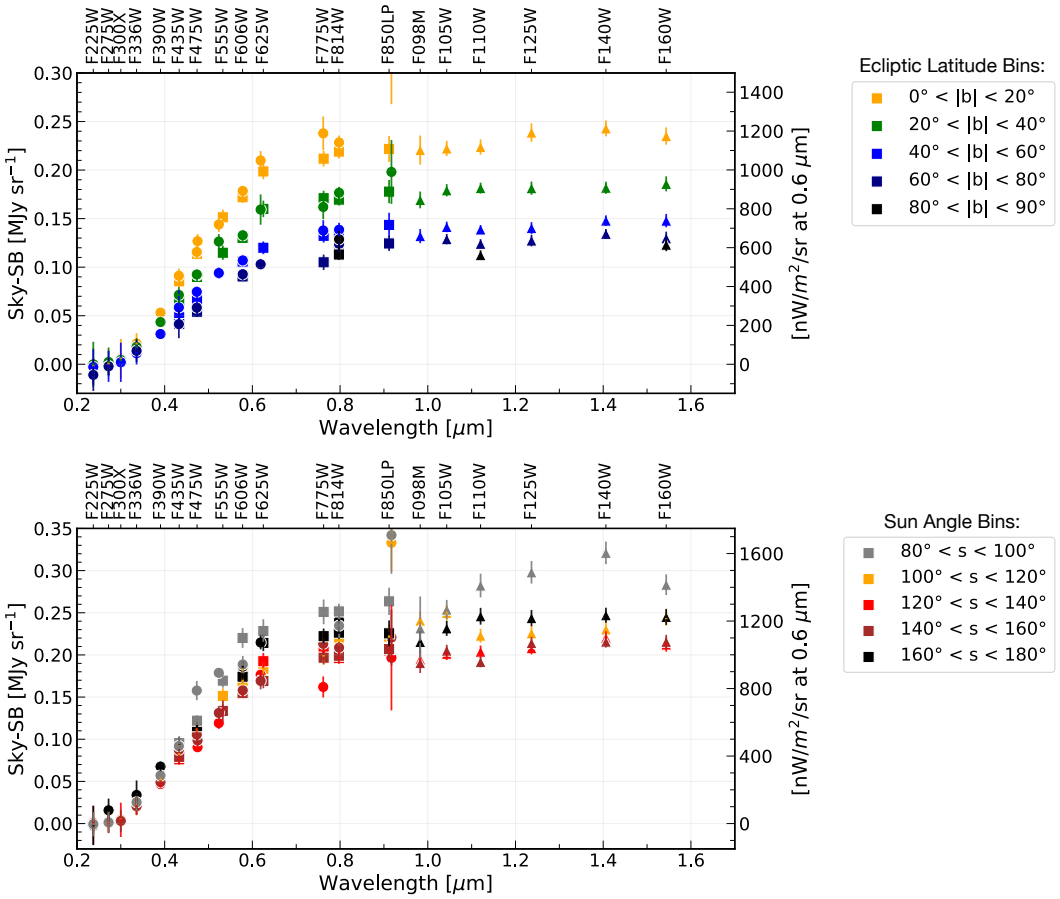

Figure 15. SKYSURF sky-SB SED for different Ecliptic Latitude (b, where each bin includes the absolute value of b) and Sun angle (s) bins. Since Sun angle can be correlated with Ecliptic Latitude, the bottom plot has a fixed range in Ecliptic Latitude of $-30° < b < 30°$. Each point is a ACS/WFC (squares), WFC3/UVIS (circles) or WFC3/IR (triangles) 3σ-clipped median sky-SB measurement. The error bars are scaled in the same way described in Figure 14.

find the shape of our sky-SB SED to depend on Sun angle at wavelengths between 0.9–1.4 μm. For low Sun angles (grey points), the sky-SB shows a clear peak at $\sim 1.4\mu$m. At higher Sun angles, the sky-SB SED flattens between 0.9–1.4 μm. Although the reason for this change in shape is unknown, it could be caused by scattered light, or indicate that the scattering of solar photons off the IPD is non-isotropic. In other words, it could suggest that the anisotropy of the scattering phase function may change as a function of wavelength. In addition, there may be an additional component to

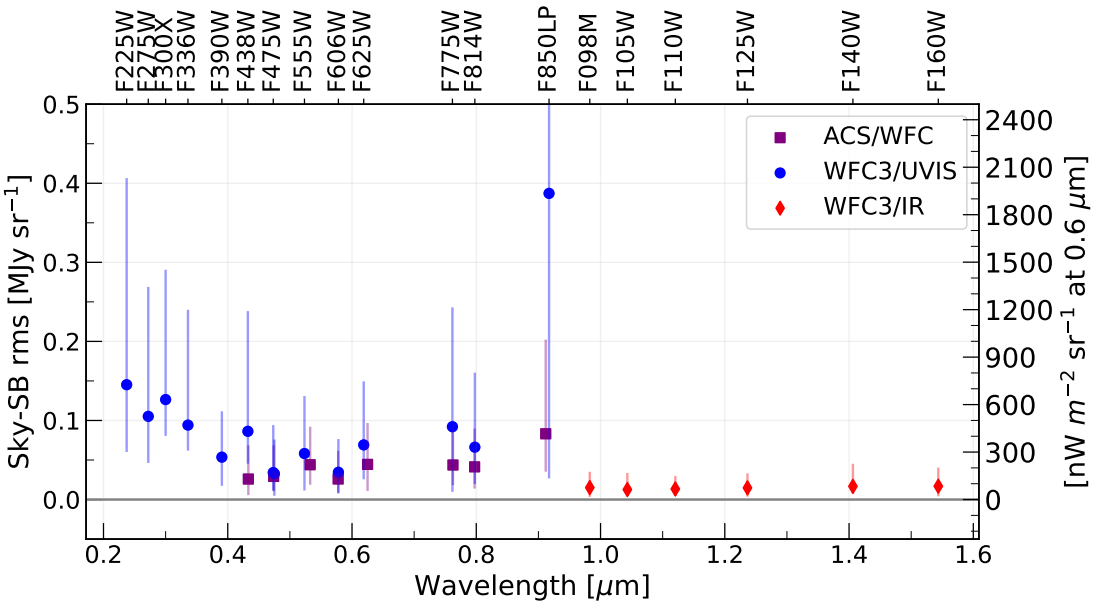

Figure 16. Median sky-SB rms for each filter. The error bars show the 16th- and 84th-percentiles of the rms distributions. The sky-SB rms trends seen here are likely due to the different pixel sizes of each camera.

ZL (e.g., Kawara et al., 2017; Korngut et al., 2022) that interacts with photons with wavelengths between 1.1–1.6 μm differently.

2.4.3 Sky-SB rms

In Figure 16, we show the median measured sky-SB rms for each filter. WFC3/IR shows lower measured sky-SB rms values likely due to the larger pixel size compared to WFC3/UVIS and ACS/WFC (see pixel sizes described in Section 2.8.5).

We note that the F850LP has consistently more scatter when compared to other filters, which is most clearly seen in Figure 16. This is likely driven by the small number of WFC3/UVIS F850LP observations, most of which are at ecliptic latitudes $< 30°$ (Figure 11), where the sky-SB and the sky-SB rms is higher.

2.5 Updated Diffuse Light Limits

The main goal of SKYSURF is to provide Diffuse Light (DL) measurements using HST's vast archive. SKYSURF-2 presents DL upper limits using preliminary sky-SB measurement algorithms that are meant to be conservative (and computationally faster), and provide initial DL limits using three pilot near-infrared filters: F125W, F140W and F160W. With the improved sky-SB measurement algorithms in this work, we update the DL limits presented in SKYSURF-2 for the F125W, F140W and F160W filters. DL measurements for all filters, using improved SKYSURF ZL models, will be presented in future work.

The DL upper limits from SKYSURF-2 are estimated using the Lowest Fitted Sky (LFS) method, where they fit a *sech* curve to the darkest thermal-dark corrected sky-SB values measured for SKYSURF. They fit a similar curve to the Kelsall et al. (1998) ZL emission predictions and estimate a DL signal by comparing the two curves. DGL and unresolved EBL still present in HST images is also subtracted during this process. SKYSURF-2 DL limits are presented as upper limits due to uncertainties in thermal dark, which will be updated in Carleton et al. (in prep).

Revised DL upper limits are shown in Table 4. We estimate these limits by calculating the 3σ-clipped median difference in sky-SB values between the sky-SB measurements in this work and the sky-SB measurements used in SKYSURF-2. In Section 2.8.6, we confirm that a 3σ-clipped median difference is a good representation of the darkest sky-SB measurements used in SKYSURF-2. The Kelsall et al. (1998) Zodiacal model predictions do not change between this work and SKYSURF-2. The improved algorithms in this work result in sky-SB measurements that are $\sim 1-2\%$ lower than the F125W, F140W, and F160W measurements in SKYSURF-2. These

Filter	F125W	F140W	F160W
SKYSURF-2 DL Limit [MJy sr^{-1}]	$\lesssim$0.012	$\lesssim$0.018	$\lesssim$0.015
[nW m^{-2} sr^{-1}]	$\lesssim$29	$\lesssim$40	$\lesssim$29
Sky-SB / SKYSURF-2 Sky-SB	0.983	0.986	0.988
Sky-SB − SKYSURF-2 Sky-SB [MJy sr^{-1}]	-0.003	-0.003	-0.002
This Work: DL Limit [MJy sr^{-1}]	**$\lesssim$0.009**	**$\lesssim$0.015**	**$\lesssim$0.013**
[nW m^{-2} sr^{-1}]	**$\lesssim$22**	**$\lesssim$32**	**$\lesssim$25**

Table 4. Updated SKYSURF Diffuse Light limits. We compare sky-SB measurements for F125W, F140W, and F160W from SKYSURF-2 to this work. The first row lists the DL limits from SKYSURF-2. The second row shows the same results in units of nW m^{-2} sr^{-1}. The third row shows the median ratio between sky-SB measurements from this work and those from SKYSURF-2. The fourth row shows the difference in these sky-SB values, in units of MJy sr^{-1}. We subtract this difference from the SKYSURF-2 DL limit in the first row to estimate a DL limit for this work, shown in the fifth row. The last row shows the same DL limits from the fifth row in units of nW m^{-2} sr^{-1}. We adopt the same error from SKYSURF-2: 0.005 MJy sr^{-1}($\sim$ 10 nW m^{-2} sr^{-1}).

updated sky-SB measurements result in DL upper limits that are typically 20–30% lower than the conservative limits from SKYSURF-2.

DL limits for the entire HST wavelength range will be estimated in future papers, using a ZL model constrained by the sky-SB measurements in this paper, and supplemented by star and galaxy counts using the SKYSURF database.

2.6 Public Data Products

We provide several data products on the official SKYSURF website[3]. Relevant to this paper are: 1) sky-SB measurements for all SKYSURF images, and 2) FITS files containing the sky sub-regions used for our algorithm. In addition, the SKYSURF website presents the Pro-med algorithm used for sky-SB estimation in this work.

[3]http://skysurf.asu.edu

2.6.1 Sky-SB Data Tables

For every image, we provide a SKYSURF sky-SB measurement in the native units of the `flt`/`flc` files, as well as in calibrated flux units of MJy sr^{-1}. The process for converting our images to units of flux density is described in Section 2.8.5. Estimates of the thermal dark levels will be presented in Carleton et al. (in prep) and are included in the public files for all WFC3/IR measurements. We provide sky-SB measurements with and without thermal dark corrections.

We include an uncertainty for each sky-SB measurement using Table 1. The error is calculated as following:

$$\sigma_{\rm sky} = \sqrt{\sigma_{\rm add}^2 + (\sigma_{\rm mult} \times S_{\rm chip})^2}, \tag{2.4}$$

where $\sigma_{\rm sky}$ is the total sky-SB error in units of electrons or electrons per second, $\sigma_{\rm add}$ is the additive error in units of electrons or electrons per second, $\sigma_{\rm mult}$ is the multiplicative error in units of percent, and $S_{\rm chip}$ is the measured sky-SB in units of electrons or electrons per second. The sky-SB error is also presented in units of MJy sr^{-1}.

Every sky-SB measurement has a corresponding flag that designates images with too many bad sub-regions, too high of a sky-SB rms, images marked during the manual inspections, located within galactic plane, located close to the Earth's limb, located at high Sun altitude's, contains a large common object, or has too many pixels affected by persistence. We refer to corresponding documentation on the public files for more information.

2.6.2 Subregion FITS Files

We provide FITS files containing the sub-regions created during our algorithm described in Section 2.3. Each FITS file, which we refer to as a SUB file, has a single sky value associated with each sub-region where each sub-region takes up a single pixel. For example, a 1014×1014 pixel WFC3-IR image that is divided into 26×26 pixel sub-regions will have a corresponding SUB file that is 26×26 pixels in size.

They contain one primary header and two data extensions. The primary header is copied from the original `flt`/`flc` image, where the extension name (EXTNAME) is changed to SUB_SKY. The two data extensions are labeled 'SKY' and 'RMS' and contain the sky-SB and sky-SB rms sub-region data. In the SKY and RMS extensions only, WCS keywords are updated so that the SUB files map onto the true sky to within 0.3 arcseconds.

2.7 Conclusion

We present sky-SB algorithms and measurements for project SKYSURF, an HST archival program with the end goal of constraining an all-sky DL signal. SKYSURF is the first study of the sky-SB with HST at this scale and encompassing HST's entire wavelength range. The SKYSURF database includes more than 140,000 HST images, spanning 0.2–1.6 μm.

We utilize the Pro-med algorithm to measure the sky-SB (Figure 8) for all images in our database. As a function of ecliptic latitude, Figures 10 – 15 follow expected trends by peaking near the ecliptic plane. There are almost no outliers falling outside the expected trend, highlighting the success of our ability to filter our unreliable

sky-SB measurements. The sky-SB SED shows that our measurements generally agree well with other measurements. The overall shape of our sky-SB SED for low Sun angles does not match that of higher Sun angles, where the low Sun angle sky-SB SED shows a peak between $\sim 1.1 - 1.6$ μm. The cause for this remains unknown, yet we propose it may be due to the anisotropy of the scattering phase function of interplanetary dust, or due to an additional ZL component in the inner Solar System.

As shown in Table 4, we estimate DL limits based on the methods of SKYSURF-2 for F125W, F140W, and F160W. The DL limits in SKYSURF-2 are conservative, and the DL limits in this work are lower those in SKYSURF-2, ranging from 0.009 MJy sr^{-1} to 0.015 MJy sr^{-1}. The DL limits presented here are still designed to be conservative, and measurements of DL using an updated ZL model for the entire HST wavelength range will be provided in future papers. Overall, these estimates provide the most stringent all-sky constraints in this wavelength range, and show a significant DL component of unknown origin.

We hope that these sky-SB measurements will not only benefit Project SKYSURF, but will provide valuable data and methods for future programs. SKYSURF data products are released to the public (Section 2.6), including tables of all SKYSURF sky-SB measurements, as well as FITS files that show the sub-regions used during our sky-SB estimation. We also make our sky-SB algorithms available to the public. Aside from using our methods to study the sky-SB itself, reliable sky-SB algorithms are crucial for reliable photometry for low surface-brightness studies, where it is imperative that signal from real objects does not contaminate the measured sky-SB.

SKYSURF's large database gives us the unique ability to independently and consistently derive galaxy counts (and therefore create a SKYSURF EBL model), as well as constrain ZL emission at HST wavelengths. We can compare our sky-SB

measurements to a SKYSURF EBL model based on galaxy counts and a SKYSURF ZL emission model for a final estimate of DL. Future work includes generating source counts using the entire SKYSURF database, updated Thermal Dark signals, constraining a ZL model utilizing SKYSURF data, and measuring an EBL signal using these results.

2.8 Supplemental Information

2.8.1 Simulated Images

In order to develop and test reliable sky-SB measurement algorithms, we created simulated images where we know the true sky-SB and noise levels. We discuss here how these simulated images were created and the different kinds of simulated images that were produced.

We use GALSIM version 2.2.4 (Rowe et al., 2015) to generate simulated images due to its ability to generate realistic galaxies and stars easily. These simulated images include stars, galaxies, cosmic rays, and sky gradients (see Figure 17). All simulated images were produced to match WFC3/IR F125W flat-fielded images: 1014×1014 pixels, with a 0.13"/pixel pixel scale. Therefore, star counts, galaxy counts, PSF sizes (necessary for GALSIM) and sky levels were also based on WFC3/IR F125W data. We produced a total of 344 images with a flat sky and 444 images with a sky gradient, with exposure times from 50s to 1302s, sky-SB levels ranging from 0.22 e^- to 3.14 e^-, and sky gradients ranging from a 0% change to a 20% change edge-to-edge. We choose a wider range of sky-SB, noise, and sky gradient levels than is typical to ensure the robustness of our algorithms.

2.8.1.1 Star and galaxy counts

The star and galaxy counts for our simulated images are taken from Windhorst et al. (2011). The star count slope for WFC3/IR data, shown in Equation 2.5, results in nearly 1 star per 1.0 mag bin within our chosen field of view. The number of stars in each simulated image is calculated as follows:

$$N_{\mathrm{stars},m_{\mathrm{AB}}} = 10^{0.04(m_{\mathrm{AB}}-18)} \tag{2.5}$$

where $N_{\mathrm{stars},m_{\mathrm{AB}}}$ is the number of stars per integer AB magnitude (m_{AB}) bin, where we assume an 18 mag bin contains exactly one star (as approximated from Figure 11 of Windhorst et al., 2011).

Stars are restricted to $18 \leq m_{\mathrm{AB}} \leq 26$ to avoid unusually bright stars and stars below the F125W detection limit. This resulted in a total of ~ 13 stars generated in each simulated image. Every star was generated as a Gaussian with a full width at half maximum (FWHM) of 0.136". The position of each star in the simulated images was randomly selected with the condition that a star's center be within the 1014×1014 grid.

The galaxy count slope is steeper at around 0.26 dex/deg. The number of galaxies in each simulated image was calculated as follows:

$$N_{\mathrm{gal},m_{\mathrm{AB}}} = 10^{0.26(m_{\mathrm{AB}}-18)} \tag{2.6}$$

where $N_{\mathrm{gal},m_{\mathrm{AB}}}$ is the number of galaxies per 0.5 AB magnitude bin.

Galaxies are restricted to $18 \leq AB \leq 26.5$ to avoid unusually bright galaxies and galaxies below the F125W detection limit. This resulted in a total of 624 galaxies generated in each simulated image. Every galaxy was generated using a

single-component inclined Sérsic profile (refer to Rowe et al. (2015) for profile details). Similarly to the simulated stars, the position of each galaxy in the simulated images was randomly selected with the condition that the galaxy's center be within the 1014×1014 grid.

The magnitude, effective radius, sersic index and axis ratio (b/a) were sampled using two methods: a custom distribution (described in Section 2.8.1.2) and a random sampling from 3D-HST's COSMOS F125W Catalog (van der Wel et al. (2014); described in Section 2.8.1.3).

2.8.1.2 Galaxy Parameter Sampling Method 1: Custom Distribution

The custom galaxy sampling method is motivated by Windhorst et al. (2011). Images simulated with this method have the radius of each galaxy sampled from a distribution of the form:

$$p(R_e) = R_e \frac{e^{-R_e/0.2}}{0.2 \times \Gamma(2)} \tag{2.7}$$

where $p(R_e)$ is the probability density function for a galaxy with effective radius R_e, and Γ is the Gamma function. This distribution follows closely with 3D-HST COSMOS F125W galaxy counts (van der Wel et al., 2014). Due to GALSIM memory limitations, we only simulated galaxies with $R_e \leq 2.72''$. Galaxies with $R_e > 2.72''$ only account for $\ll 1\%$ of all galaxies in our field of view (follows from Equation 2.7).

Sérsic indices for the custom sampled galaxies follow:

$$p(n) = e^{0.38n} \tag{2.8}$$

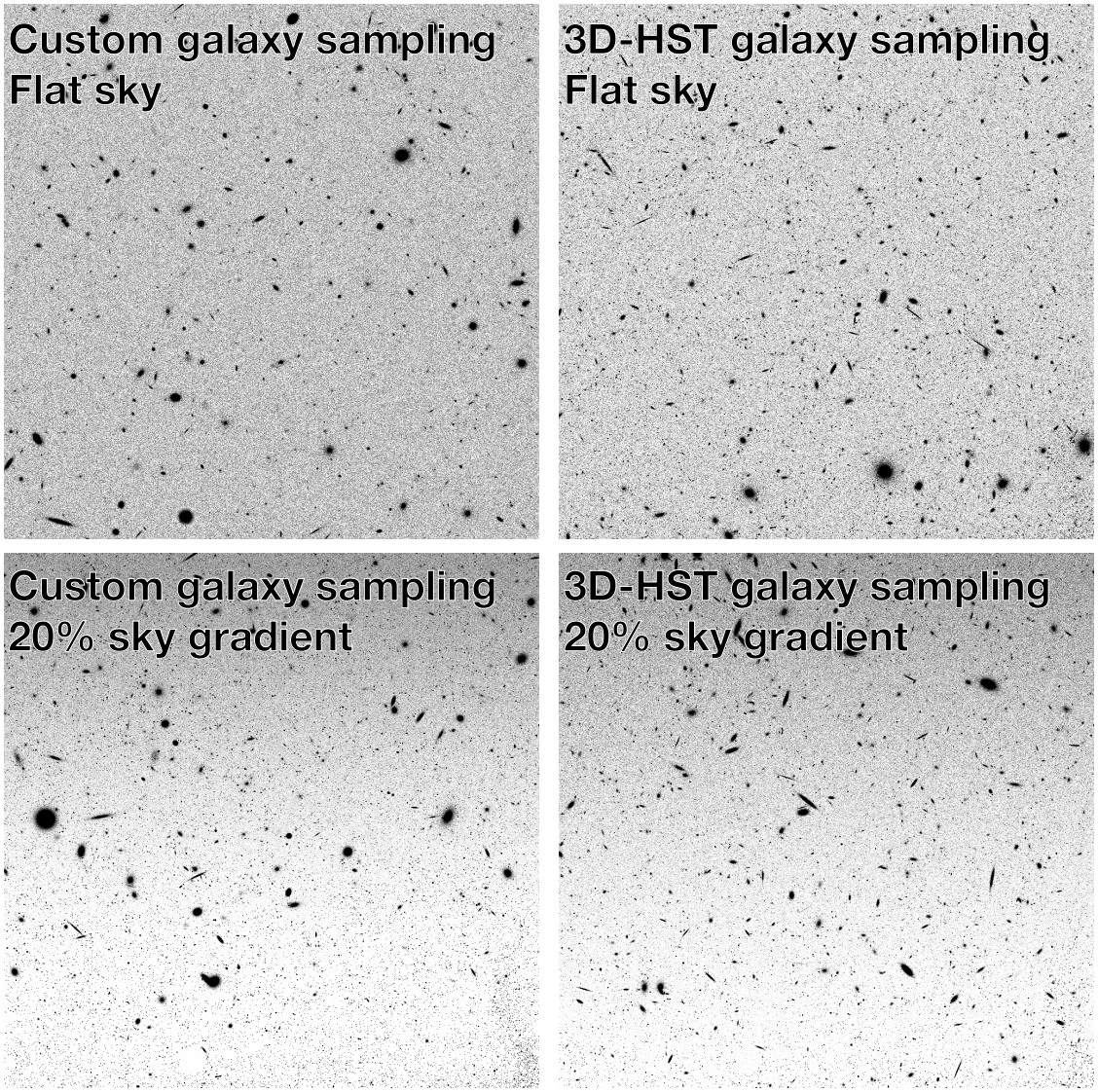

Figure 17. Example simulated images. The custom galaxy sampling method (left column) employs a distribution of galaxy parameters based on Windhorst et al. (2011). The COSMOS galaxy sampling method randomly selects galaxies from the COSMOS F125W database. The top images have no sky gradient added, while the bottom images have a sky gradient imposed on them.

where $p(n)$ is the probability density function for a galaxy with Sérsic index n. Because the allowed range of Sérsic indices for GALSIM is $0.3 \leq n \leq 6.2$, this is the range of Sérsic index values present for the galaxies in the simulated images.

AB magnitudes for the custom sampled galaxies follow:

$$p(m_{\mathrm{AB}}) = \frac{1}{\beta} \exp(\frac{m_{\mathrm{AB}} - 26.5}{\beta}), \tag{2.9}$$

where $\beta = \frac{1}{0.26 \times \ln(10)}$ and $p(m_{\mathrm{AB}})$ is the probability density function for a galaxy with AB magnitude $18 < m_{\mathrm{AB}} < 26.5$.

Lastly, the inclination of each galaxy produced from this method was randomly selected from the range 0 to $\frac{\pi}{2}$ radians.

2.8.1.3 Galaxy Parameter Sampling Method 2: 3D-HST COSMOS F125W Catalog

Images simulated with this method used parameters directly sampled from the 3D-HST COSMOS F125W catalog (van der Wel et al., 2014). In other words, galaxies were taken directly from the 3D-HST COSMOS F125W catalog and inserted into our simulated images. Inclinations were estimated using:

$$\cos^2 i = \frac{(b/a)^2 - \alpha^2}{1 - \alpha^2} \tag{2.10}$$

where b/a is the axis ratio and $\alpha = 0.22$ (Unterborn & Ryden, 2008).

2.8.1.4 Cosmic rays, noise and sky gradients

Cosmic rays (CRs) in the simulated images were generated by randomly selecting CRs from a WFC3/IR cosmic ray template and inserting them directly into the

simulated images. The cosmic ray template was generated by identifying spikes in the individual reads of a random 1302 second HST image. This resulted in a rate of 14.6 CRs per second over the course of the exposure. The number of CRs inserted into a simulated image is given by:

$$N_{CRs} = R_{CR} \times t \tag{2.11}$$

where N_{CRs} is the number of cosmic rays in the simulated image, R_{CR} is the CR rate of the cosmic ray template (14.6 CR's per second), and t is the exposure time of the simulated image.

Noise was generated for the simulated images using combination of Poisson noise (shot noise) and Gaussian read noise:

$$\text{RMS} = \frac{\sqrt{S_{sky} \times t + RN^2}}{t} \tag{2.12}$$

where S_{sky} is the sky background value, t is the exposure time, and RN is read noise. A read noise of 12 e^- was used for all simulated images, and various different sky-SB and exposure time values were used. Poisson noise was added to the images first, followed by Gaussian read noise.

Some simulated images were modeled with linear sky gradients. Real sky gradients may appear in images where an image is pushed too close to the Earth's limb, although these are often <10% edge-to-edge. For this work, we include a sky gradient to also represent any type of light contamination that may appear in an image, such as Earth's limb, the extended halos of galaxies, faint stars, extended point spread functions, and optical ghosts. This allows us to test how well algorithms perform against *any* source of stray light. Sky gradients were generated according to:

$$N_{row} = O_{row} + \frac{P}{100}\frac{R_{num}}{R_{tot}}O_{row} \tag{2.13}$$

where N_{row} are the gradient adjusted pixel values for a particular row of pixels in the image, O_{row} are the non-gradient adjusted pixel values, P is the percent change between the bottom and top row of the image, R_{num} is the row number being adjusted, and R_{tot} is the total number of rows in the image.

This method ensures that the true sky value in the gradient images is the lowest end of the gradient, aligning with our philosophy that the true sky value of a real HST image will have the least amount of light contamination and thus be the lowest sky value in an image.

2.8.2 Choosing the most reliable algorithms

Nine independent sky-SB measurement algorithms were originally created for SKYSURF, with an end goal of using the most reliable and robust methods for SKYSURF. The chosen algorithms should be able to measure the true sky-SB accurately, even for cases with sky-SB contamination. As described in Section 2.8.1, we create simulated images with sky gradients to simulate sky-SB contamination. We present these algorithms here for users who might wish to implement their own sky-SB algorithms.

The left-hand side of Figure 18 shows that there are many methods that can retrieve the true input sky-SB to less than 0.1% error. However, many of these methods (Methods 3, 4, 6, 7) assume a flat sky and can not account for sky gradients. We therefore developed several methods that account for sky gradients (Methods 1, 2, 5, 8 and 9; see right-hand plot in Figure 18). With SKYSURF's end goal of constraining a Diffuse Light signal, it is crucial that we are able to robustly ignore possible sources of sky-SB contamination. These could be sky gradients in the field of view due to Earth's limb, or the extended light profiles of galaxies. We choose the two algorithms that are able to best retrieve the known input sky-SB level from the simulated images with sky gradients: Method 2 (the Percentile-clip method) and Method 8 (the ProFound Median method).

The ProFound Median performs very well for flat images (less than 0.05% error on average). The Percentile-clip method will underestimate the sky-SB in the case of a flat sky. The median sky-SB rms for WFC3/IR F125W images in our SKYSURF database is ~ 0.05 electrons per second. Figure 18 shows that the Percentile-clip method can still retrieve the known input sky-SB level to within 0.3% for images with a flat sky and a sky-SB rms less than 0.05 electrons per second.

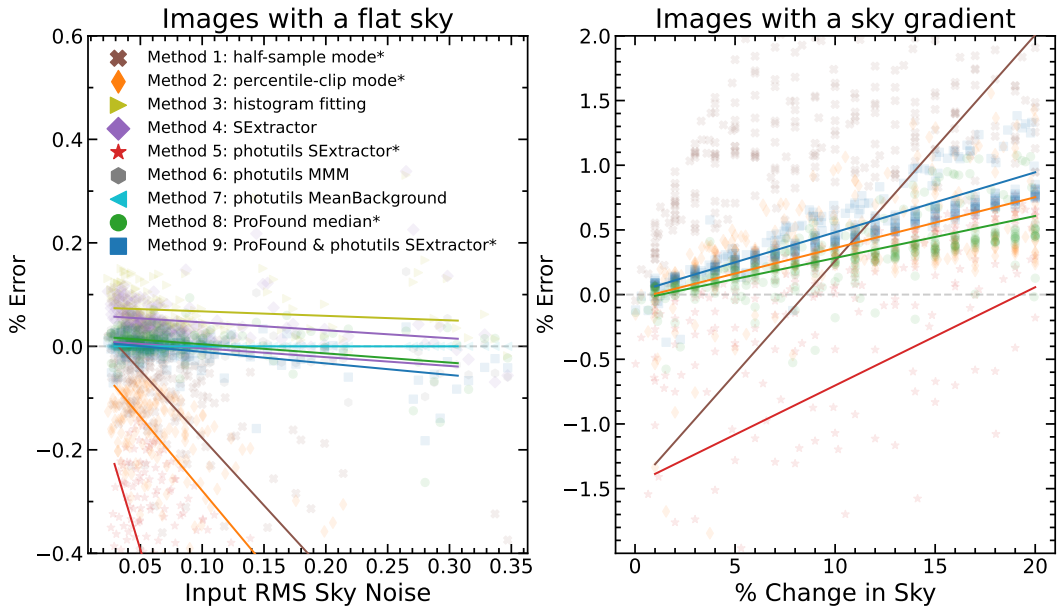

Figure 18. Results of running various sky-SB estimation algorithms (Methods 1-9) on simulated HST WFC3/IR F125W images, where % Error = (Measured Sky - Input Sky) / Input Sky $\times$100%. The solid colored lines represent the linear best fit for binned data where each bin contains 10-11 simulated images. Methods listed with an asterisk (*) are able to account for sky gradients, and are thus included in the right panel. **Left:** Algorithm performance on simulated images with no sky gradient, plotted against the known, true sky-SB rms of the simulated image. **Right:** Algorithm performance on simulated images with a sky gradient, plotted against the known sky gradient of the image.

These algorithms are extremely similar, as the Percentile-clip method uses a 5th-percentile to approximate the sky-SB, while the ProFound Median uses a median. In addition, the ProFound Median method uses ProFound SKY maps, while the Percentile-clip method does not. Besides these two differences, the algorithms are identical. We confirm that the use of ProFound SKY Maps typically results in a $\lesssim$0.5% difference in sky-SB measurements when all other steps in the pipeline are the same, and decide to proceed with using ProFound SKY maps for *both* methods. The new Percentile-clip method with ProFound SKY maps is named the ProFound-5th method. The main paper focuses on the ProFound Median method, while the ProFound-5th method is described in Section 2.8.3.

Here we describe each method in detail as it appears on Figure 18:

Method 1: Half-sample mode - This method divides the image into 39×39 square pixel regions, then 3σ clips each sub-region. For each sub-region, it calculates the half-sample mode and rms, where the rms is determined to be the median absolute deviation multiplied by 1.48. This is able to estimate the mode of a sample by numerically finding the smallest interval that contains half of the points in a sample and iterating until obtaining an interval with only two points (e.g., Bickel & Fruehwirth 2005). The mode of the sample is approximated to be the average of the remaining two points. This method then identifies "good" cutout regions, assuming that the true (ZL+EBL) sky-SB of an image is closest to the LPS values in an image.

Method 2: Percentile-clip - This method is described in Section 2.8.3.

Method 3: Histogram fitting - This method fits a histogram of sky-SB values from -3σ to $+1\sigma$ using a clipped sigma as a first guess, and performs 2 iterations.

Method 4: SourceExtractor - This method uses `SourceExtractor` (Bertin & Arnouts, 1996a) to calculate the sky-SB, where we assume that each object has a different surrounding sky.

Method 5: photutils SourceExtractor - This method masks all sources in an image then splits each image into 26×26 square pixel regions with a 30 pixel border surrounding each image that is subsequently ignored. It estimates the sky-SB value of each cutout using the `photutils SourceExtractor` algorithm (Bradley et al., 2020). The sky-SB rms is estimated using the `photutils` median absolute deviation algorithm. It rejects sub-regions with a measured sky-SB greater than the lowest sky-SB + the average sky-SB rms of all sub-regions. It also rejects sub-regions with a measured sky-SB rms greater than twice the

average rms of all sub-regions. This method then estimates the sky-SB gradient of the image using the brightest 7% of cutout regions and the dimmest 7% of cutout regions. Using this calculated gradient, the algorithm determines a threshold (N) for which to include images in the final calculation, where N ranges from 4% to 35% for large to small gradients, respectively. The sky-SB of the image is the lowest N% of good cutout regions.

Method 6: photutils MMM - This method masks all the sources in the image, then calculates the sky-SB using a `photutils` method based on the `DAOPHOT MMM` algorithm (Bradley et al., 2020; Stetson, 1987).

Method 7: photutils Mean - Method 7 masks the sources in an image, 1.3σ clips the entire image, then calculates the sky-SB using `photutils MeanBackground`.

Method 8: ProFound median - This method is described in Section 2.3.

Method 9: ProFound & photutils Source-Extractor - This method utilizes Method 5 (photutils SourceExtractor) on ProFound SKY maps.

2.8.3 The ProFound-5th Algorithm

As stated in SKYSURF-1, we measure the sky-SB for all images in our database using our two best algorithms. In this section, we describe the second algorithm that is not described in the main paper: the ProFound-5th (Pro-5th) method. It follows the same methodology as the Pro-med method, but uses a 5th-percentile of unflagged sub-regions rather than a median. In other words, the final sky-SB level of a chip, $S_{\rm chip}$, is the 5th-percentile of the remaining $S_{\rm sub}$ values. The final sky-SB rms of a chip, $\sigma_{\rm chip}$, is the mean of all the $\sigma_{\rm sub}$ values.

In contrast to the Pro-med method, the Pro-5th method recovers the darkest measurable sky-SB for every HST image. Many SKYSURF images contain light from the extended profiles of galaxies (Ashcraft et al., 2018), the extended point-spread functions (PSFs) of stars (Borlaff et al., 2019), thermal foregrounds (SKYSURF-2), and the Earth's atmosphere (Caddy et al., 2022). While explicitly modeling and subtracting these features of the measured sky-SB is out of the scope of SKYSURF, we reduce the probability of unaccounted-for sources of flux that may contaminate our sky-SB measurements by choosing to isolate the darkest area in an image.

As shown in Figure 19, the Pro-5th measurements fall below zero in UV wavelengths. The lack of objects (because hot stars are rare) in this wavelength range means that Pro-5th method more severely underestimates sky than in longer wavelengths. In addition, the measurement noise in UV wavelengths is larger than at other wavelengths, as shown in Section 2.4.3. This effect will also cause the Pro-5th method to be more biased with respect to the true value. Figure 18 shows that a 5th-percentile method (method #2) underestimates the true sky-SB by a larger margin as the sky-SB rms increases.

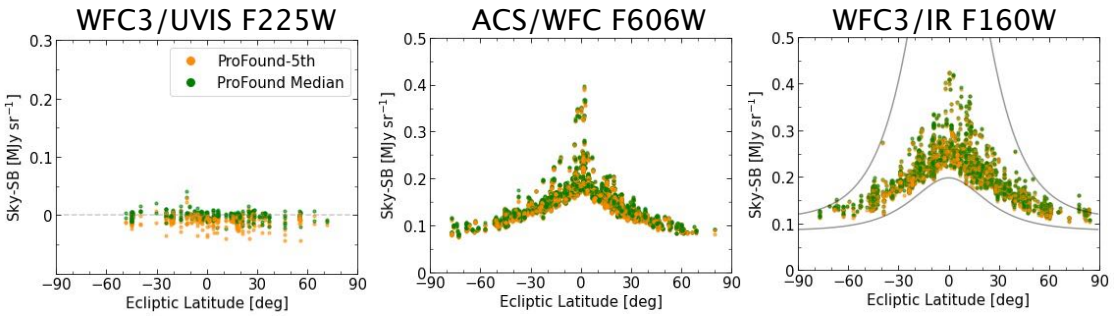

Figure 19. SKYSURF sky-SB measurements versus Ecliptic Latitude for three example filters. We compare the Pro-med method (green) to the Pro-5th method (orange). As an example of the sky-SB measurements we expect, we include the WFC3/IR F160W *sech* curve from Figure 2 of SKYSURF-2, which is derived to match Kelsall COBE/DIRBE model predictions. Our measurements fall conservatively within these limits.

Following the same methods of Section 2.5, we calculate DL limits for the Per-clip algorithm. We estimate DL limits of 0.008 MJy/sr for F125W, 0.015 MJy/sr for F140W, and 0.012 MJy/sr for F160W. This method still provides DL limits that are in excellent agreement (to within error) to the Pro-med method.

2.8.3.1 Comparison of the two methods

We compare the sky-SB levels of the Pro-med and Pro-5th algorithms for each HST filter. As shown in Figure 20, the Pro-med method gives sky-SB values that are on average 2% higher for ACS/WFC, 4% higher for WFC3/UVIS, and 0.6% higher for WFC3/IR than the Pro-5th method. This is an expected difference, as the Pro-5th method will always result in a lower sky-SB because it probes the darkest part of an image.

The trend seen as a function of wavelength in Figure 20 is due to trends of the average sky-SB rms (Figure 16). This can be inferred from the fact that a lower sky-SB rms results in a smaller variation in the sky pixels. In other words, a lower average

sky-SB rms results in a smaller difference between methods because the difference between the median and the 5th-percentile of a gaussian distribution is smaller when the rms is lower. Although these trends are driven by Poisson statistics, other factors that could affect the sky-SB rms include increased contamination from contaminants or sky gradients.

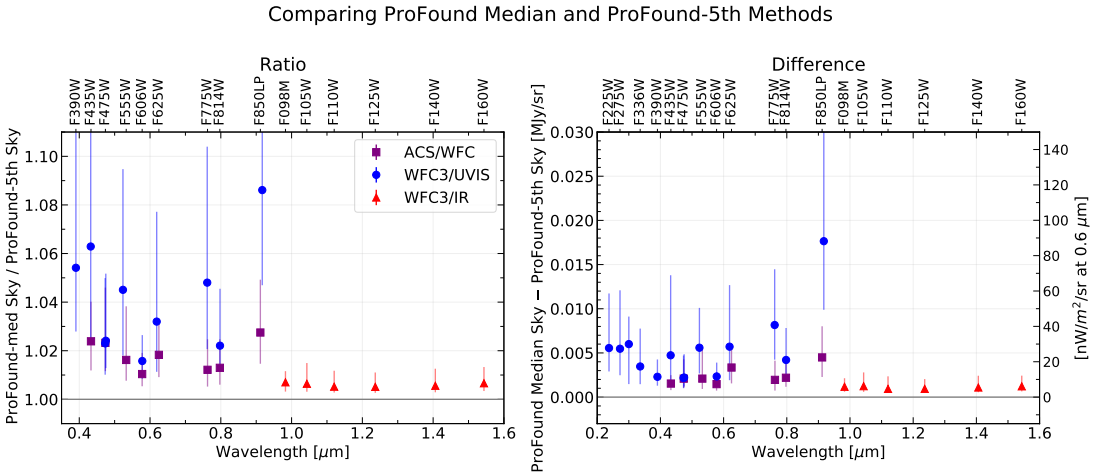

Figure 20. Comparison of the Pro-med method and the Pro-5th algorithms. The error bars show the 16th- and 84th-percentiles of the y-axis distributions. **Left:** Median ratio of the Pro-med sky-SB divided by the Pro-5th sky-SB. The bluest filters are excluded because the sky-SB is nearly zero, such that the ratios become extreme values. **Right:** Median difference in Pro-Med and Pro-5th method. The left y-axis shows units of MJy $sr^{-1}$and the right axis shows nW m^{-2} sr^{-1} at 0.6 μm.

2.8.4 Sources of Uncertainty

In this section, we expand on the uncertainties presented in Section 2.3.3.

2.8.4.1 WFC3/UVIS Uncertainties

Flat-field errors are $\leq$1% (Mack et al., 2016). However, errors can be larger in the corner of the UVIS1 chip where the point-spread function focus is highly variable due to the telescope breathing effects (Sabbi & Bellini, 2013), and this impacts the flat field correction. Also, small offsets between the two different WFC3/UVIS detectors are present in some filters, with a maximum difference between one corner of a detector to the other of $\sim$3% (Mack et al., 2016) for a few ultraviolet filters. These variations in flat-field could potentially bias our results. In Section 2.8.4.6, we independently explore maximum possible uncertainties in the flat-fields by taking advantage of the large SKYSURF database. We do this by comparing the systematically darkest and brightest sub-regions, with a typical offset of 2–4%, which agrees with Mack et al. (2016). This is a maximum difference between the darkest and brightest sub-regions, but our algorithms automatically ignore the very darkest and brightest sub-regions. We therefore adopt the Mack et al. (2016) flat-field uncertainty of 1%.

We use the new photometric zeropoint calibrations explained in Calamida et al. (2022), where they account for variations in WFC3/UVIS zeropoints over time. We adopt the photometric errors listed in Table 8 of Calamida et al. (2022), which on average represent a $<$0.2% 1σ dispersion (Table 8 of Calamida et al. 2022).

A bias offset is added to HST detectors to avoid presenting a negative voltage to the analog-to-digital converter. This offset is always subtracted during post-processing,

and uncertainty in the bias level introduces error to the sky-SB. Figure 5 of McKay & Baggett (2017) shows a scatter in individual bias levels of ~ 0.2 electrons. Figure 17 from Bourque & Baggett (2016) shows that the scatter in determining the dark current is $\sim$2 e-/hr or $\sim$0.0006 electrons per second.

Different versions of the standard WFC3 calibration pipeline correct for CTE trails differently. We quantify the effects of different pipeline versions in Section 2.8.4.7. We find the measured sky-SB between different versions of the pipeline to be $\sim 0.007\%$ for wavelengths longer than 0.4 microns. We therefore do not include CTE effects in our error budget. As discussed in SKYSURF-1, we adopt a post-flash subtraction error of 1%, corresponding to 0.16 electrons for a F606W image with an exposure time of 500 seconds.

2.8.4.2 WFC3/IR Uncertainties

Mack et al. (2021) present residuals in the sky flats of 0.5–2%. We adopt a conservative WFC3/IR flat field uncertainty of 2%. As described in SKYSURF-1, WFC3/IR photometric zeropoints have roughly remained constant to within 1.5% (rms) since 2009. Therefore, we adopt a zeropoint uncertainty of 1.5% for WFC3/IR.

As described in The WFC3 Instrument Handbook, the WFC3/IR detector responds non-linearly to incident photons. The WFC3 calibration pipeline corrects for this with a $\sim 0.5\%$ uncertainty. We therefore adopt a $\sim 0.5\%$ uncertainty in the non-linearity of WFC3/IR. WFC3/IR detector artifacts, most notably the IR blobs, are ignored by masking corresponding pixels flagged in the DQ array.

As described in SKYSURF-1, we adopt a dark/ bias uncertainty of 1% for WFC3/IR, corresponding to 0.005 electrons per second for a F125W image. We

define the thermal dark signal to be thermal noise from the telescope assembly and instruments (see SKYSURF-2). It is strongly dependent on wavelength, where it is negligible below 1 μm and significant above 1.4 μm. As shown in SKYSURF-2, the maximum error we expect is 2.7% for F160W, with lower uncertainties for F125W and F140W. To be conservative, we adopt 0.01 electrons per second uncertainty in the thermal dark signal for all WFC3/IR sky-SB measurements in this report. Carleton et al. (in prep) will provide better constraints on the thermal dark signal.

During manual inspection of images, we noticed clear amplifier offsets. These effects are known to be due to differences in the noise and gain between amplifiers. In Section 2.8.4.5, we explore the effect this has on sky-SB estimates. We find median differences in pixel column values close to the amplifier boundaries to be $< 0.2\%$ for all WFC3/IR filters. We therefore do not include amplifier differences in our WFC3/IR error budget.

2.8.4.3 ACS/WFC Uncertainties

Cohen et al. (2020) find that the newest ACS/WFC flat-fields result in a photometric scatter of point sources that range from 0.5% to 3%. They claim this could be contributions from various reference files and CTE losses that are underestimated. In Section 2.8.4.6, and mentioned in Section 2.8.4.1, we independently explore uncertainties in the flat-fields by taking advantage of the large SKYSURF database. On average, our results agree with Cohen et al. (2020). Following Windhorst et al. (2022), we adopt the conservative uncertainty in the ACS/WFC flat field to be 2.2%. As described in SKYSURF-1, we adopt a zeropoint uncertainty for ACS/WFC to be 1% (Figure 2 Bohlin et al. 2020).

ACS/WFC exhibits bias offsets that vary from amplifier to amplifier, as described in Lucas & Rose (2021). The accuracy of the bias level subtraction is limited by random variations of about 0.3 DN (0.6 electrons). As described in SKYSURF-1, the ACS/WFC exhibits dark current uncertainty of 0.001 electrons per pixel per second. Figure 3 from Anand et al. (2022) shows a scatter in the ability to determine the ACS/WFC dark current to be ∼0.001 electrons per second (0.5 electrons for a 500 second exposure). Finally, we adopt a postflash uncertainty for ACS/WFC to be 0.37 electrons (SKYSURF-1).

2.8.4.4 Crosstalk

The CCD's on ACS are known to suffer from crosstalk (Giavalisco et al., 2004), where artificial "ghosts" from bright objects appear in mirror-symmetric positions in other ACS quadrants. These ghosts will appear as depressions relative to the background, with strengths of only a few electrons per pixel. However, the sky-SB itself can be on the order of a few electrons per pixel, so it is necessary we take crosstalk into consideration. Therefore, we correct for crosstalk to see how it affects our sky-SB measurements. For this simple test, we focus on ACS F775W images, where we analyze each ACS chip independently. Our default algorithm masks sky sub-regions that likely contain discrete objects. To correct for crosstalk, we reflect all masked regions to the opposite quadrant to mask the ghost corresponding to any bright objects. After reflecting masked regions, we recalculate the sky-SB. We find that crosstalk affects the sky-SB by only 0.008% for 68% of measurements. 95% of the measurements have a 0.08% difference. We conclude that our algorithm is robust enough that crosstalk does not significantly impact sky-SB levels.

2.8.4.5 Amplifier Differences

The readout amplifiers can introduce additional errors to our analysis. Differences in readout noise and gain between amplifiers can cause artificial variations in the sky-SB level. Differences in sky-SB will appear as additive differences in the background for the part of the detector that is read out to a corresponding amplifier. Correcting for this without affecting the true sky-SB level is very difficult. It requires identification of differences in background level exactly at the amplifier boundaries without taking light from objects into account. This would mean only using pixels close to the amplifier boundaries, many of which are likely contaminated by discrete objects. We consider this task to be past the scope of this project. However, we test for systematic differences across our database by measuring how the mean pixel value of a pixel column varies across amplifier boundaries. The median difference between the 20 pixel columns to the left of the amplifier boundary and the 20 pixel columns to the right of the amplifier boundary is always $< 0.2\%$ for WFC3/IR images in our database. We therefore do not include amplifier differences into our uncertainty estimations.

2.8.4.6 Trends in darkest sub-regions on the CCD

If there are regions on a detector that have systematically lower sky-SB values due to flat-field error, bias error, or geometrical distortion, this could potentially bias our results. We run our algorithm (described in Section 2.3) using `flt`/`flc` files as input instead of ProFound SKY maps, as ProFound can smooth over the CCD structures we want to study (i.e. flat-field and distortion). We test for systemically darker sub-regions by creating two-dimensional histograms of the darkest 5% of sub-regions

from our sky estimation algorithms. We refer to these as the "darkest sub-regions" for this discussion.

The resulting histograms are shown in Figures 21-23. To best probe CCD structure, we use *all* images in our SKYSURF database. Each two-dimensional histogram includes $N \simeq 1000 - 27,000$ images, so any subtle effects on the sky-SB from a particular detector location can be sampled this way. Bluer boxes indicate regions where most SKYSURF images contain a darkest sub-region in the corresponding location on the detector. In other words, bluer regions are systematically darker. Redder boxes indicate regions where most SKYSURF images do not contain a darkest subregion in the corresponding location on the chip. For ACS/WFC and WFC3/UVIS, there is a clear structure in the histograms that resemble the flat-fields (Mack et al., 2017; Dressel, 2021). The structure for WFC3/IR is less obvious, where the darkest sub-regions instead tend along the WFC3/IR amplifier boundaries.

The residual flat-field seen in Figures 21-23 could potentially affect sky-SB measurements. Because these figures resemble the flat fields, we use them to quantify uncertainties in flat field estimates. We use the histograms in Figures 21-23 to find the systematically darkest (darkest 5% of sub-regions) and brightest regions (brightest 5% of sub-regions). For every SKYSURF image in a filter, we take the mean sky-SB of the previously identified darkest regions and the mean sky-SB of the brightest regions. Note that these regions are the *same* for every image in a filter because they are determined using Figures 21-23.

We can compare the mean of the darkest and brightest regions to estimate the maximum level of uncertainty that the structure seen in Figures 21-23 add to surface

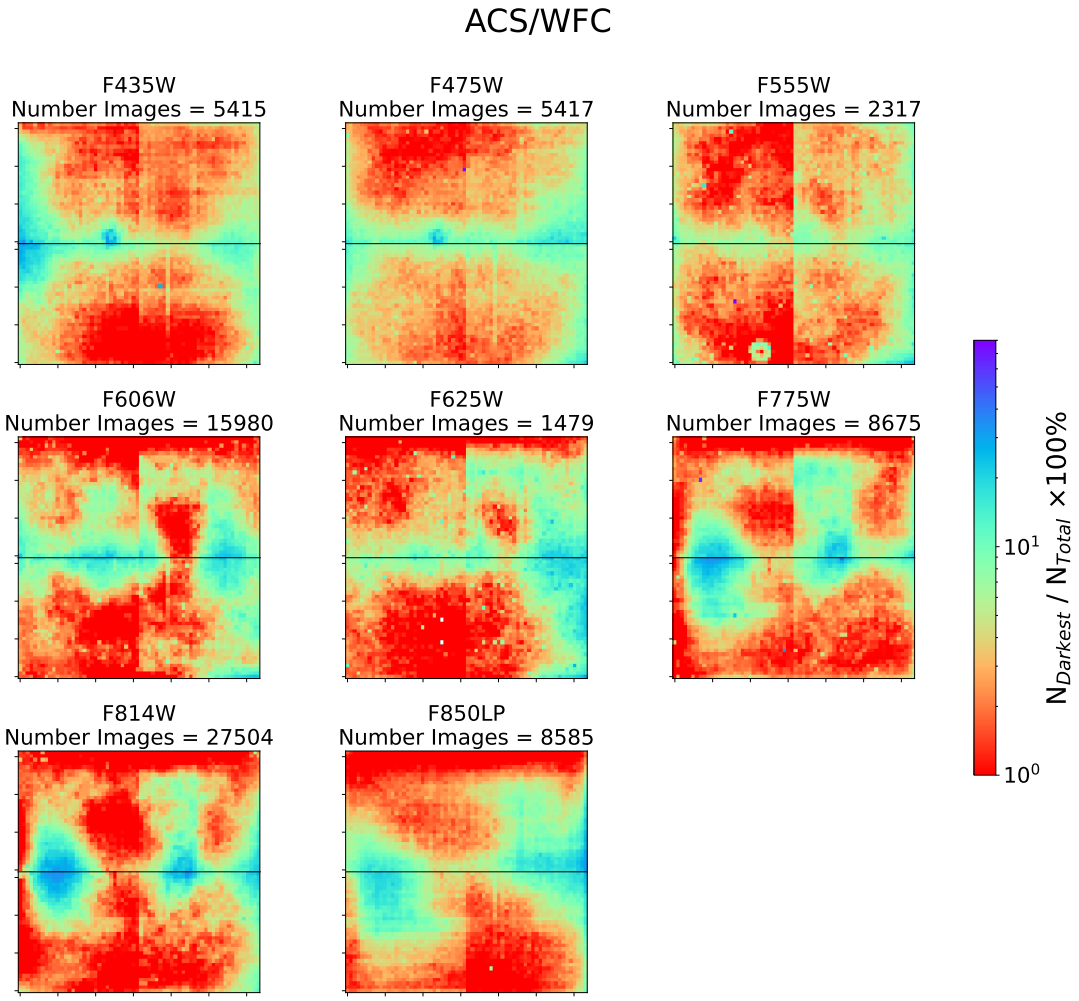

Figure 21. Two-dimensional histograms of the darkest sub-regions for all the images in every filter in ACS/WFC. The colorbar indicates the percent of images ($N_{\rm Darkest}/N_{\rm Total} \times 100\%$ where $N_{\rm Darkest}$ is the number of darkest sub-regions and $N_{\rm Total}$ is the total number of images) in this filter that contain a darkest sub-region in the corresponding location. In other words, regions that are more blue/ purple have systematically lower sky-SB levels across the entire filter. These histograms resemble the ACS/WFC flat-fields, indicating a residual flat-field exists in a majority of images in our database.

brightness measurements. Figure 24 shows the ratio of the brightest and dimmest sub-regions. We find that WFC3/IR does not show significant sky-SB differences between the darkest and brightest regions. However, WFC3/UVIS and ACS/WFC tend to show $\sim 2-5\%$ differences.

This is a unique test of flat-field uncertainty due to SKYSURF's massive database and corresponding sky-SB measurements. Although not necessarily relevant for this work, this test gives a maximum possible flat-field uncertainty on aperture photometry. We still adopt Mack et al. (2016) as our flat field uncertainty for SKYSURF sky-SB measurements.

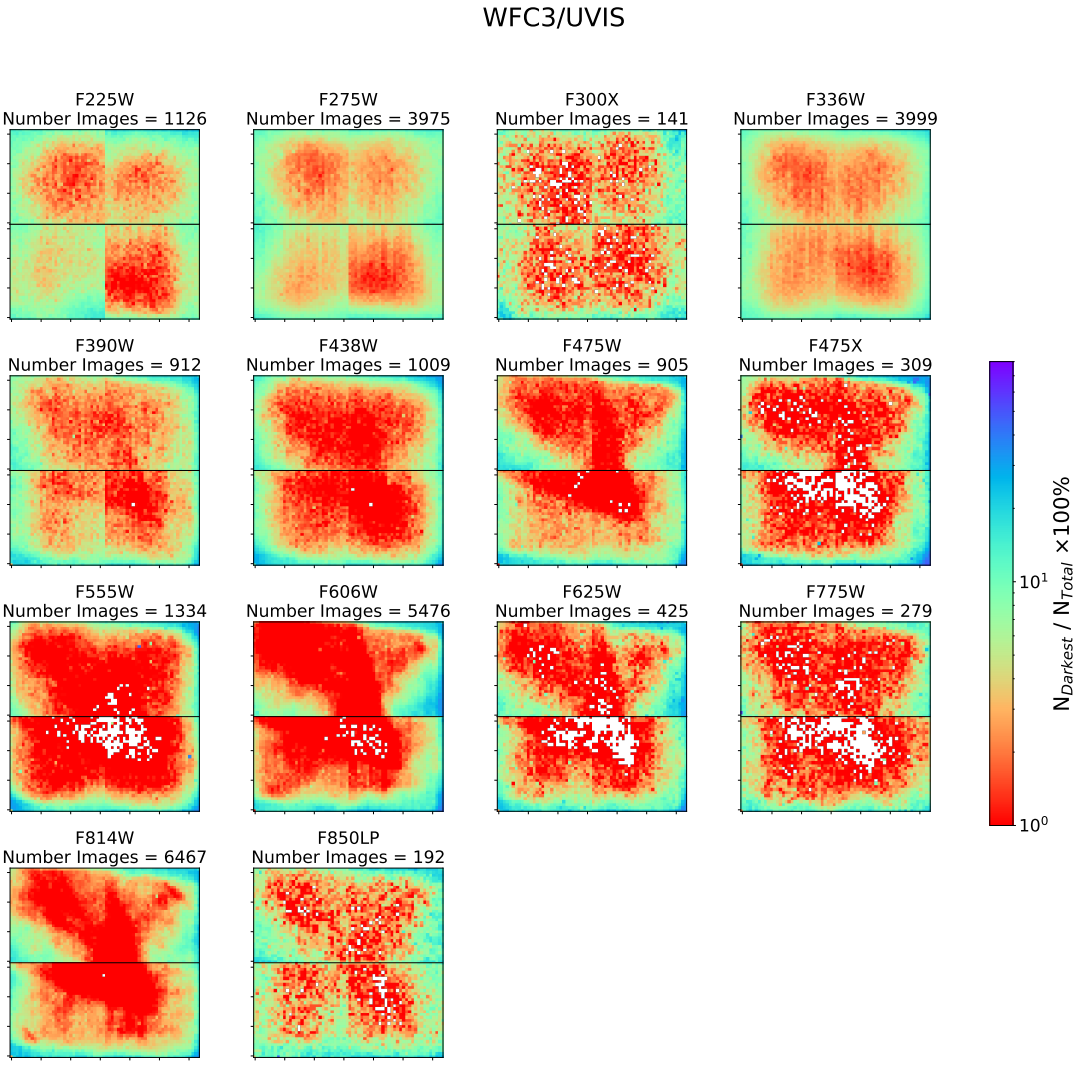

Figure 22. Two-dimensional histograms of the darkest sub-regions for all the images in every filter in WFC3/UVIS. The colorbar indicates the percent of images ($N_{\rm Darkest}/N_{\rm Total} \times 100\%$ where $N_{\rm Darkest}$ is the number of darkest sub-regions and $N_{\rm Total}$ is the total number of images) in this filter that contain a darkest sub-region in the corresponding location. In other words, regions that are more blue/ purple have systematically lower sky-SB levels across the entire filter. White indicates regions that are always ignored due to detector artifacts or regions that always contain a bright object. These histograms resemble the WFC3/UVIS flat-fields, indicating a residual flat-field exists in a majority of images in our database.

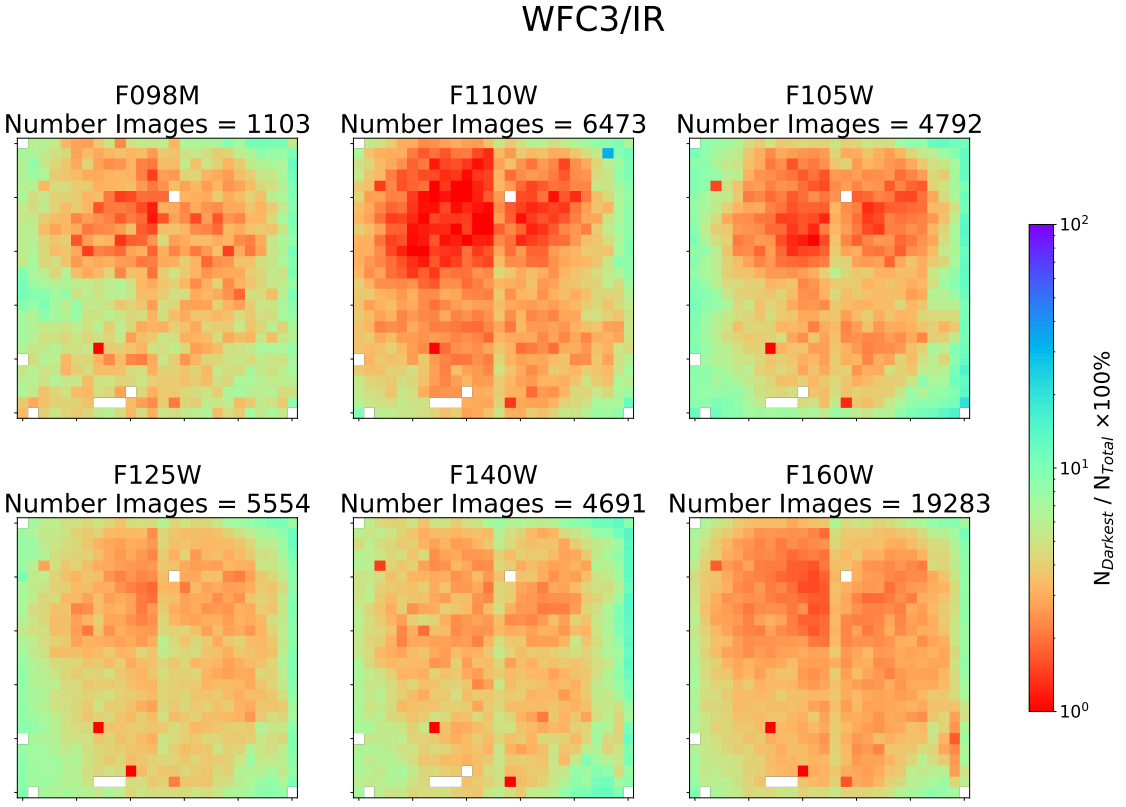

Figure 23. Two-dimensional histograms of the darkest sub-regions for all the images in every filter in WFC3/IR. The colorbar indicates the percent of images ($N_{\rm Darkest}/N_{\rm Total} \times 100\%$ where $N_{\rm Darkest}$ is the number of darkest sub-regions and $N_{\rm Total}$ is the total number of images) in this filter that contain a darkest sub-region in the corresponding location. In other words, regions that are more blue/ purple have systematically lower sky-SB levels across the entire filter. White indicates regions that are always ignored due to detector artifacts. Known artifacts that are always masked are the "death star" (bottom middle) and "wagon wheel" (bottom right corner).

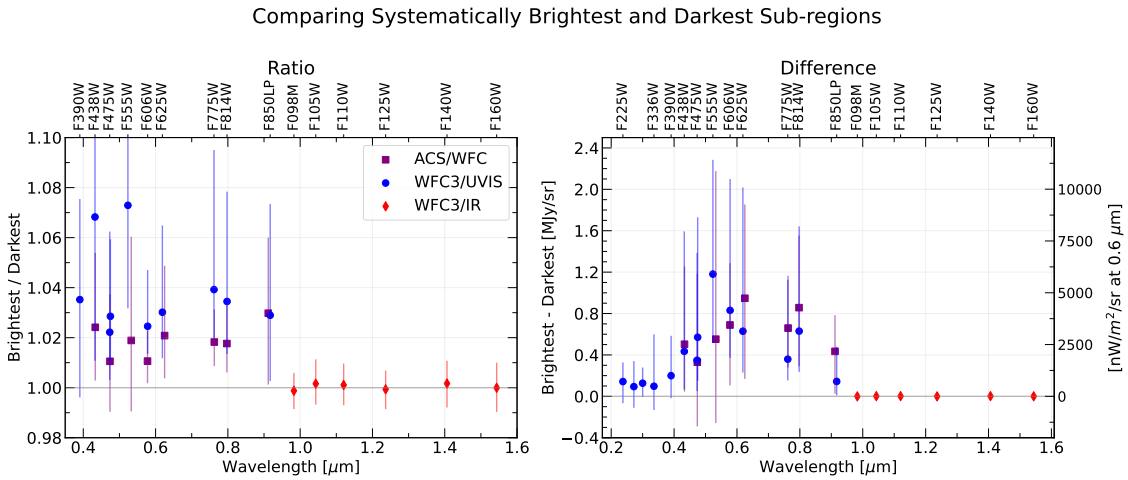

Figure 24. Comparison of the systematically brightest and darkest sub-regions. The error bars for both plots show the 16th- and 84th-percentiles of the y-axis distribution. **Left:** Median ratio of the brightest sub-regions over the darkest sub-regions. The bluest filters are excluded because the sky-SB is nearly zero. **Right:** Median difference of the brightest sub-regions over the darkest sub-regions. The left y-axis shows units of MJy sr^{-1} and the right axis shows nW m^{-2} sr^{-1} at 0.6 μm.

2.8.4.7 Testing how different CTE corrections affect the WFC3/UVIS sky-SB

As described in Appendix B.2 of SKYSURF-1, we redownloaded WFC3/UVIS images calibrated with the newest `calwf3` version at the time: `calwf3` v3.6.0. This version of the standard calibration pipeline presents updates to the CTE corrections. Since CTE corrections adjust pixels containing a sky-SB signal, we ensure these updated corrections do not significantly affect sky-SB measurements. Results are shown in Table 5. The sky-SB rms improves for all filters, with sky-SB rms values typically being 2–5% lower with the v3.6.0 corrections. We find an average median offset in sky-SB between both pipelines of $\sim 0.007\%$ for filters longward of 0.4 μm and an average median offset between both pipelines of $\sim 1.9\%$ for filters shortward 0.4 μm.

Filter	Median Sky Ratio	Median Sky rms Ratio
F225W	0.979750	0.978251
F275W	0.877970	0.969360
F300X	1.037716	0.952036
F336W	1.014963	0.979252
F390W	0.997349	0.975110
F438W	1.002838	0.975508
F475X	1.008633	0.964548
F475W	1.000642	0.969892
F555W	0.999497	0.970605
F606W	1.001499	0.958634
F625W	0.999005	0.962439
F775W	0.987096	0.973376
F850LP	0.999113	0.972571
F814W	1.001019	0.963322

Table 5. Median ratio of the calwf3 v3.5.0 / calwf3 v3.6.0 sky-SB values and sky-SB rms values. Only reliable sky-SB measurements are used in this comparison.

2.8.5 Converting to Flux Units

Given the confusion that sometimes arises on this topic, in this section we explain our methods to convert our sky-SB measurements to units of spectral flux density. The conversions for each camera are highlighted in Equations 2.14-2.16. We adopt the pixel areas described in the WFC3 Instrument Handbook (Dressel, 2021) and the ACS Instrument handbook (Ryon, 2021): 0.135×0.121 arcsec^2 for WFC3/IR, 0.0395×0.0395 arcsec^2 for WFC3/UVIS and 0.050×0.050 arcsec^2 for ACS/WFC.

$$I_{\lambda,\mathrm{WFC3/IR}} = \frac{S_{\mathrm{chip}} \times \texttt{PHOTFNU}}{A} \tag{2.14}$$

$$I_{\lambda,\mathrm{WFC3/UVIS}} = \frac{S_{\mathrm{chip}} \times \texttt{PHTFLAM}(\mathrm{converted})}{A} \tag{2.15}$$

$$I_{\lambda,\mathrm{ACS/WFC}} = \frac{S_{\mathrm{chip}} \times \texttt{PHTFLAM}(\mathrm{converted})}{A} \tag{2.16}$$

For WFC3/IR in Equation 2.14, S_{chip} is the measured sky-SB in units of electrons per second (e^-/s), `PHOTFNU` is the inverse sensitivity taken from the image header in units of Jy/(e^-/s), and A is the average pixel area in units of steradians. When using SKYSURF sky-SB measurements for SKYSURF, a thermal dark signal must be subtracted (Carleton et al., 2022). Please refer to Carleton et al. (in prep) for updated estimates on thermal dark levels.

For all images in our database, a flux correction (indicated by keyword `FLUXCORR`) is performed to bring the sensitivity of UVIS2 (one of the WFC3/UVIS chips) to the same sensitivity of UVIS1. However, the `PHOTFNU` keyword does not update with this change. Instead, the the chip-dependent inverse sensitivity, `PHOTFLAM`, is updated, so we use this keyword instead. `PHTFLAM` is used for both WFC3/UVIS

and ACS/WFC, where we convert it from units of erg cm^{-2} $Å^{-1}$ s^{-1} to units of Jy (`PHTFLAM`(converted)) using the chip-dependent pivot wavelength listed in the header (`PHTPLAM`). This conversion is done using `astropy.units` (Astropy Collaboration et al., 2013, 2018).

2.8.6 Ensuring A Reliable Diffuse Light Estimate

We ensure our methods described in Section 2.5 result in a reliable Diffuse Light estimate. Figure 25 shows a one-to-one plot of sky-SB measurements used in SKYSURF-2 and those presented in this work. There are no noticeable trends in Figure 25, meaning that at first order, taking a median difference between SKYSURF-2 and this work will result in consistent results, whether or not we utilize the darkest or the brightest sky-SB values.

SKYSURF-2 uses the Lowest Fitted Sky (LFS) method to estimate the DL, which utilizes the darkest sky-SB measurements. To ensure our calculated sky-SB difference represents the darkest sky-SB values necessary for the LFS method, we plot the difference in sky-SB (This Work − SKYSURF-2) as a function of the sky-SB measured in SKYSURF-2. The red lines show the median difference used to estimate DL in Table 4. The red lines agree with the darkest sky-SB measurements, confirming that the method to estimate DL limits in this work is consistent with the LFS method from SKYSURF-2.

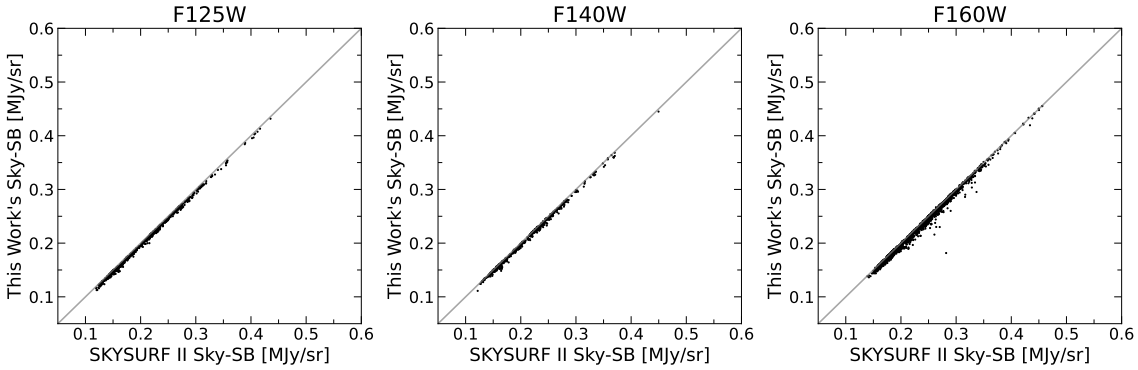

Figure 25. One-to-one relationship of the sky-SB measurements in this work (using the Pro-med algorithm) and the measurements in SKYSURF-2. The x-axis shows sky-SB measurements from SKYSURF-2 and the y-axis shows sky-SB measurements from this work. The grey line is a one-to-one relationship.

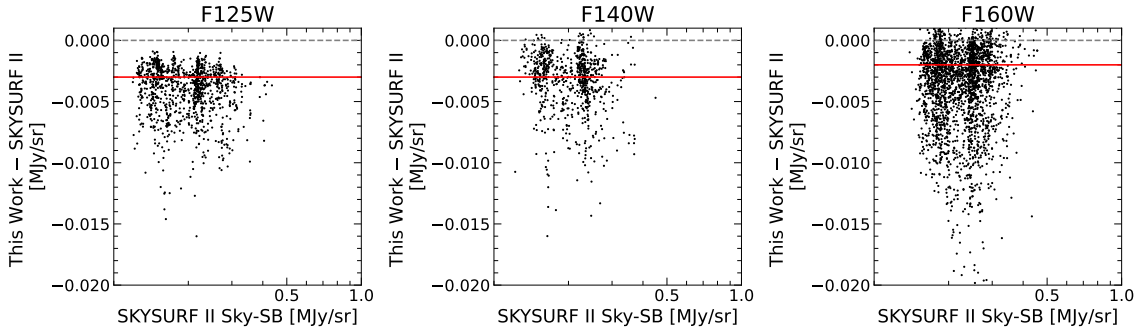

Figure 26. Relationship of the sky-SB measurements in this work (using the Pro-med algorithm) and the measurements in SKYSURF-2. The x-axis shows sky-SB measurements from SKYSURF-2 and the y-axis shows the difference in sky-SB values between this work and SKYSURF-2. The red lines indicate the median differences shown in Table 4 used for DL estimations. The red lines agree with the darkest sky-SB measurements from SKYSURF-2.

Chapter 3

TREASUREHUNT: TRANSIENTS AND VARIABILITY DISCOVERED WITH HST IN THE JWST NORTH ECLIPTIC POLE TIME DOMAIN FIELD

3.1 Introduction

With the successful launch, commissioning, and first year of science observations, the James Webb Space Telescope (JWST) has opened new opportunities for the study of the faint (potentially m_{AB} >30 mag) variable Universe. After discovering time-varying phenomena (i.e., transients and objects that vary in brightness or position), one would need the capacity to monitor these objects at their astrophysically relevant timescales, to determine the nature of their variability. For example, rapid follow-up of supernovae (SNe) is crucial to determine their types and distances. Flexible follow-up of active galactic nuclei (AGN) allows the timescale of AGN variability (which can range from several days to several years) to be measured, which can be linked to properties of the supermassive black hole (SMBH) at the center of its host galaxy (e.g., Vanden Berk et al., 2004). However, transient follow-up and variability monitoring with JWST become difficult when Sun angle restrictions, power generation, and micrometeoroid mitigation limit when any particular area of the sky can be observed. The Continuous Viewing Zones (CVZs) centered on the ecliptic poles are the only locations where JWST can observe at any time of the year and avoid these constraints.

Jansen & Windhorst (2018) selected a particularly suitable area within JWST's northern CVZ, the JWST North Ecliptic Pole (NEP) Time Domain Field (TDF), to enable the exploration of time-varying phenomena with JWST at high redshifts, but

also within the halo of our own Galaxy, and in the extreme outer Solar System at high ecliptic latitudes. The JWST NEP TDF is a $>14'$ diameter field centered on $(\mathrm{RA, Dec})_{\mathrm{J2000}} = (17{:}22{:}47.896, +65{:}49{:}21.54)$, that was carefully chosen to minimize foregrounds, to be devoid of stars brighter than $m_K \sim 15.5$ mag, and maximize the observing efficiency for time-domain science with JWST. Its location near the NEP allows for follow-up of transients and variable sources at any cadence and at any time of the year. In addition, the NEP suffers minimal Zodiacal foregrounds, with minimal variation in the course of a year, naturally allowing for more sensitive observations per unit time. While the ecliptic latitude of the JWST NEP TDF is very high ($b_{\mathrm{ecl}} \simeq 86.2°$), it is located at intermediate Galactic latitude ($b^{II} \simeq 33.6°$), providing a clear but relatively long sight-line through the halo of our Galaxy. This makes the field useful for deep Galactic time-domain science with JWST as well.

This field serves as an important testbed for advancing our understanding of the time-varying universe at fainter limits than can be reached from the ground at optical and near-IR wavelengths, where transients and variability can hold cosmological significance (e.g., dark energy, cosmic star formation rate, and the evolution of supermassive blackholes). Type Ia SNe are often used as standard candles to provide critical constraints on the Hubble constant, the mass density of the universe, the cosmological constant, the deceleration parameter, and the age of the Universe (e.g., Riess et al., 1998). Core Collapse (CC) SNe are equally important, as they not only provide most of the heavy elements in our universe (e.g., Matteucci & Greggio, 1986), but also should trace the rate of instantaneous massive star formation. CC SNe rates and their connection to cosmic star formation rates remains poorly understood, as there seems to be a significant mismatch between observed CC SNe rates and what is expected (see, e.g., Cappellaro, 2014).

In addition to studying transient events like SNe, we can uncover new insights into the nature of astrophysical processes that lead to AGN variability. AGN are powered by matter accreting onto a SMBH (Lynden-Bell, 1969). All massive galaxies host central SMBHs (e.g., Magorrian et al., 1998; Kormendy & Ho, 2013), and irregular or varying rates of infall, as well as turbulence and temperature fluctuations, can cause variations in brightness over time. The study of these variable AGN can provide a better understanding of the complex, unstable processes occurring around supermassive black holes (e.g., Shakura & Sunyaev, 1976; Ulrich et al., 1997; Kawaguchi & Mineshige, 1999). As AGN are linked to the evolution of their host galaxy (e.g., Gebhardt et al., 2000; Ferrarese & Merritt, 2000; Kormendy & Ho, 2013), this would also allow a better understanding of the co-evolution of galaxies and their central black holes.

AGN are often identified via X-ray or mid-IR emission, colors, or spectroscopic signatures, however, these methods can miss AGN that are intrinsically faint or lack X-ray emission. Variability in particular provides a unique way to identify AGN that might be missed via these other methods (e.g., Boutsia et al., 2009; Pouliasis et al., 2019). Lyu et al. (2022) explore various AGN selection methods in GOODS-S, including those based on X-ray emission, UV to mid-IR spectral energy distributions (SEDs), mid-IR colors, radio emission, and variability, and find $\sim$10% of the AGN in this field to exhibit optical variability[4]. We refer to Lyu et al. (2022) and Lyu et al. (2023) for a broader treatment of the role of various AGN selection methods.

Variability proves especially promising for identifying faint AGN, as there appears to exist an anti-correlation between AGN brightness and variability amplitude (Hook et al., 1994; Trevese et al., 1994; Cristiani et al., 1997; Giveon et al., 1999; Vanden

[4]The optical variable sample is selected from Pouliasis et al. (2019) (10 year baselines, and 5 epochs per object).

Berk et al., 2004; Wilhite et al., 2008; Zuo et al., 2012). In addition, the amplitude or timescale of AGN variability is correlated accretion disk size, and therefore black hole mass (e.g., Xie et al., 2005; Wold et al., 2007; Li & Cao, 2008; Wilhite et al., 2008; Burke et al., 2021) and redshift (Cristiani et al., 1990; Hook et al., 1994; Trevese et al., 1994; Vanden Berk et al., 2004). A variability survey can thus provide a more complete census of the AGN population and its evolution over cosmic time. In addition, AGN identified through variability may be spectroscopically confirmed at any later time.

A large number of studies focusing on AGN variability have been published in the last few years (for a recent review, see Lyu & Rieke, 2022). At optical wavelengths, AGN have been identified via their variability on scales from weeks to years (Cohen et al., 2006; Morokuma et al., 2008; Villforth et al., 2010; Sarajedini et al., 2003, 2011).

As part of Hubble Space Telescope (HST) programs GO 15278 (PI: R. Jansen) and GO 16252/16793 (TREASUREHUNT; PIs: R. Jansen & N. Grogin) UV–Visible imaging of the JWST NEP TDF was secured with the F275W (0.272 μm), F435W (0.433 μm), and F606W (0.592 μm) filters. Areas of partial overlap between individual visits of the observations allow a first look at 2- to 4-epoch object variability and transients in this field. For a detailed description of the observational design of these HST surveys, data reduction, stacked images, and source photometry, we refer the reader to Jansen et al. (2024a,b; in prep.).

While previous HST variability studies like Sarajedini et al. (2003) (Hubble Deep Field North) and Cohen et al. (2006) (Hubble Ultra Deep Field) achieved impressive depths (29.0 and 30.5 mag, respectively), they are limited to approximately $\sim$6.5 arcmin^2. Villforth et al. (2010), on the other hand, leveraged the expansive area (>500 arcmin^2) of the Great Observatories Origins Deep Survey (GOODS), but to a relatively shallow depth ($\sim$26.0 mag). At the same exquisite angular resolution (full width half

max <0.09"), TREASUREHUNT observations provide a unique combination of depth ($m_{AB} < 29.5$ mag) and area ($\sim$88 arcmin^2) for a variability analysis.

In this work, we provide the first time-domain study of the JWST NEP TDF at visible wavelengths, presenting 12 transients (supernova candidates) and $\sim$100 variable candidates (AGN candidates) identified using TREASUREHUNT data. In § 3.2, we briefly summarize the TREASUREHUNT HST data, and data processing specific to the detection of transients and variable objects. § 3.3 explains our methods for identifying transients and variability in the NEP TDF. In § 3.4.1 and § 3.4.2 we showcase our supernova candidate detections and our variable AGN candidates, respectively. All magnitudes are in AB units[5] (Oke & Gunn, 1983). Where relevant, we adopt a flat ΛCDM cosmology with $H_0 = 68$ km s^{-1} Mpc^{-1}, $\Omega_m = 0.32$, and $\Omega_\Lambda = 0.68$ (Planck Collaboration et al., 2016a, 2020a).

3.2 Data and Processing

3.2.1 HST Observations and Data Processing

Observations from HST GO 15278 were taken between 2017 October 1 and 2019 February 9, and those from GO 16252+16793 (TREASUREHUNT[6]) between 2020 September 25 and 2022 October 31. The former program targeted the central ($r < 5'$) portion of the JWST NEP TDF, and the latter an outer annulus to $r \sim 7'.8$. Together, these programs provide near-contiguous coverage with the Wide Field Camera 3

[5]Defined as $m_{AB} = -2.5\log(F_\nu) + 8.90$ mag, where the flux density F_ν is in Jy.

[6]We will loosely refer to the observations and data of the GO 15278 program as also part of TREASUREHUNT hereafter, as the intent and survey strategy were identical.

(WFC3/UVIS) in the F275W filter ($\lambda_c \sim 0.272\ \mu$m) and with the Advanced Camera for Surveys (ACS/WFC) in the F435W and F606W filters ($\lambda_c \sim 0.433$ and $\sim$0.592 μm), with a total area of $\sim$194 arcmin^2 (ACS/WFC). The full HST coverage of the JWST NEP TDF is shown in Figure 27.

As described in more detail in Jansen et al. (2024a,b; in prep.), both programs used 4-orbit CVZ and pseudo-CVZ[7] visits to reach 2-σ limiting depths of $m_{AB} \simeq 28.0$, 28.6, and 29.5 mag in F275W, F435W and F606W, respectively. These limiting depths were determined using the `SourceExtractor` (Bertin & Arnouts, 1996b) `MAG_AUTO` aperture, within areas with single-epoch coverage (lighter grey in Figure 27), and are the adopted nominal survey depths.

The TREASUREHUNT data were retrieved from MAST and post-processed (after the standard ACS and WFC3 calibration pipeline steps of flatfielding and correction for Charge Transfer Efficiency (CTE) effects) to mask satellite trails, remove residual CTE trails, and fit and subtract the background (Jansen et al. 2024a,b; in prep.). The latter was needed because the observing strategy deliberately used the full duration of CVZ orbits, as well as pseudo-CVZ orbits where HST was allowed to dip closer to the Earth limb than the nominal limit for CVZ orbits. This resulted in excess background light that helped fill charge traps in the F275W exposures with their exceedingly dark natural sky background (e.g., O'Brien et al., 2023), but also rendered the observed background level meaningless.

The background-subtracted images were corrected for geometric distortion and aligned to the Gaia/DR3 (Gaia Collaboration et al., 2016, 2023) astrometric reference grid using the `DrizzlePac` tasks `TweakReg` and `AstroDrizzle` (see Hoffmann

[7]True CVZ orbits imply Earth Limb angles $\gtrsim 15.5°$, but uninterrupted observations can be implemented at smaller angles down to $\sim 7.6°$ away from the Earth limb when phased to execute when that limb is dark. We term these possible but non-standard opportunities "pseudo-CVZ".

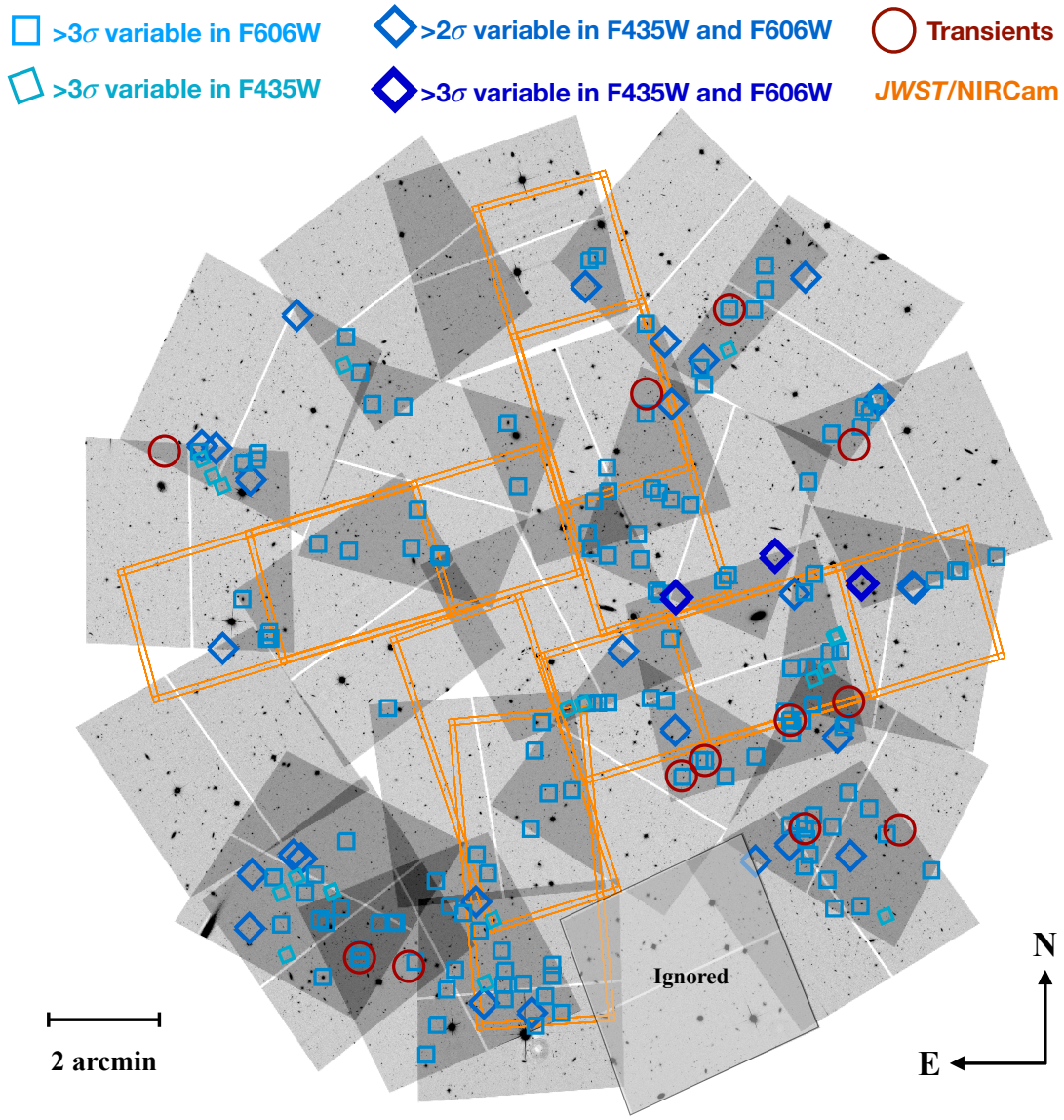

Figure 27. Full extent of HST ACS/WFC coverage of the JWST NEP TDF. Regions of overlap between visits in the mosaic are highlighted in progressively darker shades of grey for areas of 2-, 3-, and 4-epoch overlap. This paper focuses on these regions of overlap, with a total area of 87.94 arcmin^2, to investigate transients and variable sources. Red circles mark the positions of the 12 identified transients, while blue squares and diamonds mark the 190 unique variable candidates discovered in this study. We expect ∼80 of these sources to be false positives (see § 3.3.2). Symbol shapes and colors identify the samples from which individual variables were selected, as indicated by the legend at the top of the figure. For comparison, the JWST/NIRCam coverage of this field is outlined in orange. We estimate photometric redshifts (§ 3.4.3) for objects with both HST and JWST photometry. One visit (`jeex02`; at bottom right) with a bad astrometric solution was ignored in this work.

et al., 2021). The `AstroDrizzle` software also flags cosmic-rays, a crucial step when identifying faint variability, where cosmic ray induced signals could cause spurious variability if not properly removed. We expect, and tested (as discussed in more detail in the Appendix), that all cosmic ray and other image artifacts were largely removed through the `AstroDrizzle` step, as each single 4-orbit visit resulted in 8–9 exposures per filter that were stacked together.

All 8–9 exposures per visit were taken at the same pointing with small $\leq 0.2''$ dither offsets in RA and Dec. For each visit, we drizzle-combined the individual post-processed, rectified and aligned exposures per filter (Jansen et al. 2024a,b; in prep.). For ACS/WFC F606W and F435W, this resulted in 24 rectified and aligned science images (and 24 associated weight maps), and for WFC3/UVIS F275W in 23 images and associated weight maps, each at a pixel scale of 0.030" pix^{-1} and centered on the nominal field center of the JWST NEP TDF. We also use the full mosaics of all drizzle-combined images per filter, generated with the same image dimensions and pixel scale, and aligned to Gaia/DR3 to within 0.008" in RA and Dec.

The footprints of individual ACS/WFC (and to a lesser extent WFC3/UVIS) visits partially overlap one another, with a cumulative area of overlap of $\sim$88 arcmin^2. These overlapping regions are key to searching for transients and variability within this field. Figure 27 showcases the overlapping regions in progressively darker shades of grey for areas of 2-, 3- and 4-epoch overlap. The time interval between observations in these regions of overlap range between 1 day and 4+ years.

We note that while the very small number of epochs and sparse time sampling can catch transients like SNe and variable sources like AGN, they cannot provide a light curve to trace their evolution. Further epochs would provide a more robust

identification of variable sources, where we may characterize the scatter in the measured brightness (e.g., Pouliasis et al., 2019; Sokolovsky et al., 2017).

While our primary focus is the identification of time variable objects within the TREASUREHUNT HST data, we opt to incorporate ancillary data to better understand certain objects of interest. Specifically, we incorporate JWST/NIRCam (0.8–5 μm), NuSTAR and XMM-Newton, Chandra, and MMT/Binospec data.

3.2.2 JWST Observations and Data Processing

JWST/NIRCam observations within the JWST NEP TDF were obtained between 2022 August 25 and 2023 May 30 as part of JWST GTO 2738 (PIs: R. Windhorst & H. Hammel) in 7 broadband filters (F090W through F444W) and 1 mediumband filter (F410M) as part of the PEARLS program (Windhorst et al., 2023). Figure 27 shows the JWST observations outlined in orange, highlighting the 4 epochs, corresponding to the four orthogonal "spokes". Each spoke consists of two NIRCam pointings that partially overlap in the center. Each pointing includes a total exposure time of 3.5 hours across all 8 filters, or about 3000 sec per filter. Each spoke has an area of $13'.7$, totaling $54'.7$ of JWST observations.

The data were retrieved from MAST and post-processed by the PEARLS team using their custom pipeline to mitigate $1/f$ noise, alleviate wisps in the NIRCam/SW filters, mask snowball artifacts, and flatten the background across read-out amplifier boundaries. The individual post-processed images where rectified and aligned to Gaia/DR3 independent of the HST images, but using nearly identical methods. Full mosaics of the field were created for each filter with a 0.03" platescale. The 5 sigma point-source limit is typically between 28.0 and 29.1 mag, depending on the filter. For

more details on the reduction, calibration and post-processing, we refer to Windhorst et al. (2023), Robotham et al. (2023), and Jansen et al. 2024c (in prep.). In § 3.4.3, we will use PEARLS aperture photometry of transient and varying objects discovered in areas with both HST and JWST coverage to fit SEDs.

3.2.3 X-Ray Observations and Data Processing

The JWST NEP TDF has also been observed extensively in X-rays with NuSTAR, XMM-Newton, and Chandra. NuSTAR has monitored the field since Cycle 5 (PID 5192, 6218, 8180, and 9267; PI: F. Civano). For this work we use the Cycle 5+6 data and catalog published in Zhao et al. (2021a,b, 2024). The 21 NuSTAR observations took place over 28 months (between 2019 September and 2022 January), while the three XMM-Newton observations (part of the NuSTAR cycle 6 program) were taken over 15 months (between 2020 October and 2022 January). The total NuSTAR exposure from Cycle 5+6 is 1.5 Ms, reaching a flux limit of $3.3\times10^{-14}\,\mathrm{erg\,cm^{-2}\,s^{-1}}$ in the 3–24 keV band. We note that this is the deepest NuSTAR field taken thus far. The total XMM-Newton exposure time is 62 ks, reaching a limit of $8.7\times10^{-16}\,\mathrm{erg\,cm^{-2}\,s^{-1}}$ in the 0.5–2 keV band.

We also use the first 1.3 Ms of Chandra observations of the JWST NEP TDF (PID 19900666, 20900658, 21900294 and 22900038; PI: W.P. Maksym) spanning cycles 19–23. Chandra observed the field 46 times between 2018 April 12 and 2022 September 25 (a span of 4.6 years), with exposures ranging from 9 to 59.9 ks. Beginning 2021 August 29, these occurred in 90 ks epochs every 3 months, typically broken into 2 or more individual visits (OBSIDs) spanning no more than 30 days per epoch. We reprocessed and reduced the data using `ciao` (Fruscione et al., 2006), corrected the

cross-observations using source catalogs generated by `wavdetect`, and astrometrically registered them to Pan-STARRS (Chambers et al., 2016). We then used `merge_obs` to generate combined event files and exposure maps. The faintest 3σ detection in the catalog is 1.35×10^{-16} erg s^{-1} cm^{-2} in the full 0.5–7 keV band assuming galactic absorption and a $\Gamma = 1.4$ power law.

3.2.4 Ground Based Spectroscopy

MMT/Binospec (Fabricant et al., 2019) observations of the JWST NEP TDF in 2019 September (PI: C. Willmer) used a 270 lines/mm grating and a 1″ slit width to yield spectra spanning ∼3900–9240Å sampled at 1.30Å/pix and with a resolution of ∼4.9Å (full width half max) at 6500Å. The exposure time was 1 hr (4×900 s), reaching $S/N \sim 5$ at $m_{AB} \sim 22.5$ mag for quiescent galaxies, and a magnitude deeper for galaxies with significant emission lines.

3.3 Methods to Identify Transients and Variability

In this section, we detail our methods for identifying transients and variability in the 55 areas of overlap (shown as darker shades of grey in Figure 27) with a combined area of ∼88 arcmin^2.

Transients are usually defined as objects that only appear for a short duration. For this work, where we expect most transients to be SNe, we consider relatively bright point sources that are present in one epoch, yet do not appear in another. We searched for transients using difference images, and considered any source detected therein a transient candidate. In contrast, variable sources tend to show less extreme

differences in brightness and are not as evident in difference images. Variable sources are therefore identified after measuring the source flux and its associated uncertainty within a small aperture. Consequently, some sources we identify as transients may be variable sources with extreme amplitudes of variability (e.g., quasars), and some variable sources may be dim transients or transients caught well away from peak brightness (e.g., SNe). Nonetheless, we assume most transients we discover will be SNe, while most variable sources will be weak AGN. However, the methods presented here may identify a variety of objects, including variable stars, tidal disruption events, gamma ray bursts, or quasars. We did not identify any objects that showed appreciable movement between visits. For all objects discovered here, further analysis is required to determine their true nature.

3.3.1 Transient Search

Transients were identified by visual inspection of difference images, each of which was created as follows. First, we bring the drizzled images of individual visits to the same pixel grid using their Gaia-aligned WCS and the Astropy (Astropy Collaboration et al., 2013, 2018, 2022) affiliated package `reproject`. Then, we generate two distinct difference images for each overlapping region in the deeper F606W images, i.e., 110 difference images for the 55 overlapping areas. For instance, if Visit 1 overlaps with Visit 2, we generate a difference image by subtracting Visit 2 from Visit 1, and another difference image by subtracting Visit 1 from Visit 2. In each difference image we then visually identify sources with positive flux that are consistent in appearance with bearing the imprint of the point spread function (PSF). We did not use the F435W images for our transient search, because they are $\sim$0.9 mag shallower.

Although rare, bright cosmic ray (CR) induced signals can sometimes survive in final drizzled products and subsequently appear in difference images. We inspected the individual pipeline-calibrated, flat-fielded exposures at the corresponding position of each transient candidate to ensure they appear in each exposure, bear the imprint of the PSF, and are not (residuals of) CRs or other spurious noise. We originally found 20 transient candidates, of which 8 were confirmed to be due to CRs and were removed from further consideration.

We measured the apparent F606W magnitudes of each transient using the difference images. To measure transient magnitudes, we centered a circular aperture with a radius of 8 pixels on the transient in the difference image, and measured its magnitude within that aperture. These apertures are $\gtrsim 5\times$ the full width half max (FWHM) of the PSF and encompass the transient signal. We used the Python photometry package `Photutils` (Bradley et al., 2022) and specified the exact center of each aperture. We created a difference error map by adding the weight (WHT) maps from the individual visits in quadrature, then taking ERR $= 1/\sqrt{\mathrm{WHT}}$. We direct this error map into `Photutils` to derive an uncertainty on the reported flux. Magnitude errors are then calculated as $\Delta m = (2.5/\ln 10) \cdot \sigma_F / F$, with F the measured flux, and σ_F the uncertainty thereon, both as reported by `Photutils`.

For each transient, we also performed matched-aperture photometry on a subset of F435W difference images, generated for those regions of overlap that contained a transient.

Table 6. Relevant `SourceExtractor` parameters for variability identification and aperture photometry.

Parameter	Variability Aperture	Full Aperture
Aperture Size	0.24"	`FLUX_AUTO`
`DETECT_MINAREA`	5	5
`DETECT_THRESH`	1.5	1.5
`ANALYSIS_THRESH`	1.5	1.5
`DEBLEND_MINCONT`	0.001	0.06
`FILTER_NAME`	gauss_3.0	gauss_3.0
`GAIN`	*median exposure time*	
`BACK_SIZE`	128	128
`BACK_FILTERSIZE`	3	3
`BACKPHOTO_THICK`	50	50

Note. For each `SourceExtractor` parameter in the first column, the second an third columns list its value for identifying variable sources and for full aperture photometry, respectively. We used a circular aperture with a diameter of 0.24" diameter for variability identification, specified using the `PHOT_APERTURES` parameter, and the `FLUX_AUTO` aperture for full aperture photometry. We set the `GAIN` value to the median exposure time of the individual exposures combined per visit.

3.3.2 Variability Search

To detect variability in galaxies, we first constructed source catalogs using `SourceExtractor`, with object positions and aperture photometry for each visit. For initial object detection, as summarized in Table 6, we require an object to be detected at the 1.5σ level above the local sky level (given a gain value corresponding to the median exposure time of the individual exposures in that visit and filter) after smoothing with a Gaussian kernel with a FWHM of 3 pixels, and require a minimum number of 5 contiguous pixels to minimize detection of spurious sources. For the same reason, we also generously masked the pixels along the detector borders, where fewer contributing exposures result in excess noise and imperfect rejection of CR signal.

We compared brightness measurements across distinct visits to identify potential

variables. We specifically focus on detecting variability in the F435W and F606W filter observations, as the F275W filter magnitude limit is substantially brighter, the total area of overlap between individual F275W visits is substantially smaller, and the WFC3 F275W observations are not contemporaneous with the ACS/WFC F435W and F606W ones.

3.3.2.1 Photometry

Our goal is to leverage HST's high resolution to isolate the potentially varying nuclei within galaxies and SNe near their core while ignoring the non-varying extended component. To achieve this, we first set the minimum contrast for deblending in `SourceExtractor` (`DEBLEND_MINCONT`) to 0.001. This value is lower than is typical, but allows isolating the nuclei of galaxies *and* potentially locate variability in bright regions that may not be in the very center of a galaxy. In addition to a low deblending threshold, we opted to use apertures close to the FWHM of stellar objects. For our resolution of $<0\farcs09$, we used a circular aperture with a diameter of $0\farcs24$ (8 pixels). For apertures much larger than this the surrounding galaxy tends to dilute any variability of a compact central source. We henceforth refer to this small aperture as the $0\farcs24$ aperture, and to the corresponding magnitudes as $m_{0.24}$. The radius of this aperture is shown as the dashed blue vertical line in Figure 28 to facilitate comparison with detected stellar objects.

With `DEBLEND_MINCONT` = 0.001, the measured variability sometimes appears offset from the centers of galaxies. This could be due to off-center SNe or SMBHs that have yet to settle onto the centers of their host galaxies. To measure host galaxy properties for these offset events, we also ran `SourceExtractor` with `DEBLEND_MINCONT` = 0.06,

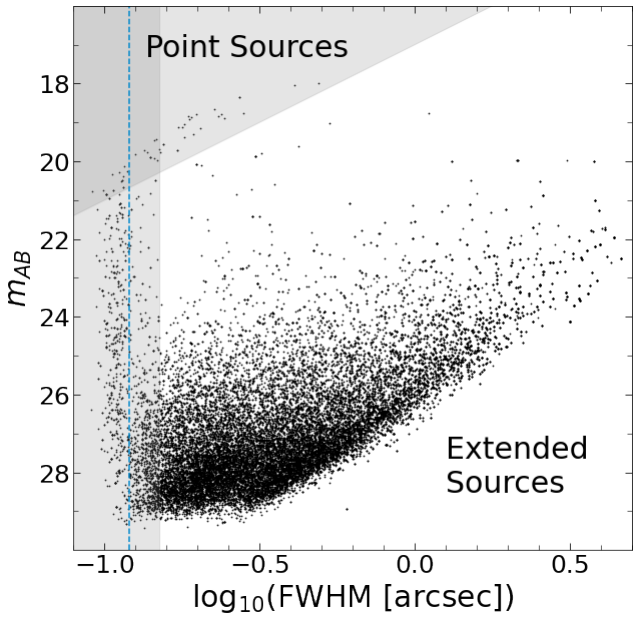

Figure 28. Star-galaxy separation, following Windhorst et al. (2011), using the `SourceExtractor` `MAG_AUTO` magnitudes in F606W versus full width at half maximum (FWHM). Objects within grey regions, with FWHM $< 0\farcs15$ or $m_{AB} < 17 - 4\log_{10}$(FWHM), are flagged as stars and are not considered in this study. We also show the radius ($0\farcs12$) of the aperture used to identify variability as a vertical blue dashed line.

which reduces deblending of galaxies into individual clumps. We thus have two types of aperture photometry for each source: 1) within the small circular $0\farcs24$ diameter aperture used to identify variability, and 2) for the full Kron aperture, as identified by `SourceExtractor`. Table 6 summarizes the relevant `SourceExtractor` parameters used for these two types of measurements. For our matched aperture F435W photometry, we used `SourceExtractor` in dual image mode, employing the full F606W mosaic as the detection image.

To identify variability, we need to first carefully match the objects from one visit catalog to another. We did so using the Astropy `match_coordinates_sky` function, which finds the nearest object in the catalog from one visit to a given object in a catalog from another. To ensure slight differences in position do not contribute to the

measured variability, we only considered two sources to be a match across two different visits if they are within one pixel of each other (0.″03). We increased this threshold to 0.″08 when matching the F606W catalog to the F435W catalog, to account for the fact that objects may have different PSF and surface brightness distributions at different wavelengths. Matches between the `DEBLEND_MINCONT` = 0.001 and `DEBLEND_MINCONT` = 0.06 catalogs were identified using a search radius of 3 arcsec, since the highly deblended catalog may find variability in the outskirts of host galaxies, and thus the positions may be offset by much more than our astrometric uncertainties and pixel size.

We opted to ignore stars in our variability analysis due to uncertainties in the ACS PSF (e.g., Villforth et al., 2010). We flagged as stars all objects with a FWHMt less than 0.″15 or $m_{AB} < 17 - 4\log_{10}(\mathrm{FWHM})$ mag. Grey shading in Figure 28 indicates the stars and faint point-like sources that were removed from our analysis. In addition, we ignored objects with a `SourceExtractor FLAGS`[8] > 2, including objects with saturated pixels, truncated footprints, corrupted apertures/footprints, or other issues. Last, we also ignored all objects within the `jeex02` visit in the F606W filter, as it has a poor astrometric solution that hampers reliable alignment and variability measurements (Jansen et al. 2024a,b; in prep.).

Some variable candidates, like variable stars and ultra-bright AGN like quasars, will be point-like and excluded by our methods. Missing quasars in particular may bias our final AGN estimates. Nonetheless, these objects are relatively rare. In addition, our methods would miss any AGN that does not vary on the timescales we probe. Variability identified in this paper is therefore the *minimum* amount of variability expected in this field.

[8]https://sextractor.readthedocs.io/en/latest/Flagging.html

3.3.2.2 Variable Source Selection

Sources were identified as variable if they varied by more than 3× their combined photometric uncertainty. Therefore, careful consideration of uncertainties is crucial to ensure variable sources are robustly identified. Combining and resampling multiple lower-resolution images into a higher-resolution composite image (using, e.g., the drizzle algorithm) causes both the signal and the noise in adjacent pixels to become correlated. Photometric uncertainties are known to be underestimated when correlated pixel noise is not taken into account (e.g., Casertano et al., 2000; Labbé et al., 2003; Blanc et al., 2008; Whitaker et al., 2011; Papovich et al., 2016). In addition, the ACS PSF is known to vary due to telescope breathing (e.g., Villforth et al., 2010), which could potentially contaminate variability identification performed within small apertures. Finally, cosmic rays may cause changes in brightness if not filtered out properly. We employed an empirical approach to statistically account for correlated pixel noise and PSF changes, as well as other sources of error, regardless of their origin.

Figure 29 highlights our method to best calibrate photometric uncertainties, which is based on the variability search methods of Cohen et al. (2006). Measured magnitudes were compared for all objects that appear in more than one visit. For each such object, Figure 29 shows the magnitude difference, $\Delta m_{0.24}$, versus the mean magnitude, $m_{0.24}$. We used the distribution of these magnitude differences to calibrate the empirical (true) photometric scatter, where the inner brown curves contain ∼68.26% of the data points in each magnitude bin (shown as black circles and curves). To account for correlated pixel noise, a varying PSF, and other unaccounted-for sources of error, we multiplied all `SourceExtractor` magnitude errors by a fixed scale factor (1.15 for

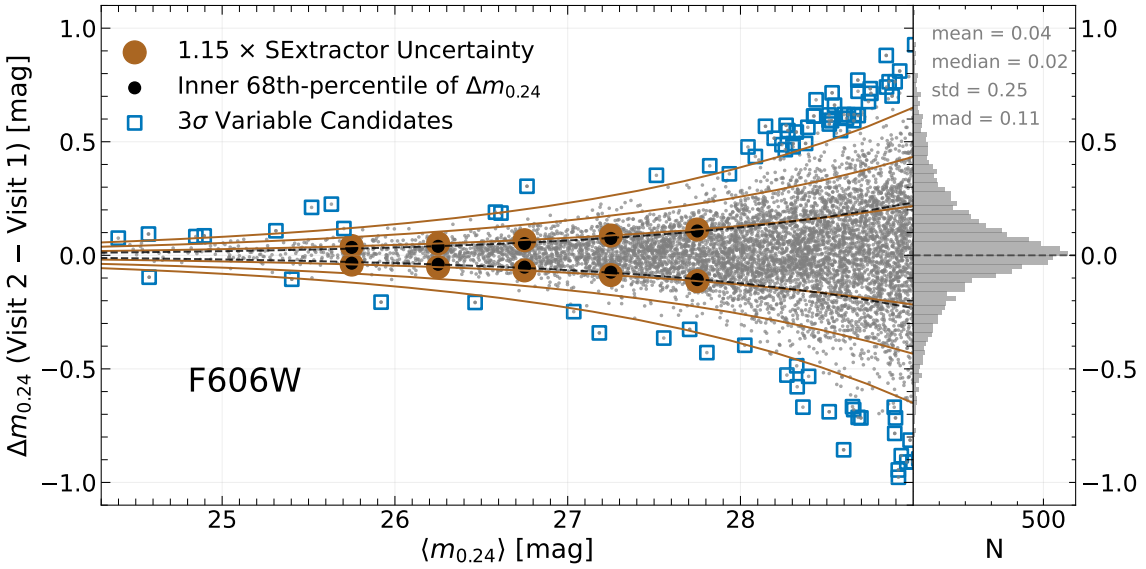

Figure 29. Calibration of photometric uncertainties to identify variable sources. We plot the difference in measured F606W magnitude, $\Delta m_{0.24}$, versus the average measured F606W magnitude, $m_{0.24}$, for objects observed more than once in regions of overlapping HST coverage, where $\Delta m_{0.24}$ is defined in the sense Visit 2 − Visit 1. Each small grey point is an individual object, as detected and measured with `SourceExtractor`. The large brown circles depict `SourceExtractor` photometric errors, scaled by a factor 1.15 to match the observed distribution of magnitude differences (shown as small black circles) measured in 0.5 mag wide bins for $25.5 < m_{0.24} \leq 28.0$ mag such that ∼68.3% of all data points fall between them. The dashed black curves represent the inner ∼68.3% range of the distribution at each magnitude and are polynomial fits to the black points. The brown curves therefore represent *median* 1, 2 and 3σ ranges as fit to the brown circles. Blue squares identify objects that vary at $\geq 3\sigma_{\Delta m}$ in F606W, where $\sigma_{\Delta m}$ is defined in Equation 3.1. The histogram on the right-hand side illustrates the distribution of magnitude differences for all objects detected in the field. In grey, we list mean, median, standard deviation, and median absolute deviation of the y-axis distribution.

F606W and 1.35 for F435W) to best match the observed distribution of photometric scatter. The scaled result is represented by the large brown circles. Magnitude difference uncertainties (for F606W) were calculated as:

$$\sigma_{\Delta m} = 1.15 \times (2.5\, N / \ln 10)\, \sqrt{(\sigma_1/F_1)^2 + (\sigma_2/F_2)^2}, \tag{3.1}$$

with N the number of sigma, F_1 (F_2) the measured flux for Visit 1 (Visit 2), and σ_1 (σ_2) the corresponding scaled flux error.

We emphasize that Figure 29 is used to calibrate photometric uncertainties and *not* to identify variable candidates. The blue squares represent objects flagged as variable at $\geq 3\sigma_{\Delta m}$ in F606W. These objects are determined to be those which vary by more than $3\times$ their individual photometric uncertainty. In general, these sources fall outside the brown 3σ curves in Figure 29, but this isn't always the case. Some objects outside the brown 3σ curves are not flagged as variable if their individual photometric uncertainties are larger than the median. Similarly, some objects inside the brown 3σ curves are flagged as variable if their individual photometric uncertainties are smaller than the median.

In general, we do not expect zeropoint offsets between visits to be a concern, as changes in zeropoint over the duration of the TREASUREHUNT program are <1% for ACS/WFC (Bohlin et al., 2020; O'Brien et al., 2023). The histogram on the right side of Figure 29 is centered at $\Delta m_{0.24} = 0.02$ mag (with a standard deviation of 0.25 mag that is dominated by the photometric uncertainties of faint sources), and therefore shows that the zeropoints between detectors and different regions on the same detector as calibrated by the standard HST pipeline are correct to $\lesssim 0.02$ mag.

We only considered objects brighter than $m_{0.24} \simeq 28.6$ mag in F435W or $m_{0.24} \simeq 29.5$ mag in F606W (corresponding to the predicted 2σ magnitude limits for sources in the field) in at least one epoch. We manually sorted through variable candidates, and removed 63 sources that are either contaminated by diffraction spikes from a bright star, or are close to the edge of a detector. In a vast majority of these cases a diffraction spike overlapped the object in one visit but not in another, observed at a different orientation.

We created a variability catalog for objects that vary more than $3\sigma_{\Delta m}$ in F435W, and similarly a variability catalog for objects that vary more than $3\sigma_{\Delta m}$ and $5\sigma_{\Delta m}$ in

F606W. In addition, we created catalogs with sources that vary (in the same direction) in *both* filters with $2\sigma_{\Delta m}$ and $3\sigma_{\Delta m}$ significance. The significance of the catalogs for objects that vary in both filters to $2\sigma_{\Delta m}$ is $\sqrt{2}\,(2\sigma_{\Delta m}) \simeq 2.83\sigma_{\Delta m}$, and to $3\sigma_{\Delta m}$ is $\sqrt{2}\,(3\sigma_{\Delta m}) \simeq 4.24\sigma_{\Delta m}$. We consider the latter sample (variability detected in both filters to $3\sigma_{\Delta m}$) to be our most conservative, robust sample, as objects that vary in both filters are most likely to be true variables, although the shallower F435W images severely limit their number.

3.3.2.3 Accounting for False Detections

Since variable sources are identified using $2\sigma_{\Delta m}$ or $3\sigma_{\Delta m}$ significance levels, we can expect false detections (e.g., noise peaks). We herein refer to the individual variable sources identified in this work as variable candidates, since we cannot determine which individual sources exhibit genuine variability and which are spurious detections.

We predict the number of false detections using Gaussian statistics. As demonstrated in Figure 30, we observe a Gaussian distribution in $\Delta m_{0.24}$ for all 4,059 galaxies with $28.0 < m_{AB} < 28.5$ mag. We confirm that brightness bins of $25.0 < m_{AB} < 27.0$ (2,550 galaxies), $27.0 < m_{AB} < 28.0$ (4,892 galaxies), and $28.5 < m_{AB} < 29.0$ mag (5,336 galaxies) similarly follow a Gaussian distribution.

Given a Gaussian distribution, we expect a false detection rate of 0.27% (assuming a two-tailed test, where the difference in magnitude can either be positive or negative) for variable candidates identified at $3\sigma_{\Delta m}$ significance. That rate falls rapidly for levels higher than $3\sigma_{\Delta m}$. We also identify variable candidates that vary in *both* filters (in the same direction) with $2\sigma_{\Delta m}$ and $3\sigma_{\Delta m}$ significance. Since we implement the

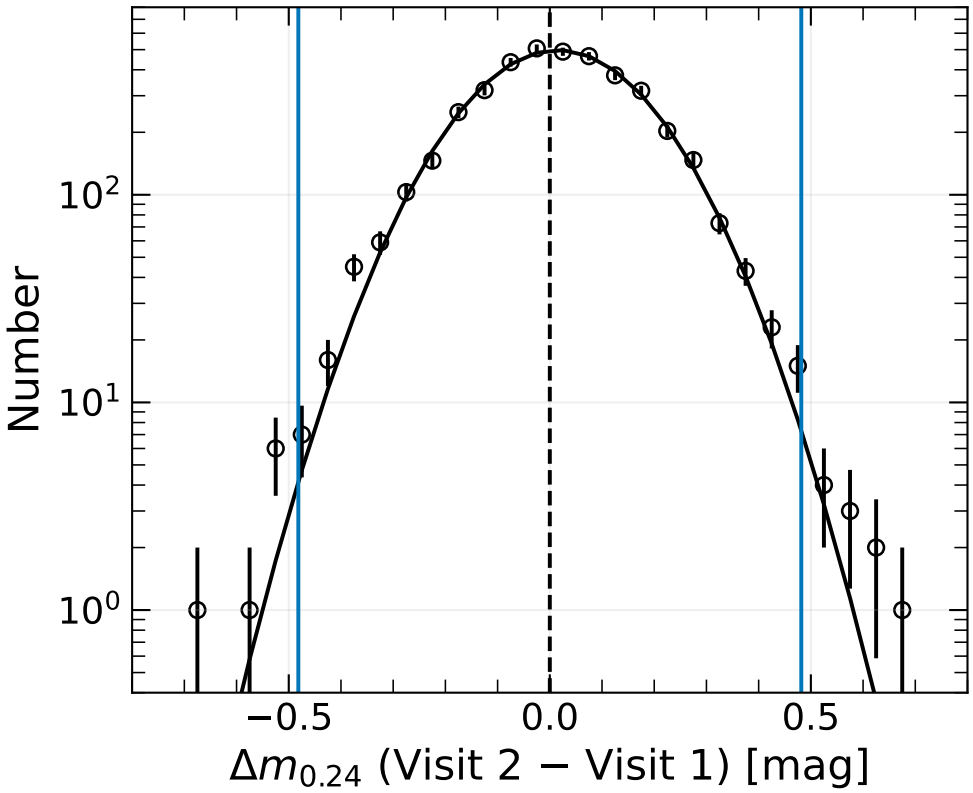

Figure 30. Histogram of the distribution of magnitude differences measured between two epochs ($\Delta m_{0.24}$) for all galaxies (4,059 total) between $28.0 < m_{AB} < 28.5$ mag. The black circles show the number of galaxies (N) for each $\Delta m_{0.24}$ bin, where the error bar is $\sqrt{N}$. The solid black curve is a Gaussian fit to the data. The vertical blue lines represent the 3σ thresholds based on the Gaussian fit. This proves that the distribution of $\Delta m_{0.24}$ follows a Gaussian distribution, such that the false detections can be assumed to follow Gaussian statistics (see Section 3.3.2.3).

requirement that the variability must be of the same sign in both filters, we estimate the amount of false detections using a one-tailed test (i.e., 0.135% false detections at $3\sigma_{\Delta m}$) for these samples.

To demonstrate the methodology by which we assessed the number of false positives as a function of the significance of the detected variability, Figure 31 shows the number of detected variable candidates, the expected number of false positives (and percentage of the total number of objects in the parent sample), and the number of genuine

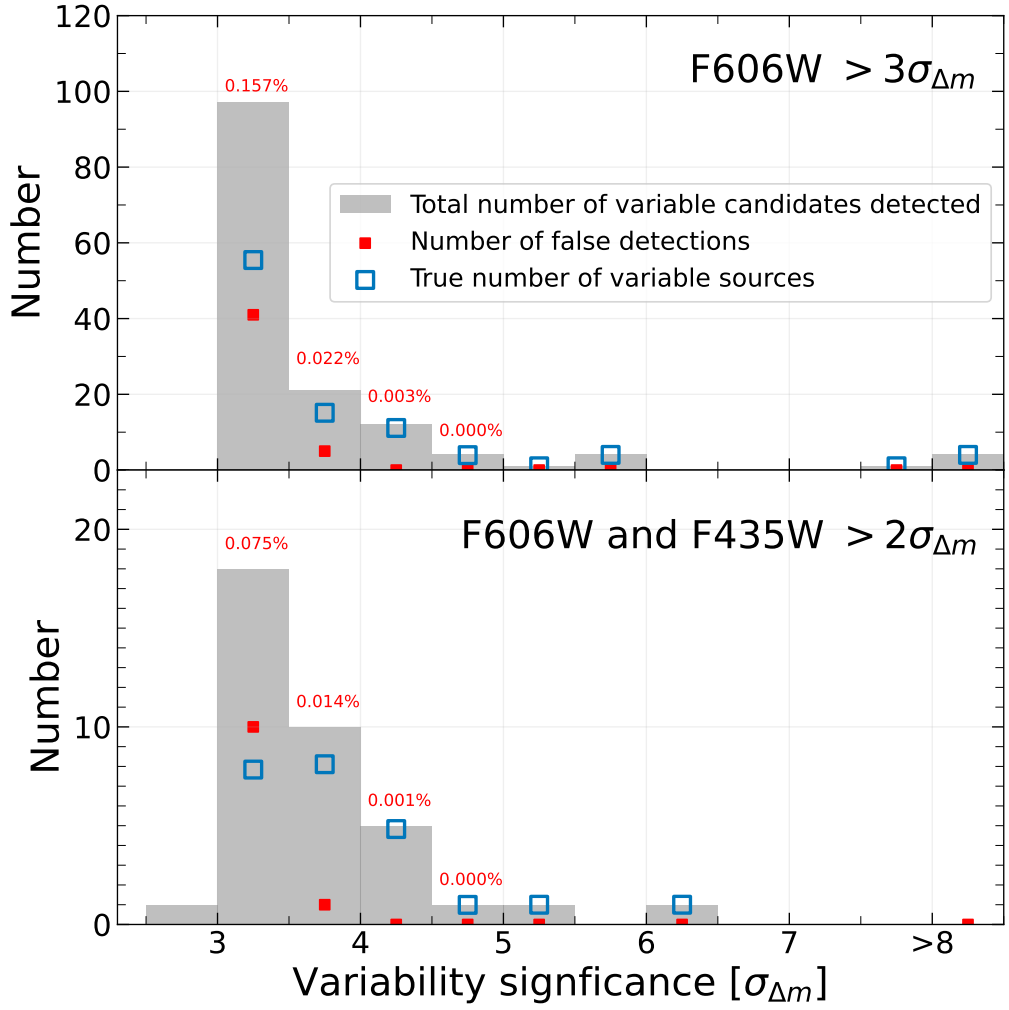

Figure 31. Histograms of the number of variable candidates (light grey) and estimated numbers of false positives (red) and genuine variable sources (blue) as a function of the significance (in units of $\sigma_{\Delta m}$) of the variability detected. The number of genuine variables and false positives add up to the total number of candidates in each bin. The red labels above each bin show the percentage of all objects in the field that are expected to be false positives for that $\sigma_{\Delta m}$-bin. The top panel is for sources that varied by more than $3\sigma_{\Delta m}$ in F606W, and the bottom panel for sources that varied by more than $2\sigma_{\Delta m}$ in both F606W and F435W, and did so in the same sense. Hence, assuming Gaussian statistics, the upper panel reflects a two-sided test, and the lower panel a one-sided test. In total, we estimate $\sim$80 false positives in the sample of sources that varied by more than $3\sigma_{\Delta m}$ in F606W, the sample of sources that varied by more than $3\sigma_{\Delta m}$ in F435W, and the sample of sources that varied by more than $2\sigma_{\Delta m}$ in both F606W and F435W.

variable sources in $0.5\sigma_{\Delta m}$ wide bins for the F606W sample that varies by more than $3\sigma_{\Delta m}$ and the F435W+F606W sample that varies by more than $2\sigma_{\Delta m}$.

In addition to false detections due to Gaussian statistics, image artifacts like cosmic rays, hot pixels, bias stripping, amplifier offsets, CTE trails, dust motes, optical ghosts, and cross-talk, may cause artificial variability to be detected. Of these, cosmic rays are the brightest and most prevalent, yet will not affect our results due to robust flagging and having 8 exposures (per pointing, filter and epoch) to stack using the `AstroDrizzle` software. We explore this in more detail in the Appendix. The other image artifacts are largely removed by the standard HST pipeline. Therefore, we do not expect and find no evidence for image artifacts to bias our results. Nonetheless, confirmation of which individual sources genuinely vary will require follow-up observations.

3.4 Results

In this section, we present our findings regarding the identification and characterization of transients and variable objects in our data set. We detected a total of 12 transients, including two quasar candidates, and 190 unique galaxies exhibiting variability (where $\sim$80 are expected to be false positives). Figure 27 provides a visual representation of the locations of both the transient (red circles) and variable candidates (blue squares and diamonds). Variable candidates are identified in almost all areas of overlap, except those with insufficient astrometric precision or excess noise.

We note that the techniques used to identify transients and variable candidates (as described in §3.3) cause some objects detected as variable candidates to also be classified as transient candidates (e.g., the quasars). Rather than appearing and then

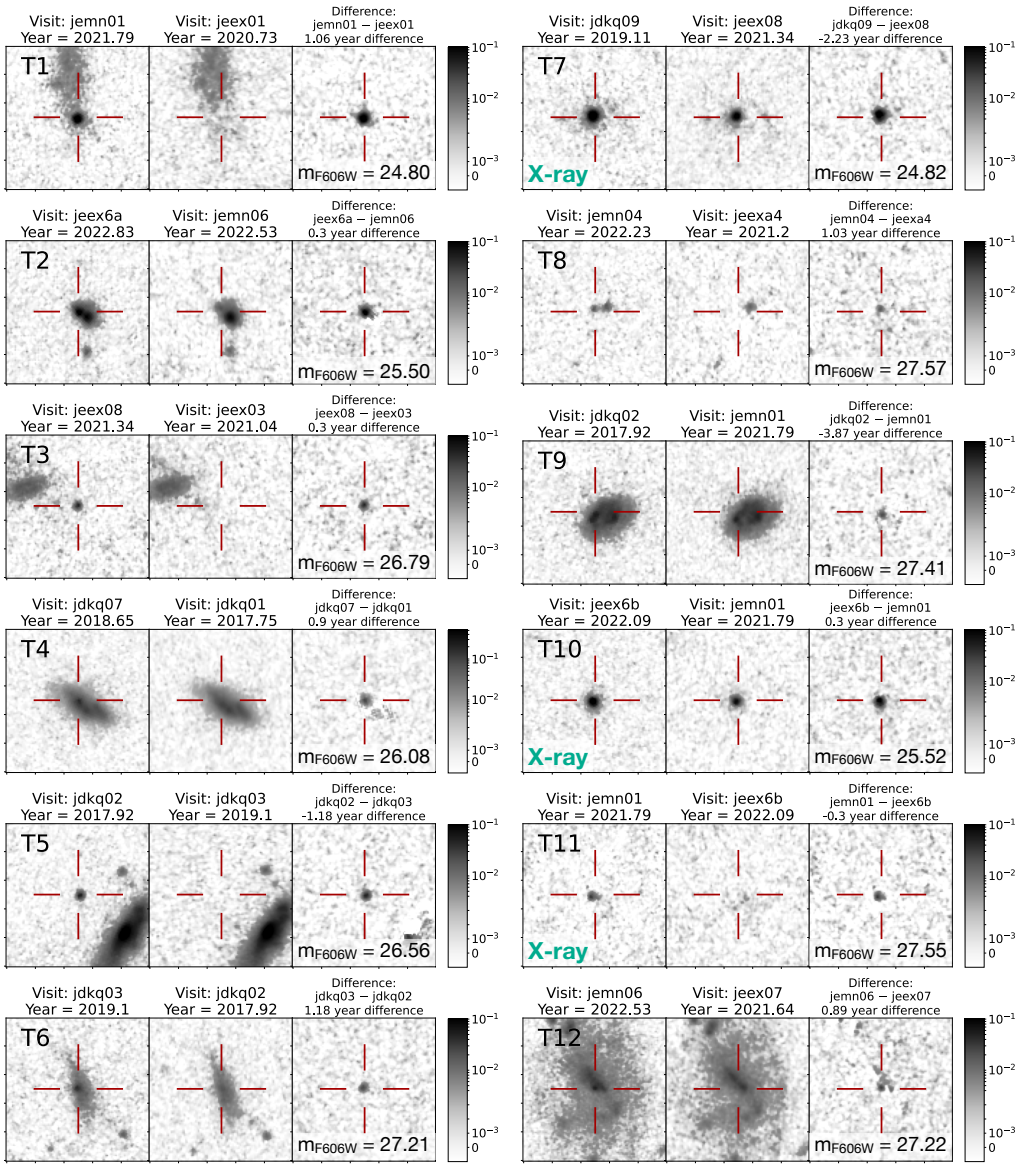

Figure 32. F606W images of each of the 12 transients identified within the JWST NEP TDF. For each transient we show a 3-panel composite of 100×100 pixel (3″×3″) cutouts from the image in which the transient is present (left), the image in which the transient is absent (middle), and the difference image (right). Labels give the transient ID, the visit IDs and dates of observation, the time interval between epochs, and the apparent F606W magnitude of the transient. Transients T7, T10 and T11 were also detected in X-rays (see Table 8), with T7 and T10 likely quasars. Grey-scale bars to the right of each 3-panel set are in units of e^-/s.

Table 7. Transients identified in HST TREASUREHUNT observations of the JWST NEP TDF

ID	R.A. (deg)	Decl. (deg)	Visit 1	Visit 2	t_1 (yr)	t_2 (yr)	Δt (yr)	$m_{\rm F435W}$ (mag)	$m_{\rm F606W}$ (mag)
T1	260.505468	65.798221	jemn01	jeex01	2021.789	2020.733	1.056	···	24.80 (0.05)
T2	260.585670	65.906841	jeex6a	jemn06	2022.830	2022.530	0.300	25.89 (0.29)	25.50 (0.09)
T3	260.835152	65.727517	jeex08	jeex03	2021.344	2021.035	0.309	···	26.79 (0.33)
T4	260.641524	65.883517	jdkq07	jdkq01	2018.647	2017.749	0.898	26.49 (0.59)	26.08 (0.16)
T5	260.618390	65.777831	jdkq02	jdkq03	2017.918	2019.101	−1.183	26.45 (0.52)	26.56 (0.26)
T6	260.602593	65.782095	jdkq03	jdkq02	2019.101	2017.918	1.183	···	27.21 (0.45)
T7	260.802040	65.725119	jdkq09	jeex08	2019.106	2021.344	−2.238	24.44 (0.08)	24.82 (0.05)
T8	260.967884	65.867384	jemn04	jeexa4	2022.227	2021.204	1.023	···	27.57 (0.67)
T9	260.544912	65.793210	jdkq02	jemn01	2017.918	2021.789	−3.871	···	27.41 (0.53)
T10	260.471298	65.762740	jeex6b	jemn01	2022.093	2021.789	0.304	25.59 (0.21)	25.52 (0.09)
T11	260.535175	65.763209	jemn01	jeex6b	2021.789	2022.093	−0.304	27.75 (1.70)	27.55 (0.66)
T12	260.501418	65.869263	jemn06	jeex07	2022.530	2021.637	0.893	···	27.22 (0.44)

Notes: Table columns (1) through (8) list the transient ID, the celestial coordinates (identified by eye) of the transient in decimal degrees, the root names of the visit where the transient is present (Visit 1) and where it is absent (Visit 2), the corresponding dates of observation, and the time interval Δt between Visits 1 and 2. The two final columns list the measured F435W and F606W magnitudes of the transient (m_{AB} at t_1 relative to t_2, measured within a circular aperture centered on the transient with a radius of 8 pixels), where the magnitude uncertainties are given in parentheses.

disappearing, these actually vary in brightness over time with a sufficiently large amplitude that they were detectable in our difference images.

3.4.1 Transients in the JWST NEP Time Domain Field

We identified a total of 12 transients, for each of which we show $3'' \times 3''$ cutouts of the F606W images from the relevant visits and of the corresponding difference image in Figure 32. For each of these transients, Table 7 lists the coordinates, dataset IDs and date of observation of each visit, time interval between epochs, as well as the measured apparent brightness (difference in magnitude between the two epochs) in F606W. We also report the F435W magnitude, if the matched-aperture flux exceeded the F435W detection limit. We call the epoch in which the transient signal appears "Visit 1". The transients range in brightness from $m_{AB} \sim 24.8$ mag to ∼27.5 mag in F606W. This may not correspond to the peak brightness of the transient, as the measured brightness

depends on when the transient event image was taken during its respective light-curve. At magnitudes fainter than $m_{AB} \sim 27.5$ mag, the difference images become dominated by image noise, preventing reliable identification of transients.

In all, we detected ~ 0.14 transients per arcmin^2 of overlapping area, or ~ 491 deg^{-2}. Since two epochs are needed to detect a transient, the areal density per epoch is therefore ~ 0.07 transients per arcmin^2 (~ 245 deg^{-2}), or ~ 0.77 per ACS/WFC footprint per epoch. For comparison, Dahlen et al. (2012) searched for SNe in the GOODS fields (using the ACS/F850LP filter), and identified 118 SNe in a total area of 1 deg^2 to $m_{F850LP} \sim 26$ mag. If we only consider the 4 transients with $m_{F606W} \lesssim 26.0$ mag, we find an areal density of $\sim$164 deg^{-2}, consistent with Dahlen et al. (2012) when factoring in differences in detection filter, SNe colors and redshift distribution, and small number statistics. We also note that it is likely that not all our transients are SNe.

3.4.1.1 Transients with Significant X-ray Detections

Next, we checked whether any of the transients were detected in X-rays within XMM-Newton, NuSTAR, or Chandra observations of the field. We matched the transient positions with published and preliminary X-ray source catalogs, and found that 3 of the transients are noticeable X-ray emitters. While an in-depth analysis of the X-ray observations of these sources is beyond the scope of the present paper and is deferred to future work, we present the measured XMM-Newton, NuSTAR, and Chandra fluxes in Table 8.

For the XMM-Newton and NuSTAR catalogs, we used a matching radius of $5''$ and $30''$, respectively, and found a likely match for transients T7, T10, and T11.

Table 8. Transients identified in HST observations of the JWST NEP TDF with significant X-ray detections

Transient	Detected by	Flux [erg s^{-1} cm^{-2}]	Band [keV]
T7	Chandra	$(5.36\pm0.64)\times10^{-15}$	0.5–7
T7	XMM-Newton	$(1.41\pm0.41)\times10^{-15}$	0.5–2
T7	XMM-Newton	$<9.03\times10^{-15}$	2–10
T10	Chandra	$(2.68\pm0.53)\times10^{-15}$	0.5–7
T10	XMM-Newton	$(1.26\pm0.42)\times10^{-15}$	0.5–2
T10	XMM-Newton	$<4.97\times10^{-15}$	2–10
T11	NuSTAR	$(1.14\pm0.41)\times10^{-14}$	3–8

Note. Table columns list (1) the transient ID, (2) the X-ray observatory that also detected the transient source, (3) the measured X-ray flux, and (4) the energy band in which that flux was measured. The XMM-Newton 2–10 keV upper limits correspond to the 90% confidence level.

We inspected the Chandra 0.5–7 keV event-file images for obvious sources, and here also identified sources consistent with T7 and T10. For the other transients, we extracted source counts from a region with a radius of $2''$ and background counts from a nearby source-free region with a radius of $10''$, but found no evidence for any X-ray counterparts above 1σ significance. Chandra upper limits vary across the field due to detector geometry, as well as vignetting and PSF spreading for off-axis sources, but we expect typical 3σ upper limits of $\sim1.4\times10^{-5}$ ct s^{-1} for the full 1.3 Ms exposure. For T7 and T10, we then extracted source fluxes using the `ciao` tool `srcflux` on the cross-registered event files for each OBSID. To convert count rates to fluxes, we used a model with assumed Galactic absorption and a $\Gamma = 1.4$ power law. At $r \simeq 6.5'$ from the field center (characteristic of T7 and T10), this corresponds to 3σ upper limits of 3.2×10^{-16} erg s^{-1} cm^{-2}. Note, however, that the epochs of individual X-ray observations do not necessarily match or overlap with specific HST visits in which a transient was observed or absent.

3.4.1.2 Notes on Individual Transients

Transient T1 is detected only in F606W (although it is faintly discernible also in F435W) and appears in or superimposed on the outskirts of a diffuse, possibly clumpy disk galaxy, ∼1.″08 S and 0.″16 W of the estimated galaxy center. It has a red (*F435W*−*F606W*) color compared to the galaxy in a color composite image, and its point-like morphology and complete absence in Visit 2 (1.06 yr earlier) suggest it is a supernova (SN) within this $m_{F606W} \sim 23.9$ mag host galaxy.

Transient T2 is detected in both F606W and F435W and appears off-center in a centrally concentrated galaxy (possibly an elliptical galaxy) or in its fainter and partially overlapping apparent companion galaxy. It is located ∼0.″14 E and 0.″09 N of the core of the brighter ($m_{F606W} \sim 24.5$ mag) galaxy and closer in projected distance (∼0.″07 W and 0.″10 S) to the center of the fainter one (not separately photometered by `SourceExtractor`). Its point-like morphology and complete absence in Visit 2 (0.30 yr earlier) suggest it is a SN within either galaxy, with a visible color similar to that of its host.

Transient T3 is detected only in F606W. Its very red color is similar to that of a nearby extended disk galaxy or grouping of galaxies that is barely visible in F435W. Its point-like morphology and complete absence in Visit 2 (0.31 yr earlier) suggest it is a SN associated with this m_{F606W} ∼24.0 mag host galaxy, appearing ∼1.″11 W and 0.″32 S of the center of the brightest region, although the relatively large separation from the main body of this potential host may allow different interpretations.

Transient T4 is detected in both F606W and F435W within a $m_{F606W} \sim 23.0$ mag disk galaxy with knots of apparent star formation and a secure MMT/Binospec spectroscopic redshift of $z = 0.615$. It appears ∼0.″10 N and 0.″10 E (a projected

distance of ∼1.0 kpc) of the estimated galaxy center, and its color is similar to that of the host. T4 appears point-like and is completely absent in Visit 2 (0.90 yr earlier), but is much fainter than its host galaxy, suggesting a SN caught either before or significantly past its peak brightness. T4 is presently the only transient with a spectroscopic redshift.

Transient T5 is detected in both F606W and F435W and appears well outside a nearby, highly inclined disk galaxy. It is located ∼0.″10 E and 0.″01 N of the core of that bright $m_{F606W} \sim 22.5$ mag galaxy, with a color that is similar or slightly bluer. No hint of this point-like source is discernible in Visit 2 (1.18 yr later), suggesting that T5 may be a SN associated with the disk galaxy, although the relatively large separation from this potential host allows other interpretations.

Transient T6 is detected only in F606W (with perhaps a hint discernible in F435W) within a red and diffuse disk galaxy, ∼0.″09 E and 0.″09 N of the estimated galaxy center. It has a red color consistent with that of the galaxy, and its point-like morphology and complete absence in Visit 2 (1.18 yr earlier) suggest it is a SN within this m_{F606W} ∼ 24.4 mag host galaxy.

Transient T7 is detected in both F606W and F435W, appears point-like and isolated. It lacks any nearby potential host galaxy, although there may be a hint of signal ∼0.″59 due E and due W, and ∼0.″23 due S, as well as some "fuzz" ∼0.″42 to the NW in both Visits that could be due to a very faint potential host or galactic companions. Unlike most transients reported here, T7 is also clearly detected in Visit 2 (2.24 yr later) and has significant X-ray detections by both Chandra and XMM-Newton (see Table 8). This transient is thus unlikely to be a SN, but rather a quasar that exhibits significant variation in brightness.

Transient T8 is detected only in F606W and is our faintest transient at $m_{F606W} =$

27.57 mag. It appears ∼0.″27 E and 0.″04 S of a faint ($m_{F606W} \sim 27.3$ mag) and small nearby galaxy that may be similar in color, although possibly not quite as red. This point source is absent in Visit 2 (1.02 yr earlier), and the proximity to a potential host galaxy suggests that it could be a SN.

Transient T9 is detected only in F606W (although it is faintly discernible also in F435W) and appears in what looks like either a spiral arm of a relatively face-on disk galaxy or in an interacting galaxy pair[9], ∼0.″20 E and 0.″08 N of the estimated galaxy center. Its color is redder than that of an adjacent clump in the same spiral arm, but is consistent with the color of most of the disk. Its point-like morphology, projected location within a spiral arm, and absence in Visit 2 (3.87 yr later) suggest that T9 is a Type II SN associated with massive star formation within this $m_{F606W} \sim 23.4$ mag host galaxy.

Transient T10 is detected in both F606W and F435W, appears point-like and is isolated, lacking any nearby potential host galaxy. Unlike most transients reported here, T10 is also clearly detected in Visit 2 (0.30 yr earlier) and has significant X-ray detections by both Chandra and XMM-Newton (Table 8). This transient is thus unlikely to be a SNe, but rather a quasar that exhibits significant variation in brightness.

Transient T11 is detected in both F606W and F435W, appears point-like and is isolated. The nearest galaxies are ∼2.″3 to the S and ∼2.″6 to the N, both >3 galaxy diameters away. Its color is relatively blue, allowing it to be clearly visible in F435W though $m_{F606W} = 27.55$ mag. This point source is absent in Visit 2 (0.30 yr later). Interestingly, T11 was detected with NuSTAR in the 3–8 keV band, and thus is unlikely to be a SNe.

[9]A configuration resembling, e.g., NGC 5278/79 (Arp 239) or NGC 6050/IC 1179 (Arp 272).

Transient T12 is detected only in F606W and appears adjacent to a stellar bar across the center of an extended face-on spiral disk galaxy, ∼0.″12 S and 0.″02 E of the estimated galaxy center. Its color is redder than that bar, but consistent with the color of other portions of the faint disk. Its point-like morphology, projected location within the disk close to the central portions, and absence in Visit 2 (0.89 yr earlier) suggest that T12 is a SN within this $m_{F606W} \sim 22.5$ mag host galaxy.

The four brightest transients, T1, T2, T7, and T10, all of which are brighter than 25.6 mag, may be bright SNe or quasars. The significant X-ray detections of T7 and T10 specifically argue for the latter. In contrast, one of the faintest transients in this study, T11 with $m_{AB} \sim 27.5$ mag, is especially interesting as it is the only transient without a potential host detected in F606W, yet with noticeable X-ray emission.

3.4.2 Variability in the JWST NEP Time Domain Field

We identified 190 unique candidate variable candidates that meet the selection criteria of various samples discussed in § 3.3.2, of which we estimate ∼80 to be false positives (the exact number depends on how many false detections appeared in multiple variability samples). Figure 27 shows the locations of all 190 variable candidates. Symbol shapes (squares and diamonds) and hues identify the sample in which each variable was identified. Tables 10-14 (at the end of this paper) provides a full list of IDs, celestial coordinates, dataset IDs and date of observation of each visit, as well as brightest measured apparent magnitude for each variable candidate. We also list the change in brightness between visits (in the sense Visit 2 − Visit 1), and the significance of variability in units of $\sigma_{\Delta m}$, for both the F435W and F606W filters.

Table 9. Number of variable candidates identified and inferred in F606W and F435W.

Sample	All Objects	Apparent Variables	False Positives	Inferred Variables	% variable
F606W ($3\sigma_{\Delta m}$)	26,468	145	48	97	0.37%
F606W ($5\sigma_{\Delta m}$)	26,468	10	0	10	0.04%
F435W ($3\sigma_{\Delta m}$)	13,574	23	18	5	0.04%
F606W and F435W ($2\sigma_{\Delta m}$)	13,574	38	13	25	0.18%
F606W and F435W ($3\sigma_{\Delta m}$)	13,574	3	< 1	3	0.02%

Note. Table columns list (1) the sample of variable candidates, with the significance limit given between parentheses, (2) the total number of sources in the parent sample, limited to the F435W parent sample in the case of a combined F606W+F435W selection, (3) the number of objects satisfying the criteria at face value, (4) the number of false positive detections expected, (5) the number of genuine variable sources after statistical correction for false positives, and (6) the inferred percentage of sources in the parent sample that are variable.

We emphasize that we can not claim any individual variable candidate varying at $< 5\sigma_{\Delta m}$ significance to be a genuine variable. We can only place strong constraints on the overall number of variables in the area samples in a statistical sense. Conversely, we also do not exclude any specific sources as false detections from this final variability catalog, because we can only account for false positives in a statistical sense. We acknowledge that when an individual source is of interest, the source should be carefully analyzed and may require additional observations to ensure it is a genuine variable.

More relevant for population statistics, Table 9 lists the inferred number of genuine variable candidates, factoring in false detections, for different significance levels in either the F606W or F435W filters, or both. Figure 33 shows 3-color composite cutouts for a representative sample of 12 variable candidates. The bottom row shows our most conservative sample of 3 galaxies that vary in both F435W and F606W at $\geq 3\sigma_{\Delta m}$ significance. Examples of variable sources drawn from the less restrictive samples are shown in the first three rows.

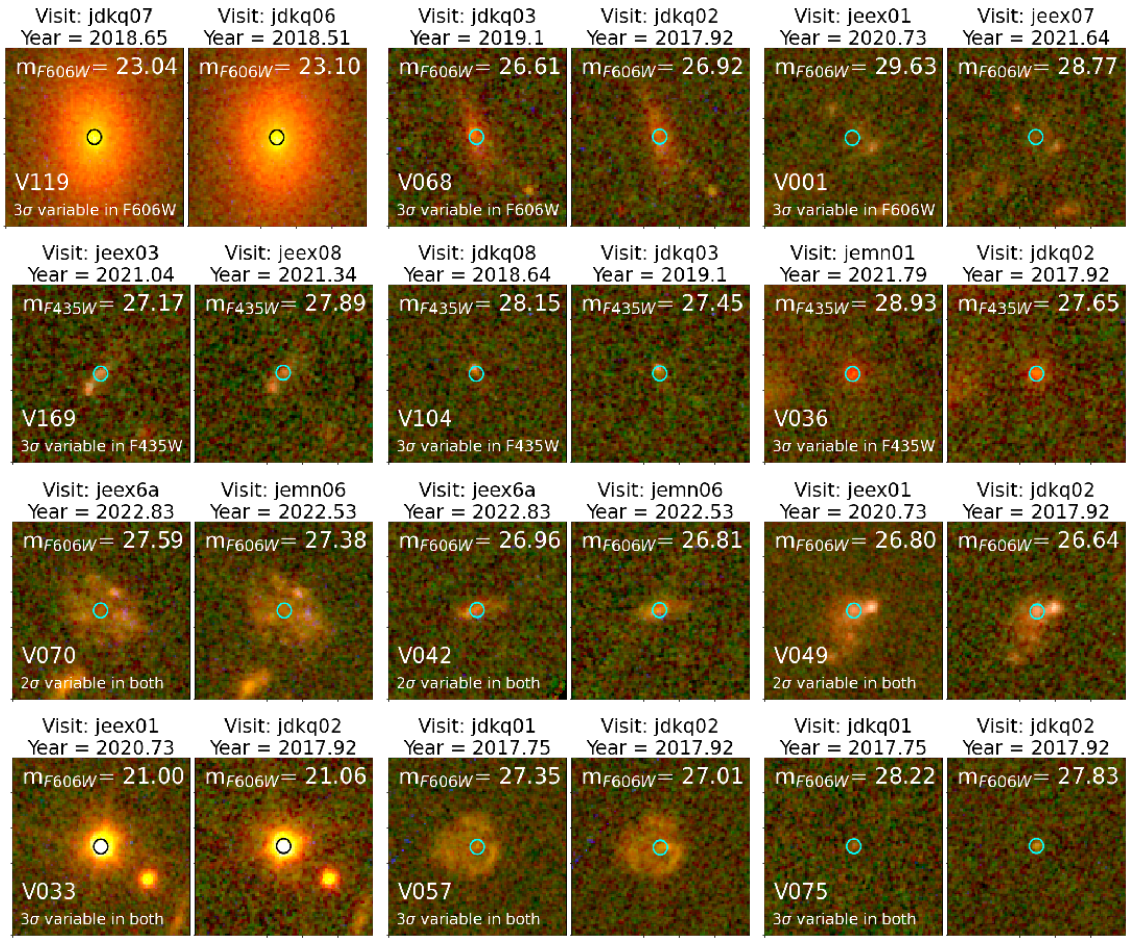

Figure 33. Color composites of 12 representative variable candidates, with F606W, F435W, and F275W shown in red, green, and blue hues, respectively. Each row of 100×100 pixel ($3''\times3''$) cutouts correspond to a different sample: 1) F606W-only $3\sigma_{\Delta m}$, 2) F435W-only $3\sigma_{\Delta m}$, 3) F435W and F606W $2\sigma_{\Delta m}$, and 4) F435W and F606W $3\sigma_{\Delta m}$ variability. A cyan or black circle at the center of each cutout represents the $0''.24$ aperture in which variability was detected. Above each cutout, we note the visit identifier and decimal year of observation. At the top of each cutout, we include the measured $m_{0.24}$ magnitude for that visit. In the left panel of each pair of cutouts, at the bottom, we list the variable candidate identification number and whether it is variable in the F606W filter, the F435W filter, or both. Most of the variable candidates will be AGN, although some will be faint or obscured SNe.

We estimate the total number of variable sources using the 1st, 3rd, and 4th rows of Table 9, since variables in the 2nd and 5th rows have more stringent selection criteria and are already included within these less restrictive samples. There are 206 objects listed in these specific rows of Table 9, where 16 are duplicates (i.e., matching more

than one of these sample selection criteria), leaving 190 unique variable candidates. With an estimated ∼80 false positives, this results in ∼110 unique variable sources, or 0.42% of all 26,468 detected sources in the field. This is the maximum variable source fraction inferred in this work, as these samples are not necessarily independent. Our most conservative sample of $\geq 3\sigma_{\Delta m}$ variable objects in both F435W and F606W only makes up 0.02% of the parent population.

We also estimate the areal density of variable sources using the total number of inferred genuine variables. These ∼110 unique variable candidates translate to ∼1.25 variables per arcmin^2 (∼4500 deg^{-2}) of overlapping area. We can therefore expect ∼14 new variable sources per additional fully overlapping ACS/WFC footprint (∼11.3 arcmin^2), assuming F606W imaging to similar depths as the TREASUREHUNT observations.

The $3\sigma_{\Delta m}$ threshold, which determines by what magnitude a galaxy must vary to be flagged as variable, is key to putting our findings in context with other work. Higher noise levels naturally result in fewer detected galaxies, so the threshold helps to normalize these variations. The solid brown curves in Figure 29 show the $1\sigma_{\Delta m}$, $2\sigma_{\Delta m}$, and $3\sigma_{\Delta m}$ thresholds (for the F606W filter) as a function of magnitude. For all sources with $m_{0.24} \sim 26.0$ mag (a 1.0 mag wide bin centered on 26.0 mag), the median $3\sigma_{\Delta m}$ threshold is $\Delta m_{0.24} = 0.14$ mag. In other words, a typical 26.0 mag source would need to vary by at least 0.14 mag to be flagged as variable for this specific data set. For bins centered on 27.0 and 28.0 mag, the $3\sigma_{\Delta m}$ thresholds are 0.24 and 0.41 mag, respectively. For the F435W filter, the $3\sigma_{\Delta m}$ thresholds for bins centered on 26.0, 27.0, and 28.0 mag are 0.26, 0.44, and 0.82 mag, respectively.

Although our variability identification pipeline was developed to identify variable AGN, we still detect 6 out of the 12 transients presented in Section 3.4.1. Specifically,

it identifies transients T2, T3, T5, T6, T9, and T11. Transients T7 and T10 were originally identified to exhibit variability, but were flagged and removed as star candidates due to their small FWHM. Transients T1, T4, T8 and T12 did not satisfy the $3\sigma_{\Delta m}$ threshold due their relatively large photometric uncertainties.

3.4.3 Photometric Redshift Estimation and SED Fits

To gain a better understanding of the transients and variable candidates in the field, we estimated photometric redshifts using `EAZY` (Brammer et al., 2008). This specifically allows us to understand the distances of the variable candidates, and to explore various properties of them, such as their masses, ages, dust extinction, and specific star formation rates (sSFRs).

Since that would be impossible with just the three HST filters, we also used PEARLS JWST/NIRCam images (see § 3.2). Consequently, we estimate redshifts only for the subset of galaxies that fall within the overlapping coverage of both HST and JWST. We opted to not use the HST F275W filter for photometric redshift estimations, because most objects remain undetected at sufficient significance. We thus employed a total of 10 filters for estimating photometric redshifts: HST/ACS F435W and F606W, and JWST/NIRCam F090W, F115W, F150W, F200W, F277W, F356W, F410M, and F444W. To ensure the HST and JWST images are on the same pixel scale, we reprojected each HST image onto the PEARLS F444W image pixel grid using `reproject`. In each filter, we set all pixels without coverage in all 10 filters to NaN values, facilitating flagging of objects at image edges.

We created photometric catalogs for input into `EAZY` using `SourceExtractor`. Recognizing that some galaxies exhibit variability that may bias a redshift estimation,

we ran SourceExtractor on HST drizzled images of each individual visit instead of the full HST mosaic, and use the measurement with the fainter flux. We assume the fainter measurement represents the photometry if no variability were present —galaxies may temporarily brighten, but they cannot get dimmer on human time scales. For the JWST data, we used the full mosaics, since only a single epoch yet exists at any given location within the field. The NIRCam F444W image served as the SourceExtractor detection image in all cases. For HST images, we set MAG_ZEROPOINT to 26.49 mag for F606W and to 25.65 mag for F435W. For our JWST images, MAG_ZEROPOINT was set to 28.0865 mag for all filters, as appropriate for their 0.″030 platescale, to convert from MJy sr^{-1} (see Windhorst et al., 2023). Other relevant parameters are the same for HST and JWST, and are as listed in the right-most column of Table 6.

EAZY(v1.0) was run on the resulting 10-band photometry. Following the approach outlined in Figure 29, we scale SourceExtractor magnitude uncertainties by a factor of 3 upon input into EAZY. This factor of 3 is larger than the factor of 1.15 used for scaling the 0.″24 aperture magnitudes in §3.3.2, primarily due to the larger aperture sizes used here. We used the eazy_v1.0 templates on a redshift grid spanning 0.01 $\leq z \leq$ 15, allowing only single templates to be fit. We adopted z_ml as the redshift estimate and did not include any priors.

We used the EAZY redshifts as input to a custom IDL spectral energy distribution (SED) fitting code that was also recently used by Meinke et al. (2021, 2023). This code starts with Bruzual & Charlot (2003; BC03) SED models assuming a Salpeter IMF and an exponentially decaying star-formation history specified by the decay scale, τ, which ranges from 0.01 to 100 Gyr in 16 logarithmically spaced steps. Extinction by dust is specified on a grid of $0.0 \leq A_V \leq 4.0$ mag in steps of 0.2 mag assuming a Calzetti et al. (2000) extinction law. For a given redshift, the age, T, is not allowed

to exceed the age of the Universe (assuming a Planck Collaboration et al. (2020a) cosmology). The best-fit model is chosen by minimizing the χ^2 and scaling for the stellar mass, M. The (unweighted) present-day value of the star formation rate, $\Psi(T)$, is computed using the best-fit stellar mass, decay scale (τ), and age (T) from $\Psi(T) = \Psi_0 e^{-T/\tau}$, where Ψ_0 is the star formation rate at time $T = 0$. Given that $M = \int_0^T \Psi(t)dt$, we can solve Ψ_0 analytically from $\Psi_0 = (M/\tau)/(1 - e^{-T/\tau})$.

With 10-band, 0.4–5 μm photometry, we required $\chi^2 < 10$ and $z < 5.5$. Since all objects of interest are detected in F606W, they must be at $z < 5.5$. However, these cuts alone will not eliminate all bad fits, especially if the photometric uncertainties in some crucial filters are large. We added an additional condition that the limits on the 2σ confidence interval in redshift probability distribution, $p(z)$, as computed by `EAZY` (namely `l95` and `u95`) must not differ by more than 1 redshift unit. These conditions result in a sample with reliable photometric redshift estimates that includes 22 galaxies exhibiting variability (28% of the original sample of 79 variables that fall within the HST and JWST footprints) and 3296 normal galaxies (31% of the 10,664 galaxies that fall within the HST and JWST footprints). We only considered galaxies that were already marked as reliable in § 3.3.2.1 (the 26,468 sources in Table 9).

Due to the necessarily limited grid of SED model parameters, any galaxy with an inferred sSFR $< 10^{-5}$ yr^{-1} is categorized as "quiescent" and its sSFR is set to 10^{-5} yr^{-1}. Our templates also cannot distinguish stellar population ages younger than 10 Myr, so we set all apparent age solutions <0.01 Gyr to 0.01 Gyr. Given that age is inversely correlated with the inferred sSFR, where $\log_{10}(\text{Age}) \sim -2$ corresponds to $\log_{10}(\text{sSFR}) \sim 2$, we also set all $\log_{10}(\text{sSFR}) > 2$ to 2. This adjustment is solely made to assess collective trends in galaxies with variability.

In Figure 34, we compare photometric redshift (z_{ph}), stellar mass, stellar population

age, specific star formation rate (sSFR), and dust extinction (A_V) of galaxies that exhibit variability to typical galaxies in the general population. Overall, we sample a broad range of redshifts, masses, ages, star formation histories, and dust extinction. The most prominent peaks in the fraction of galaxies with variability with respect to the general galaxy population (expressed in %) occur at a redshift of $z_{ph} \simeq 2.5$, a stellar mass of $\sim 10^8$ and $\sim 10^{10}$ $M_\odot$, an age of $\sim 10^{-0.5}$ Gyr, a sSFR of $\sim 10^{-5}$ Gyr^{-1}, and an attenuation $A_V \simeq 1.0$ mag. The median redshift of our variability sample is $z_{ph} = 1.3$, but we sample variability up to $z_{ph} = 2.9$. Similarly, our galaxies with variability sample masses $M = (0.02\text{–}20) \times 10^9$ $M_\odot$, ages $T = (0.01\text{–}2)$ Gyr, sSFR = $(10^{-5}\text{–}10^2)$ Gyr^{-1}, and $A_V = (0.0\text{–}2.4)$ mag.

Three transients fell within an area that also has PEARLS 8-filter JWST/NIRCam coverage, yet all three had `EAZY` photometric redshifts with a $\chi^2 > 10$. This could be due to a significant non-thermal component from an AGN, or due to the presence of strong emission lines that could mimic a continuum break. As transient T4 has a secure MMT/Binospec spectroscopic redshift of $z = 0.615$, we used the Code Investigating GALaxy Emission (`CIGALE`) (Boquien et al., 2019) to better fit the SED of its host galaxy. `CIGALE` has the benefit of incorporating emission lines into its models, while the previously mentioned SED fitting algorithm does not and resulted in poorer fits for this transient host. We used a delayed burst-quench star-formation history model (Ciesla et al., 2017), since the standard exponentially declining model can struggle to reproduce higher SFRs, and its morphology suggests that the transient host likely underwent a recent star-formation episode. The e-folding times tested were 1, 3, 5, and 8 Gyr, the main stellar population spanned 1–8 Gyr in increments of 1 Gyr, the burst/quench age ranged from 0.1, 0.5, and 1 Gyr, and the possible SFR ratios before and after these burst ages were 0.1, 0.3, and 0.6. Our stellar component used

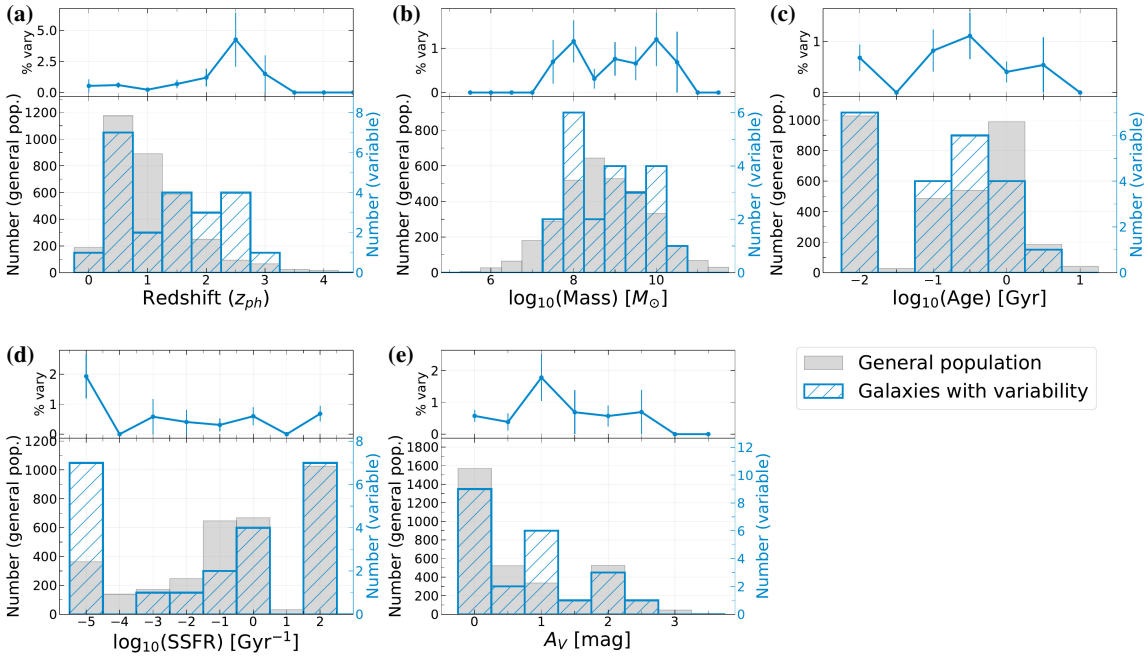

Figure 34. Comparison of galaxy properties in the general galaxy population and in galaxies that exhibit variability. Shown are distributions of (a) photometric redshifts (z_{ph}), (b) stellar mass, (c) stellar population age, (d) specific star formation rate (sSFR), and (e) extinction by dust (A_V), for the general population (solid grey) and galaxies with variability (blue hatched). The y-axis labels on the left-hand side of each plot represents the number of galaxies in the general population, and those on the right-hand side (in blue) the number of galaxies with variability. Above each histogram panel, we plot the fraction of galaxies with variability ($100\% \times N_{var}/N_{general}$) for each bin. The uncertainties assume Poisson statistics with $\sigma_N \propto \sqrt{N}$.This comparison only includes the subset of galaxies already flagged as reliable in § 3.3.2.1, with both HST and JWST imaging (where photometric redshifts and SEDs can be fit), with $z_{ph} < 5.5$, $\chi^2 < 10$, and where the 2σ confidence interval in $p(z)$ spans <1 redshift unit.

the BC03 library using the Salpeter IMF, testing metallicities of 0.004, 0.02, and 0.05 $Z_\odot$ with young stellar ages being either 10 or 100 Myr. We included a nebular component to account for emission lines using all the default parameters, where the nebular component is self-consistent with the stellar population in the sense that its strength is determined by the Lyman continuum of the total SED. To account for dust attenuation, we used Calzetti et al. (2000) extinction with possible modified

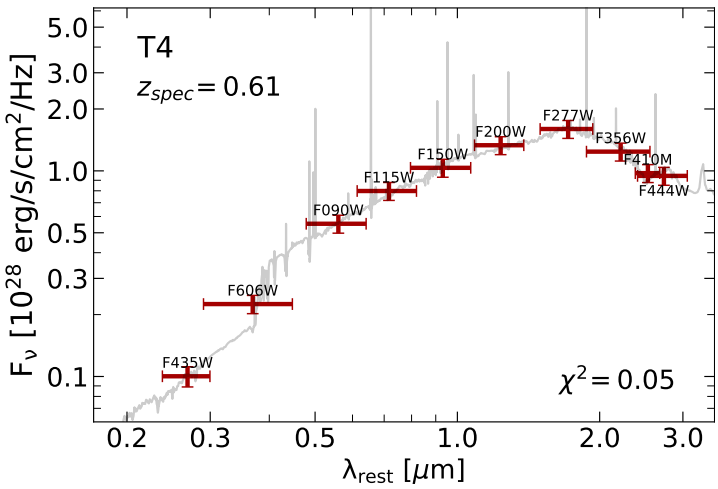

Figure 35. SED fit of transient T4 with `CIGALE`, adopting the MMT/Binospec spectroscopic redshift of 0.615. The red points with vertical error bars show the measured fluxes of the transient host and their associated uncertainties. The horizontal bars on each data point represent the width of the bandpass. The light grey spectrum represents the best `CIGALE` fit, with the reduced χ^2 value shown.

power-law slopes of -0.4, 0.2, and 0. For dust *emission*, we used the Dale et al. (2014) model with α slopes of 1.0, 2.0, and 3.0 .

The best fit SED for the T4 host galaxy is shown in Figure 35 and corresponds to a stellar population age of 3.6 Gyr, $A_V = 0.5$ mag of attenuation by dust, and a stellar mass of $1.2{\times}10^{10}$ $M_\odot$. Its sSFR is 0.5 $M_\odot$ Gyr^{-1}. The reported best-fit value of 0.05 of the reduced χ^2 indicates that the (conservative) photometric uncertainties upon input to `CIGALE` were overestimating the actual ones somewhat.

3.5 Discussion

An analysis of the detailed properties of individual transients and variable candidates is beyond the scope of this paper. We can, however, make some general statements about the properties of these source populations, using their observed optical light distributions (morphology) and `EAZY` SED fits. From the point-like morphology and off-center locations at small projected distances to likely host galaxies, we infer that the majority of the discovered transients are SNe. The majority of the variable candidates, on the other hand, are found either in or very near the center of galaxies or are isolated without a discernible host, and are surmised to be AGN. Most of these AGN are normal SMBHs in galaxies, with stochastically fluctuating accretion at lower luminosities than seen in quasars. Nonetheless, it is important to consider that other phenomena, such as SNe from central starbursts, stochastic microlensing events, or tidal disruption events, could also contribute to the observed central variability. SNe that are heavily obscured and SNe that are caught at very early or at late times can contribute to variability detected in local peaks in surface brightness well away from host galaxy centers.

3.5.1 Classification of Transients

Based on their positions relative to likely host galaxies and the PSF-like appearance in the difference images, we propose that nine of the transients (T1, T2, T3, T4, T5, T6, T8, T9, and T12) are SNe. It is reasonable to expect that $\sim$40–50% of detected SNe are Type Ia, as suggested by previous studies (Dahlen et al., 2012; Graur et al., 2014; Rodney et al., 2014; Cappellaro et al., 2015). If we assume that we have a

minimum of nine SNe, we can anticipate a minimum of three Type Ia SNe with the remainder being CC SNe.

The TREASUREHUNT observing strategy provided piecemeal UV–Visible imaging rather than time-domain monitoring. As a result, these SN candidates will have long faded and can no longer be followed up for spectroscopic identification. Nonetheless, now that this initial imaging exists, future monitoring observations could efficiently expand the present sample and would allow such spectroscopic follow-up. The sum of the areas of overlap used in this work samples $\sim$88 arcmin^2, which is about half of the total HST coverage of this field ($\sim$194 arcmin^2). Therefore, we can expect about 2$\times$ as many transients if this field were observed again. Full overlapping coverage of this field could yield at least six new Type Ia supernovae, and coupled with spectra and rapid follow-up, can provide essential constraints on fundamental cosmological parameters like the Hubble constant, the mass density of the universe, the cosmological constant, the deceleration parameter, and the age of the Universe (e.g., Riess et al., 1998, 2023). In addition to Type Ia SNe, comprehensive HST coverage of this field could yield at least six CC SNe observations. Particularly when combined with ancillary data, this could contribute significantly to resolving the observed discrepancies in CC SN rates compared to theoretical models (Cappellaro, 2014). With a sufficiently large sample, the SN rate as a function of redshift could also be constrained. Furthermore, the increased volume of observations enhances the likelihood of capturing rare or unexpected events, potentially leading to groundbreaking discoveries in the field.

At least three of the transients are unlikely to be SNe. They either were detected in both epochs or they are isolated with no apparent host galaxy. When considering only the optical emission, transients T7 and T10 exhibit substantial changes in brightness between the two epochs, of $\Delta m = 0.83 \pm 0.06$ mag and 0.82 ± 0.09 mag, respectively.

That would be equivalent to the presence of an additional source with $m_{AB} \sim 24.82$ and 25.52 mag. The observed centroid positions in both epochs match to within $0\farcs001$, such that the additional signal is indistinguishable from being due to a nuclear source that changed brightness. We therefore suggest that T7 and T10 may be quasars. The fact that they both were detected in soft X-rays at flux levels $>2\times10^{-15}$ erg s^{-1} cm^{-2} lends additional evidence to this interpretation.

T11 is a unique transient with no visible host, yet was detected in hard X-rays by NuSTAR. If that X-ray emission is indeed associated with T11 then it could be a faint ($m_{AB} \gtrsim 29$ mag), high-redshift quasar that briefly flared up to be detectable in F606W. If the X-ray emission is unrelated, then we speculate that T11 may represent a SN located within an undetected host galaxy. That host could be a faint dwarf galaxy at $z \lesssim 6$, or a more massive host at $z \gtrsim 6$ to explain the non-detection in F606W in the second visit. Unfortunately, T11 falls outside the area with JWST coverage, so we cannot distinguish between these two scenarios at this time. Chakrabarti et al. (2018) have demonstrated that the rates of SNe in dwarf galaxies can be three times higher (per unit volume) than in typical spiral galaxies. Given the limited understanding of star formation in dwarf galaxies, a substantial number of SN candidates like T11 could offer a unique opportunity to identify otherwise undetected dwarf galaxies and gain more insights into their star formation rates.

Overall, determining the nature of each transient remains challenging without spectroscopic data secured close in time. Nonetheless, these detected events showcase the considerable potential and effectiveness of transient science within the JWST NEP TDF.

3.5.2 Properties of Variable Candidates

Our methods were developed to isolate variable candidates that are coincident with local maxima in surface brightness that can be isolated and photometered using `SourceExtractor`. This naturally optimizes detection of variable AGN, but faint SNe are also detected when located offset from the center of the host galaxy. In addition, some offset variability may also be due to accretion disks of SMBHs that have not yet settled in the center of the host galaxy (e.g., Reines et al., 2020). Examples of offset variables are shown in Figure 33 (objects V001 and V169).

In general, the number of variable sources inferred here is expected to be fewer than the true number in the field, as some sources will vary on timescales that were not probed in this work. Constructing a sample of genuine variable sources in the field requires follow-up observations at various time sampling intervals, possibly extending over decades.

Figure 34 shows that galaxies exhibiting variability span a broad range of stellar mass, stellar population age, star formation history, and dust extinction. This underscores that rest-frame UV–Visible variability can be a powerful tactic to identify accreting AGN in a wide cross section of the galaxy population. Especially notable is that AGN were detected through their variability even in dusty galaxies with $A_V \gtrsim 2$ mag.

The top portion of each panel in Figure 34, of the fraction of galaxies with variability within each histogram bin for the quantity plotted, shows peaks in most of the panels, although the formal significance of these peaks (assuming Poisson counting statistics) is generally $lsim2\sigma$ due to small number statistics in individual bins.

First, in Figure 34*a*, we find a relatively high fraction of galaxies with variability

around $z \sim 2.5$, while at both lower and higher redshifts variability appears to be more rare. This is in contrast with both Villforth et al. (2012), who find optical–near-infrared variable AGN predominantly toward lower redshifts, and Sarajedini et al. (2011), who find an increase in optically varying AGN with increasing redshift. Zhong et al. (2022) find a similar number of optically variable AGN to peak at $z \sim 1$. We suspect that the number of variable sources as a function of redshift is influenced by cosmic variance of a relatively rare source population, and thus differs depending on the field observed. The fraction of variable sources may be flat over the $0 \lesssim x \lesssim 3$ redshift range when averaged over an area of sufficient size.

The observed stellar mass distribution (Figure 34*b*) of galaxies exhibiting variability shows an apparent excess at both $\sim 10^8$ $M_\odot$ and $\sim 10^{10}$ $M_\odot$. We do not detect variability in the most massive galaxies, either due to small number statistics (most likely) or because their SMBHs are less likely to accrete at a sufficient rate to be detectable or have a longer period of relative quiescence between major accretion events. We also do not detect variability in galaxies with $M \lesssim 10^7$ $M_\odot$, likely due to a combination of both small number statistics and larger photometric uncertainties in these faint systems, such that our $3\sigma_{\Delta m}$ threshold is less likely to be met for a given amplitude of variability. If the relative distribution is taken at face values, then it could also hint at the presence of two separate populations of sources with variability: one associated with lower mass $\sim 10^8$ $M_\odot$ hosts, and another associated with higher mass hosts $\sim 10^{10}$ $M_\odot$. Such could be the case if variability associated with CC SNe favors lower mass host galaxies, and variability associated with SN Ia and AGN favors higher mass hosts.

In Figure 34*c* and *d* we see that a significant fraction of the galaxies with variability are best fit with stellar population models characterized by active star formation (young ages $\lesssim 30$ Myr and high sSFR $\gtrsim 30$ Gyr^{-1}). Conversely, there is also a sizable

fraction that is quiescent (sSFR $\lesssim 0.01$ Gyr^{-1}) with stellar populations older than 1 Gyr. A possible excess appears for intermediate population ages (60–600 Myr).

Last, Figure 34*e* shows that while the galaxies exhibiting variability largely track the distribution of extinction seen in the general population, there may be an excess in the variability sample for $A_V \sim 1$ mag.

3.5.3 Constraints on SMBH Mass, Accretion and Radiation Lifetimes

The sparse and random time sampling of this field does not allow us to trace the evolution of faint AGN, but may still teach us various properties of them. AGN brightness varies on timescales corresponding to the light crossing time in the accretion disks and gas clouds surrounding SMBHs. For example, for a SMBH with a mass $M \sim 10^8\,M_\odot$, the timescale for variability cannot be shorter than ∼1 week in the rest-frame (e.g., Xie et al., 2005). For the majority of sources where the variability is due to AGN activity, that variability originates close to the central SMBH. If the timescale we sample is the minimum timescale of variation, we can provide rough constraints on the SMBH masses following Xie et al. (2005). According to Schwarzschild Black Hole Theory (SBHT), the mass of a black hole ($M_\bullet$ in $M_\odot$) is equal to the minimum timescale of variation (Δt_{min} in yr) as $M_\bullet = 4.29{\times}10^{11}\,\Delta t_{min}$. Time intervals between observations in various areas of overlap in the TREASUREHUNT data range from 1 day (0.0027 yr) to 4.78 yr. At the median redshift of our variable candidate sample, $z_{ph} = 1.3$, the range in rest-frame timescales becomes 0.001–2.08 yr, giving SMBH masses of $5.1{\times}10^8 \lesssim M_\bullet \lesssim 8.9{\times}10^{11}\ M_\odot$. SMBH masses $\gtrsim 10^{11}\ M_\odot$ are unreasonable: objects within the region of overlap with a 4.78 yr interval between observations likely vary on much shorter timescales and we did not sample the minimum timescale of

variation. Even a more typical time interval of $\sim$1 yr between epochs will yield a $\sim 10^{11}$ $M_{\odot}$ SMBH mass. Taking the full range in redshifts sampled into account, we will therefore only claim that in select areas of overlap we can probe SMBHs with masses of $M_{\bullet} \gtrsim (3\text{–}9) \times 10^{8}$ $M_{\odot}$, but with no firm upper limit.

We can also frame our finding that a maximum of 0.42% of the general field galaxy population shows significant variability in the context of the accretion and radiation lifetimes of AGN. If we assume that: 1) all galaxies seen in this field with HST have a central SMBH (e.g., Kormendy & Ho, 2013), 2) the central SMBH is always visible when accreting, and 3) that a currently accreting AGN will be variable, then we would deduce that the AGN in our field are actively accreting for 0.42% of the time. Assumptions 2) and 3) are simplified, as some AGN will be hidden at rest-frame UV–Visible wavelengths by surrounding dust. This fraction could be as large as 2/3 of all AGN, if we use the $\sim$30% average Lyman continuum escape fraction of weak AGN (Smith et al., 2018, 2020, 2024) as proxy for the fraction of AGN with direct unobscured sight lines to the observer. Figure 34*c* implies an average SED age of $\sim 10^{8}$ years ($\sim$100 Myr) for the parent population, although the spread in age is wide (0.01–10 Gyr). A 0.42% fraction of visibly variable AGN would correspond to an implied average AGN activity lifetime of $0.42\% \times 10^{8} \sim 4 \times 10^{5}$ yr (and a range of 4×10^{4}–4×10^{7} yr). For comparison, Rawes et al. (2015) estimated the optical synchrotron electron life times of AGN with visible jets observed with HST and Chandra at $\sim 10^{4}$ yr. However, these authors state that their estimated synchrotron lifetimes may be too short by at least a factor of two, and may be longer if synchrotron electrons are re-accelerated in the ambient magnetic field. On the other end of the activity scale, Jakobsen et al. (2003) show that at least some quasars can remain active more or less continuously for $\gtrsim$ 10 Myr. With these assumptions and significant uncertainties, a visible AGN

accretion time of $\sim 10^4$ to 10^7 yr could indeed result in a 0.42% variability fraction in a galaxy population characterized by an average SED age of $\sim$100 Myr (and a range of 0.01–10 Gyr) whose stars and gas feed that central engine.

Future work will need to secure and analyze larger samples of optically variable sources with deep X-ray imaging to better constrain UV–Visible synchrotron lifetimes, and wider and deeper HST+JWST images with spectroscopic (NIRISS or NIRSpec) redshifts to improve redshifts and the characterization of their stellar population.

3.5.4 Caveats and Estimated Population Size

It is important to note that with HST data alone, distinguishing between variability caused by variable AGN and faint SNe is challenging. Variability at locations offset from the cores of galaxies could potentially indicate SN events or SMBHs that have not yet reached the galaxy center. In all four catalogs, we identify a total of 25 cases showing variability at locations other than the core, as identified through visual inspection. Identifying AGN will require complementing this work with ancillary observations of the field to determine whether galaxies exhibiting variability also emit mid-IR emission. Prolonged monitoring of variable objects within this field will contribute to a deeper understanding of SMBHs within galaxies, including their evolution over time and their influence on galactic physics.

We also note that the variable candidates presented here are a *strict lower bound* to the number present in the field: many genuine variable sources, even if at $z \lesssim 6$ and detectable in F606W, were certainly missed because they did not vary sufficiently between specific individual visits to meet our $3\sigma_{\Delta m}$ threshold, or if the timescale of their variability exceeded the duration of the TREASUREHUNT program. In the

present study, the photometric uncertainties in each epoch of observation contributed equally to that $3\sigma_{\Delta m}$ threshold. Any future additional observations to similar depths would reduce the photometric uncertainty in the reference magnitudes, thus lowering the variability detection threshold. The magnitude and level of variability for all sources in this work is collected in Tables 10-14, so that they can be compared in future studies within the JWST NEP TDF.

Although significant (i.e., $>3\sigma_{\Delta m}$) direct detections of variability to such exceeding faint limits through systematic monitoring campaigns with HST, JWST, or Roman would require a very large community investment, it is not outside the realm of what is possible. Even at slightly shallower depths, and employing similar extrapolations, variability could account for a large fraction of all accreting SMBHs.

3.6 Assessment of the Potential Impact of Cosmic Rays on Detected Variability

For variability searches with the two HST cameras — WFC3 and ACS — that have been in the telescope for over 15-20 years it is prudent to consider the number of cosmic rays (CRs) that will have hit our detectors and may have survived the CR-clipping that happens during the drizzling process. First, we consider how constant the CR-flux may be on HST's detectors. A summary of the best on-orbit data on the CR-flux is given by, e.g., Ryon (2019, their section 7.5) for ACS[10], by Dressel (2016, their section 5.4.10) for WFC3[11], and by McMaster & Biretta (2010, their Section 4.9)

[10]see also https://www.stsci.edu/files/live/sites/www/files/home/hst/documentation/_documents/acs/acs_ihb_cycle28.pdf

[11]see also https://www.stsci.edu/files/live/sites/www/files/home/hst/documentation/_documents/wfc3/wfc3_ihb_cycle24.pdf

for WFPC2[12]. Section 4.9 of McMaster & Biretta (2010) suggest that the WFPC2 CR energy distribution follows a Weibull distribution, which resembles a Poisson curve with a distinct low-energy cutoff.

A good recent summary of over 1.2 billion CRs analyzed during the 30 year operational lifetime of these four cameras inside HST is given by, e.g., Miles et al. (2021). Their Table 6 shows that both ACS, WFPC2, and WFC3 have a remarkably similar density of CR-hits of $\sim$1.1$\pm$0.1 hits/sec/cm^2 of detector area. Miles et al. (2021) provide a better physically motivated Landau distribution of the CR-energies for all HST cameras, which resembles the earlier Weibull distribution of McMaster & Biretta (2010). These CR energy distributions are thus representative of the typical CR-distribution and frequency in typical HST images, as long as one stays away from transitions through the South Atlantic Anomaly (SAA), where the CR-flux can be temporarily much higher. Our NEP TDF images always avoid the SAA transitions, and therefore, we will assume that the CR-flux is as given in these respective Instrument Handbooks and Miles et al. (2021).

Following the Instrument Handbooks, at minimum four independent exposures of $\sim$1200 sec are needed to minimize multiple CR impacts on the same object, and we use a much more conservative N=8 exposures per pointing in each filter. Windhorst et al. (1994) investigate from 12-exposure pointings how much the CR-rejection improves if fewer than N=12 exposures are stacked, and find that for N=8 the sky-mean and sky-sigma converge to the best achievable values (from the N=12 maximum exposure case) if one clips at the level of 3–3.5σ, where σ is the local sky rms noise-level. So starting with CR-clipping on 8 exposures for every pointing should be robust.

[12]see also https://www.stsci.edu/files/live/sites/www/files/home/hst/documentation/_documents/wfpc2/wfpc2_ihb_cycle17.pdf and https://www.stsci.edu/files/live/sites/www/files/home/hst/documentation/_documents/wfpc2/wfpc2_dhb_v5.pdf

Nonetheless, we cannot rule out that the CR flux may occasionally be considerably higher than average, and so must account for the possibility that even while using N=8 exposures for each pointing in each filter, some CR's may have survived the clipping procedure upon drizzling and mimic variable objects at the 3.0σ level. For this reason, we also performed additional tests, as described below.

Cosmic rays are flagged in the Data Quality extension of ACS images with values of 4096 and 8192. For every variable object, we create a 8×8 pixel box at the center of the measurement, corresponding closely to the 8-pixel diameter aperture used to identify variability (see Section 3.3.2). We count the number of pixels within this box that may be affected by residual cosmic ray flux. We define cosmic-ray-affected pixels (CR-affected) to be those where a cosmic ray appears in that exact location in at least half of the stacked exposures (4 or more exposures). The location is determined by the WCS in the image header of each individual exposure. For every object, we do this for both epochs, and compare the number of cosmic rays in the two epochs. A source is determined to be CR-affected if it has at least one CR-affected pixel within the 8×8 pixel box in either epoch. A CR-affected source, as defined here, *may* be affected by comic rays, although it is likely not due to the stacking of 8 individual exposures with `AstroDrizzle`.

In Figure 36, we plot the measured change in flux of the objects (between two epochs) versus the combined number of CR-affected pixels. We also plot the difference in the number of pixels affected by cosmic rays between the two epochs, because if one epoch has significantly more CR-affected pixels, this could cause artificial variability. The exercise demonstrates that cosmic rays do not affect our variability detections because the measured flux difference does not depend on the number of CR-affected

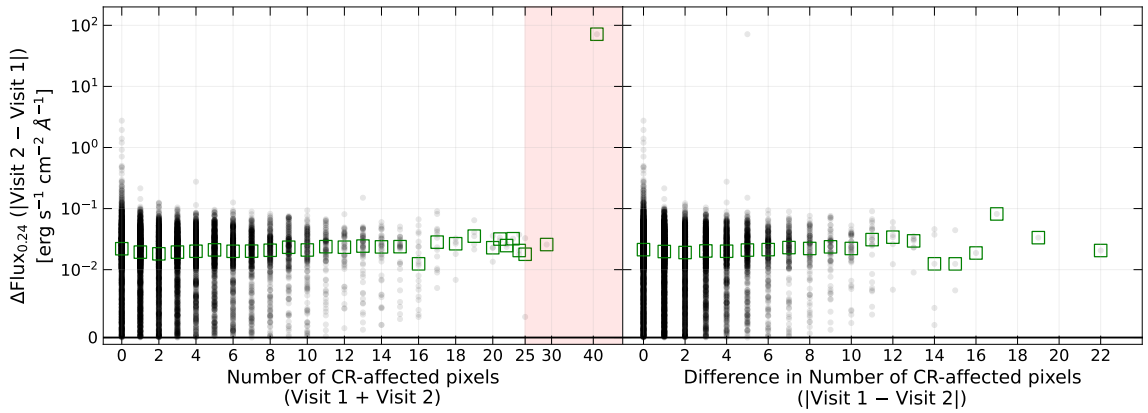

Figure 36. We analyze the potential effect of cosmic rays on the measured flux difference of variable objects in an 8×8 pixel (0.″24×0.″24) area centered on each object. A pixel is considered at risk of cosmic ray contamination if it encounters a cosmic ray in four or more contributing exposures. Plotted is a random selection of 10,000 galaxies (represented by black points), with median values indicated by green boxes. **Left:** The absolute value of the difference in measured F606W flux versus the total number of pixels (in Visit 1 + Visit 2) possibly impacted by cosmic rays. The red shaded region shows objects that are removed for containing too many cosmic rays. The y-axis is logarithmically scaled except between -0.1 and 0.1, which is scaled linearly. The x-axis is linearly scaled up to 20, where it is then logarithmically scaled to 50. **Right:** The absolute value of the difference in measured F606W flux versus the difference in the number of pixels potentially affected by cosmic rays.

pixels or the difference in the number of CR-affected pixels. Moreover, ∼31% of the 10,000 galaxies sampled in Figure 36 have zero CR-affected pixels in both epochs.

One object with very high measured differences in flux also have a large number of pixels with cosmic rays. We opt to reject and remove two objects with more than 25 pixels (∼25% of the pixels in the aperture) affected by cosmic rays. There were no variable candidates that met this criteria.

We also confirm the distribution of $\Delta m_{0.24}$ is Gaussian for sources potentially affected by cosmic rays, shown in Figure 37. More importantly, since a majority (∼ 80%) of sources in our dataset are potentially affected by cosmic rays, our empirical uncertainties in Section 3.3.2.2 already account for cosmic ray affects. This is specifically represented by the fact that the Gaussian fit to the CR-affected sources

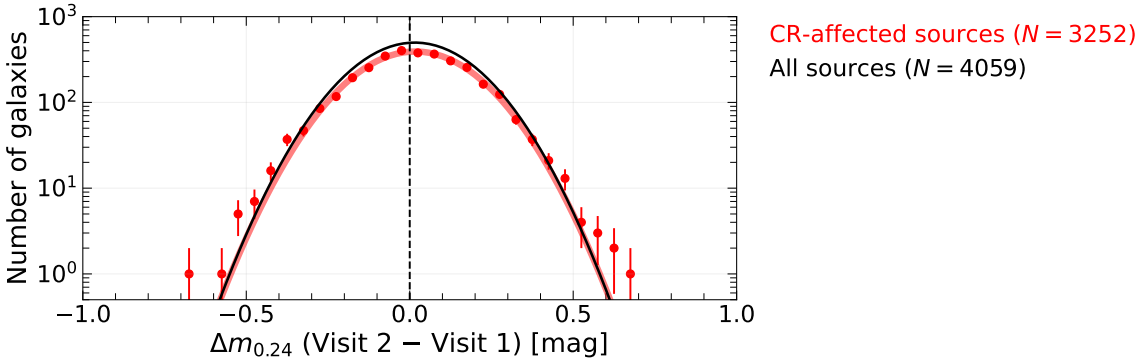

Figure 37. Histogram of the distribution of magnitude differences measured between two epochs ($\Delta m_{0.24}$) for 4,059 galaxies between $28.0 < m_{AB} < 28.5$. We compare the sample of CR-affected galaxies (red) to the full sample (black). The points show the fraction of CR-affected galaxies (N) for each $\Delta m_{0.24}$ bin, where the error bar is $\sqrt{N}$. The solid lines are Gaussian fits to the data. The black solid line represents the Gaussian fit to the full sample. Our empirical uncertainties estimated in Figure 29 already account for cosmic ray effects, as shown by the black line closely following the red line.

(red line) is within 0.01 mag to the Gaussian fit for the full data (black line). The latter (black line) was used to calibrate our empirical uncertainties in Section 3.3.2.2. We note that, by eye, there appears to be a slight divergence from the Gaussian fit at $\sigma_{\Delta m} < -0.5$ and $\sigma_{\Delta m} > 0.5$. However, only the outer-most points seem to contribute to this trend, corresponding to less than 5 sources (or less than 0.2% of sources).

In conclusion, this evidence suggests that cosmic rays rarely appear in the final drizzled images. The spurious transients (in Section 3.3.1) were likely outliers, and any other spurious cosmic rays to this degree would have been identified during the transient search. In addition, if cosmic rays affect the brightness of sources regularly, our empirical estimation of uncertainties in Section 3.3.2.2 already accounts for this. Nonetheless, we do not completely eliminate the possibility that some (albeit very few) of our variable candidates may be affected by cosmic rays that cause artificial variability. In other words, although we assume a majority of our sources are not affected by cosmic rays, follow-up observations remain necessary to confirm which

sources are truly variable, as well as reveal other sources that were missed in this work.

3.7 Conclusion

This study highlights the JWST NEP TDF as an exceptional site for investigating time-variable astronomical phenomena, including SNe and (weak) variable AGN. We identified 12 transients and ∼100 variable sources in ACS/WFC F606W and F435W images from the HST TREASUREHUNT program. We provide positional information, dates of observation, intervening time interval, and magnitudes for each of the 12 transients, which range in brightness from ∼24.8 to ∼27.5 mag. Their areal density is ∼0.07 transients per arcmin^2 (∼245 per deg^2) per epoch. We argue that the vast majority of these transients are SNe. Three transients (T7, T10, and T11) were detected in X-rays, of which two (T7 and T10) appear isolated and point-like and are likely newly identified quasars. Transient T11 has no visible host galaxy, and its nature remains uncertain. We suspect it to be a faint quasar if the X-ray detection is indeed associated, or otherwise either part of a very faint dwarf galaxy at $z \lesssim 6$, or a transient in a more massive host at $z \gtrsim 6$. One transient (T4) has a spectroscopic redshift $z = 0.615$ from MMT/Binospec.

Our variability search revealed that 0.42% of the general $z \lesssim 6$ field galaxy population exhibits variability at $\gtrsim 3\sigma_{\Delta m}$ significance to depths of 29.5 mag in F606W and 28.6 mag in F435W, with an areal density of ∼1.25 variables per arcmin^2 (∼4500 per deg^2). We carefully identified variable candidates, using the measured distribution of magnitude differences for objects observed more than once to calibrate our photometric uncertainties, where the scaled photometric uncertainty is $\sigma_{\Delta m}$, as

defined in Equation 3.1. Sources are flagged as variable if they varied by more than $3\sigma_{\Delta m}$ in F435W or F606W, or varied by more than $2\sigma_{\Delta m}$ in both filters in the same sense. This revealed 190 unique variable candidates, of which we estimated $\sim$80 to be false positives (using Gaussian statistics). Most of the variable candidates are coincident with the cores of galaxies, indicating potential AGN variability, while a smaller fraction appears associated with faint SNe. We also estimate photometric redshifts for our sample, from which we estimate masses, ages, dust extinction, and sSFRs. We briefly explore ways to estimate SMBH mass and AGN timescales using the time interval between overlapping visits and the observed rates of variability.

In conclusion, this work firmly establishes the JWST NEP TDF as a pivotal field for time-domain science with an initial harvest of transients and galaxies exhibiting variability. We emphasize the ability to identify AGN through their variability in the JWST NEP TDF. Future follow-up observations with HST or JWST could greatly increase the numbers of directly detected variables and to lower variability amplitudes.

Table 10. (A) Variable Sources identified in HST TREASUREHUNT observations of the JWST NEP TDF

ID	CatID	R.A. (deg)	Decl. (deg)	Visit 1	Visit 2	t_1 (yr)	t_2 (yr)	Δt (yr)	$m_{0.24}$ (mag)	$\Delta m_{0.24}$ (mag)	$\sigma_{\Delta m}$	$m_{0.24}$ (mag)	$\Delta m_{0.24}$ (mag)	$\sigma_{\Delta m}$
(1)	(2)	(3)	(4)	(5)	(6)	(7)	(8)	(9)	(10)	(11)	(12)	(13)	(14)	(15)
V001	19364	260.4052851	65.8382044	jeex01	jeex07	2020.733	2021.637	−0.904	28.86 (0.34)	−0.83	1.79	28.77 (0.21)	−0.86	3.64
V002	19815	260.4300229	65.8342205	jeex01	jeex07	2020.733	2021.637	−0.904	28.84 (0.47)	−0.74	1.17	28.69 (0.33)	1.15	3.04
V003	19785	260.4326188	65.8345545	jeex01	jeex07	2020.733	2021.637	−0.904	27.93 (0.24)	0.79	2.40	28.00 (0.15)	0.55	3.23
V004	20003	260.4473218	65.8318503	jeex01	jeex07	2020.733	2021.637	−0.904	28.65 (0.40)	0.68	1.27	28.23 (0.17)	0.59	3.04
V005	41428	260.4502146	65.7515390	jemn01	jeex6b	2021.789	2022.093	−0.304	29.10 (0.50)	0.43	0.63	28.84 (0.33)	1.13	3.00
V006	20130	260.4604344	65.8296368	jeex01	jeex07	2020.733	2021.637	−0.904	28.33 (0.46)	1.37	2.20	28.75 (0.23)	0.62	2.36
V007	20104	260.4622684	65.8300200	jeex01	jeex07	2020.733	2021.637	−0.904	27.49 (0.15)	0.56	2.74	27.49 (0.09)	0.28	2.84
V008	40135	260.4800396	65.7615899	jemn01	jeex6b	2021.789	2022.093	−0.304	28.97 (0.68)	0.93	1.02	28.67 (0.30)	1.05	3.10
V009	42426	260.4811656	65.7389668	jemn01	jeex6b	2021.789	2022.093	−0.304	24.68 (0.03)	−0.12	3.13	23.39 (0.01)	−0.04	2.97
V010	48837	260.4847004	65.8816131	jemn06	jeex07	2022.530	2021.637	0.893	27.92 (0.28)	−0.81	2.17	27.65 (0.10)	−0.26	2.14
V011	48800	260.4850911	65.8819144	jemn06	jeex07	2022.530	2021.637	0.893	27.17 (0.13)	−0.19	1.09	28.66 (0.36)	−1.29	3.12
V012	48831	260.4857008	65.8816066	jemn06	jeex07	2022.530	2021.637	0.893	27.92 (0.28)	−0.81	2.17	28.55 (0.32)	1.23	3.33
V013	48977	260.4903910	65.8782280	jemn06	jeex07	2022.530	2021.637	0.893	28.33 (0.26)	−0.35	1.02	28.29 (0.19)	0.77	3.52
V014	39334	260.4918589	65.7687739	jemn01	jeex6b	2021.789	2022.093	−0.304	28.75 (0.33)	−0.06	0.13	28.52 (0.22)	0.81	3.24
V015	48934	260.4943736	65.8797585	jemn06	jeex07	2022.530	2021.637	0.893	28.53 (0.41)	0.68	1.24	28.22 (0.17)	0.59	3.07
V016	19975	260.4965078	65.8309014	jeex01	jeex07	2020.733	2021.637	−0.904	19.18 (0.01)	0.03	7.62	19.46 (0.03)	0.13	3.42
V017	49160	260.4965104	65.8742828	jemn06	jeex07	2022.530	2021.637	0.893	28.43 (0.26)	0.12	0.36	28.03 (0.13)	0.47	3.14
V018	42276	260.4979360	65.7417349	jemn01	jeex6b	2021.789	2022.093	−0.304	28.77 (0.35)	−0.04	0.08	28.57 (0.23)	−0.81	3.03
V019	40970	260.5045403	65.7556663	jemn01	jeex6b	2021.789	2022.093	−0.304	28.12 (0.33)	0.89	2.03	29.00 (0.34)	0.92	2.37
V020	39013	260.5060240	65.7731007	jemn01	jeex6b	2021.789	2022.093	−0.304	28.86 (0.41)	−0.08	0.14	27.98 (0.13)	0.57	3.71
V021	38120	260.5075136	65.7925038	jemn01	jdkq02	2021.789	2017.918	3.871	29.06 (0.64)	−0.83	0.96	28.74 (0.29)	1.13	3.37
V022	38237	260.5090095	65.7913053	jemn01	jdkq02	2021.789	2017.918	3.871	28.63 (0.32)	−0.01	0.02	28.31 (0.17)	0.60	3.05
V023	17632	260.5109164	65.8123441	jeex01	jdkq02	2020.733	2017.918	2.815	28.90 (0.43)	−0.45	0.76	28.61 (0.26)	0.89	3.01
V024	38331	260.5132040	65.7883638	jemn01	jdkq02	2021.789	2017.918	3.871	28.16 (0.44)	1.24	2.09	28.79 (0.24)	0.62	2.22
V025	17466	260.5132587	65.8165789	jeex01	jdkq02	2020.733	2017.918	2.815	27.85 (0.28)	−1.16	3.07	29.40 (0.35)	−0.42	1.06
V026	17481	260.5139809	65.8162782	jeex01	jdkq02	2020.733	2017.918	2.815	27.85 (0.28)	−1.16	3.07	29.28 (0.37)	0.71	1.66
V027	17482	260.5148620	65.8162530	jeex01	jdkq02	2020.733	2017.918	2.815	27.85 (0.28)	−1.16	3.07	28.13 (0.13)	−0.28	1.95
V028	42324	260.5156057	65.7410733	jemn01	jeex6b	2021.789	2022.093	−0.304	28.62 (0.34)	0.16	0.36	27.34 (0.09)	0.35	3.45
V029	49278	260.5165718	65.8723986	jemn06	jeex07	2022.530	2021.637	0.893	29.37 (0.51)	0.01	0.02	28.17 (0.18)	−0.86	4.10
V030	39884	260.5168553	65.7637201	jemn01	jeex6b	2021.789	2022.093	−0.304	29.02 (0.59)	0.66	0.83	28.04(0.15)	−0.58	3.43
V031	17642	260.5181754	65.8119968	jeex01	jdkq02	2020.733	2017.918	2.815	25.73 (0.05)	0.01	0.11	25.52 (0.03)	0.23	5.72
V032	41667	260.5200938	65.7490569	jemn01	jeex6b	2021.789	2022.093	−0.304	28.80 (0.43)	−0.36	0.61	28.59 (0.28)	1.02	3.14
V033	17861	260.5203993	65.8073115	jeex01	jdkq02	2020.733	2017.918	2.815	21.56 (0.01)	−0.04	4.18	21.00 (0.01)	0.06	14.72
V034	17017	260.5285670	65.8336403	jeex01	jdkq02	2020.733	2017.918	2.815	25.52 (0.04)	−0.01	0.15	24.85 (0.02)	0.09	3.37
V035	17815	260.5286942	65.8079924	jeex01	jdkq02	2020.733	2017.918	2.815	28.89 (0.41)	0.32	0.58	28.12 (0.15)	0.61	3.58
V036	37564	260.5290447	65.8045199	jemn01	jdkq02	2021.789	2017.918	3.871	27.65 (0.29)	−1.28	3.28	26.37 (0.05)	0.01	0.25
V037	39503	260.5295628	65.7668789	jemn01	jeex6b	2021.789	2022.093	−0.304	27.11 (0.12)	−0.24	1.47	28.53 (0.27)	−1.14	3.63
V038	37829	260.5301461	65.7975577	jemn01	jdkq02	2021.789	2017.918	3.871	28.69 (0.40)	−0.50	0.92	28.40 (0.19)	0.68	3.10
V039	40938	260.5321327	65.7559458	jemn01	jeex6b	2021.789	2022.093	−0.304	28.72 (0.68)	−1.23	1.34	28.58 (0.25)	−0.90	3.18
V040	5015	260.5324664	65.8591989	jdkq01	jeex07	2017.749	2021.637	−3.888	24.38 (0.03)	0.07	2.13	22.35 (0.01)	−0.07	8.83
V041	37499	260.5337585	65.8079004	jemn01	jdkq02	2021.789	2017.918	3.871	24.84 (0.03)	−0.08	1.79	23.51 (0.01)	0.08	5.92
V042	33111	260.5339889	65.9156836	jeex6a	jemn06	2022.830	2022.530	0.300	27.20 (0.14)	−0.40	2.20	26.81 (0.06)	−0.15	2.09
V043	40338	260.5343798	65.7602481	jemn01	jeex6b	2021.789	2022.093	−0.304	29.16 (0.52)	−0.11	0.16	28.08 (0.14)	−0.49	3.07
V044	39949	260.5351364	65.7631956	jemn01	jeex6b	2021.789	2022.093	−0.304	27.97 (0.25)	0.41	1.21	27.69 (0.19)	1.27	5.95
V045	17127	260.5351702	65.8285103	jeex01	jdkq02	2020.733	2017.918	2.815	29.56 (0.59)	−0.11	0.14	28.62 (0.25)	0.88	3.05

Note. — Columns (1) through (9) list the variable source ID, an internal `SourceExtractor` catalog ID, the celestial coordinates (determined by `SourceExtractor` for the position corresponding to $m_{0.24}$) of the variable source in decimal degrees, the root names of the overlapping visits in which the variable source was detected (Visit 1 and Visit 2), the corresponding UT dates of observation, and the time interval Δt between Visits 1 and 2. Table columns (10) through (12) list for the F435W filter the brightest $m_{0.24}$ of the two visits (with the magnitude uncertainty given in parentheses), the change in brightness ($\Delta m_{0.24}$, using the same definition as in Figure 29) between the two visits, and the significance of the variability (σ_{var}). Table columns (13) through (15) list the same but for the F606W filter.

Table 11. (B) Variable Sources identified in HST TREASUREHUNT observations of the JWST NEP TDF

ID	CatID	R.A. (deg)	Decl. (deg)	Visit 1	Visit 2	t_1 (yr)	t_2 (yr)	Δt (yr)	$m_{0.24}$ (mag)	$\Delta m_{0.24}$ (mag)	$\sigma_{\Delta m}$	$m_{0.24}$ (mag)	$\Delta m_{0.24}$ (mag)	$\sigma_{\Delta m}$
(1)	(2)	(3)	(4)	(5)	(6)	(7)	(8)	(9)	(10)	(11)	(12)	(13)	(14)	(15)
V046	41298	260.5354508	65.7527669	jemn01	jeex6b	2021.789	2022.093	−0.304	28.75 (0.43)	−0.42	0.73	27.86 (0.14)	0.57	3.58
V047	38098	260.5366516	65.7930824	jemn01	jdkq02	2021.789	2017.918	3.871	28.25 (0.27)	0.31	0.86	28.17 (0.16)	0.72	3.86
V048	39683	260.5391875	65.7652426	jemn01	jeex6b	2021.789	2022.093	−0.304	28.13 (0.25)	−0.34	0.98	28.60 (0.28)	−1.05	3.25
V049	17165	260.5419552	65.8281206	jeex01	jdkq02	2020.733	2017.918	2.815	26.82 (0.10)	−0.34	2.63	26.64 (0.06)	−0.16	2.42
V050	38172	260.5436430	65.7915235	jemn01	jdkq02	2021.789	2017.918	3.871	28.01 (0.26)	0.79	2.20	27.80 (0.11)	0.48	3.79
V051	38266	260.5439886	65.7895398	jemn01	jdkq02	2021.789	2017.918	3.871	29.64 (0.73)	−0.22	0.23	28.69 (0.25)	0.86	3.03
V052	17831	260.5441742	65.8076230	jeex01	jdkq02	2020.733	2017.918	2.815	28.48 (0.38)	−0.85	1.67	28.73 (0.33)	1.16	3.06
V053	38122	260.5449020	65.7931821	jemn01	jdkq02	2021.789	2017.918	3.871	26.56 (0.08)	−0.03	0.26	25.82 (0.04)	−0.21	4.62
V054	39765	260.5451659	65.7641522	jemn01	jeex6b	2021.789	2022.093	−0.304	29.01 (0.54)	0.58	0.80	28.54 (0.24)	−0.91	3.30
V055	40721	260.5457177	65.7587033	jemn01	jeex6b	2021.789	2022.093	−0.304	28.12 (0.32)	−0.87	2.01	28.31 (0.17)	−0.49	2.54
V056	37972	260.5485168	65.7954958	jemn01	jdkq02	2021.789	2017.918	3.871	28.55 (0.31)	−0.16	0.38	28.41 (0.30)	1.42	4.11
V057	48	260.5548528	65.8386224	jdkq01	jdkq02	2017.749	2017.918	−0.169	27.15 (0.12)	−0.49	3.00	27.01 (0.07)	−0.34	4.06
V058	33274	260.5610833	65.9123618	jeex6a	jemn06	2022.830	2022.530	0.300	28.39 (0.41)	0.82	1.47	28.21 (0.18)	0.66	3.23
V059	32938	260.5613045	65.9189714	jeex6a	jemn06	2022.830	2022.530	0.300	29.43 (0.64)	0.16	0.19	28.50 (0.22)	−0.78	3.11
V060	6238	260.5683705	65.7831566	jdkq03	jdkq02	2019.101	2017.918	1.183	28.78 (0.46)	0.52	0.84	27.37 (0.09)	−0.36	3.35
V061	41126	260.5686500	65.7542573	jemn01	jeex6b	2021.789	2022.093	−0.304	28.31 (0.42)	1.15	2.01	28.27 (0.15)	0.36	2.05
V062	33539	260.5688549	65.9067578	jeex6a	jemn06	2022.830	2022.530	0.300	29.17 (0.57)	−0.40	0.52	28.29 (0.17)	0.62	3.13
V063	33524	260.5855449	65.9068262	jeex6a	jemn06	2022.830	2022.530	0.300	25.57 (0.05)	0.16	2.27	25.41 (0.03)	0.21	5.59
V064	34022	260.5865160	65.8956540	jeex6a	jemn06	2022.830	2022.530	0.300	22.45 (0.01)	−0.07	4.92	29.03 (0.22)	−0.06	0.23
V065	234	260.5868385	65.8333537	jdkq01	jdkq02	2017.749	2017.918	−0.169	28.37 (0.23)	−0.08	0.25	28.32 (0.18)	−0.71	3.40
V066	6629	260.5886084	65.7776747	jdkq03	jdkq02	2019.101	2017.918	1.183	28.05 (0.25)	0.59	1.71	28.74 (0.24)	0.89	3.17
V067	320	260.5901557	65.8318573	jdkq01	jdkq02	2017.749	2017.918	−0.169	23.25 (0.01)	0.02	1.05	21.70 (0.01)	0.02	3.63
V068	6334	260.6025353	65.7820869	jdkq03	jdkq02	2019.101	2017.918	1.183	27.59 (0.15)	−0.05	0.23	26.61 (0.06)	0.30	4.42
V069	34339	260.6027231	65.8860494	jeex6a	jemn06	2022.830	2022.530	0.300	28.42 (0.38)	0.98	1.89	28.79 (0.30)	1.08	3.11
V070	34133	260.6032077	65.8928444	jeex6a	jemn06	2022.830	2022.530	0.300	27.61 (0.18)	−0.55	2.28	27.38 (0.08)	−0.21	2.21
V071	34238	260.6051718	65.8906921	jeex6a	jemn06	2022.830	2022.530	0.300	29.87 (0.82)	0.07	0.07	28.70 (0.24)	−0.85	3.09
V072	6269	260.6061960	65.7821730	jdkq03	jdkq02	2019.101	2017.918	1.183	24.62 (0.03)	−0.02	0.50	23.86 (0.02)	−0.07	4.09
V073	3339	260.6121812	65.8528375	jdkq01	jdkq07	2017.749	2018.647	−0.898	28.75 (0.32)	0.21	0.48	28.12 (0.16)	0.61	3.38
V074	6605	260.6177291	65.7775875	jdkq03	jdkq02	2019.101	2017.918	1.183	25.31 (0.04)	−0.06	1.01	24.53 (0.02)	−0.10	4.11
V075	663	260.6220866	65.8272493	jdkq01	jdkq02	2017.749	2017.918	−0.169	27.68 (0.20)	−0.86	3.24	27.83 (0.11)	−0.40	3.01
V076	5684	260.6225709	65.7904307	jdkq03	jdkq02	2019.101	2017.918	1.183	27.92 (0.31)	1.02	2.45	28.44 (0.17)	0.46	2.42
V077	1294	260.6246197	65.8807391	jdkq01	jdkq07	2017.749	2018.647	−0.898	27.98 (0.20)	−0.53	2.01	28.03 (0.12)	−0.40	2.81
V078	3134	260.6252980	65.8542599	jdkq01	jdkq07	2017.749	2018.647	−0.898	28.44 (0.27)	−0.21	0.59	28.13 (0.15)	−0.53	3.05
V079	11949	260.6257482	65.8157473	jdkq08	jdkq02	2018.645	2017.918	0.727	28.87 (0.42)	−0.61	1.09	28.43 (0.22)	−0.98	3.89
V080	5284	260.6287600	65.7986047	jdkq03	jdkq02	2019.101	2017.918	1.183	29.42 (0.68)	−0.30	0.32	28.78 (0.31)	−1.18	3.33
V081	32136	260.6292399	65.8979164	jeex6a	jdkq07	2022.830	2018.647	4.183	27.79 (0.21)	0.76	2.67	26.81 (0.06)	0.18	2.51
V082	11609	260.6327010	65.8281680	jdkq08	jdkq02	2018.645	2017.918	0.727	28.59 (0.27)	−0.36	0.99	28.56 (0.19)	−0.67	3.09
V083	2974	260.6335344	65.8561320	jdkq01	jdkq07	2017.749	2018.647	−0.898	23.61 (0.02)	−0.01	0.60	21.91 (0.01)	−0.02	3.69
V084	4711	260.6350207	65.8290677	jdkq01	jdkq08	2017.749	2018.645	−0.896	28.87 (0.36)	−0.32	0.67	28.61 (0.31)	−1.23	3.46
V085	2872	260.6381441	65.8573742	jdkq01	jdkq07	2017.749	2018.647	−0.898	28.66 (0.35)	−0.57	1.21	28.37 (0.17)	0.62	3.07
V086	5236	260.6391309	65.7993893	jdkq03	jdkq02	2019.101	2017.918	1.183	26.39 (0.07)	0.04	0.37	24.53 (0.02)	0.09	4.18
V087	31994	260.6421239	65.9029309	jeex6a	jdkq07	2022.830	2018.647	4.183	23.99 (0.02)	−0.01	0.26	22.26 (0.01)	0.03	4.12
V088	1426	260.6421779	65.8780433	jdkq01	jdkq07	2017.749	2018.647	−0.898	28.76 (0.29)	0.15	0.37	28.51 (0.20)	0.76	3.24
V089	4463	260.6460086	65.8377478	jdkq01	jdkq08	2017.749	2018.645	−0.896	28.77 (0.28)	0.01	0.02	28.51 (0.24)	−0.91	3.29
V090	3860	260.6476671	65.8447077	jdkq01	jdkq07	2017.749	2018.647	−0.898	29.00 (0.40)	0.35	0.64	28.77 (0.35)	−1.20	3.01

Note. — Columns (1) through (9) list the variable source ID, an internal `SourceExtractor` catalog ID, the celestial coordinates (determined by `SourceExtractor` for the position corresponding to $m_{0.24}$) of the variable source in decimal degrees, the root names of the overlapping visits in which the variable source was detected (Visit 1 and Visit 2), the corresponding UT dates of observation, and the time interval Δt between Visits 1 and 2. Table columns (10) through (12) list for the F435W filter the brightest $m_{0.24}$ of the two visits (with the magnitude uncertainty given in parentheses), the change in brightness ($\Delta m_{0.24}$, using the same definition as in Figure 29) between the two visits, and the significance of the variability (σ_{var}). Table columns (13) through (15) list the same but for the F606W filter.

Table 12. (C) Variable Sources identified in HST TREASUREHUNT observations of the JWST NEP TDF

ID	CatID	R.A. (deg)	Decl. (deg)	Visit 1	Visit 2	t_1 (yr)	t_2 (yr)	Δt (yr)	$m_{0.24}$ (mag)	$\Delta m_{0.24}$ (mag)	$\sigma_{\Delta m}$	$m_{0.24}$ (mag)	$\Delta m_{0.24}$ (mag)	$\sigma_{\Delta m}$
(1)	(2)	(3)	(4)	(5)	(6)	(7)	(8)	(9)	(10)	(11)	(12)	(13)	(14)	(15)
V091	12341	260.6578804	65.8123865	jdkq08	jdkq03	2018.645	2019.101	−0.456	28.23 (0.35)	−1.02	2.15	27.85 (0.11)	−0.28	2.22
V092	2939	260.6676957	65.8565418	jdkq01	jdkq07	2017.749	2018.647	−0.898	28.10 (0.21)	0.33	1.17	28.23 (0.17)	0.58	3.03
V093	12870	260.6677285	65.7981739	jdkq08	jdkq03	2018.645	2019.101	−0.456	28.88 (0.36)	−0.06	0.13	27.54 (0.09)	−0.33	3.14
V094	4423	260.6680216	65.8388153	jdkq01	jdkq08	2017.749	2018.645	−0.896	27.10 (0.10)	0.06	0.43	28.63 (0.25)	0.90	3.13
V095	2469	260.6684303	65.8631755	jdkq01	jdkq07	2017.749	2018.647	−0.898	29.23 (0.43)	0.09	0.15	28.24 (0.33)	−1.57	4.18
V096	12868	260.6747247	65.7980539	jdkq08	jdkq03	2018.645	2019.101	−0.456	28.62 (0.43)	−0.86	1.48	28.49 (0.24)	−0.88	3.22
V097	48064	260.6753285	65.9216637	jemn05	jeex6a	2022.377	2022.830	−0.453	28.21 (0.22)	0.01	0.04	28.63 (0.24)	−0.89	3.16
V098	15034	260.6772860	65.8538229	jdkq08	jdkq07	2018.645	2018.647	−0.002	28.04 (0.19)	0.09	0.36	28.10 (0.15)	0.68	3.84
V099	3932	260.6794726	65.8408931	jdkq01	jdkq07	2017.749	2018.647	−0.898	29.21 (0.49)	0.58	0.88	28.13 (0.14)	0.49	3.09
V100	48124	260.6803062	65.9204980	jemn05	jeex6a	2022.377	2022.830	−0.453	28.10 (0.20)	0.15	0.57	28.17 (0.16)	−0.69	3.82
V101	15545	260.6815935	65.8449714	jdkq08	jdkq07	2018.645	2018.647	−0.002	28.85 (0.33)	0.22	0.50	28.48 (0.21)	0.76	3.23
V102	12867	260.6822444	65.7979657	jdkq08	jdkq03	2018.645	2019.101	−0.456	26.89 (0.10)	−0.24	1.78	28.72 (0.26)	0.94	3.17
V103	48474	260.6830765	65.9131667	jemn05	jeex6a	2022.377	2022.830	−0.453	27.95 (0.29)	−0.98	2.53	28.17 (0.14)	−0.42	2.51
V104	12872	260.6845500	65.7978732	jdkq08	jdkq03	2018.645	2019.101	−0.456	27.45 (0.17)	−0.70	3.11	27.60 (0.09)	−0.09	0.85
V105	7585	260.6923363	65.7739049	jdkq04	jdkq03	2018.221	2019.101	−0.880	28.17 (0.26)	−0.61	1.74	28.44 (0.21)	−0.95	3.88
V106	12912	260.6948845	65.7964272	jdkq08	jdkq03	2018.645	2019.101	−0.456	23.61 (0.02)	−0.17	6.58	23.30 (0.01)	0.01	0.88
V107	46007	260.6995940	65.7123076	jemn02	jdkq09	2021.940	2019.106	2.834	26.96 (0.09)	−0.01	0.06	24.36 (0.02)	0.08	3.83
V108	44457	260.7055562	65.7256191	jemn02	jdkq09	2021.940	2019.106	2.834	27.12 (0.11)	0.19	1.27	26.52 (0.05)	0.19	3.21
V109	44621	260.7056172	65.7226130	jemn02	jdkq09	2021.940	2019.106	2.834	28.16 (0.40)	−1.14	2.11	28.63 (0.24)	−0.86	3.15
V110	7638	260.7078911	65.7730268	jdkq04	jdkq03	2018.221	2019.101	−0.880	28.83 (0.55)	−1.05	1.43	28.64 (0.26)	0.95	3.22
V111	45164	260.7102095	65.7169415	jemn02	jdkq09	2021.940	2019.106	2.834	28.80 (0.40)	0.32	0.59	28.38 (0.27)	1.36	4.32
V112	13412	260.7123985	65.7927245	jdkq08	jdkq04	2018.645	2018.221	0.424	27.84 (0.16)	−0.20	0.93	26.91 (0.06)	−0.25	3.47
V113	45918	260.7167982	65.7087560	jemn02	jdkq09	2021.940	2019.106	2.834	27.88 (0.21)	−0.16	0.60	26.49 (0.05)	0.19	3.11
V114	7098	260.7175478	65.7848453	jdkq04	jdkq03	2018.221	2019.101	−0.880	24.53 (0.03)	−0.01	0.41	22.81 (0.01)	0.03	3.23
V115	45686	260.7192384	65.7123368	jemn02	jdkq09	2021.940	2019.106	2.834	27.88 (0.25)	−0.73	2.20	27.82 (0.12)	−0.37	2.78
V116	8197	260.7200109	65.7631919	jdkq04	jdkq03	2018.221	2019.101	−0.880	24.17 (0.02)	−0.02	0.57	23.40 (0.01)	0.06	4.30
V117	44851	260.7250941	65.7203820	jemn02	jdkq09	2021.940	2019.106	2.834	28.83 (0.40)	−0.05	0.10	28.32 (0.19)	−0.67	3.07
V118	11469	260.7287189	65.8579825	jdkq07	jdkq06	2018.647	2018.511	0.136	28.35 (0.34)	0.89	1.94	28.38 (0.19)	0.73	3.36
V119	10689	260.7358381	65.8754246	jdkq07	jdkq06	2018.647	2018.511	0.136	24.60 (0.03)	0.04	0.91	23.04 (0.01)	0.06	5.33
V120	44649	260.7372179	65.7239799	jemn02	jdkq09	2021.940	2019.106	2.834	28.27 (0.24)	−0.09	0.28	28.01 (0.15)	−0.53	3.07
V121	45250	260.7375391	65.7161188	jemn02	jdkq09	2021.940	2019.106	2.834	28.80 (0.50)	−0.64	0.96	28.77 (0.31)	1.09	3.07
V122	44894	260.7383881	65.7200561	jemn02	jdkq09	2021.940	2019.106	2.834	28.63 (0.33)	−0.13	0.29	28.11 (0.16)	0.56	3.16
V123	44048	260.7396362	65.7294908	jemn02	jdkq09	2021.940	2019.106	2.834	27.74 (0.18)	−0.21	0.86	28.57 (0.26)	−1.09	3.60
V124	43264	260.7454366	65.7380214	jemn02	jdkq09	2021.940	2019.106	2.834	19.25 (0.01)	0.07	13.92	19.50 (0.02)	−0.33	13.27
V125	16264	260.7488596	65.7509596	jdkq09	jdkq04	2019.106	2018.221	0.885	28.41 (0.28)	0.44	1.16	28.54 (0.21)	−0.72	3.03
V126	44831	260.7505188	65.7205403	jemn02	jdkq09	2021.940	2019.106	2.834	27.61 (0.29)	−1.18	3.01	27.89 (0.12)	−0.11	0.77
V127	45380	260.7514847	65.7150048	jemn02	jdkq09	2021.940	2019.106	2.834	27.73 (0.23)	−0.75	2.37	27.51 (0.10)	−0.24	2.15
V128	43642	260.7545349	65.7350399	jemn02	jdkq09	2021.940	2019.106	2.834	28.56 (0.32)	0.29	0.67	28.30 (0.16)	0.55	3.04
V129	15975	260.7564058	65.7560911	jdkq09	jdkq04	2019.106	2018.221	0.885	29.24 (0.46)	0.07	0.11	28.32 (0.20)	0.72	3.16
V130	42985	260.7569328	65.7430011	jemn02	jdkq09	2021.940	2019.106	2.834	27.87 (0.21)	0.58	2.01	27.85 (0.11)	0.34	2.67
V131	43199	260.7654001	65.7398784	jemn02	jdkq09	2021.940	2019.106	2.834	29.29 (0.59)	0.21	0.26	28.63 (0.28)	1.02	3.22
V132	44494	260.7709607	65.7242314	jemn02	jdkq09	2021.940	2019.106	2.834	28.30 (0.30)	−0.44	1.10	28.32 (0.18)	−0.68	3.33
V133	43060	260.7745589	65.7419473	jemn02	jdkq09	2021.940	2019.106	2.834	28.12 (0.28)	0.72	1.90	28.35 (0.17)	0.62	3.13
V134	45001	260.7764730	65.7187770	jemn02	jdkq09	2021.940	2019.106	2.834	26.10 (0.06)	−0.05	0.55	25.65 (0.03)	0.12	3.04
V135	9852	260.7809939	65.8383387	jdkq06	jdkq05	2018.511	2018.363	0.148	27.94 (0.21)	0.46	1.63	27.63 (0.10)	0.39	3.45

Note. — Columns (1) through (9) list the variable source ID, an internal `SourceExtractor` catalog ID, the celestial coordinates (determined by `SourceExtractor` for the position corresponding to $m_{0.24}$) of the variable source in decimal degrees, the root names of the overlapping visits in which the variable source was detected (Visit 1 and Visit 2), the corresponding UT dates of observation, and the time interval Δt between Visits 1 and 2. Table columns (10) through (12) list for the F435W filter the brightest $m_{0.24}$ of the two visits (with the magnitude uncertainty given in parentheses), the change in brightness ($\Delta m_{0.24}$, using the same definition as in Figure 29) between the two visits, and the significance of the variability (σ_{var}). Table columns (13) through (15) list the same but for the F606W filter.

Table 13. (D) Variable Sources identified in HST TREASUREHUNT observations of the JWST NEP TDF

ID	CatID	R.A. (deg)	Decl. (deg)	Visit 1	Visit 2	t_1 (yr)	t_2 (yr)	Δt (yr)	$m_{0.24}$ (mag)	$\Delta m_{0.24}$ (mag)	$\sigma_{\Delta m}$	$m_{0.24}$ (mag)	$\Delta m_{0.24}$ (mag)	$\sigma_{\Delta m}$
(1)	(2)	(3)	(4)	(5)	(6)	(7)	(8)	(9)	(10)	(11)	(12)	(13)	(14)	(15)
V136	9811	260.7820403	65.8390785	jdkq06	jdkq05	2018.511	2018.363	0.148	27.51 (0.14)	0.17	0.93	28.53 (0.19)	0.70	3.18
V137	45900	260.7829845	65.7089929	jemn02	jdkq09	2021.940	2019.106	2.834	28.00 (0.26)	0.64	1.83	28.06 (0.14)	0.49	3.03
V138	16432	260.7838837	65.7488263	jdkq09	jdkq04	2019.106	2018.221	0.885	28.42 (0.38)	−0.86	1.70	28.48 (0.21)	0.74	3.12
V139	46426	260.7901866	65.7007683	jemn02	jdkq09	2021.940	2019.106	2.834	28.16 (0.22)	0.00	0.01	27.59 (0.10)	−0.43	3.74
V140	8862	260.7966543	65.8514172	jdkq06	jdkq05	2018.511	2018.363	0.148	25.51 (0.05)	−0.08	1.30	25.35 (0.03)	−0.11	3.06
V141	31209	260.7976797	65.7264133	jeex08	jdkq09	2021.344	2019.106	2.238	29.20 (0.55)	−0.57	0.76	28.40 (0.22)	0.88	3.53
V142	9654	260.8007573	65.8408780	jdkq06	jdkq05	2018.511	2018.363	0.148	27.83 (0.20)	0.48	1.82	28.65 (0.26)	0.98	3.34
V143	28674	260.8063693	65.8799829	jeex05	jdkq06	2021.347	2018.511	2.836	28.27 (0.20)	0.44	1.59	27.76 (0.09)	0.36	3.44
V144	30070	260.8105090	65.7371529	jeex08	jdkq09	2021.344	2019.106	2.238	27.49 (0.15)	−0.18	0.88	28.05 (0.15)	0.54	3.16
V145	30045	260.8122328	65.7373452	jeex08	jdkq09	2021.344	2019.106	2.238	28.47 (0.47)	−1.10	1.73	28.71 (0.35)	1.23	3.04
V146	8477	260.8163753	65.7965563	jdkq05	jdkq04	2018.363	2018.221	0.142	26.81 (0.09)	−0.02	0.18	26.36 (0.05)	−0.21	3.53
V147	30059	260.8219253	65.7371863	jeex08	jdkq09	2021.344	2019.106	2.238	28.63 (0.45)	0.76	1.25	28.27 (0.22)	1.14	4.52
V148	28638	260.8274735	65.8806602	jeex05	jdkq06	2021.347	2018.511	2.836	28.37 (0.23)	−0.15	0.48	28.00 (0.14)	0.49	3.09
V149	22712	260.8347912	65.7296116	jeex03	jdkq09	2021.035	2019.106	1.929	28.36 (0.27)	0.06	0.16	28.32 (0.17)	0.62	3.10
V150	27404	260.8352185	65.7275413	jeex03	jeex08	2021.035	2021.344	−0.309	29.01 (0.70)	−0.69	0.73	27.38 (0.24)	−2.08	7.53
V151	47730	260.8358472	65.8893731	jemn04	jeex05	2022.227	2021.347	0.880	28.32 (0.30)	0.86	2.10	28.52 (0.22)	1.10	4.33
V152	9712	260.8429092	65.8400901	jdkq06	jdkq05	2018.511	2018.363	0.148	28.72 (0.34)	−0.39	0.85	28.68 (0.25)	0.93	3.24
V153	23869	260.8442446	65.7597401	jeex03	jeex08	2021.035	2021.344	−0.309	28.85 (0.39)	0.30	0.57	28.69 (0.29)	−1.10	3.27
V154	47372	260.8451666	65.8991518	jemn04	jeex05	2022.227	2021.347	0.880	28.80 (0.68)	−0.83	0.90	28.77 (0.33)	−1.21	3.17
V155	47667	260.8468371	65.8914197	jemn04	jeex05	2022.227	2021.347	0.880	27.66 (0.25)	1.03	3.01	27.96 (0.12)	0.28	2.04
V156	22013	260.8477623	65.7413624	jeex03	jdkq09	2021.035	2019.106	1.929	28.30 (0.47)	1.24	1.96	28.61 (0.25)	0.92	3.23
V157	25243	260.8539353	65.7457044	jeex03	jeex08	2021.035	2021.344	−0.309	27.75 (0.32)	1.33	3.12	28.44 (0.17)	−0.06	0.33
V158	25240	260.8541929	65.7458702	jeex03	jeex08	2021.035	2021.344	−0.309	27.75 (0.32)	1.33	3.12	27.48 (0.09)	−0.06	0.59
V159	30067	260.8578555	65.7371669	jeex08	jdkq09	2021.344	2019.106	2.238	28.25 (0.26)	−0.48	1.37	28.07 (0.13)	0.48	3.16
V160	27723	260.8600711	65.7221800	jeex03	jeex08	2021.035	2021.344	−0.309	24.03 (0.02)	−0.03	1.06	21.98 (0.01)	−0.03	4.86
V161	22223	260.8619972	65.7380793	jeex03	jdkq09	2021.035	2019.106	1.929	28.21 (0.27)	0.64	1.73	28.34 (0.16)	−0.72	3.79
V162	9531	260.8638246	65.8420120	jdkq06	jdkq05	2018.511	2018.363	0.148	29.46 (0.63)	−0.51	0.59	28.70 (0.27)	1.01	3.25
V163	24676	260.8653220	65.7504766	jeex03	jeex08	2021.035	2021.344	−0.309	28.42 (0.51)	−0.97	1.41	28.40 (0.20)	0.71	3.09
V164	25310	260.8719766	65.7454975	jeex03	jeex08	2021.035	2021.344	−0.309	28.54 (0.33)	0.22	0.50	28.03 (0.16)	−0.67	3.68
V165	24248	260.8746031	65.7549045	jeex03	jeex08	2021.035	2021.344	−0.309	27.52 (0.20)	−0.67	2.49	27.00 (0.07)	−0.22	2.64
V166	24737	260.8778166	65.7497988	jeex03	jeex08	2021.035	2021.344	−0.309	26.33 (0.09)	−0.40	3.27	26.27 (0.05)	−0.07	1.31
V167	47239	260.8785658	65.9050944	jemn04	jeex05	2022.227	2021.347	0.880	27.33 (0.18)	0.65	2.73	27.16 (0.08)	0.22	2.40
V168	24124	260.8799575	65.7558947	jeex03	jeex08	2021.035	2021.344	−0.309	27.77 (0.58)	−1.77	2.26	27.29 (0.08)	−0.24	2.55
V169	27313	260.8844831	65.7282510	jeex03	jeex08	2021.035	2021.344	−0.309	27.17 (0.15)	0.71	3.44	27.25 (0.08)	0.11	1.29
V170	26382	260.8880858	65.7366434	jeex03	jeex08	2021.035	2021.344	−0.309	28.41 (0.30)	0.34	0.86	28.54 (0.23)	0.93	3.44
V171	25315	260.8883667	65.7454453	jeex03	jeex08	2021.035	2021.344	−0.309	27.37 (0.17)	0.75	3.26	27.35 (0.08)	0.08	0.92
V172	24771	260.8931970	65.7496619	jeex03	jeex08	2021.035	2021.344	−0.309	29.00 (0.64)	−0.69	0.80	28.65 (0.27)	−1.03	3.32
V173	36203	260.8957973	65.8157113	jeexa4	jdkq05	2021.204	2018.363	2.841	28.61 (0.28)	0.34	0.87	28.36 (0.16)	0.59	3.32
V174	36152	260.8966926	65.8174593	jeexa4	jdkq05	2021.204	2018.363	2.841	26.22 (0.06)	−0.01	0.17	23.86 (0.01)	0.21	12.76
V175	36188	260.8977353	65.8156259	jeexa4	jdkq05	2021.204	2018.363	2.841	25.16 (0.04)	−0.02	0.37	24.81 (0.02)	0.08	3.17
V176	36219	260.8981358	65.8157672	jeexa4	jdkq05	2021.204	2018.363	2.841	25.49 (0.05)	−0.04	0.65	25.26 (0.03)	0.11	3.22
V177	36471	260.9048765	65.8670380	jeexa4	jemn04	2021.204	2022.227	−1.023	27.99 (0.25)	0.31	0.92	27.87 (0.12)	0.44	3.23
V178	36634	260.9055490	65.8651822	jeexa4	jemn04	2021.204	2022.227	−1.023	28.71 (0.46)	−0.79	1.29	28.20 (0.17)	0.62	3.25
V179	24684	260.9077303	65.7505134	jeex03	jeex08	2021.035	2021.344	−0.309	27.63 (0.20)	0.76	2.75	27.82 (0.11)	0.27	2.12
V180	26527	260.9094296	65.7355841	jeex03	jeex08	2021.035	2021.344	−0.309	26.13 (0.07)	0.19	2.07	25.04 (0.03)	0.08	2.58

Note. — Columns (1) through (9) list the variable source ID, an internal `SourceExtractor` catalog ID, the celestial coordinates (determined by `SourceExtractor` for the position corresponding to $m_{0.24}$) of the variable source in decimal degrees, the root names of the overlapping visits in which the variable source was detected (Visit 1 and Visit 2), the corresponding UT dates of observation, and the time interval Δt between Visits 1 and 2. Table columns (10) through (12) list for the F435W filter the brightest $m_{0.24}$ of the two visits (with the magnitude uncertainty given in parentheses), the change in brightness ($\Delta m_{0.24}$, using the same definition as in Figure 29) between the two visits, and the significance of the variability (σ_{var}). Table columns (13) through (15) list the same but for the F606W filter.

Table 14. (E) Variable Sources identified in HST TREASUREHUNT observations of the JWST NEP TDF

ID	CatID	R.A. (deg)	Decl. (deg)	Visit 1	Visit 2	t_1 (yr)	t_2 (yr)	Δt (yr)	$m_{0.24}$ (mag)	$\Delta m_{0.24}$ (mag)	$\sigma_{\Delta m}$	$m_{0.24}$ (mag)	$\Delta m_{0.24}$ (mag)	$\sigma_{\Delta m}$
(1)	(2)	(3)	(4)	(5)	(6)	(7)	(8)	(9)	(10)	(11)	(12)	(13)	(14)	(15)
V181	37131	260.9097335	65.8596199	jeexa4	jemn04	2021.204	2022.227	−1.023	28.03 (0.30)	−1.04	2.53	28.20 (0.15)	−0.48	2.72
V182	36713	260.9145485	65.8642884	jeexa4	jemn04	2021.204	2022.227	−1.023	29.00 (0.85)	0.78	0.68	27.94 (0.14)	0.52	3.23
V183	35903	260.9149584	65.8265971	jeexa4	jdkq05	2021.204	2018.363	2.841	25.20 (0.04)	−0.04	0.62	23.07 (0.01)	0.06	4.82
V184	47170	260.9280848	65.8129725	jemn03	jeexa4	2022.085	2021.204	0.881	27.47 (0.16)	0.54	2.49	27.08 (0.08)	0.21	2.45
V185	37073	260.9288557	65.8578725	jeexa4	jemn04	2021.204	2022.227	−1.023	27.19 (0.15)	−0.63	3.12	27.47 (0.09)	−0.05	0.48
V186	36333	260.9330472	65.8683621	jeexa4	jemn04	2021.204	2022.227	−1.023	24.58 (0.03)	−0.09	2.41	24.65 (0.02)	−0.06	2.32
V187	37009	260.9354158	65.8606655	jeexa4	jemn04	2021.204	2022.227	−1.023	27.68 (0.30)	−1.30	3.17	28.08 (0.15)	−0.43	2.47
V188	36313	260.9427395	65.8689954	jeexa4	jemn04	2021.204	2022.227	−1.023	27.81 (0.24)	−0.83	2.55	27.66 (0.10)	−0.26	2.20
V189	36623	260.9429745	65.8653180	jeexa4	jemn04	2021.204	2022.227	−1.023	27.51 (0.24)	−1.14	3.57	27.59 (0.10)	0.18	1.62
V190	36449	260.9444992	65.8672901	jeexa4	jemn04	2021.204	2022.227	−1.023	28.37 (0.40)	−1.01	1.86	28.62 (0.34)	1.22	3.11

Note. — Columns (1) through (9) list the variable source ID, an internal `SourceExtractor` catalog ID, the celestial coordinates (determined by `SourceExtractor` for the position corresponding to $m_{0.24}$) of the variable source in decimal degrees, the root names of the overlapping visits in which the variable source was detected (Visit 1 and Visit 2), the corresponding UT dates of observation, and the time interval Δt between Visits 1 and 2. Table columns (10) through (12) list for the F435W filter the brightest $m_{0.24}$ of the two visits (with the magnitude uncertainty given in parentheses), the change in brightness ($\Delta m_{0.24}$, using the same definition as in Figure 29) between the two visits, and the significance of the variability (σ_{var}). Table columns (13) through (15) list the same but for the F606W filter.

Chapter 4

A ZODIACAL LIGHT MODEL OPTIMIZED FOR OPTICAL WAVELENGTHS

4.1 Introduction

Zodiacal light is a diffuse glow brightly seen in UV-to-IR observations, caused by sunlight scattering and remitting off interplanetary dust particles within our Solar System (Leinert et al., 1998). These dust grains, which vary in size, shape, and composition, are primarily produced by Jupiter-family comets, with smaller contributions from asteroids and Oort-cloud comets (e.g., Dermott et al., 1992; Nesvorný et al., 2010; Rowan-Robinson & May, 2013).

Its structure is shaped by solar radiation, the solar wind, and the Sun's gravitational and magnetic influence (Burns et al., 1979). Individual dust grains are continuously pushed outward by radiation pressure or drawn inward by Poynting–Robertson drag, resulting in overall brightness of zodiacal light to be remarkably steady over time (Leinert et al., 1982; Mann et al., 2000). The resulting local interplanetary dust cloud that contributes the to zodiacal light stretches from near the Sun (e.g., Stenborg et al., 2021) to ∼3.3 AU (Hanner et al., 1974; Matsumoto et al., 2018).

There are several known components to the interplanetary dust cloud (Dermott et al., 1996; Leinert et al., 1998). There is a large smooth cloud component that hugs the ecliptic plane. This component exhibits a slight inclination relative to the ecliptic plane (Leinert et al., 1980). The radial density of the smooth cloud decreases with distance from the Sun, following a power-law distribution (e.g., Levasseur-Regourd, 1996). In addition there are smaller structures, like dust bands due to asteroidal dust

(Low et al., 1984; Spiesman et al., 1995), and a circumsolar ring that trails Earth (Reach et al., 1995).

In general, zodiacal light becomes negligible beyond ∼3.3 AU. It has been argued that much of the mass of the inteplanetary dust cloud resides beyond the Kuiper Belt (e.g., Poppe et al., 2019), but these components would be too distant to contribute significantly to zodiacal light (e.g., Dwek et al., 1998).

4.1.1 Zodiacal Light As A Foreground Contaminant

Zodiacal light is the dominant contributor the the total sky brightness in space-based ultraviolet to infrared observations, accounting for over 90% of the total signal space telescopes receive (e.g., Windhorst et al., 2022). While this makes it a valuable probe of interplanetary dust within our Solar System, it also poses a major challenge: zodiacal light is the brightest foreground that must be subtracted to study the faint universe beyond. Accurately modeling zodiacal light helps us understand the physical and dynamic properties of interplanetary dust, improves measurements of diffuse light from both the Milky Way and distant galaxies, and is essential for isolating the extragalactic background light (EBL). Reliable models are also key for predicting foreground contamination in sky surveys and offer insights into how debris disks may behave in exoplanetary systems.

The brightness and structure of zodiacal light depend on several factors: the observer's position along Earth's orbit, the viewing geometry relative to the Sun, and the wavelength of observation. Over the years, many models have been developed to describe zodiacal light, including phenomenological models (Kelsall et al., 1998; Wright, 1998; Hahn et al., 2002; Rowan-Robinson & May, 2013) and physically motivated

dynamical models (Jones & Rowan-Robinson, 1993; Nesvorný et al., 2010; Poppe, 2016). Spectral models often approximate zodiacal light as a reddened solar spectrum (Leinert et al., 1998; Aldering, 2001), and absolute brightness has been measured through both direct photometry (Levasseur & Blamont, 1973; Leinert et al., 1981; Hanner et al., 1976; Matsumoto et al., 2018; Krick et al., 2012) and spectroscopy (Hanzawa et al., 2024; Tsumura et al., 2013, 2010; Reach et al., 2003; Korngut et al., 2022).

Zodiacal light is just one component of the total sky surface brightness (sky-SB) observed from space, alongside diffuse Galactic light (DGL) and the EBL. DGL originates from starlight in our Milky Way that is scattered or re-emitted by interstellar dust. It is brightest toward the Galactic center and is typically isolated by subtracting a zodiacal light model (e.g., Brandt & Draine, 2012; Ienaka et al., 2013; Arai et al., 2015; Sano et al., 2016; Kawara et al., 2017; Onishi et al., 2018; Chellew et al., 2022). Accurate zodiacal light modeling is thus a prerequisite for properly characterizing DGL.

The faintest component of the sky-SB, the EBL, is the accumulated light from all stars, galaxies, dust, and AGN throughout cosmic history (e.g., Franceschini et al., 2008; Hauser & Dwek, 2001; Domínguez et al., 2011; Finke et al., 2010; Andrews et al., 2018). It provides critical insights into galaxy formation, black hole growth, and dust evolution over time. However, its direct measurement is notoriously difficult, requiring the careful subtraction of bright foregrounds like zodiacal light and DGL (e.g., Driver, 2021).

EBL predictions from known galaxy counts, known as integrated galaxy light (IGL), generally fall short of direct EBL measurements by an order of magnitude (e.g., Driver et al., 2016). This persistent discrepancy raises the possibility that current

zodiacal light models may be underestimating a faint, isotropic component of zodiacal light, thus contributing to an excess known as "diffuse light" (e.g., Windhorst et al., 2022; Carleton et al., 2022; O'Brien et al., 2023; McIntyre et al., 2025). Even a small modeling error, amounting to ∼5% of the total ZL, could mimic a significant EBL excess. New Horizons data, collected beyond 40 AU where zodiacal light is negligible, report a much lower direct measurement of EBL (Postman et al., 2024) that better matches IGL predictions, reinforcing this concern.

Aside from measurements of DGL and EBL, understanding our own zodiacal cloud is essential to interpreting exozodiacal light around other stars. As future missions (e.g., Habitable Worlds) aim to characterize Earth-like planets in nearby systems, it is critical to account for foreground dust in those systems, which may be analogous to our own. Our ability to detect and characterize exoplanets may ultimately depend on how well we understand the light scattered by our Solar System's dust (e.g., Currie et al., 2025; Hom et al., 2024; Ollmann et al., 2023; Bryden et al., 2023; Guyon et al., 2006; Stark et al., 2014).

Finally, accurate zodiacal light modeling is crucial for preparing efficient and reliable sky surveys. Many space-based telescopes (e.g., HST, JWST, Roman, Euclid, SPHEREx) operate in wavelengths where zodiacal light dominates the photon budget, and their science return depends on our ability to model and predict this foreground. Many recent works adapt the Kelsall et al. (1998) or Wright (1998) models for use in foreground modeling in the optical and near-IR (e.g., Rigby et al., 2023; San et al., 2024; Crill et al., 2025). These three-dimensional models make use of daily imaging from NASA's Cosmic Background Explorer (COBE) Diffuse Infrared Background Experiment (DIRBE).

The Kelsall model was first zodiacal light model to fully leverage data from COBE

DIRBE, with the end goal to constrain the cosmic infrared background. By analyzing the annual modulation of zodiacal light brightness across the sky, the Kelsall model produced a three-dimensional, parameterized description of the interplanetary dust cloud, spanning wavelengths from 1.25 to 240 μm.

Wright (1998) proposed an alternative model, also based on COBE DIRBE data, under the assumption that the faintest 25 μm sky-SB at high ecliptic latitudes originates entirely from zodiacal light. This approach is sensitive to any isotropic component in the zodiacal light signal. However, recent comparisons show that the Wright model likely overestimates the zodiacal light contribution seen by HST (Carleton et al., 2022). Nonetheless, together, these early models laid the groundwork for modern zodiacal studies but were designed primarily for infrared wavelengths. These models were optimized for DIRBE's nominal wavelengths only: 1.25, 2.2, 3.5, 4.9, 12, 25, 70, 100, 140, and 240 μm. At these wavelengths, these models are still considered the state-of-the-art.

Nonetheless, since the Kelsall and Wright models were originally tuned to the DIRBE instrument's bandpasses (the shortest of which is 1.25 μm), these models are not easily extrapolated to optical wavelengths. To date, no three-dimensional zodiacal light model exists that is optimized specifically for the UV–optical regime. Improved zodiacal light models are urgently needed, not only to enable accurate EBL measurements, but also to better understand exozodiacal light, and support the science goals of current and future space observatories.

4.1.2 The SKYSURF Project

The SKYSURF[13] project (Windhorst et al., 2022) offers a powerful and data-rich approach to modeling zodiacal light and separating it from other diffuse sky components. SKYSURF is a Hubble Space Telescope (HST) archival program designed to measure the sky-SB and disentangle its main contributors: zodiacal light, DGL, and EBL. By leveraging the vast HST archive, spanning multiple instruments, filters, and thousands of independent sky pointings, SKYSURF provides an unprecedented view of how these components vary across the sky at optical wavelengths. Thus far, SKYSURF has produced seven publications (Windhorst et al., 2022; Carleton et al., 2022; O'Brien et al., 2023; Kramer et al., 2022; Bhatia et al., 2024; McIntyre et al., 2025; Conrad et al., 2025), including publicly released measurements, catalogs, and code. These data serve as a foundation for new models of zodiacal light and DGL, enabling improved constraints on EBL and diffuse light.

Sky-SB measurements were published in O'Brien et al. (2023). A key next step is to isolate and quantify the individual contributions of zodiacal light, DGL, and EBL from the observed sky-SB. However, progress has been limited by the lack of a zodiacal light model specifically tuned to optical wavelengths. Most existing models, including those by Kelsall and Wright, were developed for infrared datasets and rely on assumptions that break down below 1.25 μm. JWST modeling of the sky-SB (Rigby et al., 2023) has shown that these models underperform at shorter wavelengths, highlighting the need for an updated optical-optimized model. In this paper, we present a new zodiacal light model built upon the structure of the widely used Kelsall et al. (1998) framework, but calibrated and optimized for optical observations.

[13] http://skysurf.asu.edu

4.2 The Parametric Zodiacal Light Model

The widely used zodiacal light model developed by Kelsall et al. (1998) remains a foundational model in foreground analysis, and is used as a baseline for the modeling in this paper. DIRBE's daily motion sampled zodiacal light at a variety of solar elongations (angles relative to the Sun), enabling constraints on the albedo and scattering phase function. The phase function describes the angular probability of light scattering off a dust particle, effectively acting as a probability density function for scattering angles.

The Kelsall zodiacal light intensity follows as

$$Z_\lambda(\hat{\mathbf{p}}, t) = \sum_c \int n_c(X, Y, Z)[A_\lambda F_\lambda^\odot \Phi_\lambda(\theta) + (1 - A_\lambda) E_\lambda B_\lambda(T) K_\lambda(T)] ds. \tag{4.1}$$

The zodiacal dust cloud has three main components (denoted with c): a smooth cloud, dust bands, and a circumsolar ring. Each has its own density ($n_c(X, Y, Z)$) for position (X, Y, Z) within the cloud. The albedo (A_λ), solar flux ($F_\lambda^\odot$), phase function (Φ_λ), and emissivity (E_λ) are optimized for each DIRBE nominal wavelength. $B_\lambda(T)$ is the blackbody thermal radiance function. $K_\lambda(T)$ is a DIRBE color-correction factor from the COBE Diffuse Infrared Background Experiment DIRBE Explanatory Supplement[14] used to make the model values consistent with the DIRBE datebase. The dust grain temperature T is assumed to vary with distance from the Sun as $T(R) = T_0 R^\delta$, with a best fit of $\delta = 0.467$. These values are integrated over the line-of-sight (ds), where the observer in the DIRBE model is Earth as it orbits around

[14]https://lambda.gsfc.nasa.gov/data/cobe/dirbe/doc/des_v2_3.pdf

the Sun. Therefore, the zodiacal light intensity is dependent on time (t) and viewing direction ($\hat{\mathbf{p}}$).

This model optimized various parameters of each component of the dust cloud, including temperature, density, shape, and position. Their optimized values are shown in Tables 1 and 2 of Kelsall et al. (1998). We consider a majority of their parameters to be well optimized. In this work, we focus on optimizing the model specifically for optical wavelengths. The parameters that most strongly contribute to changes in optical intensity of zodiacal light based on viewing position are the scattering phase function and the albedo.

Because DIRBE observations were restricted to solar elongations of 94°± 30°, the model is poorly constrained at large backscattering angles, especially near 180°, where the optical phenomenon known as gegenschein appears (e.g., Roosen, 1970). In addition, the Kelsall model did not include any isotropic component (e.g., a spherical shell at > 1 AU). Since this model characterized the annual modulation of zodiacal light, any nearby isotropic components could not have been detected.

The Kelsall model assumes the albedo is zero for wavelengths greater than 3.5 μm. It also assumes that the emissivity is zero for wavelengths less than 3.5 μm. For this work, we will therefore ignore the emissivity. We slightly redefine the Kelsall function to be optimized for optical wavelengths as follows:

$$Zodi2025(\lambda, b, l, SA, t) = \sum_c \int n_c(X, Y, Z)[A(\lambda)F^{\odot}(\lambda)\Phi(\theta; \lambda)]ds, \tag{4.2}$$

where θ is the scattering angle.

4.2.1 A New Scattering Phase Function

Modifying the Kelsall phase function is key to creating a model that works at optical wavelengths. The Kelsall model defines the scattering phase function as follows:

$$\Phi(\theta;\lambda)(\theta) = N[C_{0,\lambda} + C_{1,\lambda}\theta + e^{C_{2,\lambda}\theta}]. \tag{4.3}$$

The phase function parameters $C_{0,\lambda}$, $C_{1,\lambda}$, and $C_{2,\lambda}$ were specifically fitted to the nominal DIRBE wavelengths (1.25, 2.2, 3.5, 4.9, 12, 25, 70, 100, 140, and 240 μm). However, this phase function formulation is non-linear. In other words interpolating between $C_{0,\lambda}$, $C_{1,\lambda}$, and $C_{2,\lambda}$ for various wavelengths does not yield reasonable solutions.

Figure 38 showcases the resulting phase function when $C_{0,\lambda}$, $C_{1,\lambda}$, and $C_{2,\lambda}$ are interpolated, as well as a more realistic phase function if the Kelsall phase function was instead linear. For this reason, it is impossible to reliably extend the Kelsall model beyond the nominal DIRBE wavelengths. For a more realistic (i.e., linear) phase function (shown in green in Figure 38), we simply interpolate the y-values between both curves. This could be done to interpolate between DIRBE's norminal wavelengths and attain a reliable zodiacal light estimate. However, unless the evolution of the shape of the phase function with wavelength is known, it is difficult to do extrapolate correctly for wavelengths less than 1.25 μm (DIRBE's shortest nominal bandpass).

To provide a better interpolation and extrapolation, we follow Hong (1985) and replace the Kelsall phase functions with functions that are the weighted sum of 3 Henyey-Greenstein (HG) functions (Henyey & Greenstein, 1941). The benefit of this approach is that is allows the forward and backward scattering strengths to be adjusted separately for each wavelength. As such, the Hong (1985) formulation has

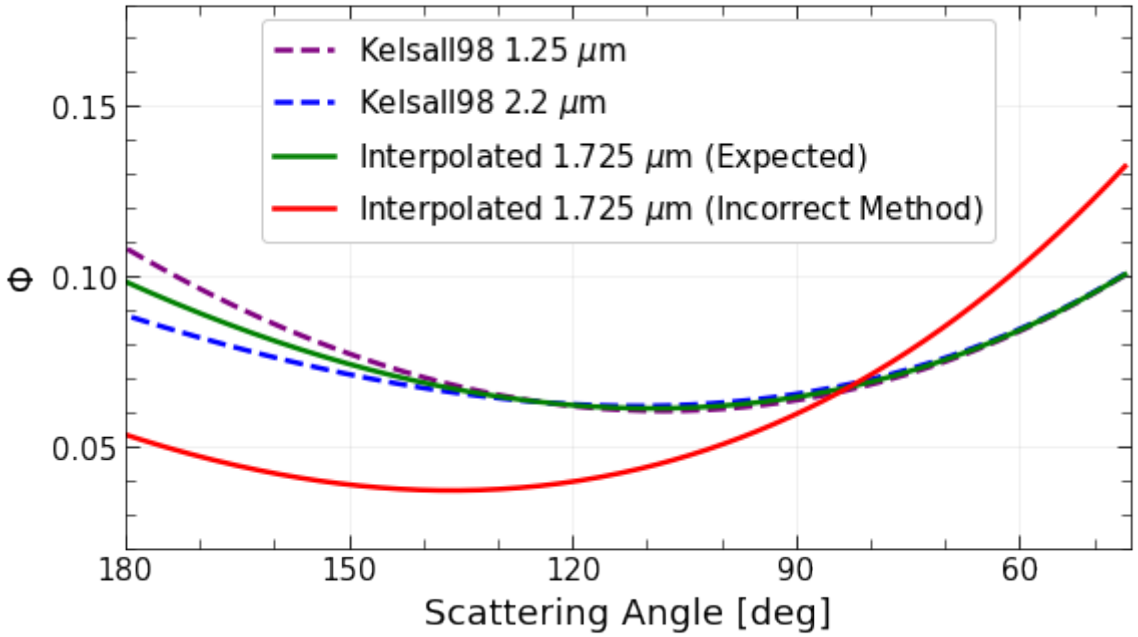

Figure 38. Comparison of scattering phase functions from the Kelsall model. The dashed lines show phase functions at DIRBE's nominal wavelengths of 1.25 μm (blue) and 2.2 μm (purple). The red curve illustrates an incorrect phase function at 1.725 μm, obtained by directly interpolating the model coefficients ($C_{0,\lambda}$, $C_{1,\lambda}$, and $C_{2,\lambda}$) between 1.25 μm and 2.2 μm. The green curve demonstrates a more accurate approach, where the phase function at 1.725 μm is obtained by interpolating directly between the two original phase function curves rather than their coefficients. This method yields a realistic representation, although accurately applying it below 1.25 μm remains challenging without knowing the wavelength dependence on the shape of the phase function.

been widely used to model the scattering of interplanetary dust. The new scattering phase function used in this work has the following form:

$$\Phi(\theta;\lambda) = \sum_{i=1}^{i=3} w_i(\lambda) \frac{1 - g_i(\lambda)^2}{[1 + g_i(\lambda)^2 - 2g_i(\lambda)\cos(\theta)]^{3/2}}. \tag{4.4}$$

In this formulation, we define $i = 1$ to correspond to a forward-scattering component, $i = 2$ to correspond to the backward-scattering component, and $i = 3$ to correspond to the gengenschein component.

4.3 Data Overview

To optimize the zodiacal light model, particularly the scattering phase function and albedo, we use sky-SB measurements from the SKYSURF project (O'Brien et al., 2023; McIntyre et al., 2025). SKYSURF developed an algorithm that accurately measures the sky-SB in HST images with better than 1% precision, with total uncertainties (including flat-fielding, dark current, and bias corrections) below 4%. These measurements agree well with both predictions and independent observations, making them among the most reliable all-sky datasets for this wavelength range.

The public SKYSURF release contains over 150,000 sky-SB measurements spanning the full HST wavelength range, from 0.2 to 1.6 μm. These measurements cover a wide range of Sun angles (from 80° to 180°), allowing HST to probe a broad range of scattering angles. This is crucial for constraining how the zodiacal light phase function and albedo evolve with wavelength, especially into the ultraviolet, where few other measurements exist. Each measurement includes an uncertainty that accounts for algorithmic errors, flat-fielding, photometric zeropoints, WFC3/IR nonlinearity, bias, dark current, post-flash, and thermal dark contributions (see McIntyre et al., 2025).

To ensure data quality, SKYSURF implements a detailed flagging system to identify reliable measurements for studying zodiacal light and EBL. Following O'Brien et al. (2023), we exclude all sky-SB values flagged as unreliable. Flags are applied for the following conditions:

- More than 30% of the image is contaminated by large, discrete galaxies or stars, as determined by the SKYSURF sky-SB algorithm.
- The sky-SB rms is higher than 2.5× the expected rms, based on Gaussian and Poisson noise.

- The image was flagged during manual inspection.
- Exposure taken within 20°of the Galactic plane.
- Exposure taken with an Earth Limb angle of less than 40°.
- Exposure taken with a Sun Altitude greater than 0°.
- Exposure taken with a Sun Angle less than 80°.
- Exposure taken with a Moon Angle less than 50°.
- Image taken close to large (in terms of spatial sky area), nearby galaxies.
- Exposure significantly affected by persistence.

Because many HST observations revisit the same sky positions, either to build depth or monitor variability, we avoid biasing the model toward oversampled regions by restricting our sample to "independent pointings". We define a pointing as independent if it is taken at least 10 arcminutes and 2 days apart from any other observation.

However, revisiting a region does improve sky-SB measurement precision. So, for dependent pointings (those close in sky position and time), we group them and compute a single representative measurement. For each group, we take the median values of sky position (ecliptic and Galactic coordinates), day-of-year, sky-SB, and Sun angle. The group's uncertainty is the median individual uncertainty divided by the square root of the number of images in the group. This reduces statistical noise without over-weighting heavily observed fields.

We also apply thermal dark corrections using the refined estimates from McIntyre et al. (2025), which are based on HST's pick-off arm temperature and empirical models of the primary and secondary mirror thermal emission. These thermal dark values are listed in Table 15 and are subtracted from the original SKYSURF sky-SB values.

The final number of independent, quality-controlled sky-SB measurements used

for this zodiacal light analysis is a few dozen to many hundred, depending on the filter, and is summarized in Table 16.

Filter	Thermal Dark (e/s/px)	Thermal Dark (MJy/sr)
F098M	0.0044	0.0023
F105W	0.0044	0.0013
F110W	0.0047	0.0008
F125W	0.0047	0.0014
F140W	0.0217	0.0054
F160W	0.0820	0.0327

Table 15. Updated thermal dark corrections (from McIntyre et al. (2025)) used in this work.

4.4 Diffuse Galactic Light Estimates

DGL consists of the emission and scattering from the Milky Way's interstellar medium, and can be highly uncertain at optical wavelengths due to uncertainties in the scattering properties of DGL. Measuring DGL directly can be difficult since zodiacal light is almost always a foreground contaminant. Most studies utilize the Kelsall model or other infrared-based models to subtract zodiacal light before doing DGL estimation (Brandt & Draine, 2012; Ienaka et al., 2013; Arai et al., 2015; Sano et al., 2016; Kawara et al., 2017; Onishi et al., 2018; Chellew et al., 2022), which can lead to high uncertainties in the absolute brightness of DGL at optical wavelengths. Although we expect DGL estimates to be less than $\sim$0.003 MJy sr^{-1} for most SKYSURF images used in this work (Carleton et al., 2022), it is still important that careful consideration be taken into account when estimating DGL.

To obtain an optical DGL measurement for each SKYSURF pointing, we follow the methods presented in Postman et al. (2024). This work obtained measurements of

Camera	Filter	Wavelength [μm]	Number
WFC3/UVIS	F336W	0.34	107
WFC3/UVIS	F390W	0.39	84
WFC3/UVIS	F438W	0.43	25
WFC3/UVIS	F475X	0.48	14
WFC3/UVIS	F475W	0.47	57
WFC3/UVIS	F555W	0.52	22
WFC3/UVIS	F606W	0.58	253
WFC3/UVIS	F625W	0.62	15
WFC3/UVIS	F775W	0.76	13
WFC3/UVIS	F850LP	0.92	19
WFC3/UVIS	F814W	0.80	289
ACS/WFC	F435W	0.43	225
ACS/WFC	F475W	0.47	190
ACS/WFC	F555W	0.53	42
ACS/WFC	F606W	0.58	726
ACS/WFC	F625W	0.63	72
ACS/WFC	F775W	0.76	255
ACS/WFC	F814W	0.80	1258
ACS/WFC	F850LP	0.91	543
WFC3/IR	F098M	0.98	71
WFC3/IR	F105W	1.04	353
WFC3/IR	F110W	1.12	214
WFC3/IR	F125W	1.24	357
WFC3/IR	F140W	1.41	336
WFC3/IR	F160W	1.54	820

Table 16. The HST filters used to model zodiacal light in this work. We list the HST camera, the filter name, and the corresponding pivot wavelength. The final column shows the number of SKYSURF sky-SB measurements in that filter used for model fitting.

the cosmic optical background using the Long-Range Reconnaissance Imager (LORRI) onboard NASA's New Horizons spacecraft. At nearly 57 AU from the sun, there is virtually no zodiacal light. This means that any empirical methods to estimate DGL with New Horizons will be independent from highly uncertain zodiacal light models. It is standard to correlate optical DGL emission with 100 μm intensity (Arai et al., 2015; Brandt & Draine, 2012; Guhathakurta & Tyson, 1989; Ienaka et al., 2013; Kawara

et al., 2017; Onishi et al., 2018; Symons et al., 2023; Witt et al., 2008; Zagury et al., 1999). However, in developing an independent DGL estimator, Postman et al. (2024) found that 350 μm and 550 μm were better indicators. They suggest that this is due to variations in dust temperature: the 100 μm band falls on the shorter-wavelength side of the peak for a 20 K blackbody spectrum, making it more sensitive to temperature changes compared to the 350 μm and 550 μm bands. With 24 fields, they empirically related Planck 350 μm and 850 μm imaging and their measured DGL, where their measured DGL is assumed to be the total sky-SB they measure with all other known components subtracted. They find the following relationship for the LORRI bandpass (centered at $\sim$0.6 μm):

$$\begin{aligned}\mathrm{DGL}_{\mathrm{Postman}}(b_{\mathrm{gal}}, l_{\mathrm{gal}})\ [\mathrm{nW\ m^{-2}\ sr^{-1}}] = \\ g(b_{\mathrm{gal}})[48.01\ I_{550}(l_{\mathrm{gal}}, b_{\mathrm{gal}}) + \\ 0.96\left(\frac{I_{550}(b_{\mathrm{gal}}, l_{\mathrm{gal}})}{I_{350}(b_{\mathrm{gal}}, l_{\mathrm{gal}})} - 3.66\right)],\end{aligned} \quad (4.5)$$

$$g(b_{\mathrm{gal}}) = \frac{1 - 0.67\sqrt{\sin(|b_{\mathrm{gal}}|)}}{0.376}. \quad (4.6)$$

where $(b_{\mathrm{gal}}, l_{\mathrm{gal}})$ are galactic coordinates. I is the CIB-subtracted FIR intensity: $I(\lambda) - \mathrm{CIB}_{\mathrm{Anisotropies}}(\lambda) - \mathrm{CIB}_{\mathrm{Monopole}}$. The Planck High Frequency Instrument (HFI) maps (Planck Collaboration et al., 2020b) provide the FIR intensities at 350 μm and 550 μm. The $\mathrm{CIB}_{\mathrm{Anisotropies}}(\lambda)$ maps are provided by Planck Collaboration et al. (2016b), and utilize the generalized needlet internal linear combination (GNILC; see Remazeilles et al. 2011) method to separate CIB anisotropies from thermal dust emission in the HFI maps. These are essentially a field-dependent correction to the CIB monopole, and remains necessary when working with HSTs small field of view.

$\mathrm{CIB}_{\mathrm{Monopole}}$ is the CIB monopole as measured by recalibrating Planck HFI maps, separating the Galactic emission using the HI column density, and determining the CIB monopole by extrapolating the HI density to zero (Odegard et al., 2019): 0.576 MJy sr^{-1} for 350 μm and 0.371 MJy sr^{-1} at 550 μm.

The function $g(b_{\mathrm{gal}})$ accounts for changes in scattering effects based on galactic latitude (b_{gal}) during the conversion of thermal emission intensity into optical intensity, where scattering is more significant (e.g., Jura, 1979; Zemcov et al., 2017). Since the scattering properties change as a function of wavelength, we rewrite $g(b_{\mathrm{gal}})$ following Zemcov et al. (2017):

$$g(\lambda, b_{\mathrm{gal}}) = \frac{1 - 1.1 \times f_\lambda \times \sqrt{\sin(|b_{\mathrm{gal}}|)}}{1 - 1.1 \times f_\lambda \times \sqrt{\sin(60^\circ)}}. \tag{4.7}$$

The scattering asymmetry factor (f_λ) represents the degree of forward scattering. It is defined as $f_\lambda \equiv \cos\theta$, where θ denotes the scattering angle from the forward direction (e.g., Sano et al., 2016). This indicates that $f_\lambda = 0$ represents isotropic scattering and $f_\lambda = 1$ represents completely forward scattering. We normalize $g(b_{\mathrm{gal}})$ at a galactic latitude of 60° so that $g(b_{\mathrm{gal}})$ only accounts for the relative changes in scattering properties.

Weingartner & Draine (2001) evaluate f_λ (they label it as g) for several size distributions for carbonaceous and silicate grain populations in different regions of the Milky Way, LMC, and SMC. Their Figure 15 shows how f_λ varies as a function of wavelength. As the scattering properties of DGL vary as a function of wavelength, we must also adjust f_λ and $g(b_{\mathrm{gal}})$ accordingly. We follow Figure 15 of Weingartner & Draine (2001) for f_λ.

Equation 4.5 is specifically designed for the LORRI instrument. To apply this

approach to the HST bandpasses, we first convolve both the LORRI bandpass and each HST bandpass with a reference DGL spectrum. By comparing the results, we can adjust Equation 4.5 based on how the LORRI instrument relates to the HST bandpasses. This process is represented in Figure 39. The reference DGL spectrum is from Brandt & Draine (2012). This spectrum is created using sky spectra from the Sloan Digital Sky Survey (SDSS), and therefore only extends from ~ 0.4 to 0.9 μm. For longer wavelengths, we logarithmically interpolate between the Brandt & Draine (2012) spectrum and the AKARI (first Japanese infrared astronomical satellite) spectrum from Tsumura et al. (2013), which begins ~ 0.8 μm. We normalize the spectrum so the LORRI result is defined to be equal to 1.0. The DGL measurement for each HST filter is scaled according to the blue points in Figure 39. Our final DGL estimator is therefore

$$\begin{aligned}\mathrm{DGL}(\lambda, b_{\mathrm{gal}}, l_{\mathrm{gal}})\ [\mathrm{nW\ m^{-2}\ sr^{-1}}] = \\ g(\lambda, b_{\mathrm{gal}})[48.01\ I_{550}(l_{\mathrm{gal}}, b_{\mathrm{gal}}) + \\ 0.96\left(\frac{I_{550}(b_{\mathrm{gal}}, l_{\mathrm{gal}})}{I_{350}(b_{\mathrm{gal}}, l_{\mathrm{gal}})} - 3.66\right)] \times A(\lambda) \quad (4.8)\end{aligned}$$

$A(\lambda)$ is the filter-dependent scale factor from Figure 39. I_{350} and I_{550} are estimated using the Planck HFI `HEALPix`[15] maps. We isolate a circular area with a diameter close to that of HST's field of view (202″ for ACS/WFC, 162″ for WFC3/UVIS, 130″ for WFC3/IR) in each `healpy` map at the location of the SKYSURF image.

Uncertainties in DGL are taken from Postman et al. (2024) (average from their Table 4): 1.03 nW m^{-2} sr^{-1}. This uncertainty represents the rms obtained in their empirical DGL calculation, and was calculated using 10,000 Monte Carlo realizations.

[15]https://healpy.readthedocs.io/en/latest/

We estimate the uncertainty in the Brandt & Draine (2012) spectrum using Figure 3 from their paper: $\sigma(\lambda I_\lambda/\nu I_\nu(100\mu\text{m})) \simeq 0.01$. This uncertainty represents $\sim 6\%$ of the peak of the DGL spectrum (at $\lambda I_\lambda/\nu I_\nu(100\mu\text{m}) \simeq 0.17$). Therefore, we adopt an uncertainty in the DGL spectrum to be 6%.

Our total DGL is a combination of two independent estimators: the Postman et al. (2024) measurement of DGL multiplied by a scale factor A. The uncertainties for these two estimators is described in the previous paragraph. Therefore, the final uncertainty in DGL is:

$$\sigma_{\text{DGL}} \quad [\text{nW m}^{-2}\text{ sr}^{-1}] \quad = \quad |\text{DGL}|\sqrt{\left(\frac{1.03}{\text{DGL}_{\text{Postman}}}\right)^2 + \left(\frac{0.025 \times \text{DGL}}{A}\right)^2}.$$

We ignore all images taken within 20 degrees of the galactic plane (see Section 4.3), and therefore, the average DGL uncertainty is $\sim$0.0003 MJy sr^{-1}. The uncertainty on DGL is added in quadrature with the uncertainty in the sky-SB, calculated in O'Brien et al. (2023), where the uncertainty in the sky-SB dominates, making the average uncertainty in the Sky-SB$-$DGL $\simeq 0.005$ MJy sr^{-1}.

We compare our DGL estimates to other works in Figure 40. Since most studies are correlated with 100 μm intensity, we also compare our measured DGL intensity with respect to 100 μm maps. We utilize a combination of the Improved Reprocessing of the IRAS Survey (IRIS) maps (Miville-Deschênes & Lagache, 2005) and the Schlegel, Finkbeiner, and Davis (SFD Schlegel et al., 1998) map released in the Planck Data Release 2 (Planck Collaboration et al., 2014). Specifically, we use the 100 μm combined IRIS+SDF map with no point sources. In general, the methods described in this work agree well with other studies. The scatter in DGL levels shown in Figure 4 across different studies is likely due to variations in the sky regions being observed, as

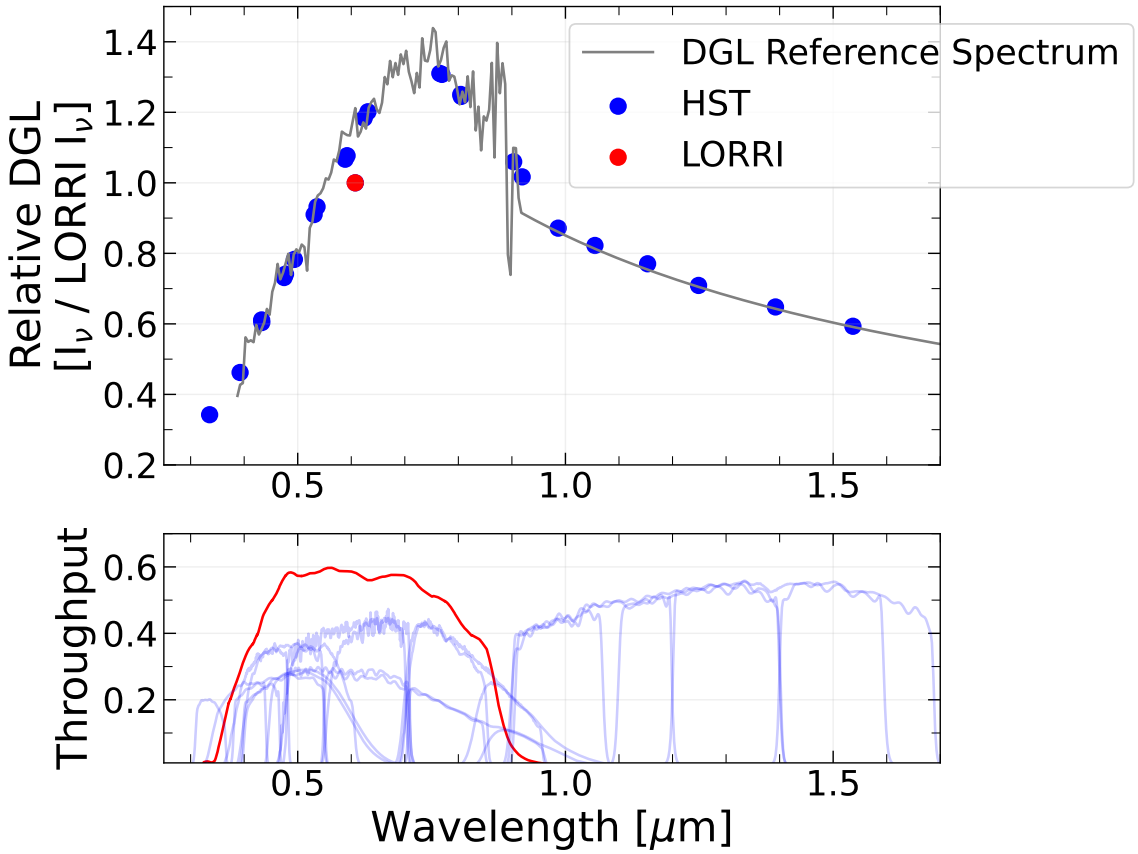

Figure 39. DGL surface brightness for all HST bandpasses (blue), relative to the LORRI bandpass (red). The reference spectrum (grey solid line) is from Brandt & Draine (2012) for wavelengths between 0.4 μm to 0.9 μm and then transitions logarithmically to Tsumura et al. (2013), which begins at 1.8 μm. The bottom panel illustrates each instrument's bandpass, while the top panel shows the result of convolving these bandpasses with the reference spectrum. The entire spectrum is normalized so the LORRI surface brightness equals 1.0 (red point). As shown in Equation 4.8, to estimate DGL, we multiply the LORRI-based measurement (Equation 4.5) by the corresponding scale factor (A_λ) for each HST filter, represented by the blue points.

different areas have different DGL contributions and 100-micron calibrations. This is especially true for our data points, as each represents a different combination of regions of the sky. Additionally, since we did not use 100 μm maps for calibration, there will naturally be some scatter compared to the 100-micron map.

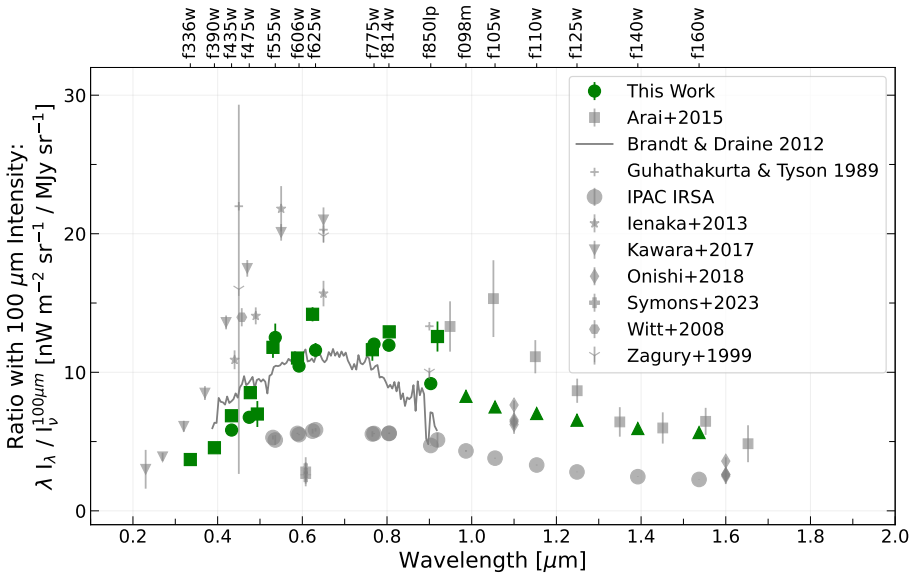

Figure 40. Ratio of DGL intensity (nW m^{-2} sr^{-1}) to 100 μm intensity (MJy sr^{-1}). DGL estimates from this work are shown as large green circles, where HST's three main cameras are distinguished by different markers: green triangles for WFC3/IR, green squares of ACS/WFC, and green circles for WFC3/UVIS. The grey points represent estimates from various other studies, where DGL is typically calibrated with 100 μm maps. The SKYSURF project originally used the IPAC IRSA Background Model to estimate DGL, shown as large grey circles. The 100 μm intensity for both the IPAC IRSA Background Model and this study's comparisons come from the IRIS+SFD maps released in Planck Data Release 2. The error bars represent the standard error. For this green points, the error bar is calculated as the standard deviation of the measurements divided by $\sqrt{N}$, where N is the number of independent pointings. Independent pointings are defined as those that are separated by more than $10'$ from each other.

4.5 Zodiacal Light Modeling Technique

Our goal is to modify the Kelsall model so that it can be properly implemented at any wavelength $0.3 - 1.6$ μm. Within the Kelsall model itself, this involves updating the solar irradiance spectrum ($F_\lambda^\odot$), the scattering phase function, and the albedo. The scattering phase function and the albedo will be optimized with HST data, while the solar irradiance spectrum is pulled from recent literature, as described below.

4.5.1 Updating the Solar Irradiance Spectrum

The current Kelsall model has individual solar irradiance measurements for every DIRBE band. Therefore, for this model to apply to HST filters, we need to provide solar irradiance values for all HST bands. We utilize the Hybrid Solar Reference Spectrum (HSRS) from Coddington et al. (2021), which present new solar irradiance reference spectrum representative of solar minimum conditions. They utilize a combination of solar spectral irradiance measurements from NASA's Total and Spectral Solar Irradiance Sensor (TSIS-1) (Richard et al., 2024) and the CubeSat Compact SIM. The TSIS-1 HSRS spans $202 - 2730$ nm at 0.01 to ~ 0.001 nm spectral resolution with uncertainties of 0.3% between 460 and 2365 nm and 1.3% at wavelengths outside that range. In Figure 41, we show the TSIS-1 HSRS and the resulting spectral irradiance values for each HST filter.

Another recent and robust solar irradiance spectrum is that from Meftah et al. (2018). They provide a reference solar irradiance spectrum from the SOLSPEC instrument on the International Space Station (ISS). The instrument accurately measured solar spectral irradiance (SSI) from 0.1 to 3 μm, resulting in a high-resolution solar spectrum with an average absolute uncertainty of 1.26%. The spectrum has a varying spectral resolution between 0.6 and 9.5 nm (0.0006 and 0.0095 μm). When comparing this reference spectrum to the TSIS-1 HSRS reference spectrum, offsets are within 4% in any given filter. Therefore, the uncertainty in the solar irradiance for a particular bandpass is considered to be up to $\sim$3%. For a comparison with other reference spectra, refer to https://sunclimate.gsfc.nasa.gov/ssi-reference-spectra.

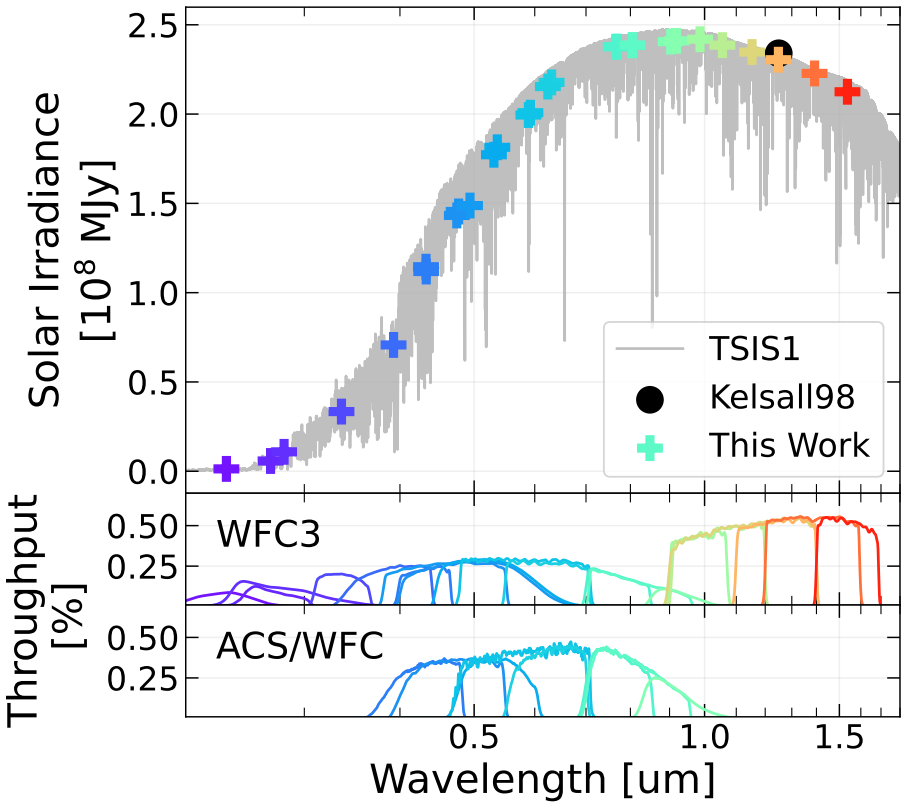

Figure 41. The reference solar spectrum used in this work (grey solid line) and the resulting spectral irradiance values used for each HST filter. The large black circle shows the solar irradiance value used in the original Kelsall model. The bottom two panels shows the filter throughput curves corresponding to each HST filter, with the filters for WFC3 shown on top and the filters for ACS/WFC shown beneath.

4.5.2 Fitting a New Phase Function and Albedo

The most critical component of the model update is the optimization of the scattering phase function and dust albedo across the wavelength range 0.3–1.6 μm. While the 3D spatial distribution of the interplanetary dust cloud is assumed to be well constrained by the Kelsall model, the brightness of zodiacal light across the sky is strongly modulated by the scattering phase function. Our goal is to derive updated

phase function parameters and albedos that best reproduce the observed SKYSURF sky-SB measurements.

As described in Section 4.3, we use sky-SB measurements from SKYSURF-4 (O'Brien et al., 2023), which include contributions from zodiacal light, DGL, and EBL. Since SKYSURF is primarily designed to constrain the EBL, we treat the EBL as a free parameter in our modeling. The DGL component is subtracted using the methods described in Section 4.4, and we assume its spatial and spectral properties are well-characterized. This leaves zodiacal light and any residual isotropic background (e.g., unmodeled EBL) as the remaining components to be modeled.

We define the observed zodiacal light intensity as:

$$Z(\lambda, b, l, \mathrm{SA}, t) \quad = \quad S(\lambda, b, l, \mathrm{SA}, t) \quad - \quad DGL(\lambda, b_{\mathrm{gal}}, l_{\mathrm{gal}}) \quad - \quad C(\lambda), \quad (4.9)$$

where λ is the wavelength, (b, l) are ecliptic coordinates, SA is the Sun Angle, t is the day of year, S is the measured sky-SB from O'Brien et al. (2023), and $C(\lambda)$ represents any remaining isotropic component. Although the EBL contributes to $C(\lambda)$, most of it is removed during measurement of the sky-SB, since most discrete stars and galaxies are ignored in this measurement. The residual EBL left in sky-SB measurements is estimated to be ~ 0.56 nW m^{-2} sr^{-1} (< 0.0002 MJy sr^{-1}; Carleton et al. 2022).

The uncertainty in Z is computed as:

$$\sigma_Z = \sqrt{\sigma_S^2 + \sigma_{\mathrm{DGL}}^2}, \quad (4.10)$$

where σ_S and σ_{DGL} are the uncertainties in the sky-SB and DGL estimates, respectively. We do not include uncertainties for $C(\lambda)$, as it is treated as a free parameter.

Our fitting pipeline proceeds in three steps:

Parameter	Prior
Isotropic Scale $C(\lambda)$	[0,0.3]
Albedo	[-∞, ∞]
g_1	[0,1]
g_2	[-1,0]
g_3	[-1,-0.6]
w_1	[0,1]
w_2	[0,1]
w_3	[0,1]

Table 17. Uniform priors used for zodiacal light model parameter fitting.

4.5.2.1 Step 1: Joint Fit of Albedo and Phase Function Parameters

We jointly fit the albedo and the six phase function parameters (g_1, g_2, g_3, w_1, w_2, w_3) defined in Equation 4.4, using the model defined in Equation 4.2. We use the `emcee` Markov Chain Monte Carlo (MCMC) sampler (Foreman-Mackey et al., 2013) to maximize the log-likelihood:

$$\log \mathcal{L} = -\frac{1}{2} \sum \frac{(Z - Zodi2025)^2}{\sigma_Z^2} - \frac{1}{2} \sum \ln(2\pi\sigma_Z^2), \tag{4.11}$$

where Zodi2025 is the model prediction for zodiacal light.

Our priors on the free parameters are shown in Table 17. We utilize these priors for both steps 1 & 2 of our fitting pipeline.

The phase function is required to integrate to 1 over 4π steradians:

$$\int_0^{2\pi} \int_0^{\pi} \Phi(\theta; \lambda) \sin(\theta) d\theta d\phi = 1. \tag{4.12}$$

Because the Henyey-Greenstein function lacks a closed-form integral, we compute this numerically using `scipy.integrate.simpson` (Virtanen et al., 2020). We apply a Gaussian prior centered at 1 with a standard deviation of 0.001.

For each HST filter, we use 25 MCMC walkers and run for 27,000 iterations. The first 15,000 steps are discarded as burn-in, although most filters converge within 1,000

iterations (verified by visual inspection). No other priors are applied. This step yields posterior distributions for the eight parameters (albedo, g_i, w_i, and $C(\lambda)$) per filter. Since the phase function and albedo are correlated (Equation 4.2), we extract the best-fit albedos and fit a linear trend across wavelength to define a consistent albedo curve. The reduced chi-squared statistic for our linear albedo relation, relative to the individual best-fit albedos for each filter, is $\chi^2_\nu = 1.06$. This best-fit linear albedo relation is used as input in Step 2.

4.5.2.2 Step 2: Refined Fit of Phase Function Parameters

We repeat the fitting procedure from Step 1, this time fixing the albedo to the best-fit wavelength-dependent curve obtained above. Fixing the albedo ensures that correlations between the albedo and the intensity of the phase function do not influence final best fits. We again use `emcee` to sample the posterior distributions of the six phase function parameters and $C(\lambda)$. For each filter, wee use 25 walkers for 4,000 iterations, with a burn-in period of 3,000 steps. Most filters converge within 500 iterations. No priors are applied beyond the normalization requirement for the phase function. The resulting median values of the phase parameters per filter are shown in Figure 43.

4.5.2.3 Step 3: Wavelength Dependence of Phase Function Parameters

Finally, we fit wavelength-dependent trends to the six phase function parameters derived in Step 2. We assume a linear relation with wavelength for g_1, g_2, w_1, and w_2. We assume constant values for g_3 and w_3 (i.e., wavelength-independent gegenschein

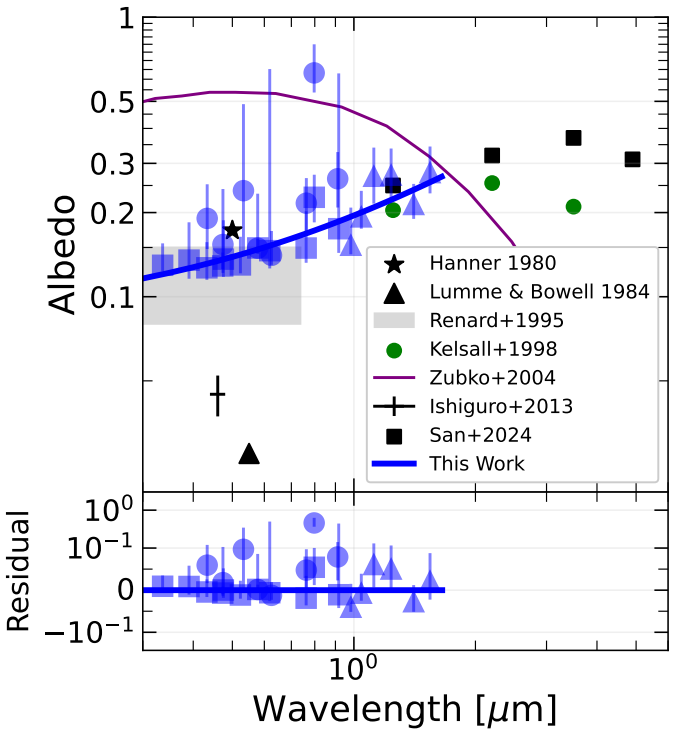

Figure 42. Albedo measurements from this work (solid blue line) compared to values from previous studies. Blue points with error bars show the best-fit albedos in each HST filter. The error bars represent the 68.27th-percentile distribution from the posterior. Different marker shapes represent different HST cameras: squares represent WFC3/UVIS, circles represent ACS/WFC, and triangles represent WFC3/IR. For reference, the green data points (solid circles) show the original albedo model from Kelsall et al. (1998). Black points show albedo measurements from other studies: Hanner et al. (1974) (Helios A and Pioneer 10), Lumme & Bowell (1985) (using polarimetric data), Renard et al. (1995) (using nodes of lesser uncertainty method), Ishiguro et al. (2013) (from the WIZARD instrument), and San et al. (2024) (a reanalysis of COBE/DIRBE data). The first two report geometric albedos, which are converted to Bond albedos for this comparison. The purple curve shows the modeled albedo of interstellar dust from Zubko et al. (2004). In the bottom panel, we show the best fit albedo for each individual HST filter (blue markers) with the linear fit (solid blue line) subtracted.

components). We again enforce phase function normalization using a Gaussian prior (mean 1, $\sigma = 0.001$) and sample the following likelihood:

$$\log \mathcal{L} = -\frac{1}{2} \sum_{\lambda} \frac{(p_\lambda - P(\lambda))^2}{\sigma_p^2} - \frac{1}{2} \sum_{\lambda} \ln(2\pi\sigma_p^2), \tag{4.13}$$

where p_λ is the median posterior value from Step 2, σ_p is the 68.27^{th} percentile width, and $P(\lambda)$ is the fit model. We use 30 walkers for 3,000 iterations with a burn-in of 1,000. Most parameters converge within 500 iterations.

Our linear fits are based only on filters with more than 300 independent pointings (see Section 4.3) to ensure statistical robustness. This results in utilizing the filters with the lowest uncertainties within their wavelength coverage, as shown in Figure 46.

4.6 Results

The final albedo values are shown as the solid blue curve in Figure 42. The final phase function parameters are shown as solid curves in Figure 43. Both of these figures show the best fits from each HST filter individually, where the solid curves represent linear fits so the best fits as a function of wavelength. These lines are fit so that this model can be applicable to any optical wavelength. The final relations are:

$$\text{Albedo} = 0.11298 \times \lambda + 0.08231 \tag{4.14}$$

$$g_1 = g_1 = 0.24958 \times \lambda + 0.11571 \tag{4.15}$$

$$g_2 = 0.05428 \times \lambda + -0.30864 \tag{4.16}$$

$$g_3 = -0.87036 \tag{4.17}$$

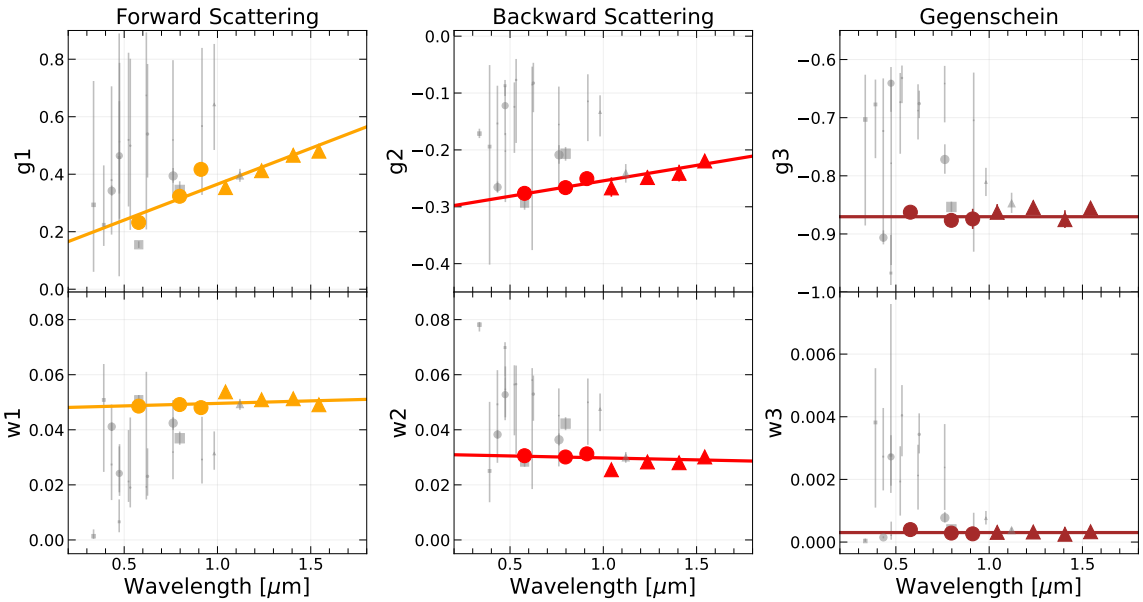

Figure 43. Fitting of phase function parameters to SKYSURF data. Each point represents the best-fit to that filter, where the albedo is fixed following Figure 42. The error bars represent the 68.27th-percentile distribution from the posterior. We fit a line to each parameter, requiring that the phase function at every wavelength integrates to 1.0. We only do the linear fitting for filters with more than 300 independent pointings, represent by colored points. We assume that the gegenschein components do not change significantly with wavelength, and instead just fit a median. The grey points are sized according to the number of unique pointings in that filter (Table 16). Different marker shapes represent different HST cameras: squares represent WFC3/UVIS, circles represent ACS/WFC, and triangles represent WFC3/IR.

$$w_1 = 0.00183 \times \lambda + 0.04775 \tag{4.18}$$

$$w_2 = -0.00143 \times \lambda + 0.03122 \tag{4.19}$$

$$w_3 = 0.00030 \tag{4.20}$$

4.6.1 Albedo Results

We find that a linear relationship between albedo and wavelength provides a good fit to our best-fit albedo values across the HST filters. While this simplified model

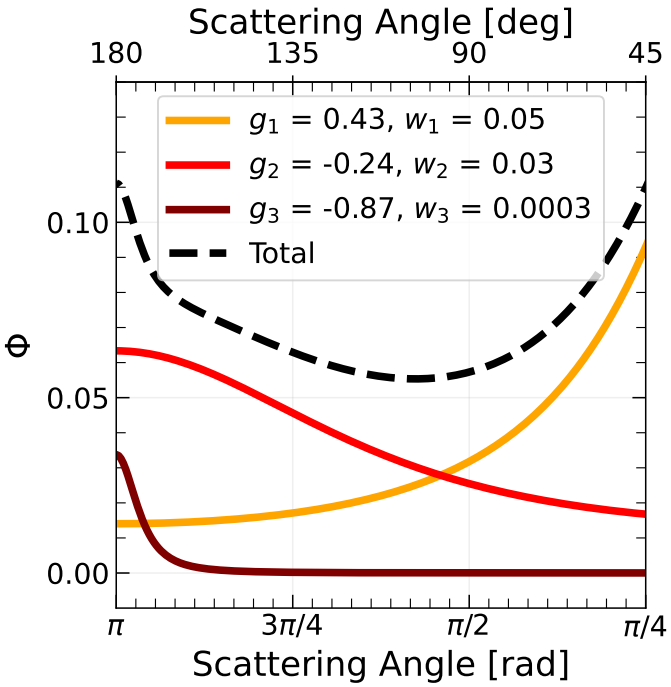

Figure 44. Relative contribution of each g parameter from Equation 4.4, for $\lambda = 1.25$ μm. The x-axis is limited to 0.8 radians ($\sim$45°), just below the minimum Sun Angle observable by HST. $g1$ represents the forward scattering component of the scattering phase function, $g2$ represents the backward scattering component, and $g3$ represents the gegenschein component.

likely does not capture the true relation between albedo and wavelength, we opted for a linear fit to avoid overfitting. Our results are shown in comparison with albedos from several previous studies. We assume the albedo is uniform across the interplanetary dust cloud and consistent across all lines of sight.

The albedos used in the original Kelsall et al. (1998) model, derived as free parameters from fitting COBE/DIRBE data, are included in Figure 42. San et al. (2024) present updated albedo estimates using a Bayesian approach that incorporates data from DIRBE, Planck, WISE, and Gaia. Their results offer a reanalysis of DIRBE-based albedos, but still differ from ours. We also compare to Ishiguro et al. (2013), who used the WIZARD instrument to observe gegenschein in the optical, deriving a

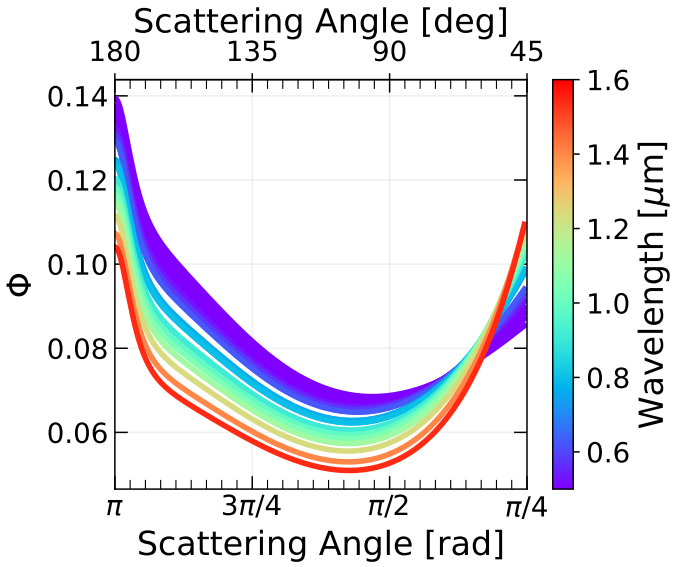

Figure 45. Scattering phase function (Φ) for the Zodi2025 model, shown for various filter wavelengths (colored lines). The x-axis is limited to 0.8 radians (∼45°), just below the minimum Sun Angle observable by HST.

geometric albedo of 0.06 ± 0.01. Hanner et al. (1974) estimated albedo by reanalyzing micrometeoroid data from Helios A and Pioneer 10, while Renard et al. (1995) used the node of lesser uncertainty method to derive albedos in the range of ∼0.08–0.15 at 1 AU. Lumme & Bowell (1985) used polarimetric observations to estimate a an albedo of 0.04.

Finally, we include modeled albedos for interstellar dust from Zubko et al. (2004), which were derived by fitting UV–IR extinction, diffuse IR emission, and elemental abundances. Although interstellar dust differs in composition and grain size from interplanetary dust, and exhibits features such as PAH emission not yet seen in zodiacal light, we include this comparison to illustrate comparison between interstellar dust and inteplanetary dust. The models from Zubko et al. (2004) find a decreasing albedo with decreasing wavelength, which agrees with our results.

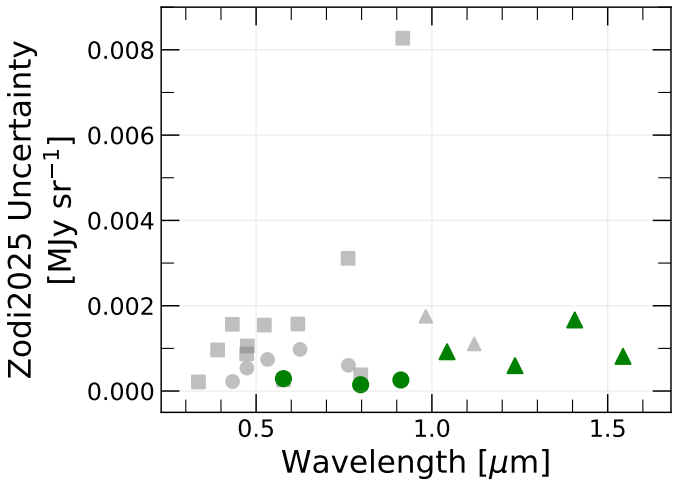

Figure 46. Zodi2025 uncertainties as a function of filter wavelength. These uncertainties (Section 4.6.3) are derived from the posterior distributions of the best fit albedo and phase function parameters. Different marker shapes represent different HST cameras: squares represent WFC3/UVIS, circles represent ACS/WFC, and triangles represent WFC3/IR. Green colored points represent filters with more than 300 independent HST pointings.

4.6.2 Phase Function Results

We find that a linear relationship between each phase function parameter and wavelength provides a good fit to the best-fit values derived from HST observations. These parameters are the weight parameters w_1, w_2, w_3 and asymmetry parameters g_1, g_2, g_3. For reference, Figure 44 illustrates the relative contributions of each parameter to the total phase function at 1.25 μm. To summarize, g_1 and w_1 describe forward scattering, g_2 and w_2 capture backward scattering, and g_3 and w_3 represent the gegenschein component.

The final linear relations, shown as solid lines in Figures 42 and 43, are used in our adopted model. As described in Section 4.5.2, we normalize the final phase function such that its integral over all scattering angles equals 1, which is accurate to within 0.003 (or 0.3%) in the final fit.

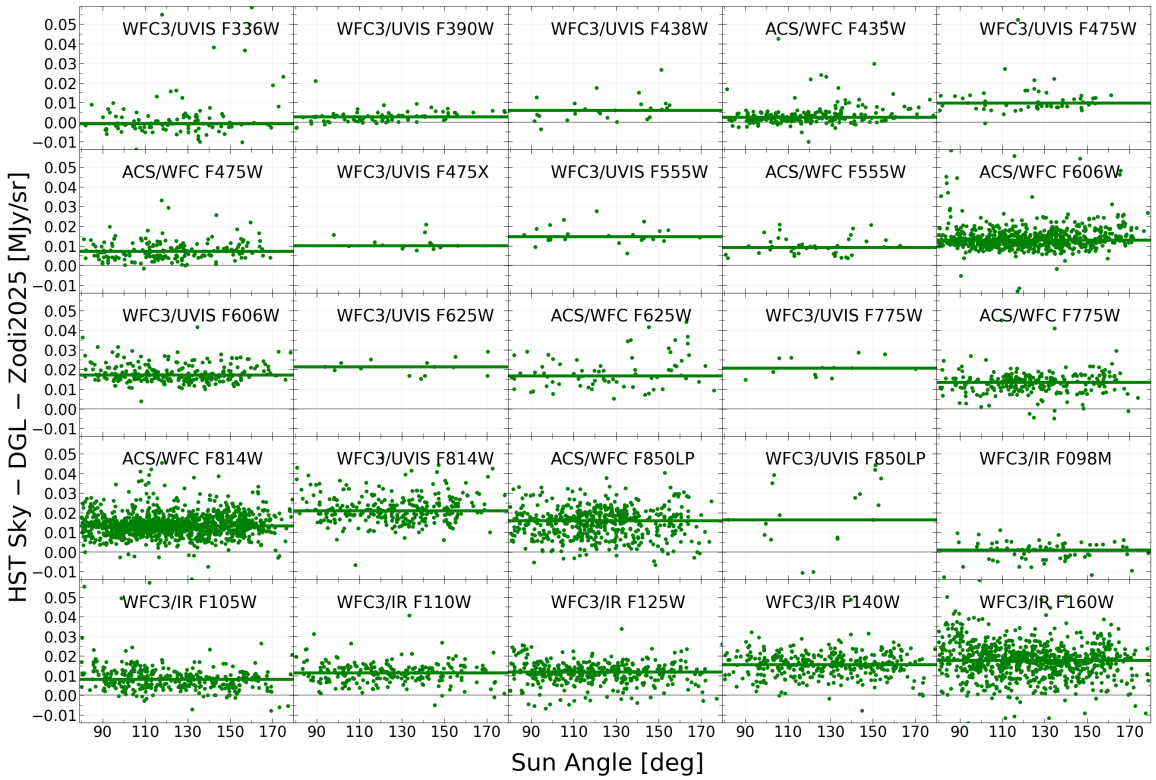

Figure 47. Diffuse light brightness (HST Sky-SB − DGL − Zodi2025) versus Sun Angle. Each green point represents an individual SKYSURF measurement (selected as described in Section 4.3), probing different scattering angles. The flat residuals (solid green lines show median offsets) indicate the assumed scattering physics is appropriate. HST camera and filter names are shown in black, and the figure panels are sorted from shortest (top-left) to longest (bottom-right) wavelength.

The final phase function parameters show clear wavelength dependence, which results in noticeable changes to the shape of the scattering phase function (Figure 45). Specifically, forward scattering becomes more prominent at longer wavelengths, as seen in the increasing trend of g_1, which changes more significantly than g_2.

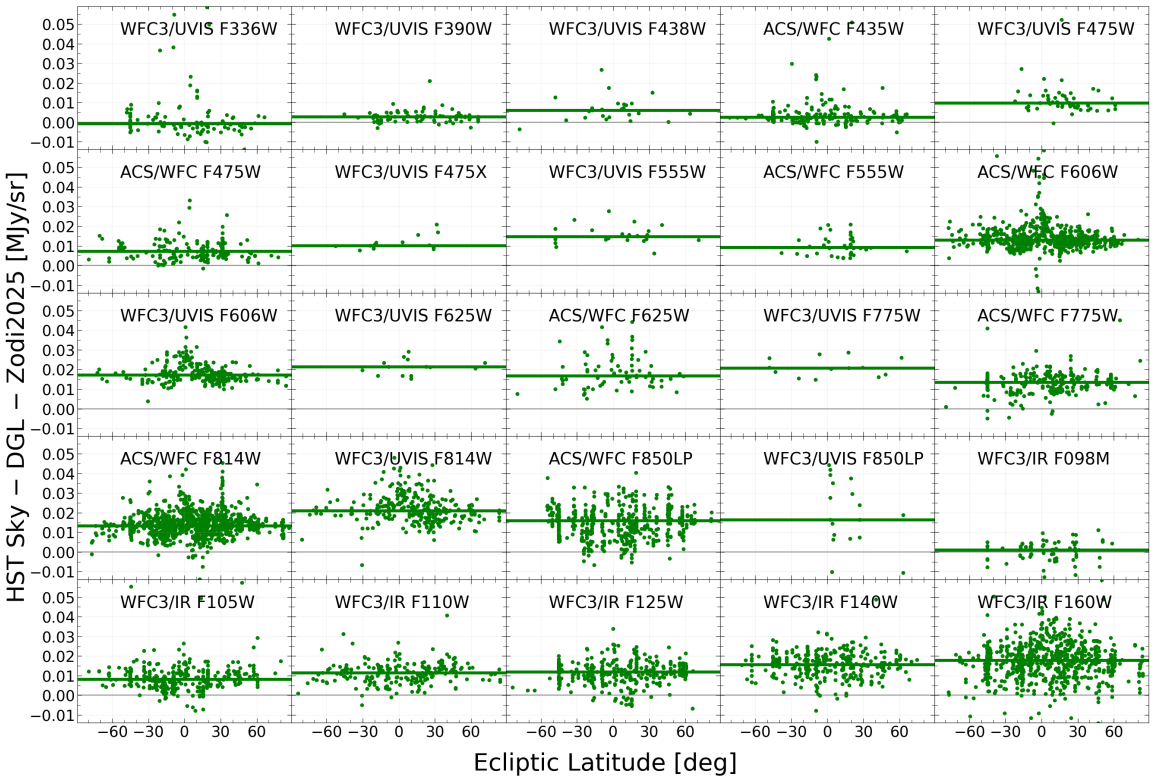

Figure 48. As Figure 47, but plotted versus Ecliptic Latitude and probing various regions of the zodiacal dust cloud. Here, flat residuals indicate that the assumed spatial distribution of zodiacal dust is appropriate.

4.6.3 Uncertainties in Zodi2025

To estimate the uncertainty in Zodi2025, we use the posterior distributions from step 1 of our MCMC fitting pipeline. This step jointly fits both the albedo and the six phase function parameters. We use posteriors from this step because it includes the largest number of free parameters. In later steps, either the albedo or phase function is held fixed, which could lead to underestimated uncertainties if those steps were used instead.

For each HST filter, we estimate the random uncertainty in our model using results from the final 1,000 MCMC steps of each of the 25 walkers, totaling 25,000 samples.

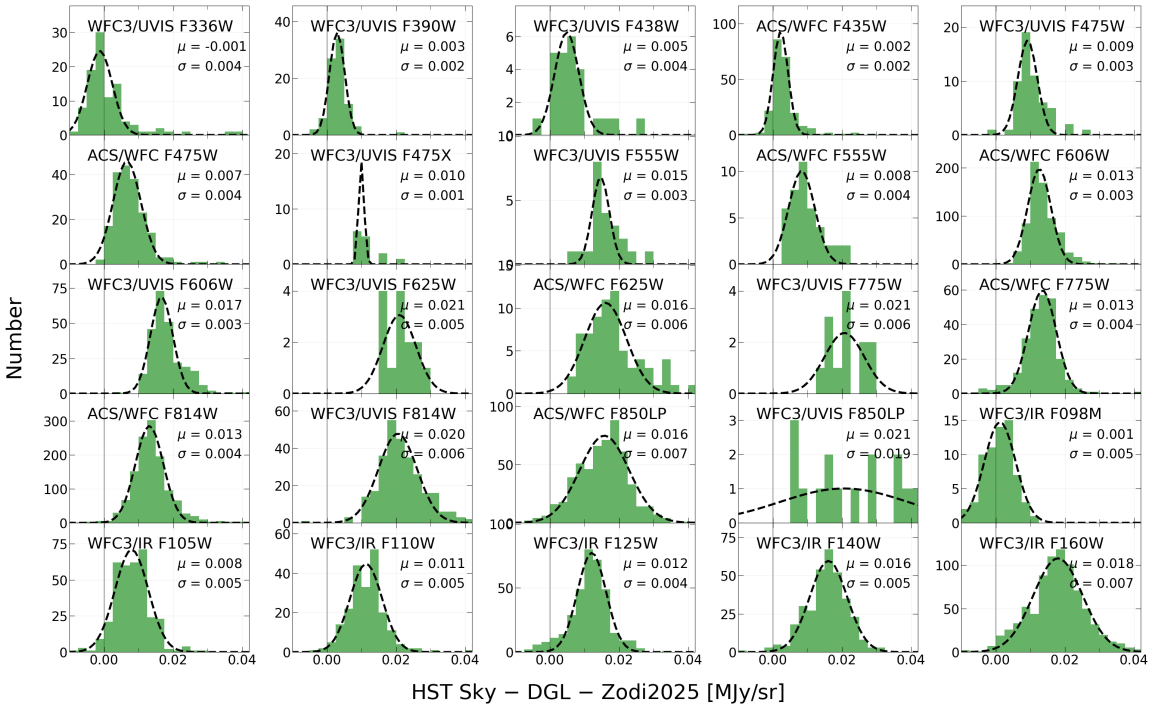

Figure 49. Histograms of the diffuse light brightness (HST Sky-SB − DGL − Zodi2025) for all HST pointings in each filter. All histograms are binned with bins 0.001 MJy sr^{-1} wide. We list the mean (μ) and standard deviation (σ) of each Gaussian fit for each filter, where the latter represents the random uncertainty in diffuse light, where the main contributor to this random uncertainty is uncertainties in the sky-SB.

At each of these 25,000 iterations, we generate model predictions for 100 simulated sky pointings, each with a randomly selected sky position and day of year. This produces 25,000 zodiacal light intensity values for each of the 100 sky pointings. For each pointing, we compute the inner 68.27th percentile of these values, which we define as the 1σ uncertainty for that specific pointing. Finally, we take the median uncertainty across all 100 sky pointings as the representative 1σ uncertainty for the given HST filter.

Figure 46 shows the resulting uncertainties as a function of wavelength for each HST filter. We quantify the uncertainties in Table 18. The median uncertainty across

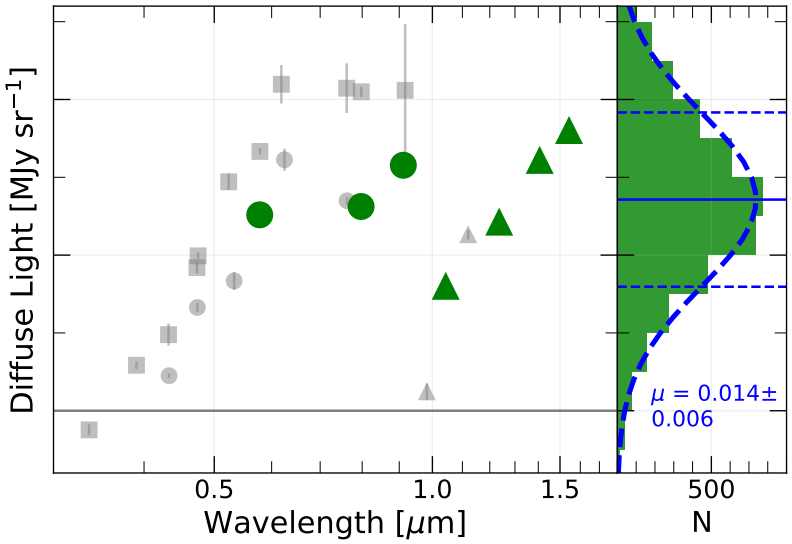

Figure 50. Comparison of diffuse light levels for each HST filter, as a function of wavelength. Each point represents an average diffuse light brightness (HST Sky-SB − DGL − Zodi2025) for that filter. Different marker shapes represent different HST cameras: squares represent WFC3/UVIS, circles represent ACS/WFC, and triangles represent WFC3/IR. Green colored points represent filters with more than 300 independent HST pointings. The errorbars represent the standard error in diffuse light for that filter (σ in Figure 49 divided by $\sqrt{N}$, where N is the number of independent pointings in that filter). These values are quantified in Table 18. The histogram on the right shows the distribution of diffuse light measurements for individual HST images, specifically for filters with at least 300 independent pointings. In blue text, we show the mean and standard deviation of this distribution, when a Gaussian profile is fit to it.

all HST filters is 0.0009 MJy sr^{-1}. For a zodiacal light level of $\sim$ 0.01 MJy sr^{-1} (typical in the ecliptic poles around 0.6 μm), this results in a random uncertainty of $< 1\%$. Filters with the most sky coverage (i.e., more than 300 independent pointings, shown in green) tend to have the smallest uncertainties, reflecting better constraints from the data.

In addition to random uncertainties, we detect a systematic offset in the model. These are estimated by examining the residual diffuse light after subtracting both

Camera	Filter	Uncertainty [MJy sr^{-1}]	Diffuse Light [MJy sr^{-1}]
wfc3uvis	F336W	0.0002	-0.0012
wfc3uvis	F390W	0.0010	0.0029
wfc3uvis	F438W	0.0014	0.0049
acswfc	F435W	0.0002	0.0022
wfc3uvis	F475W	0.0009	0.0092
acswfc	F475W	0.0006	0.0066
wfc3uvis	F475X	0.0012	0.0100
wfc3uvis	F555W	0.0017	0.0147
acswfc	F555W	0.0009	0.0083
acswfc	F606W	0.0003	0.0126
wfc3uvis	F606W	0.0003	0.0167
wfc3uvis	F625W	0.0014	0.0210
acswfc	F625W	0.0011	0.0161
wfc3uvis	F775W	0.0039	0.0207
acswfc	F775W	0.0005	0.0135
acswfc	F814W	0.0002	0.0131
wfc3uvis	F814W	0.0006	0.0205
acswfc	F850LP	0.0003	0.0158
wfc3uvis	F850LP	0.0085	0.0206
wfc3ir	F098M	0.0020	0.0012
wfc3ir	F105W	0.0007	0.0080
wfc3ir	F110W	0.0015	0.0113
wfc3ir	F125W	0.0006	0.0121
wfc3ir	F140W	0.0017	0.0161
wfc3ir	F160W	0.0009	0.0180

Table 18. Random uncertainties and systematic offset of Zodi2025. The random uncertainties are calculated by the posterior distributions resulting from our fitting pipeline (Section 4.6.3). We also show the residual diffuse light brightness (HST Sky-SB − DGL − Zodi2025). If diffuse light is purely local (i.e., a missing isotropic component to the interplanetary dust cloud), the total systematic offset of Zodi2025 can be considered to be equal to the total diffuse light level in the fourth column.

Zodi2025 and the DGL from the measured HST sky-SB. This is presented in the next section.

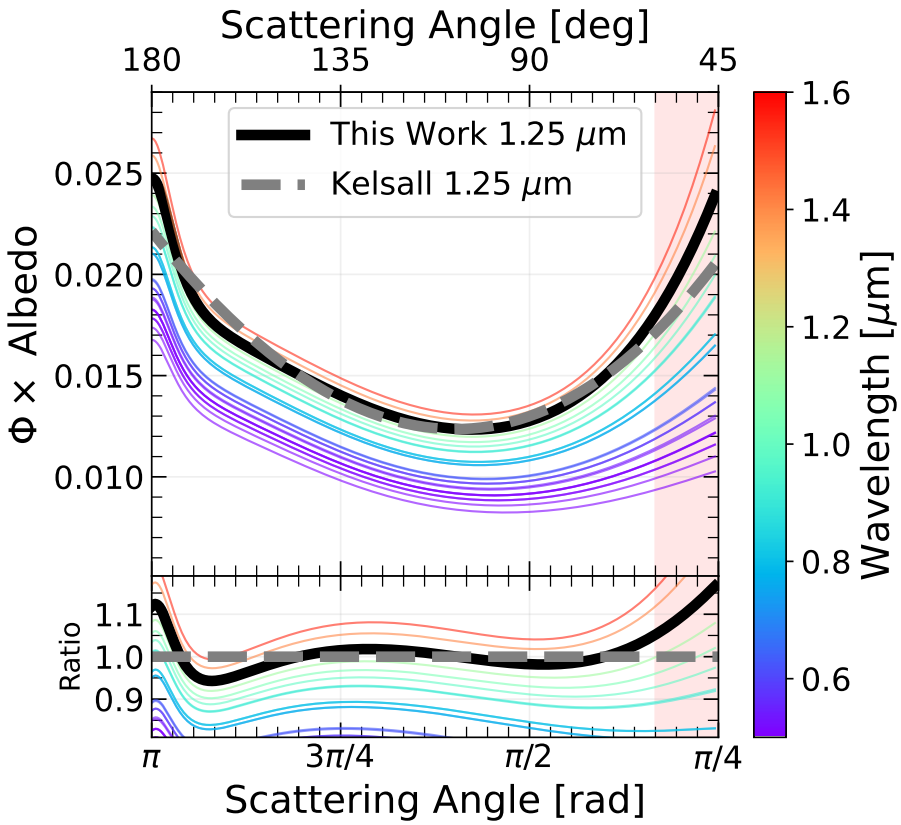

Figure 51. Scattering phase function (Φ) times albedo for the Zodi2025 model, shown for various filter wavelengths (colored lines), compared to the original Kelsall model (grey dashed line). We highlight $\Phi\times$Albedo for $\sim$1.25 μm (WFC3/IR F125W filter) from this work as a dark black line for comparison with the Kelsall model. COBE did no observe at Sun Angles$<64^{\circ}$, and therefore the Kelsall has no constraint at smaller angles (red shaded region). The top panel shows the absolute values of $\Phi\times$Albedo, while the bottom panel shows the ratio between Zodi2025 and Kelsall for each wavelength. The x-axis is limited to 0.8 radians ($\sim45^{\circ}$), just below the minimum Sun Angle observable by HST.

4.6.4 Model Performance on HST Data & Diffuse Light

We compare the diffuse light signal when using Zodi2025 with SKYSURF sky-SB measurements. Diffuse light is the residual light after subtracting foregrounds: HST Sky-SB − DGL − Zodi2025. For a perfect DGL and zodiacal light model, this would

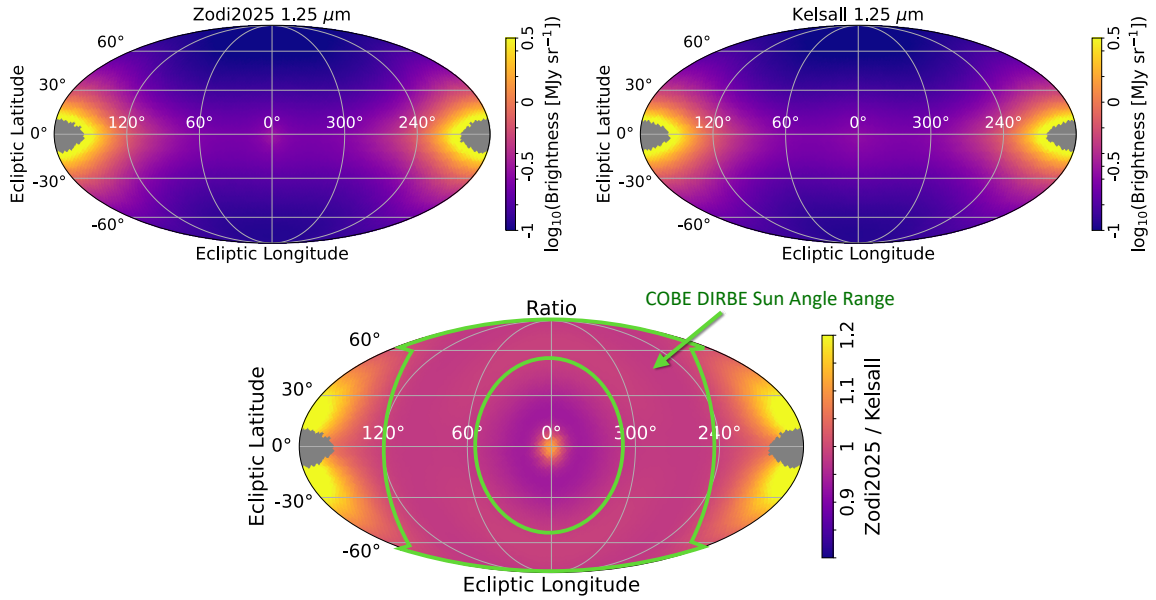

Figure 52. 2D representation of Zodi2025, compared with the Kelsall model. The top two panels show 2D representations of the model from this work (left) and the Kelsall model (right) at 1.25 μm. The bottom panel shows the ratio of the two, where COBE's main Sun Angle range is shown in green. COBE was limited to Sun Angles between 64° (outer annulus) and 124 °(inner annulus). To make this figure, we fixed the day number to be 267 so that the Sun sits at an Ecliptic Longitude ∼180°. We mask HEALpix pixels (nside= 32) with a value greater than 5.5 MJy sr^{-1}.

be considered a direct measurement of the portion of EBL that remains unresolved by HST. A small portion of diffuse light is due to know galaxies, with the remaining being unknown.

Figures 47 and 48 show the residual diffuse light signal for Zodi2025 as compared with SKYSURF sky-SB measurements, as a function of Sun angle and ecliptic latitude. The model demonstrates flat residuals for all wavelengths. The flat residual as a function of Sun angle indicates that the scattering physics in the updated model agrees well with HST observations, as a range of Sun angles also probes a range of scattering angles. The flat residuals as a function Sun angle are likely not caused by stray light

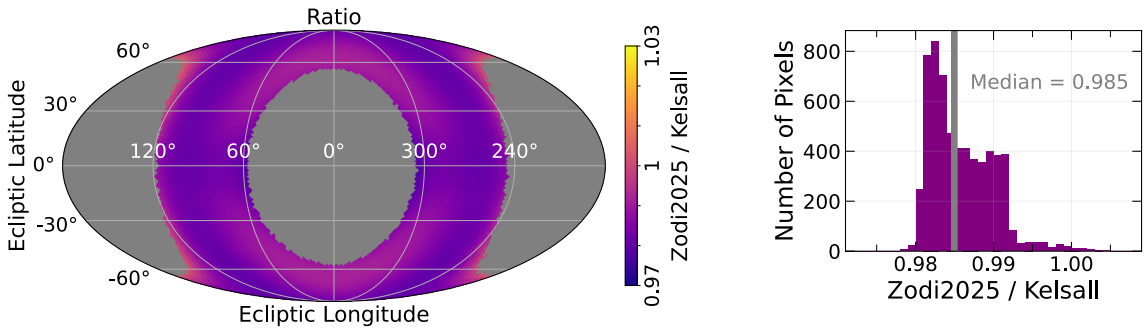

Figure 53. 2D representation of the ratio of Zodi2025 over the Kelsall model. This is similar to the bottom panel of Figure 52, but with a more narrow colorbar range. We mask HEALpix pixels (nside= 32) outside of COBE's Sun Angle range, as COBE was limited to Sun Angles between 64° (outer annulus) and 124 °(inner annulus). On the right panel, we show a histogram of all unmasked pixels, showing that the median ratio between the two models is 0.985. To make this figure, we fixed the day number to be 267 so that the Sun sits at an Ecliptic Longitude ∼180°.

entering HST's CCD, as stray light should become more significant at smaller Sun angles.

The flat residual as a function of ecliptic latitude indicates that the three-dimensional structure of the cloud is accurate. However, there is more scatter at lower ecliptic latitudes, indicating some component of the model may be improved at low ecliptic latitudes. San et al. (2024) also find a faint band along the ecliptic plane when re-examining DIRBE data, and state that high-resolution measurements of zodiacal light along the ecliptic plane may help distinguish an additional component here.

In Figure 49, we show the distribution of diffuse light levels for each HST filter, with the median and standard deviation of a Gaussian profile fit to each distribution. Typically, filters with significant independent pointings (at least ~ 300, as quantified in Table 16) fit a Gaussian well.

Figure 50 and Table 18 show the median diffuse light levels versus wavelength. The typical level of diffuse light is 0.014 ± 0.006 MJy sr^{-1} for HST filters with more than

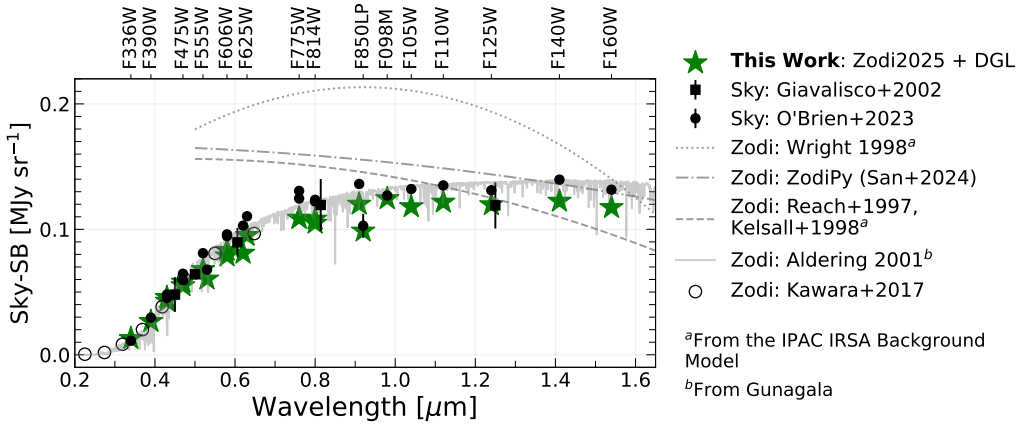

Figure 54. Comparison of Zodi2025 and other zodiacal light models (Reach et al., 1997; Wright, 1998; Aldering, 2001; San et al., 2024) to HST measurements of the sky-surface brightness (O'Brien et al., 2023; Giavalisco et al., 2002). The black circles represent sky-SB measurements from this work that are within 45° of the ecliptic poles. The error bars for these points are the standard deviation of sky-SB measurements divided by $\sqrt{N}$, where N is the number of measurements for that filter. We also show sky-SB measurements from Giavalisco et al. (2002), for comparison. For these same measurements, we estimate the total sky-SB using the modeling in this work: *Zodi*2025+DGL. Similarly, we use the IPAC IRSA Background Model[16] to retrieve the Kelsall and Wright predictions for those same observations. We also utilize the Cosmoglobe ZodiPy code (San et al., 2024) to calculate zodiacal light predictions. We fit a two-dimensional polynomial to the Kelsall, Wright, and ZodiPy predictions, which are shown as dashed grey lines. The solid grey line represents the `Gunagala`[17] implementation of the Aldering (2001) at the ecliptic pole. Zodi2025 performs best across a broad range of Sun Angles and Ecliptic Latitudes relevant for HST observations. For comparison, we also show direct measurements of zodiacal light from Kawara et al. (2017) as open black circles, taken with the HST's Faint Object Spectrograph.

300 independent pointings, where we consider filters with > 300 independent pointings to be most reliable. This is $\sim 2\times$ more than predicted levels of IGL, indicating that either the foreground components are not modeled completely accurate, or there is a significant missing source population in EBL models.

The uncertainty in measured diffuse light is taken to be the same as the Zodi2025 uncertainty. If the diffuse light signal is truly from a missing zodiacal light component,

this would represent the systematic offset in our model ($\sim 0.0104 \pm 0.006$ MJy sr^{-1}). This systematic offset should be considered when modeling the full sky-SB, but can be omitted if one is interested solely in the zodiacal light contribution.

4.6.5 Agreement with Kelsall

Figure 51 plots the product of the phase function and the albedo (essentially the effective scattering efficiency) alongside the original Kelsall model. Because albedo and the phase function are strongly correlated, changes in one can be offset by compensating changes in the other. Comparing their product therefore offers a fair, one-to-one assessment of how our updated zodiacal light model differs from Kelsall's across wavelength. The phase function results in this work agree well with Kelsall at intermediate scattering angles ($110^\circ \pm 40^\circ$). The most noticeable differences are the inclusion of gegenschein for backward scattering and more forward scattering. COBE was limited to Sun Angles between 64°and 124°. This, and the fact that the Kelsall model cuts off at 5.2 AU, means that the Kelsall model was very insensitive to the gegenschein component.

Figures 52 and 53 are 2D projection of Zodi2025, the Kelsall model, and a ratio of the two. We show how well Zodi2025 matches the original Kelsall model within COBE's observed Sun angle range. Specifically, Figure 53 demonstrates that both models agree within 2% in the appropriate sun angle range. However, outside of COBE's sun angle coverage, significant differences arise, most notably in the gegenschein region, as illustrated in Figure 51. Both models also diverge when approaching angles closer to the Sun. It's important to note that areas within 50° of the Sun are not well-constrained by either HST or COBE due to Sun Angle limitations from both

spacecraft. The 2D structure seen in Figure 53 corresponds to differences in the phase functions shown in Figure 51.

Table 7 of Kelsall et al. (1998) quotes an uncertainty in this Zodiacal Light model at 1.25 μm to be 15 nW m^{-2} sr^{-1}, which corresponds to 0.006 MJy sr^{-1}. This uncertainty is measured by comparing different cloud models, such as a simple ellipsoid, a sombrero model (Giese et al., 1986), and the widened fan model they determined to be the best fit. They took the two models with the largest difference in the region of the sky with the largest variation, and quantified that variation into the uncertainty they list in Table 7. Nonetheless, this is an order of magnitude larger than our typical random uncertainties in Zodi2025 (0.0009 MJy sr^{-1}). The total systematic offset in our model may be as high as 0.0104 MJy sr^{-1}, due to a missing istroptic component to the zodiacal light model. However, the Kelsall model would not have detected this component either since the final model was based on temporal changes in the sky-SB. The Wright (1998) model may have more properly modeled an isotropic component due their assumption that the full sky-SB at 25 μm is due to zodiacal light, but Carleton et al. (2022) has shown that this model tends to overpredict zodiacal light.

4.6.6 Comparison with Other Models

Figure 54 compares our total sky-SB model (Zodi2025+ DGL) with direct measurements (Giavalisco et al., 2002; O'Brien et al., 2023) and several existing zodiacal light models (Kelsall et al., 1998; Reach et al., 1997; Wright, 1998; Aldering, 2001; San et al., 2024). This comparison is restricted to observations taken within 45° of the ecliptic poles, where the sky is darkest.

Both the Kelsall and Wright models have been implemented into the IPAC IRSA

Background Model[18], for easy calculation for any time and sky position for wavelengths as short as 0.5 μm. Since this wavelength is considerably shorter than the shortest nominal wavelength of the DIRBE instrument, the IPAC IRSA Background Model must make assumptions about how zodiacal light predictions extend to $\lambda < 1.25$ μm. For this discussion, we will therefore refer to these models as the IPAC-Kelsall model and the IPAC-Wright model. We also compare to the The Cosmoglobe ZodiPy model (San et al., 2024). This is a Python package designed to remove foreground contamination for the Cosmoglobe project.

At 1.25 μm, our model agrees well with the IPAC-Kelsall model, as discussed in the previous section. In contrast, the IPAC-Wright model consistently overpredicts the sky brightness $\lesssim 1$ μm. The ZodiPy model from Cosmoglobe (San et al., 2024) shows similar performance to the IPAC-Kelsall model, likely because both adopt similar assumptions about scattering at optical wavelengths.

The Aldering (2001) model, based on a reddened solar spectrum and a simplified three-dimensional dust cloud, aligns well with observations in some regions. However, it tends to overestimate the sky brightness in the near-IR (> 1 μm). Because it uses a simplified cloud structure and scattering assumptions, it does not accurately capture spatial variations in dust geometry—such as the gegenschein, dust bands, or the trailing Earth cloud—where both the cloud density and the scattering phase function are more complex.

We also show direct measurements of zodiacal light from Kawara et al. (2017), taken with the HST's Faint Object Spectrograph, and are estimated for an ecliptic latitude of 85° using Table 2 and Equation (8) from Kawara et al. (2017).

Overall, our empirical model (Zodi2025 + DGL) matches the sky-SB measurements

[18]https://irsa.ipac.caltech.edu/applications/BackgroundModel/

well in the ecliptic pole regions. However, a residual component remains—an excess of diffuse light (shown in Figure 50) not explained by Zodi2025, DGL, or IGL.

4.6.7 Public Code

Zodi2025 can generate zodiacal light predictions at any day of the year, sky position, and wavelength from 0.25 μm to 1.8 μm. Outside that wavelength window the code still runs, but it simply holds the albedo and phase function parameters fixed to their boundary values at 0.25 μm or 1.8 μm, following Equations 4.14-4.20. The model is distributed as an IDL package on the SKYSURF GitHub repository and is currently being implemented to Python for easier integration with modern pipelines.

Functionally, the package is a copy of the original Kelsall model IDL routine, modified only by the improvements described in this paper. The final albedo and phase function curves follow Equations 4.14–4.20, while solar irradiance is taken from the nearest spectral point in Figure 41. Because the code treats only the scattering component of the interplanetary dust cloud, it is most reliable at wavelengths $\lesssim 3$ μm; beyond that, thermal emission dominates and users should revert to the original Kelsall model or Wright (1998) model. The JWST Cycle 3 program SKYSURF-IR will extend the present work by constraining the model's thermal emission.

Solar-irradiance values introduce a minor systematic in the final brightness. We compare filters with identical central wavelengths but different bandpasses (e.g. ACS/WFC versus WFC3/UVIS) and find that built-in irradiance spectrum is accurate to $\sim 2\%$. If a project demands tighter control, users may supply their own irradiance spectrum directly to the routine.

4.7 Conclusion

We present an updated zodiacal light model optimized for optical wavelengths (0.3–1.6 μm), building on the structure of the widely-used Kelsall et al. (1998) model. Using over 150,000 HST sky-SB measurements from the SKYSURF project, we constrain the wavelength-dependent albedo and scattering phase function of the interplanetary dust cloud. Our model updates the phase function and fits the data with sub-percent random uncertainties. Nonetheless, we detect a significant diffuse light signal of 0.0104 ± 0.006 MJy sr^{-1}, which may be a spherical isotropic-like component of the interplanetary dust cloud. Nonetheless, compared to existing models, our optical-optimized version better matches HST observations, especially in the ultraviolet and visible, where traditional infrared-based models underperform.

The final model, Zodi2025, will be made publicly available as part of the SKYSURF project (O'Brien et al., in prep) and enables improved zodiacal light subtraction for HST, JWST, Roman, Euclid, SPHEREx, and other missions. It will support future studies of diffuse background light and the search for faint astrophysical signals, while also providing a framework for understanding exozodiacal dust around other stars.

Chapter 5

SUMMARY AND FUTURE OUTLOOK

Since its launch in 1990, the Hubble Space Telescope (HST) has provided astronomers with an unprecedented window into the Universe. Orbiting above Earth's turbulent atmosphere, HST offers stable, high-resolution imaging across ultraviolet, visible, and near-infrared wavelengths. These capabilities have positioned HST as a uniquely powerful instrument for studying how the sky evolves over time. This dissertation takes full advantage of HST's strengths to examine the variable night sky through two large programs: SKYSURF and TREASUREHUNT, with the goal to understand the structure and history of our Solar System, our Galaxy, and the Universe as a whole.

This work focuses on both diffuse and discrete sources of light observed by HST. The dominant diffuse component is zodiacal light, which is sunlight scattered by interplanetary dust in our Solar System. As Earth orbits the Sun, its changing position within the dust cloud causes the observed sky brightness to vary. Zodiacal light is the primary contributor to the sky surface brightness (sky-SB) in space-based observations, though fainter components such as diffuse Galactic light (light from our galaxy, the Milky Way) and the extragalactic background light (all light coming from outside of the Milky Way, from all the galaxies in the observable universe) also contribute.

The discrete sources examined here are supernovae and active galactic nuclei (AGN). Supernovae are explosive stellar deaths that can briefly outshine entire galaxies. AGN

are powered by accretion onto supermassive black holes at the centers of galaxies and often show variability over days to years.

The first major focus of this dissertation, presented in Chapter 2, and published as O'Brien et al. (2023), is the measurement of the absolute sky-SB across the full wavelength range of HST, from 0.2 to 1.6 μm. This sky-SB is mostly zodiacal light, but includes diffuse Galactic light and extragalactic background light. Using over 150,000 HST images from the HST archive, we developed and applied a sky-SB measurement algorithm to extract robust sky-SB estimates from individual HST exposures. These measurements revealed expected trends with ecliptic latitude and Sun angle, confirming that zodiacal light is the dominant contributor to the observed sky background. The resulting all-sky sky-SB dataset provides not only essential input for foreground modeling but also a foundation for estimating a diffuse light component of unknown origin. These measurements represent the most comprehensive HST-based constraints of the sky-SB to date and are publicly released alongside our algorithms for community use.

Chapter 3, published as O'Brien et al. (2024), shifts focus to discrete time-domain astrophysics, using repeated HST imaging of the JWST North Ecliptic Pole Time-Domain Field. This field is uniquely suited for transient searches due to its continuous visibility by JWST, minimal zodiacal light contamination, and extensive multi-wavelength coverage. As part of the TREASUREHUNT program, we conducted a systematic search for time-variable sources using ACS/WFC imaging in two HST filters: F435W (~ 0.4 μm) and F606W (~ 0.6 μm). We identified 12 transient events, most likely supernovae, as well as three X-ray detected sources potentially associated with faint quasars or high-redshift transients. We also found that approximately 0.42% of field galaxies exhibit significant variability indicative of AGN activity, with

190 variable galaxy cores identified. We estimate photometric redshifts and stellar population parameters for these sources, demonstrating the rich astrophysical diversity of variability in this deep field. These results establish this field as a cornerstone for future variability studies and provide a reference dataset for future surveys.

Chapter 4 (to be published as O'Brien et al. 2025) addresses a critical challenge in interpreting sky-SB measurements: modeling zodiacal light. Building upon the structure of the widely-used Kelsall et al. (1998) model, we present a new zodiacal light model that is optimized for optical wavelengths. By updating the scattering phase function and albedo from the Kelsall et al. (1998) zodiacal light model, we derive a model that matches HST observations with sub-percent random uncertainties. Compared to models developed for infrared missions, our model performs significantly better in the UV and visible, where previous models systematically over-predict the sky background. Despite these improvements, we detect a residual diffuse light signal of 0.0104 ± 0.006 MJy sr^{-1}, which may point to a missing isotropic component of the interplanetary dust cloud. The final model will be made publicly available and is intended for use by the broader astronomical community, especially for high-precision background estimation for space-based missions (HST, JWST, Euclid, SPHEREx, and Roman).

Together, the results presented in this dissertation provide a comprehensive picture of both the static and time-varying components of the sky as seen by HST. We demonstrate that:

- Zodiacal light dominates HST's sky background but varies predictably with viewing geometry;
- A small but significant diffuse light component remains unexplained by current models;

- Time-variable phenomena such as supernovae and AGN variability can be robustly identified in HST data;
- New, wavelength-optimized models of zodiacal light can be dramatically improved with HST.

Looking ahead, the legacy of this work will support upcoming missions and surveys. Improved foreground models will reduce uncertainties in extragalactic background light measurements, enable more efficient, sensitive searches for faint galaxies, and help isolate the faint signatures of the Milky Way. Meanwhile, continued time-domain monitoring of deep fields will expand our understanding of supernova demographics, black hole growth, and galaxy evolution. HST has shown us not only what the Universe looks like, but how it changes, and this dissertation contributes to that evolving story.

REFERENCES

Aldering, G. 2001, LBNL report, LBNL-51157, 1, doi: http://www-supernova.lbl.gov/~aldering/

Alexander, D. M., Bauer, F. E., Chapman, S. C., et al. 2005, ApJ, 632, 736, doi: 10.1086/444342

Anand, G., Grogin, N., & Anderson, J. 2022, Revisiting ACS/WFC Sky Backgrounds, Instrument Science Report ACS 2022-1

Andrews, S. K., Driver, S. P., Davies, L. J., Lagos, C. d. P., & Robotham, A. S. G. 2017, arXiv, 474, 898–916, doi: 10.1093/mnras/stx2843

Andrews, S. K., Driver, S. P., Davies, L. J. M., Lagos, C. d. P., & Robotham, A. S. G. 2018, MNRAS, 474, 898, doi: 10.1093/mnras/stx2843

Arai, T., Matsuura, S., Bock, J., et al. 2015, ApJ, 806, 69, doi: 10.1088/0004-637X/806/1/69

Ashcraft, T. A., Windhorst, R. A., Jansen, R. A., et al. 2018, PASP, 130, 064102, doi: 10.1088/1538-3873/aab542

Astropy Collaboration, Robitaille, T. P., Tollerud, E. J., et al. 2013, A&A, 558, A33, doi: 10.1051/0004-6361/201322068

Astropy Collaboration, Price-Whelan, A. M., Sipőcz, B. M., et al. 2018, AJ, 156, 123, doi: 10.3847/1538-3881/aabc4f

Astropy Collaboration, Price-Whelan, A. M., Lim, P. L., et al. 2022, apj, 935, 167, doi: 10.3847/1538-4357/ac7c74

Bernardinelli, P. H., Bernstein, G. M., Montet, B. T., et al. 2021, ApJL, 921, L37, doi: 10.3847/2041-8213/ac32d3

Bernstein, G. M., Nichol, R. C., Tyson, J. A., Ulmer, M. P., & Wittman, D. 1995, AJ, 110, 1507, doi: 10.1086/117624

Bernstein, R. A. 2007, The Astrophysical Journal, 666, 663–673, doi: 10.1086/519824

Bernstein, R. A., Freedman, W. L., & Madore, B. F. 2002, The Astrophysical Journal, 571, 56–84, doi: 10.1086/339422

Bertin, E., & Arnouts, S. 1996a, A&AS, 117, 393, doi: 10.1051/aas:1996164

—. 1996b, A&AS, 117, 393, doi: 10.1051/aas:1996164

Bhatia, P., Carleton, T., Windhorst, R. A., Jansen, R. A., & O'Brien, R. 2024, Research Notes of the American Astronomical Society, 8, 154, doi: 10.3847/2515-5172/ad54c8

Bickel, D. R., & Fruehwirth, R. 2005, arXiv Mathematics e-prints, math/0505419. https://arxiv.org/abs/math/0505419

Biretta, J., & Baggett, S. 2013, WFC3 Post-Flash Calibration, Space Telescope WFC Instrument Science Report

Blanc, G. A., Lira, P., Barrientos, L. F., et al. 2008, ApJ, 681, 1099, doi: 10.1086/588018

Bohlin, R. C., Ryon, J. E., & Anderson, J. 2020, Update of the Photometric Calibration of the ACS CCD Cameras, Instrument Science Report ACS 2020-8

Boquien, M., Burgarella, D., Roehlly, Y., et al. 2019, A&A, 622, A103, doi: 10.1051/0004-6361/201834156

Borlaff, A., Trujillo, I., Román, J., et al. 2019, A&A, 621, A133, doi: 10.1051/0004-6361/201834312

Bourque, M., & Baggett, S. 2016, Space Telescope WFC3 Instrument Science Report

Boutsia, K., Leibundgut, B., Trevese, D., & Vagnetti, F. 2009, A&A, 497, 81, doi: 10.1051/0004-6361/200811092

Bradley, L., Sipőcz, B., Robitaille, T., et al. 2020, astropy/photutils: 1.0.0, 1.0.0, Zenodo, doi: 10.5281/zenodo.4044744

Bradley, L., Sipőcz, B., Robitaille, T., et al. 2022, astropy/photutils: 1.5.0, 1.5.0, Zenodo, doi: 10.5281/zenodo.6825092

Brammer, G., Pirzkal, N., McCullough, P., & MacKenty, J. 2014, Time-varying Excess Earth-glow Backgrounds in the WFC3/IR Channel, Instrument Science Report WFC3 2014-03, 14 pages

Brammer, G. B., van Dokkum, P. G., & Coppi, P. 2008, ApJ, 686, 1503, doi: 10.1086/591786

Brandt, T. D., & Draine, B. T. 2012, ApJ, 744, 129, doi: 10.1088/0004-637X/744/2/129

Bruzual, G., & Charlot, S. 2003, MNRAS, 344, 1000, doi: 10.1046/j.1365-8711.2003.06897.x

Bryden, G., Turner, N. J., Pokorny, P., et al. 2023, arXiv e-prints, arXiv:2303.07612, doi: 10.48550/arXiv.2303.07612

Burke, C. J., Shen, Y., Blaes, O., et al. 2021, Science, 373, 789, doi: 10.1126/science.abg9933

Burns, J. A., Lamy, P. L., & Soter, S. 1979, Icarus, 40, 1, doi: 10.1016/0019-1035(79)90050-2

Caddy, S. E., Spitler, L. R., & Ellis, S. C. 2022, AJ, 164, 52, doi: 10.3847/1538-3881/ac76c2

Calamida, A., Bajaj, V., Mack, J., et al. 2022, arXiv

Calzetti, D., Armus, L., Bohlin, R. C., et al. 2000, ApJ, 533, 682, doi: 10.1086/308692

Cambresy, L., Reach, W. T., Beichman, C. A., & Jarrett, T. H. 2001, The Astrophysical Journal, 555, 563–571, doi: 10.1086/321470

Cappellaro, E. 2014, in Supernova Environmental Impacts, ed. A. Ray & R. A. McCray, Vol. 296, 37–44, doi: 10.1017/S1743921313009204

Cappellaro, E., Botticella, M. T., Pignata, G., et al. 2015, A&A, 584, A62, doi: 10.1051/0004-6361/201526712

Carleton, T., Windhorst, R. A., O'Brien, R., et al. 2022, AJ, 164, 170, doi: 10.3847/1538-3881/ac8d02

Casertano, S., de Mello, D., Dickinson, M., et al. 2000, AJ, 120, 2747, doi: 10.1086/316851

Chakrabarti, S., Dell, B., Graur, O., et al. 2018, ApJL, 863, L1, doi: 10.3847/2041-8213/aad0a4

Chambers, K. C., Magnier, E. A., Metcalfe, N., et al. 2016, arXiv e-prints, arXiv:1612.05560, doi: 10.48550/arXiv.1612.05560

Chellew, B., Brandt, T. D., Hensley, B. S., Draine, B. T., & Matthaey, E. 2022, The Astrophysical Journal, 932, 112, doi: 10.3847/1538-4357/ac6efc

Ciesla, L., Elbaz, D., & Fensch, J. 2017, A&A, 608, A41, doi: 10.1051/0004-6361/201731036

Coddington, O. M., Richard, E. C., Harber, D., et al. 2021, Geophys. Res. Lett., 48, e91709, doi: 10.1029/2020GL091709

Cohen, S. H., Ryan, R. E., J., Straughn, A. N., et al. 2006, ApJ, 639, 731, doi: 10.1086/499577

Cohen, Y., Grogin, N. A., & Bellini, A. 2020, Space Telescope ACS Instrument Science Report

Conrad, L. R., O'Brien, R., Carter, D., et al. 2025, Research Notes of the American Astronomical Society, 9, 54, doi: 10.3847/2515-5172/adbbe9

Conselice, C. J., Wilkinson, A., Duncan, K., & Mortlock, A. 2016, The Astrophysical Journal, 830, 83, doi: 10.3847/0004-637x/830/2/83

Cooray, A., Bock, J. J., Keatin, B., Lange, A. E., & Matsumoto, T. 2004, ApJ, 606, 611, doi: 10.1086/383137

Crill, B. P., Bach, Y. P., Bryan, S. A., et al. 2025, arXiv e-prints, arXiv:2505.24856, doi: 10.48550/arXiv.2505.24856

Cristiani, S., Trentini, S., La Franca, F., & Andreani, P. 1997, A&A, 321, 123, doi: 10.48550/arXiv.astro-ph/9610108

Cristiani, S., Vio, R., & Andreani, P. 1990, AJ, 100, 56, doi: 10.1086/115489

Currie, M. H., Debes, J., Hasegawa, Y., et al. 2025, arXiv e-prints, arXiv:2503.19932, doi: 10.48550/arXiv.2503.19932

Dahlen, T., Strolger, L.-G., Riess, A. G., et al. 2012, ApJ, 757, 70, doi: 10.1088/0004-637X/757/1/70

Dale, D. A., Helou, G., Magdis, G. E., et al. 2014, ApJ, 784, 83, doi: 10.1088/0004-637X/784/1/83

de Vaucouleurs, G., de Vaucouleurs, A., Corwin, Herold G., J., et al. 1991, Third Reference Catalogue of Bright Galaxies

Dermott, S. F., Durda, D. D., Gustafson, B. A. S., et al. 1992, in Asteroids, Comets, Meteors 1991, ed. A. W. Harris & E. Bowell, 153

Dermott, S. F., Grogan, K., Gustafson, B. A. S., et al. 1996, in Astronomical Society of the Pacific Conference Series, Vol. 104, IAU Colloq. 150: Physics, Chemistry, and Dynamics of Interplanetary Dust, ed. B. A. S. Gustafson & M. S. Hanner, 143

DES Collaboration, Abbott, T. M. C., Acevedo, M., et al. 2024, ApJL, 973, L14, doi: 10.3847/2041-8213/ad6f9f

Dole, H., Lagache, G., Puget, J.-L., et al. 2006, A&A, 451, 417, doi: 10.1051/0004-6361:20054446

Domínguez, A., Primack, J. R., Rosario, D. J., et al. 2011, MNRAS, 410, 2556, doi: 10.1111/j.1365-2966.2010.17631.x

Dressel, L. 2016, in WFC3 Instrument Handbook for Cycle 24 v. 8, Vol. 8 (Space Telescope Science Institute), 8

—. 2021, in WFC3 Instrument Handbook for Cycle 29 v. 13, Vol. 13 (Space Telescope Science Institute), 13

Driver, S. P. 2021, arXiv e-prints, arXiv:2102.12089, doi: 10.48550/arXiv.2102.12089

Driver, S. P., Andrews, S. K., Davies, L. J., et al. 2016, The Astrophysical Journal, 827, 108, doi: 10.3847/0004-637x/827/2/108

Driver, S. P., Andrews, S. K., Davies, L. J., et al. 2016, ApJ, 827, 108, doi: 10.3847/0004-637X/827/2/108

Dwek, E., & Arendt, R. G. 1999, AIP Conference Proceedings, 470, 354–358, doi: 10.1063/1.58621

Dwek, E., & Krennrich, F. 2013, Astroparticle Physics, 43, 112, doi: 10.1016/j.astropartphys.2012.09.003

Dwek, E., Arendt, R. G., Hauser, M. G., et al. 1998, ApJ, 508, 106, doi: 10.1086/306382

Fabricant, D., Fata, R., Epps, H., et al. 2019, PASP, 131, 075004, doi: 10.1088/1538-3873/ab1d78

Ferrarese, L., & Merritt, D. 2000, ApJL, 539, L9, doi: 10.1086/312838

Finke, J. D., Razzaque, S., & Dermer, C. D. 2010, ApJ, 712, 238, doi: 10.1088/0004-637X/712/1/238

Foreman-Mackey, D., Hogg, D. W., Lang, D., & Goodman, J. 2013, PASP, 125, 306, doi: 10.1086/670067

Franceschini, A., Rodighiero, G., & Vaccari, M. 2008, A&A, 487, 837, doi: 10.1051/0004-6361:200809691

Fruscione, A., McDowell, J. C., Allen, G. E., et al. 2006, in Society of Photo-Optical Instrumentation Engineers (SPIE) Conference Series, Vol. 6270, Society of Photo-Optical Instrumentation Engineers (SPIE) Conference Series, ed. D. R. Silva & R. E. Doxsey, 62701V, doi: 10.1117/12.671760

Gaia Collaboration, Prusti, T., de Bruijne, J. H. J., et al. 2016, A&A, 595, A1, doi: 10.1051/0004-6361/201629272

Gaia Collaboration, Vallenari, A., Brown, A. G. A., et al. 2023, A&A, 674, A1, doi: 10.1051/0004-6361/202243940

Gebhardt, K., Bender, R., Bower, G., et al. 2000, ApJL, 539, L13, doi: 10.1086/312840

Gennaro, M. 2018, "WFC3 Data Handbook", Version 4.0, (Baltimore: STScI)

Giavalisco, M., Sahu, K., & Bohlin, R. C. 2002, New Estimates of the Sky Background for the HST Exposure Time Calculator, Instrument Science Report WFC3 2002-12, 9 pages

Giavalisco, M., Ferguson, H. C., Koekemoer, A. M., et al. 2004, ApJL, 600, L93, doi: 10.1086/379232

Giese, R. H., Kneissel, B., & Rittich, U. 1986, Icarus, 68, 395, doi: 10.1016/0019-1035(86)90046-1

Gilhuly, C., Merritt, A., Abraham, R., et al. 2022, ApJ, 932, 44, doi: 10.3847/1538-4357/ac6750

Giveon, U., Maoz, D., Kaspi, S., Netzer, H., & Smith, P. S. 1999, MNRAS, 306, 637, doi: 10.1046/j.1365-8711.1999.02556.x

Gong, Y., Cooray, A., Mitchell-Wynne, K., et al. 2016, The Astrophysical Journal, 825, 104, doi: 10.3847/0004-637x/825/2/104

Graur, O., Rodney, S. A., Maoz, D., et al. 2014, ApJ, 783, 28, doi: 10.1088/0004-637X/783/1/28

Guhathakurta, P., & Tyson, J. A. 1989, ApJ, 346, 773, doi: 10.1086/168058

Guyon, O., Pluzhnik, E. A., Kuchner, M. J., Collins, B., & Ridgway, S. T. 2006, ApJS, 167, 81, doi: 10.1086/507630

Hahn, J. M., Zook, H. A., Cooper, B., & Sunkara, B. 2002, Icarus, 158, 360, doi: 10.1006/icar.2002.6881

Hammel, H. B., Beebe, R. F., Ingersoll, A. P., et al. 1995, Science, 267, 1288, doi: 10.1126/science.7871425

Hanner, M. S., Sparrow, J. G., Weinberg, J. L., & Beeson, D. E. 1976, Pioneer 10 Observations of Zodiacal Light Brightness Near the Ecliptic: Changes with Heliocentric Distance, doi: 10.1007/3-540-07615-8_448

Hanner, M. S., Weinberg, J. L., DeShields, II, L. M., Green, B. A., & Toller, G. N. 1974, J. Geophys. Res., 79, 3671, doi: 10.1029/JA079i025p03671

Hanzawa, M., Matsuura, S., Takahashi, A., et al. 2024, PASJ, 76, 353, doi: 10.1093/pasj/psae016

Harms, R. J., Ford, H. C., Tsvetanov, Z. I., et al. 1994, ApJL, 435, L35, doi: 10.1086/187588

Hauser, M. G., & Dwek, E. 2001, ARA&A, 39, 249, doi: 10.1146/annurev.astro.39.1.249

Hauser, M. G., Arendt, R. G., Kelsall, T., et al. 1998, The Astrophysical Journal, 508, 25–43, doi: 10.1086/306379

Henyey, L. G., & Greenstein, J. L. 1941, ApJ, 93, 70, doi: 10.1086/144246

Hill, R., Masui, K. W., & Scott, D. 2018, Applied spectroscopy, 72, 663–688, doi: 10.1177/0003702818767133

Hoffmann, S. L., Mack, J., Avila, R., et al. 2021, in American Astronomical Society Meeting Abstracts, Vol. 53, American Astronomical Society Meeting Abstracts, 216.02

Hom, J., Douglas, E., Anche, R., et al. 2024, in AAS/Division for Extreme Solar Systems Abstracts, Vol. 56, AAS/Division for Extreme Solar Systems Abstracts, 623.02

Hong, S. S. 1985, A&A, 146, 67

Hook, I. M., McMahon, R. G., Boyle, B. J., & Irwin, M. J. 1994, MNRAS, 268, 305, doi: 10.1093/mnras/268.2.305

Hubble, E. 1929, Proceedings of the National Academy of Science, 15, 168, doi: 10.1073/pnas.15.3.168

Hubble, E. P. 1926, ApJ, 64, 321, doi: 10.1086/143018

Ienaka, N., Kawara, K., Matsuoka, Y., et al. 2013, ApJ, 767, 80, doi: 10.1088/0004-637X/767/1/80

Ishiguro, M., Yang, H., Usui, F., et al. 2013, ApJ, 767, 75, doi: 10.1088/0004-637X/767/1/75

Jakobsen, P., Jansen, R. A., Wagner, S., & Reimers, D. 2003, A&A, 397, 891, doi: 10.1051/0004-6361:20021579

Jansen, R. A., & Windhorst, R. A. 2018, PASP, 130, 124001, doi: 10.1088/1538-3873/aae476

Jauzac, M., Dole, H., Le Floc'h, E., et al. 2011, A&A, 525, A52, doi: 10.1051/0004-6361/201015432

Jones, M. H., & Rowan-Robinson, M. 1993, MNRAS, 264, 237, doi: 10.1093/mnras/264.1.237

Jura, M. 1979, ApJ, 231, 732, doi: 10.1086/157238

Kashlinsky, A. 2005, Phys. Rep., 409, 361, doi: 10.1016/j.physrep.2004.12.005

Kashlinsky, A., Arendt, R., Gardner, J. P., Mather, J. C., & Moseley, S. H. 2004, ApJ, 608, 1, doi: 10.1086/386365

Kawaguchi, T., & Mineshige, S. 1999, in Activity in Galaxies and Related Phenomena, ed. Y. Terzian, E. Khachikian, & D. Weedman, Vol. 194, 356, doi: 10.48550/arXiv.astro-ph/9811302

Kawara, K., Matsuoka, Y., Sano, K., et al. 2017, PASJ, 69, 31, doi: 10.1093/pasj/psx003

Kelsall, T., Weiland, J. L., Franz, B. A., et al. 1998, The Astrophysical Journal, 508, 44–73, doi: 10.1086/306380

Kelsall, T., Weiland, J. L., Franz, B. A., et al. 1998, ApJ, 508, 44, doi: 10.1086/306380

Khaire, V., & Srianand, R. 2015, ApJ, 805, 33, doi: 10.1088/0004-637X/805/1/33

Kormendy, J., & Ho, L. C. 2013, ARA&A, 51, 511, doi: 10.1146/annurev-astro-082708-101811

Korngut, P., Kim, M. G., Arai, T., et al. 2021, arXiv

Korngut, P. M., Kim, M. G., Arai, T., et al. 2022, ApJ, 926, 133, doi: 10.3847/1538-4357/ac44ff

Koushan, S., Driver, S. P., Bellstedt, S., et al. 2021, arXiv, 503, 2033–2052, doi: 10.1093/mnras/stab540

Kramer, D. M., Carleton, T., Cohen, S. H., et al. 2022, ApJL, 940, L15, doi: 10.3847/2041-8213/ac9cca

Krick, J. E., Glaccum, W. J., Carey, S. J., et al. 2012, ApJ, 754, 53, doi: 10.1088/0004-637X/754/1/53

Labbé, I., Franx, M., Rudnick, G., et al. 2003, AJ, 125, 1107, doi: 10.1086/346140

Lagache, G., Puget, J.-L., & Dole, H. 2005, ARA&A, 43, 727, doi: 10.1146/annurev.astro.43.072103.150606

Lauer, T. R., Postman, M., Weaver, H. A., et al. 2021, ApJ, 906, 77, doi: 10.3847/1538-4357/abc881

Lauer, T. R., Postman, M., Spencer, J. R., et al. 2022, The Astrophysical Journal Letters, 927, L8, doi: 10.3847/2041-8213/ac573d

Leinert, C., Hanner, M., Richter, I., & Pitz, E. 1980, A&A, 82, 328

Leinert, C., Richter, I., Hanner, M., et al. 1982, Data processing and results of the zodiacal light experiment E9 on HELIOS A and B, Final Report, Dec. 1981 Max-Planck-Inst. für Aeronomie, Katlenburg-Lindau (Germany, F.R.).

Leinert, C., Richter, I., Pitz, E., & Planck, B. 1981, A&A, 103, 177

Leinert, C., Bowyer, S., Haikala, L. K., et al. 1998, Astronomy and Astrophysics Supplement Series, 127, 1–99, doi: 10.1051/aas:1998105

Leinert, C., Bowyer, S., Haikala, L. K., et al. 1998, A&AS, 127, 1, doi: 10.1051/aas:1998105

Lemaître, G. 1927, Annales de la Société Scientifique de Bruxelles, 47, 49

Levasseur, A. C., & Blamont, J. E. 1973, Nature, 246, 26, doi: 10.1038/246026a0

Levasseur-Regourd, A. C. 1996, in Astronomical Society of the Pacific Conference Series, Vol. 104, IAU Colloq. 150: Physics, Chemistry, and Dynamics of Interplanetary Dust, ed. B. A. S. Gustafson & M. S. Hanner, 301

Li, J., Huang, S., Leauthaud, A., et al. 2022, MNRAS, 515, 5335, doi: 10.1093/mnras/stac2121

Li, S.-L., & Cao, X. 2008, MNRAS, 387, L41, doi: 10.1111/j.1745-3933.2008.00480.x

Low, F. J., Beintema, D. A., Gautier, T. N., et al. 1984, ApJL, 278, L19, doi: 10.1086/184213

Lucas, R. A., & Rose, S. 2021, in ACS Data Handbook v. 10.0, Vol. 10 (Space Telescope Science Institute), 10

Lumme, K., & Bowell, E. 1985, Icarus, 62, 54, doi: 10.1016/0019-1035(85)90171-X

Lynden-Bell, D. 1969, Nature, 223, 690, doi: 10.1038/223690a0

Lyu, J., Alberts, S., Rieke, G. H., & Rujopakarn, W. 2022, ApJ, 941, 191, doi: 10.3847/1538-4357/ac9e5d

Lyu, J., & Rieke, G. 2022, Universe, 8, 304, doi: 10.3390/universe8060304

Lyu, J., Alberts, S., Rieke, G. H., et al. 2023, arXiv e-prints, arXiv:2310.12330, doi: 10.48550/arXiv.2310.12330

Mack, J., Dahlen, T., Sabbi, E., & Bowers, . A. S. 2016, Space Telescope WFC3 Instrument Science Report

Mack, J., Lucas, R., Grogin, N., Koekemoer, R. B. . A., & Koekemoer, A. 2017, Space Telescope ACS Intrument Science Report

Mack, J., Olszewksi, H., & Pirzkal, N. 2021, Space Telescope WFC3 Instrument Science Report

Madau, P., & Silk, J. 2005, MNRAS, 359, L37, doi: 10.1111/j.1745-3933.2005.00031.x

Magorrian, J., Tremaine, S., Richstone, D., et al. 1998, AJ, 115, 2285, doi: 10.1086/300353

Mann, I., Krivov, A., & Kimura, H. 2000, Icarus, 146, 568, doi: 10.1006/icar.2000.6419

Matsumoto, T., Tsumura, K., Matsuoka, Y., & Pyo, J. 2018, AJ, 156, 86, doi: 10.3847/1538-3881/aad0f0

Matsumoto, T., Matsuura, S., Murakami, H., et al. 2005, The Astrophysical Journal, 626, 31–43, doi: 10.1086/429383

Matsumoto, T., Seo, H. J., Jeong, W.-S., et al. 2011, The Astrophysical Journal, 742, 124, doi: 10.1088/0004-637x/742/2/124

Matsuura, S., Arai, T., Bock, J. J., et al. 2017, The Astrophysical Journal, 839, 7, doi: 10.3847/1538-4357/aa6843

Matteucci, F., & Greggio, L. 1986, A&A, 154, 279

Maurer, A., Raue, M., Kneiske, T., et al. 2012, The Astrophysical Journal, 745, 166, doi: 10.1088/0004-637x/745/2/166

McIntyre, I. A., Carleton, T., O'Brien, R., et al. 2025, AJ, 169, 136, doi: 10.3847/1538-3881/ad946b

McKay, M., & Baggett, S. 2017, Space Telescope WFC3 Instrument Science Report

McMaster, M., & Biretta, J. 2010, WFPC2 Standard Star CTE, Instrument Science Report 2010-01, 16 pages

McVittie, G. C., & Wyatt, S. P. 1959, ApJ, 130, 1, doi: 10.1086/146688

Meftah, M., Damé, L., Bolsée, D., et al. 2018, A&A, 611, A1, doi: 10.1051/0004-6361/201731316

Meinke, J., Böckmann, K., Cohen, S., et al. 2021, ApJ, 913, 88, doi: 10.3847/1538-4357/abf2b4

—. 2023, ApJ, 952, 170, doi: 10.3847/1538-4357/ace532

Mihos, J. C. 2019, arXiv e-prints, arXiv:1909.09456. https://arxiv.org/abs/1909.09456

Miles, N. D., Deustua, S. E., Tancredi, G., et al. 2021, ApJ, 918, 86, doi: 10.3847/1538-4357/abfa9b

Miville-Deschênes, M.-A., & Lagache, G. 2005, ApJS, 157, 302, doi: 10.1086/427938

Morokuma, T., Doi, M., Yasuda, N., et al. 2008, ApJ, 676, 163, doi: 10.1086/527467

Nesvorný, D., Jenniskens, P., Levison, H. F., et al. 2010, ApJ, 713, 816, doi: 10.1088/0004-637X/713/2/816

O'Brien, R., Carleton, T., Windhorst, R. A., et al. 2023, AJ, 165, 237, doi: 10.3847/1538-3881/acccee

O'Brien, R., Jansen, R. A., Grogin, N. A., et al. 2024, ApJS, 272, 19, doi: 10.3847/1538-4365/ad3948

Odegard, N., Weiland, J. L., Fixsen, D. J., et al. 2019, ApJ, 877, 40, doi: 10.3847/1538-4357/ab14e8

Oesch, P. A., Brammer, G., van Dokkum, P. G., et al. 2016, ApJ, 819, 129, doi: 10.3847/0004-637X/819/2/129

Oke, J. B., & Gunn, J. E. 1983, ApJ, 266, 713, doi: 10.1086/160817

Ollmann, K., Wolf, S., Lietzow, M., & Stuber, T. A. 2023, A&A, 677, A187, doi: 10.1051/0004-6361/202347057

Onishi, Y., Sano, K., Matsuura, S., et al. 2018, PASJ, 70, 76, doi: 10.1093/pasj/psy070

Papovich, C., Shipley, H. V., Mehrtens, N., et al. 2016, ApJS, 224, 28, doi: 10.3847/0067-0049/224/2/28

Partridge, R. B., & Peebles, P. J. E. 1967a, ApJ, 147, 868, doi: 10.1086/149079

—. 1967b, ApJ, 148, 377, doi: 10.1086/149161

Planck Collaboration, Abergel, A., Ade, P. A. R., et al. 2014, A&A, 571, A11, doi: 10.1051/0004-6361/201323195

Planck Collaboration, Ade, P. A. R., Aghanim, N., et al. 2016a, A&A, 594, A13, doi: 10.1051/0004-6361/201525830

Planck Collaboration, Aghanim, N., Ashdown, M., et al. 2016b, A&A, 596, A109, doi: 10.1051/0004-6361/201629022

Planck Collaboration, Aghanim, N., Akrami, Y., et al. 2020a, A&A, 641, A6, doi: 10.1051/0004-6361/201833910

—. 2020b, A&A, 641, A3, doi: 10.1051/0004-6361/201832909

Poppe, A. R. 2016, Icarus, 264, 369, doi: 10.1016/j.icarus.2015.10.001

Poppe, A. R., Lisse, C. M., Piquette, M., et al. 2019, ApJL, 881, L12, doi: 10.3847/2041-8213/ab322a

Postman, M., Lauer, T. R., Parker, J. W., et al. 2024, arXiv e-prints, arXiv:2407.06273, doi: 10.48550/arXiv.2407.06273

Pouliasis, E., Georgantopoulos, I., Bonanos, A. Z., et al. 2019, MNRAS, 487, 4285, doi: 10.1093/mnras/stz1483

Rawes, J., Worrall, D. M., & Birkinshaw, M. 2015, MNRAS, 452, 3064, doi: 10.1093/mnras/stv1501

Reach, W. T., Franz, B. A., & Weiland, J. L. 1997, Icarus, 127, 461, doi: 10.1006/icar.1997.5704

Reach, W. T., Morris, P., Boulanger, F., & Okumura, K. 2003, Icarus, 164, 384, doi: 10.1016/S0019-1035(03)00133-7

Reach, W. T., Franz, B. A., Weiland, J. L., et al. 1995, Nature, 374, 521, doi: 10.1038/374521a0

Reines, A. E., Condon, J. J., Darling, J., & Greene, J. E. 2020, ApJ, 888, 36, doi: 10.3847/1538-4357/ab4999

Remazeilles, M., Delabrouille, J., & Cardoso, J.-F. 2011, MNRAS, 418, 467, doi: 10.1111/j.1365-2966.2011.19497.x

Renard, J. B., Levasseur-Regourd, A. C., & Dumont, R. 1995, A&A, 304, 602

Richard, E., Coddington, O., Harber, D., et al. 2024, Journal of Space Weather and Space Climate, 14, 10, doi: 10.1051/swsc/2024008

Riess, A. G., Filippenko, A. V., Challis, P., et al. 1998, AJ, 116, 1009, doi: 10.1086/300499

Riess, A. G., Anand, G. S., Yuan, W., et al. 2023, ApJL, 956, L18, doi: 10.3847/2041-8213/acf769

Rigby, J. R., Lightsey, P. A., García Marín, M., et al. 2023, PASP, 135, 048002, doi: 10.1088/1538-3873/acbcf4

Robitaille, T., Sipőcz, B., Tollerud, E., et al. 2022, AstroHuntsman/gunagala: v1.0.0, v1.0.0, Zenodo, doi: 10.5281/zenodo.6796532

Robotham, A. S. G., Davies, L. J. M., Driver, S. P., et al. 2018, MNRAS, 476, 3137, doi: 10.1093/mnras/sty440

Robotham, A. S. G., D'Silva, J. C. J., Windhorst, R. A., et al. 2023, PASP, 135, 085003, doi: 10.1088/1538-3873/acea42

Rodney, S. A., Riess, A. G., Strolger, L.-G., et al. 2014, AJ, 148, 13, doi: 10.1088/0004-6256/148/1/13

Roosen, R. G. 1970, Icarus, 13, 184, doi: 10.1016/0019-1035(70)90049-7

Rowan-Robinson, M., & May, B. 2013, MNRAS, 429, 2894, doi: 10.1093/mnras/sts471

Rowe, B. T. P., Jarvis, M., Mandelbaum, R., et al. 2015, Astronomy and Computing, 10, 121, doi: 10.1016/j.ascom.2015.02.002

Rudick, C. S., Mihos, J. C., & McBride, C. K. 2011, ApJ, 732, 48, doi: 10.1088/0004-637X/732/1/48

Ryon, J. E. 2019, in Advanced Camera for Surveys HST Instrument Handbook (Space Telescope Science Institute), 18

—. 2021, in ACS Instrument Handbook for Cycle 29 v. 20.0, Vol. 20 (Space Telescope Science Institute), 20

Sabbi, E., & Bellini, A. 2013, Space Telescope WFC3 Instrument Science Report

Saldana-Lopez, A., Domínguez, A., Pérez-González, P. G., et al. 2021, MNRAS, 507, 5144, doi: 10.1093/mnras/stab2393

Salvaterra, R., & Ferrara, A. 2003, MNRAS, 339, 973, doi: 10.1046/j.1365-8711.2003.06244.x

San, M., Galloway, M., Gjerløw, E., et al. 2024, arXiv e-prints, arXiv:2408.11004, doi: 10.48550/arXiv.2408.11004

Sano, K., Matsuura, S., Tsumura, K., et al. 2016, ApJL, 821, L11, doi: 10.3847/2041-8205/821/1/L11

Sano, K., Matsuura, S., Yomo, K., & Takahashi, A. 2020, ApJ, 901, 112, doi: 10.3847/1538-4357/abad3d

Santos, M. R., Bromm, V., & Kamionkowski, M. 2002, MNRAS, 336, 1082, doi: 10.1046/j.1365-8711.2002.05895.x

Sarajedini, V. L., Gilliland, R. L., & Kasm, C. 2003, ApJ, 599, 173, doi: 10.1086/379168

Sarajedini, V. L., Koo, D. C., Klesman, A. J., et al. 2011, ApJ, 731, 97, doi: 10.1088/0004-637X/731/2/97

Schlegel, D. J., Finkbeiner, D. P., & Davis, M. 1998, ApJ, 500, 525, doi: 10.1086/305772

Shakura, N. I., & Sunyaev, R. A. 1976, MNRAS, 175, 613, doi: 10.1093/mnras/175.3.613

Showalter, M. R., Hamilton, D. P., Stern, S. A., et al. 2011, Central Bureau Electronic Telegrams, 2769, 1

Showalter, M. R., Weaver, H. A., Stern, S. A., et al. 2012, IAU Circ., 9253, 1

Slipher, V. M. 1917, Proceedings of the American Philosophical Society, 56, 403

Smith, B. M., Windhorst, R. A., Jansen, R. A., et al. 2018, ApJ, 853, 191, doi: 10.3847/1538-4357/aaa3dc

Smith, B. M., Windhorst, R. A., Cohen, S. H., et al. 2020, ApJ, 897, 41, doi: 10.3847/1538-4357/ab8811

Smith, B. M., Windhorst, R. A., Teplitz, H., et al. 2024, arXiv e-prints. https://arxiv.org/abs/2401.03094

Sokolovsky, K. V., Gavras, P., Karampelas, A., et al. 2017, MNRAS, 464, 274, doi: 10.1093/mnras/stw2262

Somerville, R. S., Gilmore, R. C., Primack, J. R., & Domínguez, A. 2012, Monthly Notices of the Royal Astronomical Society, 423, 1992–2015, doi: 10.1111/j.1365-2966.2012.20490.x

Spiesman, W. J., Hauser, M. G., Kelsall, T., et al. 1995, ApJ, 442, 662, doi: 10.1086/175470

Stark, C. C., Roberge, A., Mandell, A., & Robinson, T. D. 2014, ApJ, 795, 122, doi: 10.1088/0004-637X/795/2/122

Stenborg, G., Gallagher, B., Howard, R. A., Hess, P., & Raouafi, N. E. 2021, ApJ, 910, 157, doi: 10.3847/1538-4357/abe623

Stetson, P. B. 1987, PASP, 99, 191, doi: 10.1086/131977

Symons, T., Zemcov, M., Cooray, A., Lisse, C., & Poppe, A. R. 2023, ApJ, 945, 45, doi: 10.3847/1538-4357/acaa37

Trevese, D., Kron, R. G., Majewski, S. R., Bershady, M. A., & Koo, D. C. 1994, ApJ, 433, 494, doi: 10.1086/174661

Tsumura, K., Matsumoto, T., Matsuura, S., et al. 2013, PASJ, 65, 120, doi: 10.1093/pasj/65.6.120

Tsumura, K., Battle, J., Bock, J., et al. 2010, ApJ, 719, 394, doi: 10.1088/0004-637X/719/1/394

Ulrich, M.-H., Maraschi, L., & Urry, C. M. 1997, ARA&A, 35, 445, doi: 10.1146/annurev.astro.35.1.445

Unterborn, C. T., & Ryden, B. S. 2008, ApJ, 687, 976, doi: 10.1086/591898

van de Hulst, H. C. 1947, The Astrophysical Journal, 105, 471, doi: 10.1086/144921

van der Wel, A., Franx, M., van Dokkum, P. G., et al. 2014, ApJ, 788, 28, doi: 10.1088/0004-637X/788/1/28

Vanden Berk, D. E., Wilhite, B. C., Kron, R. G., et al. 2004, ApJ, 601, 692, doi: 10.1086/380563

Villforth, C., Koekemoer, A. M., & Grogin, N. A. 2010, ApJ, 723, 737, doi: 10.1088/0004-637X/723/1/737

Villforth, C., Sarajedini, V., & Koekemoer, A. 2012, MNRAS, 426, 360, doi: 10.1111/j.1365-2966.2012.21732.x

Virtanen, P., Gommers, R., Oliphant, T. E., et al. 2020, Nature Methods, 17, 261, doi: 10.1038/s41592-019-0686-2

Weingartner, J. C., & Draine, B. T. 2001, ApJ, 548, 296, doi: 10.1086/318651

Whitaker, K. E., Labbé, I., van Dokkum, P. G., et al. 2011, ApJ, 735, 86, doi: 10.1088/0004-637X/735/2/86

Wilhite, B. C., Brunner, R. J., Grier, C. J., Schneider, D. P., & vanden Berk, D. E. 2008, MNRAS, 383, 1232, doi: 10.1111/j.1365-2966.2007.12655.x

Windhorst, R. A., Franklin, B. E., & Neuschaefer, L. W. 1994, PASP, 106, 798, doi: 10.1086/133443

Windhorst, R. A., Cohen, S. H., Hathi, N. P., et al. 2011, ApJS, 193, 27, doi: 10.1088/0067-0049/193/2/27

Windhorst, R. A., Carleton, T., O'Brien, R., et al. 2022, AJ, 164, 141, doi: 10.3847/1538-3881/ac82af

Windhorst, R. A., Cohen, S. H., Jansen, R. A., et al. 2023, AJ, 165, 13, doi: 10.3847/1538-3881/aca163

Windhorst, R. A., Summers, J., Carleton, T., et al. 2024, arXiv e-prints, arXiv:2410.01187, doi: 10.48550/arXiv.2410.01187

Wiser, L. S., Line, M. R., Welbanks, L., et al. 2024, ApJ, 971, 33, doi: 10.3847/1538-4357/ad5097

Witt, A. N., Mandel, S., Sell, P. H., Dixon, T., & Vijh, U. P. 2008, ApJ, 679, 497, doi: 10.1086/587131

Wold, M., Brotherton, M. S., & Shang, Z. 2007, MNRAS, 375, 989, doi: 10.1111/j.1365-2966.2006.11364.x

Wright, E. L. 1998, ApJ, 496, 1, doi: 10.1086/305345

Wright, E. L. 2001, The Astrophysical Journal, 553, 538–544, doi: 10.1086/320942

Xie, G.-Z., Chen, L.-E., Li, H.-Z., et al. 2005, Chinese J. Astron. Astrophys., 5, 463, doi: 10.1088/1009-9271/5/5/004

Yue, B., Ferrara, A., Salvaterra, R., Xu, Y., & Chen, X. 2013, Monthly Notices of the Royal Astronomical Society, 433, 1556–1566, doi: 10.1093/mnras/stt826

Zagury, F., Boulanger, F., & Banchet, V. 1999, A&A, 352, 645

Zemcov, M., Immel, P., Nguyen, C., et al. 2017, Nature Communications, 8, 15003, doi: 10.1038/ncomms15003

Zhao, X., Civano, F., Fornasini, F. M., et al. 2021a, VizieR Online Data Catalog, J/MNRAS/508/5176

—. 2021b, MNRAS, 508, 5176, doi: 10.1093/mnras/stab2885

Zhao, X., Civano, F., Willmer, C. N. A., et al. 2024, arXiv e-prints, arXiv:2402.13508. https://arxiv.org/abs/2402.13508

Zhong, Y., Inoue, A. K., Yamanaka, S., & Yamada, T. 2022, ApJ, 925, 157, doi: 10.3847/1538-4357/ac3edb

Zubko, V., Dwek, E., & Arendt, R. G. 2004, ApJS, 152, 211, doi: 10.1086/382351

Zuo, W., Wu, X.-B., Liu, Y.-Q., & Jiao, C.-L. 2012, ApJ, 758, 104, doi: 10.1088/0004-637X/758/2/104

APPENDIX A

INFORMATION ON PUBLISHED WORK

Chapter 2, titled "SKYSURF: Panchromatic HST All-Sky Surface-Brightness Measurement Methods and Results", was published as O'Brien et al. (2023) in the The Astronomical Journal, Volume 165, Issue 6, id.237, 25 pp. The authors on this paper are O'Brien, Carleton, Windhorst, Jansen, Carter, Tompkins, Caddy, Cohen, Abate, Arendt, Berkheimer, Calamida, Casertano, Driver, Gelb, Goisman, Grogin, Henningsen, Huckabee, Kenyon, Koekemoer, Kramer, Mackenty, Robotham, & Sherman.

Chapter 3, titled "TREASUREHUNT: Transients and Variability Discovered with HST in the JWST North Ecliptic Pole Time Domain Field", was published as O'Brien et al. (2024) in the The Astrophysical Journal Supplement Series, Volume 272, Issue 1, id.19, 27 pp. The authors on this paper are O'Brien, Jansen, Grogin, Cohen, Smith, Silver, Maksym, Windhorst, Carleton, Koekemoer, Hathi, Willmer, Frye, Alpaslan, Ashby, Ashcraft, Bonoli, Brisken, Cappelluti, Civano, Conselice, Dhillon, Driver, Duncan, Dupke, Elvis, Fazio, Finkelstein, Gim, Griffiths, Hammel, Hyun, Im, Jones, Kim, Ladjelate, Larson, Malhotra, Marshall, Milam, Pierel, Rhoads, Rodney, Röttgering, Rutkowski, Ryan, Ward, White, van Weeren, Zhao, Summers, D'Silva, Ortiz, Robotham, Coe, Nonino, Pirzkal, Yan, & Acharya.

Chapter 4, titled "A Zodiacal Light Model Optimized for Optical Wavelengths", will be published this year with Rosalia O'Brien as lead author.

All co-authors of these papers have granted permission to include these articles within this document.

APPENDIX B

ADDITIONAL ACKNOWLEDGMENTS

B.1 SKYSURF Acknowledgments

All of the data presented in this work was obtained from the Mikulski Archive for Space Telescopes (MAST). This project is based on observations made with the NASA/ESA Hubble Space Telescope and obtained from the Hubble Legacy Archive, which is a collaboration between the Space Telescope Science Institute (STScI/NASA), the Space Telescope European Coordinating Facility (ST-ECF/ESA), and the Canadian Astronomy Data Centre (CADC/NRC/CSA). Some image simulations were based on observations taken by the 3D-HST Treasury Program (GO 12177 and 12328) with the NASA/ESA HST, which is operated by the Association of Universities for Research in Astronomy, Inc., under NASA contract NAS5-26555.

We acknowledge support for HST programs AR-09955 and AR-15810 provided by NASA through grants from the Space Telescope Science Institute, which is operated by the Association of Universities for Research in Astronomy, Incorporated, under NASA contract NAS5-26555. Work by R.G.A. was supported by NASA under award number 80GSFC21M0002.

We especially thank the entire SKYSURF team for their contributions to making this project successful. We also thank the thoughtful for reviewer for the beneficial comments that helped clarify this work.

B.2 TREASUREHUNT Acknowledgments

We dedicate this work to the memory of Ms. Susan Selkirk, whose expert graphics skills helped showcase our HST and JWST images of the NEP TDF at ASU, NASA, and elsewhere.

RO, RAJ, RAW, SHC, AMK, NPH, BLF and CNAW acknowledge support from HST grants HST-GO-15278.*, 16252.* and 16793.* from the Space Telescope Science Institute, which is operated by the Association of Universities for Research in Astronomy, Inc. (AURA) under contract NAS 5-26555 from the National Aeronautics and Space Administration (NASA). RAJ, RAW and SHC also acknowledge support from NASA JWST Interdisciplinary Scientist grants NNX14AN10G, 80NSSC18K0200, NAG5-12460, and 21-SMDSS21-0013 from NASA Goddard Space Flight Center (GSFC).

CNAW acknowledges support from the NIRCam Development Contract NAS5-02105 from GSFC to the University of Arizona. DK acknowledges support from the National Research Foundation of Korea (NRF) grant funded by the Korean government (MSIT) (No. NRF-2022R1C1C2004506). M.H. acknowledges the support from the Korea Astronomy and Space Science Institute grant funded by the Korean government (MSIT) (No. 2022183005) and the support from the Global Ph.D. Fellowship Program through the National Research Foundation of Korea (NRF) funded by the Ministry

of Education (NRF-2013H1A2A1033110). S.B. acknowledges partial support from the project PID2021-124243NB-C21 funded by the Spanish Ministry of Science and Innovation. MI acknowledges the support from the National Research Foundation of Korea (NRF) grants, No. 2020R1A2C3011091, and No. 2021M3F7A1084525, funded by the Korea government (MSIT).

This work is based on observations associated with programs HST-GO-15278, 16252 and 16793 made with the NASA/ESA *Hubble* Space Telescope. We thank our Program Coordinator, Tricia Royle, for her expert help scheduling this HST program.

This work made use of observations associated with program JWST-GTO-2738 made with the NASA/ESA/CSA *James Webb* Space Telescope.

HST and JWST data were obtained from the Mikulski Archive for Space Telescopes (MAST) at the Space Telescope Science Institute, which is operated by the Association of Universities for Research in Astronomy, Inc., under NASA contracts NAS 5-26555 (HST) and NAS5-03127 (JWST). The specific observations analyzed can be accessed via https://doi.org/10.17909/wv13-qc14.

This work has also made use of data from the European Space Agency (ESA) mission Gaia (https://www.cosmos.esa.int/gaia), processed by the Gaia Data Processing and Analysis Consortium (DPAC, https://www.cosmos.esa.int/web/gaia/dpac/consortium). Funding for the DPAC has been provided by national institutions, in particular the institutions participating in the Gaia Multilateral Agreement.

This work has also made use of data obtained from the Chandra Data Archive and the Chandra Source Catalog, and software provided by the Chandra X-ray Center (CXC) in the application packages CIAO and Sherpa.

This research has made use of NASA's Astrophysics Data System (ADS) bibliographic services (Kurtz et al. 2000).